

# LHCb 小系统碰撞中 $\psi(2S)$ 和 $J/\psi$ 产额比的多重数依赖

## **Multiplicity dependence of $\psi(2S)$ -to- $J/\psi$ production ratio in small system collisions at LHCb**

(申请清华大学理学博士学位论文)

培养单位：工程物理系

学 科：物理学

研究 生：康有恩

指 导 教 师：朱相雷 副教授

二〇二四年五月



# **Multiplicity dependence of $\psi(2S)$ -to- $J/\psi$ production ratio in small system collisions at LHCb**

Dissertation submitted to

**Tsinghua University**

in partial fulfillment of the requirement

for the degree of

**Doctor of Philosophy**

in

**Physics**

by

**Youen Kang**

Dissertation Supervisor: Professor Xianglei Zhu

**May, 2024**



# 学位论文指导小组、公开评阅人和答辩委员会名单

## 指导小组名单

李 XX	教授	清华大学
王 XX	副教授	清华大学
张 XX	助理教授	清华大学

## 公开评阅人名单

无 (全隐名评  
阅)

## 答辩委员会名单

主席	CHEN SHAOMIN	教授	清华大学
委员	张黎明	副教授	清华大学
	朱相雷	副教授	清华大学
	钱文斌	教授	中国科学院大学
	杨振伟	教授	北京大学
秘书	王剑桥	助理研究员	清华大学



# 关于学位论文使用授权的说明

本人完全了解清华大学有关保留、使用学位论文的规定，即：

清华大学拥有在著作权法规定范围内学位论文的使用权，其中包括：（1）已获学位的研究生必须按学校规定提交学位论文，学校可以采用影印、缩印或其他复制手段保存研究生上交的学位论文；（2）为教学和科研目的，学校可以将公开的学位论文作为资料在图书馆、资料室等场所供校内师生阅读，或在校园网上供校内师生浏览部分内容；（3）根据《中华人民共和国学位条例暂行实施办法》及上级教育主管部门具体要求，向国家图书馆报送相应的学位论文。

本人保证遵守上述规定。

作者签名：\_\_\_\_\_

导师签名：\_\_\_\_\_

日 期：\_\_\_\_\_

日 期：\_\_\_\_\_



## 摘要

量子色动力学 (QCD) 预言在足够高的温度下物质将处在由解除囚禁的夸克和胶子形成的新物态——夸克胶子等离子体 (QGP)。在实验室中人们可通过高能重离子碰撞实验来产生并研究 QGP。近年来实验上在高多重数的质子-质子 ( $pp$ ) 以及质子-铅核 ( $p\text{Pb}$ ) 等小系统碰撞中也发现了若干 QGP 信号，但仍需其他独立测量对此进行检验。本论文基于大型强子对撞机底夸克探测器 (LHCb) 采集的  $pp$  和  $p\text{Pb}$  对撞数据，测量粲偶素截面比这一 QGP 信号随多重数的变化，研究碰撞中粲偶素的产生机制以及小系统反应动力学。

利用 LHCb 采集的质心系能量  $\sqrt{s} = 13 \text{ TeV}$ 、积分亮度  $658 \pm 13 \text{ pb}^{-1}$  的  $pp$  对撞数据，本论文分别测量了瞬发和来自底强子衰变的非瞬发  $\psi(2S)$  对  $J/\psi$  介子的截面比随多个碰撞多重数的变化。测量覆盖的粲偶素运动学区间是横动量  $0.3 < p_{\text{T}} < 20 \text{ GeV}/c$  和快度  $2.0 < y < 4.5$ 。发现各个快度和横动量区间的非瞬发的粲偶素截面比几乎不随碰撞多重数变化。而瞬发粲偶素截面比随多重数增大而显著下降，这一下降趋势对与粲偶素相同快度区间的多重数变化更为敏感，与同行粒子相互作用模型的理论预言符合较好。此外，低横动量区间的粲偶素截面比随多重数变化更为显著，而高横动量区间该截面比基本不随多重数变化。这些结果表明高多重数  $pp$  碰撞事例中粲偶素产生确实受到环境的显著影响。

利用 LHCb 采集的核子-核子质心系能量为  $\sqrt{s_{NN}} = 8.16 \text{ TeV}$ 、积分亮度为  $13.6 \pm 0.3 \text{ pb}^{-1}$  ( $p\text{Pb}$ ) 和  $20.8 \pm 0.5 \text{ pb}^{-1}$  ( $\text{Pb}p$ ) 的质子-铅核对撞数据，测量了瞬发和来自底强子衰变的非瞬发  $\psi(2S)$  对  $J/\psi$  介子的截面比随多个碰撞多重数的变化。测量覆盖的粲偶素运动学区间是横动量  $0 < p_{\text{T}} < 14 \text{ GeV}/c$  和快度  $1.5 < y^* < 4.5$  ( $p\text{Pb}$ ,  $\text{Pb}p$  是  $-5.5 < y^* < -2.5$ )。发现非瞬发的粲偶素截面比误差范围内不随碰撞多重数变化。在  $p\text{Pb}$  中，瞬发粲偶素截面比与  $pp$  碰撞类似，随多重数增大而显著下降。在  $\text{Pb}p$  中，瞬发粲偶素截面比不随多重数显著变化，但是截面比值低于  $p\text{Pb}$  和  $pp$ ，已经与  $\text{PbPb}$  碰撞中的截面比接近。这些测量结果清晰表明了瞬发粲偶素产额比的多重数依赖性，以及随着多重数持续增大而从小系统到大系统的平滑过渡。未来将进行更多相关测量系统研究粲偶素产生和压低机制的系统尺度依赖性。

**关键词：**相对论重离子碰撞；夸克胶子等离子体；重夸克偶素；多重数；LHCb 实验

## ABSTRACT

Quantum Chromodynamics (QCD) predicts that at sufficiently high temperatures, matter will exist in a new state formed by deconfined quarks and gluons, known as Quark-Gluon Plasma (QGP). In laboratory settings, QGP can be generated and studied through high-energy heavy-ion collision experiments. In recent years, several QGP signals have also been observed in small system collisions such as proton-proton ( $pp$ ) and proton-lead ( $p\text{Pb}$ ) collisions, but further independent measurements are required to verify these findings. This paper is based on data collected from  $pp$  and  $p\text{Pb}$  collision experiments using the Large Hadron Collider beauty detector (LHCb), measuring the ratio of charmonium cross-sections to study the variation of this QGP signal with multiplicity, investigating the production mechanisms of charmonium in collisions, and studying the dynamics of small systems reactions.

Using  $pp$  collision data with a center-of-mass energy of  $\sqrt{s} = 13 \text{ TeV}$  and an integrated luminosity of  $658 \pm 13 \text{ pb}^{-1}$  collected by LHCb, this paper measures the ratio of prompt and non-prompt  $\psi(2S)$  to  $J/\psi$  mesons cross-sections as a function of collision multiplicity. The measured kinematic range of charmonium covers transverse momentum  $0.3 < p_{\text{T}} < 20 \text{ GeV}/c$  and rapidity  $2.0 < y < 4.5$ . It is found that the non-prompt charmonium cross-section ratio shows little variation with collision multiplicity across different rapidity and transverse momentum intervals. However, the prompt charmonium cross-section ratio significantly decreases with increasing multiplicity, with this decrease being more pronounced in regions with similar rapidity intervals to the charmonium and exhibiting good agreement with theoretical predictions from models of charmonium interactions with co-produced particles. Additionally, the variation of charmonium cross-section ratio with multiplicity is more significant in the low transverse momentum region, while in the high transverse momentum region, this ratio remains largely unchanged. These results indicate a significant influence of the environment on charmonium production in high-multiplicity  $pp$  collision events.

Using proton-lead ( $p\text{Pb}$ ) collision data with a center-of-mass energy of  $\sqrt{s_{NN}} = 8.16 \text{ TeV}$  and integrated luminosities of  $13.6 \pm 0.3 \text{ pb}^{-1}$  ( $p\text{Pb}$ ) and  $20.8 \pm 0.5 \text{ pb}^{-1}$  ( $\text{Pb}p$ ) collected by LHCb, the paper measures the ratio of prompt and non-prompt  $\psi(2S)$  to  $J/\psi$  mesons cross-sections as a function of collision multiplicity. The measured kinematic

---

## ABSTRACT

---

range of charmonium covers transverse momentum  $0 < p_T < 14$  GeV/ $c$  and rapidity  $1.5 < y^* < 4.5$  ( $p\text{Pb}$ ,  $\text{Pb}p$  is  $-5.5 < y^* < -2.5$ ). The non-prompt charmonium cross-section ratio is found to remain constant within the error range across collision multiplicities. In  $p\text{Pb}$  collisions, the behavior of prompt charmonium cross-section ratio is similar to that in  $pp$  collisions, exhibiting a significant decrease with increasing multiplicity. In  $\text{Pb}p$  collisions, the prompt charmonium cross-section ratio does not show significant variation with multiplicity, but the ratio is lower than in  $p\text{Pb}$  and  $pp$  collisions, approaching the ratio observed in  $\text{PbPb}$  collisions. These measurements clearly demonstrate the multiplicity dependence of prompt charmonium yields and a smooth transition from small to large systems with increasing multiplicity. Future studies will further investigate the system-scale dependence of charmonium production and suppression mechanisms.

**Keywords:** Relativistic heavy-ion collisions; Quark-gluon plasma; Heavy quarkonium; Multiplicity; LHCb experiment

**TABLE OF CONTENTS**

摘要.....	I
ABSTRACT .....	II
TABLE OF CONTENTS .....	IV
LIST OF FIGURES.....	VIII
LIST OF TABLES .....	XVI
LIST OF SYMBOLS AND ACRONYMS .....	XIX
CHAPTER 1 INTRODUCTION.....	1
1.1 Standard Model .....	1
1.2 Quantum chromodynamics.....	2
1.3 Quark-gluon plasma.....	5
1.4 Heavy-ion collisions.....	7
1.5 QGP signatures in heavy-ion collisions .....	9
1.5.1 Parton energy loss.....	9
1.5.2 Collective flow.....	10
1.5.3 Strangeness enhancement .....	11
1.5.4 Quarkonium suppression .....	12
1.6 QGP signatures in small system collisions.....	13
1.7 Quarkonium production in $p\bar{p}$ collisions .....	16
1.7.1 Theoretical overview.....	16
1.7.2 Experimental results .....	21
1.8 Quarkonium production in $pA$ collisions.....	22
1.8.1 Theoretical overview.....	22
1.8.2 Experimental results .....	26
1.9 Quarkonium production in AA collisions .....	29
1.9.1 Theoretical overview.....	29
1.9.2 Experimental results .....	32
1.10 Quarkonium production in high multiplicity small system collisions.....	34
1.11 Motivation for this thesis.....	36

---

## TABLE OF CONTENTS

---

<b>CHAPTER 2 LHCb EXPERIMENT .....</b>	<b>38</b>
2.1 LHCb detector .....	39
2.2 Tracking system.....	40
2.2.1 Vertex Locator .....	40
2.2.2 Tracker Turicensis.....	42
2.2.3 T-stations .....	42
2.2.4 Magnet.....	44
2.2.5 Track reconstruction .....	45
2.3 Particle identification .....	47
2.3.1 Cherenkov detectors .....	47
2.3.2 Calorimeter.....	50
2.3.3 Muon stations .....	51
2.4 Trigger .....	53
2.4.1 L0 trigger.....	53
2.4.2 HLT .....	54
<b>CHAPTER 3 MULTIPLICITY DEPENDENCE OF <math>\sigma_{\psi(2S)}/\sigma_{J/\psi}</math> IN <math>pp</math> COLLISIONS</b>	<b>56</b>
3.1 Data and Monte Carlo samples .....	56
3.2 Analysis strategy.....	57
3.2.1 Multiplicity variables .....	58
3.3 Online and offline selections .....	60
3.3.1 Trigger and Turbo stream selections .....	60
3.3.2 Offline selections .....	61
3.4 Signal extraction .....	63
3.5 Efficiency determination.....	69
3.5.1 Geometrical acceptance .....	73
3.5.2 Reconstruction-selection efficiency.....	74
3.5.3 Muon identification efficiency .....	76
3.5.4 Trigger efficiency.....	77
3.5.5 Total efficiency.....	78
3.5.6 Variation due to different reweight samples .....	80
3.6 Systematic uncertainties .....	81
3.6.1 Uncertainty from signal extraction.....	82
3.6.2 Uncertainty from trigger efficiency .....	85

---

## TABLE OF CONTENTS

---

3.6.3 Uncertainty from tracking efficiency .....	86
3.6.4 Uncertainty from muonID efficiency .....	87
3.6.5 Uncertainty due to limit MC sample size .....	89
3.6.6 Other systematic uncertainties.....	90
<b>3.7 Results .....</b>	<b>91</b>
3.7.1 Multiplicity dependence of integrated production ratio.....	91
3.7.2 Multiplicity dependence in different kinematic regions.....	94
3.7.3 Comparisons with other measurements .....	96
<b>3.8 Conclusion.....</b>	<b>97</b>
 <b>CHAPTER 4 MULTIPLICITY DEPENDENCE OF <math>\sigma_{\psi(2S)}/\sigma_{J/\psi}</math> IN <math>p\text{PB}</math> COLLISIONS</b>	
99	
4.1 Data and simulated samples.....	99
4.2 Analysis strategy.....	100
4.3 Online and offline selection .....	101
4.3.1 Global Event Selections .....	101
4.3.2 Candidate Selection .....	103
4.4 Signal extraction .....	105
4.5 Efficiency ratio determination .....	106
4.5.1 Re-weight on Monte Carlo sample.....	107
4.5.2 Acceptance .....	109
4.5.3 Other efficiencies .....	110
4.5.4 Total efficiency.....	112
4.6 Systematic uncertainties .....	114
4.6.1 Monte Carlo statistics.....	114
4.6.2 Signal extraction.....	114
4.6.3 Trigger efficiency.....	115
4.6.4 Binning scheme of PID table .....	116
4.6.5 Summary of systematic uncertainties.....	116
4.7 Results .....	117
4.7.1 Multiplicity dependence of production ratio.....	117
4.7.2 Comparison in different collision systems .....	120
4.8 Conclusion.....	121

---

TABLE OF CONTENTS

---

CHAPTER 5 SUMMARY AND PROSPECT .....	123
5.1 Summary.....	123
5.2 Prospect.....	124
REFERENCES .....	125
RESULT TABLES OF $\psi(2S)$ -TO- $J/\psi$ RATIO IN $pp$ COLLISIONS.....	136
RESULT TABLES OF $\psi(2S)$ -TO- $J/\psi$ RATIO IN $p$ PB COLLISIONS .....	144
ACKNOWLEDGEMENTS.....	145
声    明.....	146
COMMENTS FROM THESIS SUPERVISOR.....	147
RESOLUTION OF THESIS DEFENSE COMMITTEE .....	148

## LIST OF FIGURES

Figure 1.1	Summary of elementary particles in the Standard Model. ....	2
Figure 1.2	Theoretical predictions and various measurements for $\alpha_S$ as function of $Q^2$ and $M_Z^2$ , taken from Ref <sup>[5]</sup> . ....	4
Figure 1.3	The normalized pressure, energy and entropy density as function of temperature, taken from Ref <sup>[7]</sup> . ....	5
Figure 1.4	A schematic phase diagram of strongly interacting matter as a function of baryon chemical potential and temperature. (From A. Steidl, Frankfurt University) <sup>[10]</sup> . ....	6
Figure 1.5	Time-evolution for the universe (up, taken from Particle Data Group <sup>[4]</sup> ) and heavy-ion collisions (down, taken from Ref <sup>[11]</sup> ). ....	7
Figure 1.6	Contour plot of the evolution of the energy density in a midcentral Au+Au collision at the highest RHIC energy $\sqrt{s_{NN}} = 200 \text{ GeV}$ . The horizontal axis shows the proper time $\tau$ , the vertical axis shows one of the transverse coordinates. The black dashed line delineates the hadronization hypersurface $T = T_c = 150 \text{ MeV}$ , taken from Ref <sup>[13]</sup> . ....	8
Figure 1.7	Nuclear modification factor $R_{AA}$ as function of $p_T$ for $D$ -meson in (left) PbPb collisions <sup>[21]</sup> and (right) AuAu collisions in different centrality classes <sup>[20]</sup> . Theoretical model prediction comes from Ref <sup>[24-32]</sup> ....	10
Figure 1.8	The azimuthal anisotropy parameter $v_2$ in different centrality classes from CMS <sup>[36]</sup> ....	11
Figure 1.9	The relative yield of $\Xi$ and $\Omega$ as function of number of participant $\langle N_{\text{part}} \rangle$ <sup>[39-41]</sup> ....	12
Figure 1.10	$\mathcal{B}\sigma/AB$ as function of $\eta$ , where $\mathcal{B}$ is branching ratio and $\eta \propto L$ , the average path length. Data are taken from NA3 <sup>[43]</sup> , NA51 <sup>[44]</sup> , NA38 <sup>[45-46]</sup> , and NA50 <sup>[47-48]</sup> . Figure is taken from Ref <sup>[49]</sup> ....	13
Figure 1.11	The $v_2$ values as function of reconstructed charged tracks $N_{\text{trk}}^{\text{offline}}$ <sup>[50]</sup> ...	14
Figure 1.12	Two-particle correlation of low-multiplicity sample (left) and high-multiplicity sample in $pp$ collisions <sup>[50]</sup> ....	14
Figure 1.13	Yield ratios of multi-strange particles to pion as function of charged primary tracks density in $pp$ and $p\text{Pb}$ collisions <sup>[51]</sup> ....	15

---

Figure 1.14	Integrated jet yield as function of self-normalized multiplicity for different resolution parameters $R$ <sup>[52]</sup> .....	16
Figure 1.15	The $p_T$ spectrum of $J/\psi$ and $\psi(2S)$ production in $pp$ collisions at $\sqrt{s} = 1.8$ TeV. The (dashed) curve is prediction by CSM. The cross section for $J/\psi$ is $\sim 6$ times higher and for $\psi(2S)$ is $\sim 50$ times higher than CSM prediction. Graph is taken from Ref <sup>[54]</sup> .....	17
Figure 1.16	The $\psi(2S)$ and $J/\psi$ differential cross section as function of transverse momentum .....	21
Figure 1.17	The $p_T$ -spectrum for non-prompt (left) $J/\psi$ and (right) $\psi(2S)$ production in 13 TeV $pp$ collisions, taken from Ref <sup>[64]</sup> .....	22
Figure 1.18	Illustration of the EPPS16 fit function $R_i^A(x, Q^2)$ <sup>[78]</sup> . .....	23
Figure 1.19	QCD evolution of gluons in phase space $Y$ and $\ln Q^2$ , taken from Ref <sup>[83]</sup> .....	24
Figure 1.20	The rapidity dependence (left) and $p_T$ dependence (right) of $J/\psi$ nuclear modification factor $R_{pA}$ by ALICE <sup>[93]</sup> , prediction model from Ref <sup>[87,94-99]</sup> .....	27
Figure 1.21	Nuclear modification factor in $p\text{Pb}$ collisions at 5 TeV from LHCb for prompt (left) and non-prompt (right) charmonia, top row for $J/\psi$ and bottom row for $\psi(2S)$ <sup>[100]</sup> .....	28
Figure 1.22	The $J/\psi$ nuclear modification factor $R_{pA}$ in $p\text{Au}$ collisions <sup>[92]</sup> .....	29
Figure 1.23	An illustrative sketch for sequential melting, figure taken from Ref <sup>[104]</sup> .....	30
Figure 1.24	Ratio of (left) number of $J/\psi$ to the number of continuum events, (right) production of $J/\psi$ to its Drell-Yan production, as function of transverse energy <sup>[115]</sup> .....	33
Figure 1.25	Centrality dependence of $J/\psi$ nuclear modification factor <sup>[116-118]</sup> .....	33
Figure 1.26	Multiplicity dependence of $R_{AA}$ for (left) different $\Upsilon$ states in $\text{PbPb}$ collisions <sup>[120]</sup> and (right) $J/\psi$ in $\text{AuAu}$ collisions <sup>[119]</sup> .....	34
Figure 1.27	The $\Upsilon(nS)/\Upsilon(1S)$ ratio as a function of charged track multiplicity in $pp$ collisions at LHC energies from CMS <sup>[121-122]</sup> .....	35
Figure 1.28	Multiplicity dependence of $\chi_{c1}(3872)/\psi(2S)$ in 8 TeV $pp$ collisions from LHCb <sup>[123]</sup> .....	35
Figure 1.29	Self normalised $\psi(2S)$ -to- $J/\psi$ yield ratio as function of self-normalised charged-particle multiplicity in $pp$ (left) and $p\text{Pb}$ collisions. Graph is taken from Ref <sup>[124]</sup> .....	36

---

LIST OF FIGURES

---

Figure 2.1	An illustrative schematic for LHC.	39
Figure 2.2	View of LHCb detector along the beam-going axis. The $z$ -axis is the beam-going direction, and the horizontal $x$ -axis and vertical $y$ -axis form a roght-hand coordinate system. Figure is taken from Ref <sup>[127]</sup> , figure is taken from Ref <sup>[126]</sup>	40
Figure 2.3	Cross-sectional view of VELO, figure is taken from Ref <sup>[126]</sup>	41
Figure 2.4	PV resolution for one PV reconstructed as function of charged tracks Ref <sup>[126]</sup>	41
Figure 2.5	Layout of Tracker Turicensis, figure is taken from Ref <sup>[126]</sup>	42
Figure 2.6	Layout of IT, figure is taken from Ref <sup>[126]</sup>	43
Figure 2.7	(left) Cross-sectional view of straw-tube and (right) layout for OT, figure is taken from Ref <sup>[133]</sup>	43
Figure 2.8	Perspective view of magnet system in LHCb, figure is taken from Ref <sup>[126]</sup>	44
Figure 2.9	Illustration for different track types, figure is taken from Ref <sup>[125]</sup>	46
Figure 2.10	Tracking efficiency as functions of momentum $p$ , pseudorapidity $\eta$ , number of tracks $N_{\text{tracks}}$ and number of PV reconstructed $N_{\text{PV}}$ , figure is taken from Ref <sup>[125]</sup>	46
Figure 2.11	Side view for (left) RICH1 and (right) RICH2, figure is taken from Ref <sup>[133]</sup>	49
Figure 2.12	Cherenkov angle versus particle momentum in different media, figure is taken from Ref <sup>[133]</sup>	49
Figure 2.13	The (upper) layout and cell segmentation for calorimeter system in LHCb detector, figure is taken from Ref <sup>[141]</sup>	50
Figure 2.14	Side view of muon system, figure is taken from Ref <sup>[141]</sup>	52
Figure 2.15	PID efficiency and misID rate of IsMuon as a function of momentum in different transverse momentum regions, figure is taken from Ref <sup>[144]</sup>	53
Figure 2.16	Trigger scheme for LHCb detector, figure is taken from Ref <sup>[147]</sup>	54
Figure 3.1	Multiplicity distribution in no-bias data.	59
Figure 3.2	The two-dimensional distribution of $(N_{\text{tracks}}^{\text{PV}}, N_{\text{ch}})$ for prompt $J/\psi$ .	60
Figure 3.3	Distribution of $N_{\text{tracks}}^{\text{PV}}$ , $N_{\text{bwd}}^{\text{PV}}$ and $N_{\text{fwd}}^{\text{PV}}$ under $n\text{PVs} = 1$ for $J/\psi$ (left) and $\psi(2S)$ (right) data samples. The events with $z_{\text{PV}}$ smaller than a certain range show clear deviation, hence are rejected to guarantee a uniform VELO acceptance for charged tracks.	63

---

LIST OF FIGURES

---

Figure 3.4	The background $t_z$ fit for $20 \leq N_{\text{tracks}}^{\text{PV}} < 45$ , $2 < y < 2.8$ and $2 < p_T < 4 \text{ GeV}/c$ . The left is for $J/\psi$ and the right s for $\psi(2S)$ . ....	66
Figure 3.5	Projection in (top) $t_z$ and (bottom) mass spectrum of $t_z$ -mass fit for $20 \leq N_{\text{tracks}}^{\text{PV}} < 40$ , $2 < y < 2.8$ and $2 < p_T < 4 \text{ GeV}/c$ , with left column for $J/\psi$ and right column for $\psi(2S)$ . ....	68
Figure 3.6	The (left) prompt and (right) non-prompt yields for $J/\psi$ and $\psi(2S)$ in $4 \leq N_{\text{tracks}}^{\text{PV}}$ ....	68
Figure 3.7	Reweighting the multiplicity distribution to match MC to s-weighted data, the left column is for prompt $J/\psi$ and the right column is for non-prompt $J/\psi$ . ....	70
Figure 3.8	Reweighting the multiplicity distribution to match MC to s-weighted data, the left column is for prompt $\psi(2S)$ and the right column is for non-prompt $\psi(2S)$ .....	71
Figure 3.9	The $p_T$ -y reweight in rapidity range $2 < y < 2.25$ for prompt $J/\psi$ (left) and prompt $\psi(2S)$ (right). ....	72
Figure 3.10	The $p_T$ -y reweight in $2 < y < 4.5$ and $0 < p_T < 20 \text{ GeV}/c$ for $J/\psi$ , each subplot represents the $p_T$ reweight in each $y$ bin of width 0.25. The top two rows are for prompt $J/\psi$ and the bottom two rows are for non-prompt $J/\psi$ . ....	72
Figure 3.11	The $p_T$ -y reweight in $2 < y < 4.5$ and $0 < p_T < 20 \text{ GeV}/c$ for $\psi(2S)$ , each subplot represents the $p_T$ reweight in each $y$ bin of width 0.25. The top two rows are for prompt $\psi(2S)$ and the bottom two rows are for non-prompt $\psi(2S)$ . ....	73
Figure 3.12	Geometrical acceptance efficiency for (left) $J/\psi$ and (right) $\psi(2S)$ in multiplicity bin $4 \leq N_{\text{tracks}}^{\text{PV}} < 20$ , the top row is for prompt and the bottom row is for non-prompt components.....	74
Figure 3.13	Tracking efficiency ratio between data and MC2016 simulation in bins of $p_\mu$ and $\eta_\mu$ of the muon. ....	75
Figure 3.14	Reconstruction and selection efficiency for (left) $J/\psi$ and (right) $\psi(2S)$ in multiplicity bin $4 \leq N_{\text{tracks}}^{\text{PV}} < 20$ . The top row is for prompt and the bottom row is for non-prompt components.....	76
Figure 3.15	PID efficiency for (left) $J/\psi$ and (right) $\psi(2S)$ in multiplicity bin $4 \leq N_{\text{tracks}}^{\text{PV}} < 20$ . The top row is for prompt and the bottom row is for non-prompt components. ....	77

---

LIST OF FIGURES

---

Figure 3.16	Trigger efficiency for (left) $J/\psi$ and (right) $\psi(2S)$ in multiplicity bin $4 \leq N_{\text{tracks}}^{\text{PV}} < 20$ . The top row is for prompt and the bottom row is for non-prompt components. ....	78
Figure 3.17	Total efficiency for (left) $J/\psi$ and (right) $\psi(2S)$ in multiplicity bin $4 \leq N_{\text{tracks}}^{\text{PV}} < 20$ . The top row is for prompt and the bottom row is for non-prompt components. ....	79
Figure 3.18	Total efficiency for (left) $J/\psi$ and (right) $\psi(2S)$ in multiplicity bin $95 \leq N_{\text{tracks}}^{\text{PV}} < 200$ . The top row is for prompt and the bottom row is for non-prompt components. ....	80
Figure 3.19	Two-dimensional ( $p_T$ , $y$ ) distribution for prompt and non-prompt components of different samples (high-multiplicity sample in red). ....	81
Figure 3.20	Distribution of the variation due to different reweight samples recorded in times of the statistical uncertainty. ....	81
Figure 3.21	The systematic uncertainty of $\psi(2S)$ to $J/\psi$ production ratio due to the fit model in multiplicity bin $4 \leq N_{\text{tracks}}^{\text{PV}} < 20$ . ....	83
Figure 3.22	The systematic uncertainty of (left) prompt and (right) non-prompt production ratio due to $t_z$ background fit model in multiplicity bin $4 \leq N_{\text{tracks}}^{\text{PV}} < 20$ . ....	84
Figure 3.23	The systematic uncertainty of (left) prompt and (right) non-prompt production ratio due to $t_z$ signal fit model in multiplicity bin $4 \leq N_{\text{tracks}}^{\text{PV}} < 20$ . ....	84
Figure 3.24	Summary of Systematic Uncertainties of ratio due to uncertainty of $\epsilon_{\text{trigger}}$ in differet multiplicity region. ....	85
Figure 3.25	Systematic uncertainties of ratio due to uncertainty of $\epsilon_{\text{trigger}}$ ind ifferent $p_T$ regions. ....	86
Figure 3.26	The systematic uncertainty of (left) prompt and (right) non-prompt production ratio due to the uncertainty of track table in multiplicity bin $4 \leq N_{\text{tracks}}^{\text{PV}} < 20$ . ....	87
Figure 3.27	The systematic uncertainty of (left) prompt and (right) non-prompt production ratio due to the statistical uncertainty of PID efficiency in multiplicity bin $4 \leq N_{\text{tracks}}^{\text{PV}} < 20$ . ....	88

---

Figure 3.28	The systematic uncertainty of (left) prompt and (right) non-prompt production ratio due to the binning scheme of calibration sample in multiplicity bin $4 \leq N_{\text{tracks}}^{\text{PV}} < 20$ . ....	89
Figure 3.29	The systematic uncertainty of (left) prompt and (right) non-prompt production ratio due to limit sample size in multiplicity bin $4 \leq N_{\text{tracks}}^{\text{PV}} < 20$ . ....	89
Figure 3.30	Normalised production ratio as a function of $N_{\text{tracks}}^{\text{PV}}/\langle N_{\text{tracks}}^{\text{PV}} \rangle_{\text{NB}}$ , integrated over the full $p_{\text{T}}\text{-}y$ range of $2.0 < y < 4.5$ and $0.3 < p_{\text{T}} < 20$ GeV/c with $-60 < z_{\text{PV}} < 180$ mm. The error bars represent statistical uncertainties and the boxes represent systematical uncertainties. ....	92
Figure 3.31	Normalised production ratio as a function of $N_{\text{bwd}}^{\text{PV}}/\langle N_{\text{bwd}}^{\text{PV}} \rangle_{\text{NB}}$ (left, with $-30 < z_{\text{PV}} < 180$ mm) and $N_{\text{fwd}}^{\text{PV}}/\langle N_{\text{fwd}}^{\text{PV}} \rangle_{\text{NB}}$ (right, with $-180 < z_{\text{PV}} < 180$ mm), integrated over the full $p_{\text{T}}\text{-}y$ range of $2.0 < y < 4.5$ and $0.3 < p_{\text{T}} < 20$ GeV/c. ....	92
Figure 3.32	The two-dimensional distribution of $(N_{\text{fwd}}^{\text{PV}}, N_{\text{bwd}}^{\text{PV}})$ for prompt $\psi(2S)$ ....	93
Figure 3.33	Normalised production ratio as a function of $N_{\text{fwd}}^{\text{PV}}/\langle N_{\text{fwd}}^{\text{PV}} \rangle_{\text{NB}}$ , compared to a translation of the ratio as a function of $N_{\text{bwd}}^{\text{PV}}/\langle N_{\text{bwd}}^{\text{PV}} \rangle_{\text{NB}}$ . ....	93
Figure 3.34	Normalised production ratio as a function of $dN_{\text{ch}}/d\eta$ . The width for the shaded box is the systematic uncertainty for $dN_{\text{ch}}/d\eta$ . ....	94
Figure 3.35	Normalised production ratio for (left) prompt and (right) non-prompt charmonia as a function of $N_{\text{tracks}}^{\text{PV}}/\langle N_{\text{tracks}}^{\text{PV}} \rangle_{\text{NB}}$ in different $p_{\text{T}}$ intervals, integrated over $y$ range of 2 to 4.5. ....	94
Figure 3.36	Normalised production ratio for (left) prompt and (right) non-prompt charmonia as a function of $N_{\text{fwd}}^{\text{PV}}/\langle N_{\text{fwd}}^{\text{PV}} \rangle_{\text{NB}}$ in different $p_{\text{T}}$ intervals, integrated over $y$ range of 2 to 4.5. ....	95
Figure 3.37	Normalised production ratio for (left) prompt and (right) non-prompt charmonia as a function of $N_{\text{bwd}}^{\text{PV}}/\langle N_{\text{bwd}}^{\text{PV}} \rangle_{\text{NB}}$ in different $p_{\text{T}}$ intervals, integrated over $y$ range of 2 to 4.5. ....	95
Figure 3.38	Normalised production ratio for (left) prompt and (right) non-prompt charmonia as a function of $N_{\text{tracks}}^{\text{PV}}/\langle N_{\text{tracks}}^{\text{PV}} \rangle_{\text{NB}}$ in different $y$ intervals.....	95
Figure 3.39	Normalised production ratio for (left) prompt and (right) non-prompt charmonia as a function of $N_{\text{fwd}}^{\text{PV}}/\langle N_{\text{fwd}}^{\text{PV}} \rangle_{\text{NB}}$ in different $y$ intervals.....	96

---

Figure 3.40	Normalised production ratio for (left) prompt and (right) non-prompt charmonia as a function of $N_{\text{bwd}}^{\text{PV}}/\langle N_{\text{bwd}}^{\text{PV}} \rangle_{\text{NB}}$ in different $y$ intervals.....	96
Figure 3.41	Production ratios compared to existing measurements <sup>[166]</sup> .....	97
Figure 3.42	Production ratios as a function of $p_{\text{T}}$ compared to existing measurements <sup>[166]</sup> and NRQCD models.....	97
Figure 4.1	The (left) $p\text{Pb}$ and (right) $\text{Pbp}$ configurations for proton-lead collisions ..	99
Figure 4.2	Multiplicity distribution in different $z_{\text{PV}}$ regions in (left) $p\text{Pb}$ and (right) $\text{Pbp}$ collisions. ....	102
Figure 4.3	The distribution of $N_{\text{tracks}}^{\text{PV}}$ , $N_{\text{fwd}}^{\text{PV}}$ and $N_{\text{bwd}}^{\text{PV}}$ in (left) $p\text{Pb}$ and (right) $\text{Pbp}$ no-bias data. ....	103
Figure 4.4	Mass spectrum of $\psi(2S)$ after online and offline cuts with loose PID cut (blue) and tight PID cut (red). The first row is for lowest-multiplicity class and the second row is for highest-multiplicity class.....	104
Figure 4.5	Two-dimensional fit projected on (top) $t_z$ spectrum and (bottom) mass spectrum for (left) $J/\psi$ and (right) $\psi(2S)$ (right) for $4 \leq N_{\text{tracks}}^{\text{PV}} < 45$ in $p\text{Pb}$ configuration.....	105
Figure 4.6	Prompt and non-prompt yields for $J/\psi$ and $\psi(2S)$ in $p\text{Pb}$ collisions. ....	106
Figure 4.7	Distribution of multiplicity variables for s-weighted (left column) data and (right column) MC samples in $p\text{Pb}$ configuration. ....	107
Figure 4.8	Re-weight of (top) $p_{\text{T}}$ and (bottom) $y^*$ for (left) high- (left) and low- $N_{\text{tracks}}^{\text{PV}}$ for $J/\psi$ MC samples in $p\text{Pb}$ configuration.....	108
Figure 4.9	Re-weight of (top) $p_{\text{T}}$ and (bottom) $y^*$ for (left) high- (left) and low- $N_{\text{tracks}}^{\text{PV}}$ for $\psi(2S)$ MC samples in $p\text{Pb}$ configuration.....	109
Figure 4.10	The distribution of $\psi(2S)$ to $J/\psi$ acceptance efficiency ratio, $R_c c$ , from 100 trials of reweighting tables with $N_{\text{tracks}}^{\text{PV}}$ as multiplicity variables. ....	110
Figure 4.11	Ratio between data and $p\text{Pb}$ (left) and $\text{Pbp}$ simulation of per-track tracking efficiency in bins of the track $\eta$ and $p$ . ....	111
Figure 4.12	Fit Gaussian functions on the distributions of 1000-trial $R_{eff}$ 's in different $N_{\text{tracks}}^{\text{PV}}$ classes. ....	113
Figure 4.13	The statistical uncertainties and the systematic uncertainty of $\psi(2S)$ -to- $J/\psi$ ratio arised from different signal models.....	115
Figure 4.14	Normalized $\psi(2S)$ -to- $J/\psi$ ratio as function of normalized $N_{\text{tracks}}^{\text{PV}}$ in (left) $p\text{Pb}$ (right) $\text{Pbp}$ collisions. ....	118

---

LIST OF FIGURES

---

Figure 4.15	$\psi(2S)$ -to- $J/\psi$ ratio as function of normalized $N_{\text{tracks}}^{\text{PV}}$ .....	118
Figure 4.16	Normalized $\psi(2S)$ -to- $J/\psi$ ratio as function of normalized $N_{\text{fwd}}^{\text{PV}}$ in (left) $p\text{Pb}$ (right) $\text{Pbp}$ collisions.....	119
Figure 4.17	The $\psi(2S)$ -to- $J/\psi$ ratio as function of normalized $N_{\text{fwd}}^{\text{PV}}$ in $p\text{Pb}$ and $\text{Pbp}$ collisions.....	119
Figure 4.18	Normalized $\psi(2S)$ -to- $J/\psi$ ratio as function of normalized $N_{\text{bwd}}^{\text{PV}}$ in (left) $p\text{Pb}$ and (right) $\text{Pbp}$ collisions. ....	120
Figure 4.19	The $\psi(2S)$ -to- $J/\psi$ ratio as function of normalized $N_{\text{bwd}}^{\text{PV}}$ in $p\text{Pb}$ and $\text{Pbp}$ collisions.....	120
Figure 4.20	Comparisons on the ratio of $\psi(2S)/J/\psi$ in $pp$ , $p\text{Pb}$ ( $\text{Pbp}$ ) and $\text{PbPb}$ colli- sions <sup>[178]</sup> .....	121

**LIST OF TABLES**

Table 3.1	Mean values of the three multiplicity variables in no-bias data.....	59
Table 3.2	Selection criteria in the high level trigger lines .....	61
Table 3.3	Summary of Offline Selections.....	62
Table 3.4	Summary of systematic uncertainties for the double-differential $\psi(2S)$ -to- $J/\psi$ cross-section ratio in different multiplicity bins (in %). Sources marked with † are considered to be correlated between bins. ....	90
Table 4.1	Binning schemes for different multiplicity variables. ....	101
Table 4.2	Global cuts on $z_{PV}$ .....	101
Table 4.3	Offline selections for $J/\psi$ and $\psi(2S)$ .....	104
Table 4.4	$R_{eff}$ in different $N_{\text{tracks}}^{\text{PV}}$ regions in $p\text{Pb}$ configuration.....	112
Table 4.5	Systematic uncertainty of $\epsilon_{\text{Trigger}}$ obtained by TISTOS method. ....	116
Table 4.6	Summary of systematic uncertainties on $\psi(2S)$ -to- $J/\psi$ cross-section ratio. Sources marked with † are considered to be correlated.....	117
Table 5.1	Ratios (%) of double differential production cross-section for $\psi(2S)$ to $J/\psi$ in bins of $(p_T, y)$ for $4 \leq N_{\text{tracks}}^{\text{PV}} < 20$ . The first uncertainties are statistical, the second are systematic.....	136
Table 5.2	Ratios (%) of double differential production cross-section for $\psi(2S)$ to $J/\psi$ in bins of $(p_T, y)$ for $20 \leq N_{\text{tracks}}^{\text{PV}} < 45$ . The first uncertainties are statistical, the second are systematic.....	136
Table 5.3	Ratios (%) of double differential production cross-section for $\psi(2S)$ to $J/\psi$ in bins of $(p_T, y)$ for $45 \leq N_{\text{tracks}}^{\text{PV}} < 70$ . The first uncertainties are statistical, the second are systematic.....	137
Table 5.4	Ratios (%) of double differential production cross-section for $\psi(2S)$ to $J/\psi$ in bins of $(p_T, y)$ for $70 \leq N_{\text{tracks}}^{\text{PV}} < 95$ . The first uncertainties are statistical, the second are systematic.....	137
Table 5.5	Ratios (%) of double differential production cross-section for $\psi(2S)$ to $J/\psi$ in bins of $(p_T, y)$ for $95 \leq N_{\text{tracks}}^{\text{PV}} < 200$ . The first uncertainties are statistical, the second are systematic.....	138

---

LIST OF TABLES

---

Table 5.6	Ratios (%) of double differential production cross-section for $\psi(2S)$ to $J/\psi$ in bins of $(p_T, y)$ for $0 \leq N_{\text{bwd}}^{\text{PV}} < 8$ . The first uncertainties are statistical, the second are systematic. ....	138
Table 5.7	Ratios (%) of double differential production cross-section for $\psi(2S)$ to $J/\psi$ in bins of $(p_T, y)$ for $8 \leq N_{\text{bwd}}^{\text{PV}} < 15$ . The first uncertainties are statistical, the second are systematic. ....	139
Table 5.8	Ratios (%) of double differential production cross-section for $\psi(2S)$ to $J/\psi$ in bins of $(p_T, y)$ for $15 \leq N_{\text{bwd}}^{\text{PV}} < 22$ . The first uncertainties are statistical, the second are systematic. ....	139
Table 5.9	Ratios (%) of double differential production cross-section for $\psi(2S)$ to $J/\psi$ in bins of $(p_T, y)$ for $22 \leq N_{\text{bwd}}^{\text{PV}} < 30$ . The first uncertainties are statistical, the second are systematic. ....	140
Table 5.10	Ratios (%) of double differential production cross-section for $\psi(2S)$ to $J/\psi$ in bins of $(p_T, y)$ for $30 \leq N_{\text{bwd}}^{\text{PV}} < 80$ . The first uncertainties are statistical, the second are systematic. ....	140
Table 5.11	Ratios (%) of double differential production cross-section for $\psi(2S)$ to $J/\psi$ in bins of $(p_T, y)$ for $0 \leq N_{\text{fwd}}^{\text{PV}} < 12$ . The first uncertainties are statistical, the second are systematic. ....	141
Table 5.12	Ratios (%) of double differential production cross-section for $\psi(2S)$ to $J/\psi$ in bins of $(p_T, y)$ for $12 \leq N_{\text{fwd}}^{\text{PV}} < 24$ . The first uncertainties are statistical, the second are systematic. ....	141
Table 5.13	Ratios (%) of double differential production cross-section for $\psi(2S)$ to $J/\psi$ in bins of $(p_T, y)$ for $24 \leq N_{\text{fwd}}^{\text{PV}} < 36$ . The first uncertainties are statistical, the second are systematic. ....	142
Table 5.14	Ratios (%) of double differential production cross-section for $\psi(2S)$ to $J/\psi$ in bins of $(p_T, y)$ for $36 \leq N_{\text{fwd}}^{\text{PV}} < 48$ . The first uncertainties are statistical, the second are systematic. ....	142
Table 5.15	Ratios (%) of double differential production cross-section for $\psi(2S)$ to $J/\psi$ in bins of $(p_T, y)$ for $48 \leq N_{\text{fwd}}^{\text{PV}} < 130$ . The first uncertainties are statistical, the second are systematic. ....	143
Table 5.16	Ratio(%) of production cross-section for $\psi(2S)$ to $J/\psi$ . The first uncertainties are statistical, the second are the systematic uncertainties. ....	144

---

LIST OF TABLES

---

Table 5.17	Ratio(%) of production cross-section for $\psi(2S)$ to $J/\psi$ . The first uncertainties are statistical, the second are the systematic uncertainties. ....	144
Table 5.18	Ratio(%) of production cross-section for $\psi(2S)$ to $J/\psi$ . The first uncertainties are statistical, the second are the systematic uncertainties. ....	144

## LIST OF SYMBOLS AND ACRONYMS

2D	Two Dimensional
ALICE	An experiment at the Large Hadron Collider
ATLAS	An experiment at the Large Hadron Collider
BNL	Brookhaven National Laboratory
CB	Crystal Ball function
CDF	An experiment at the Tevatron
(I)CEM	(Improved) Color Evaporation Model
CERN	European Organisation for Nuclear Research
CIM	Comover Interaction Model
CGC	Color Glass Condensate
CMS	An experiment at the Large Hadron Collider
CNM	Cold Nuclear Matter effect
COM	Color-Octet Model
CSM	Color-Singlet Model
DIS	Deep Inelastic Scattering
ECAL	Electromagnetic CALorimeter
HCAL	Hadronic CALorimeter
HLT	High-Level Trigger implemented in software
HNM	Hot Nuclear Matter effect
IP	Impact Parameter
IT	Inner Tracker
L0	Level-0 trigger implemented in hardware
LDME	Long-Distance Matrix Element
LHC	Large Hadron Collider
LHCb	An experiment at the Large Hadron Collider
LO	Leading Order
MagDown	Magnet field direction pointing Downward
MagUp	Magnet field direction pointing Upward
MC	Monte Carlo
NA(number)	An experiment at the Super Proton Synchrotron
NLL	Next-to-Leading Logarithms
NLO	Next-to-Leading Order

---

LIST OF SYMBOLS AND ACRONYMS

---

NNLO	Next-to-Next-to-Leading Order
NRQCD	Non-Relativistic Quantum ChromoDynamics
nSPDHits	Number of hits in the Scintillating-Pad Detector
OT	Outer Tracker
(n)PDF	(nuclear) Parton Distribution Function
$pA$	Proton-Nucleus
PID	Particle IDentification
$pp$	Proton-Proton
PS	PreShower detector
PV	Primary Vertex
QCD	Quantum ChromoDynamics
QED	Quantum ElectroDynamics
QGP	Quark-Gluon Plasma
RICH	Ring-Imaging CHerenkov detector
Run 1	First period of operation of the Large Hadron Collider
Run 2	Second period of operation of the Large Hadron Collider
Run 3	Third period of operation of the Large Hadron Collider
SM	Standard Model of particle physics
SPD	Scintillating-Pad Detector
T-stations	Tracking stations downstream of the magnet
SPS	The Super Proton Synchrotron
TIS	Trigger Independent of Signal
TMD	Transverse Momentum Dependent
TOS	Trigger On Signal
TT	Tracker Turicensis
VELO	VErtex LOcator

# CHAPTER 1 INTRODUCTION

## 1.1 Standard Model

The Standard Model (SM) of particle physics is a theoretical framework that describes the fundamental particles and forces of the universe. It stands as the most successful theory in the field of particle physics, has been developed and refined over many decades, and verified by numerous experiments.

The elementary particles within SM are classified into three principal categories. Fermions with spin 1/2 are the building blocks of matter, gauge bosons with spin 1 are force carriers that mediate interactions between particles, and Higgs boson with spin 0, was discovered at CERN's Large Hadron Collider (LHC) in 2012<sup>[1]</sup>, confirming its role in endowing elementary particles with mass via the Higgs mechanism.

Fermions are categorized into quarks and leptons. Quarks come in six flavors: up ( $u$ ), down ( $d$ ), charm ( $c$ ), strange ( $s$ ), top ( $t$ ), and bottom ( $b$ ). They are found inside hadrons or produced in particle collisions. Leptons are light elementary particles, starting with the discovery of the electron ( $e$ ) by J.J. Thomson. Neutrinos were proposed by Wolfgang Pauli to conserve energy in  $\beta$ -decay. The muon ( $\mu$ ) was discovered by Carl D. Anderson. The tau ( $\tau$ ) and its neutrino were discovered in the late 20th century. The discovery of different quarks has been a milestone in understanding the composition of matter.

Bosons are force carriers that mediate interactions between particles. The photon ( $\gamma$ ) mediates the electromagnetic force. Gluons bind quarks together through strong interactions, and  $W$  and  $Z$  bosons mediate weak nuclear interactions, responsible for processes like beta decay. The properties of **three types of** elementary particles are summarized in Fig 1.1.

## Standard Model of Elementary Particles

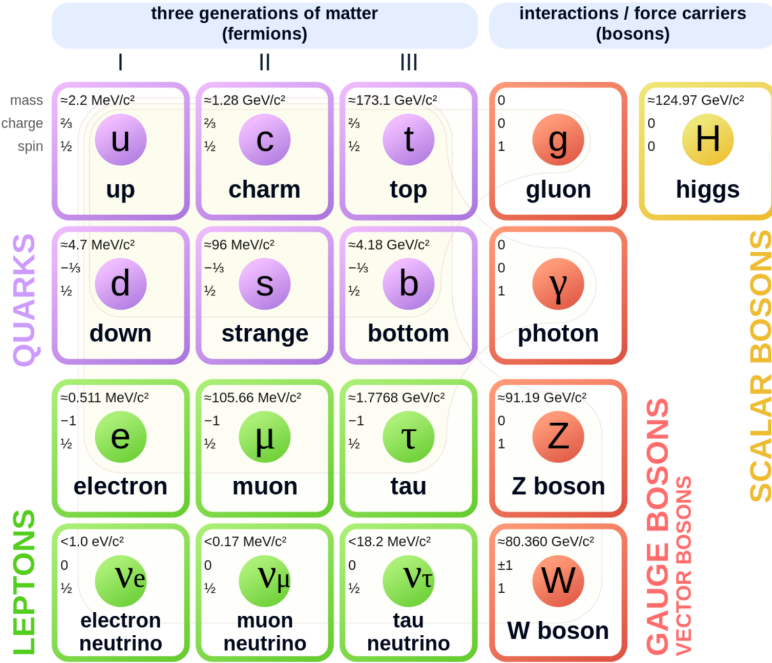


Figure 1.1 Summary of elementary particles in the Standard Model.

## 1.2 Quantum chromodynamics

Quantum chromodynamics (QCD) is a fundamental theory in particle physics that describes the strong nuclear force. It plays a key role in understanding the behavior of quarks and gluons, the building blocks of matter. At its core, QCD is defined by its Lagrangian. The gauge invariant QCD Lagrangian<sup>[2]</sup> is defined in Eq. 1.1,

$$\mathcal{L}_{\text{QCD}} = \bar{\psi}_i (i\gamma^\mu (D_{\mu i j}) - m\delta_{ij}) \psi_j - \frac{1}{4} G_{\mu\nu}^a G^{a\mu\nu}, \quad (1.1)$$

where the  $\psi_i$  represents quark field, which are dynamic functions of spacetime, and are in the fundamental representation of the SU(3) gauge group. The indices  $i$  and  $j$  range from 1 to 3, representing the color charges of quarks. The gauge covariant derivative  $D_\mu = \partial_\mu - ig_s T^a A_\mu^a$ , couples the quark field to the gluon fields  $A_\mu^a$  via the coupling strength  $g_s$ . This coupling involves the SU(3) generators as  $T_a = \frac{\lambda_a}{2}$ , where  $\lambda_a$  represents the Gell-Mann matrices<sup>[3]</sup>. The symbol  $G_{\mu\nu}^a$  represents the gauge-invariant gluon field strength tensor, which is given by,

$$G_{\mu\nu}^a = \partial_\mu \mathcal{A}_\nu^a - \partial_\nu \mathcal{A}_\mu^a + g_s f^{abc} \mathcal{A}_\mu^b \mathcal{A}_\nu^c. \quad (1.2)$$

The  $\mathcal{A}_\mu^a$  represents gluon fields, dynamic functions of spacetime, in the adjoint representation of the SU(3) gauge group, and  $a, b$  and  $c$  run from 1 to 8. And  $f^{abc}$  represents the

structure constants of SU(3) group. The variables  $m$  and  $g_s$  correspond to the quark mass and coupling of the theory, respectively, which are subject to renormalization.

Besides quark masses, the running coupling constant, often denoted as  $\alpha_S = \frac{g^2}{4\pi}$ , is the only free parameter in QCD Lagrangian. It represents the strength of the strong interaction at a given energy scale or momentum transfer  $Q^2$ . However, the coupling constant itself is not a measurable physical observable. It is typically calculated or determined within the framework of perturbation theory. Its value must be inferred from experimentally measurable observables. The mathematical expression is typically given as

$$\alpha_S(Q^2) = \frac{\alpha_S(\mu^2)}{1 + \frac{\beta_0}{4\pi} \cdot \alpha_S(\mu^2) \cdot \ln(\frac{Q^2}{\mu^2})}. \quad (1.3)$$

Where  $Q^2$  is the momentum transfer,  $\mu$  is an energy scale chosen so that  $\alpha_S(\mu^2)$  can be obtained from experiments,  $\beta_0 = \frac{33-2n_f}{3}$  is the first terms of  $\beta$ -function which is a perturbative series of  $\beta(\alpha_S)$ , and  $n_f$  is the number of quark flavors active at the scale  $Q^2$ . A quark flavor is active if its mass  $m_q^2 \ll Q^2$ , which implies  $n_f \leq 6$ .  $\beta_0$  is the leading-order term which provides good approximation. And  $\mu$  is a certain energy scale, by which we can calculate the coupling constant  $\alpha_S(Q^2)$  given the coupling constant  $\alpha_S(\mu)$  at energy scale  $\mu$ .

Unlike the coupling constant in quantum electrodynamics (QED)  $\alpha \approx 1/137$ , the coupling constant in QCD  $\alpha_S$  depends on the energy scale. The running of the strong coupling constant is a fundamental feature of QCD and is a consequence of the theory's renormalization group behavior. The concept of the running coupling constant is based on the observation that the strength of the strong force depends on the energy scale at which it is probed. In Eq. 1.3,  $n_f$  is number of active flavours, which will be no larger than 6 and hence, the function  $\alpha_S(Q^2)$  will be decreasing to 0 as  $Q^2$  goes to infinity. The theoretical predictions along with various measurements are shown in Fig 1.2<sup>[4]</sup>.

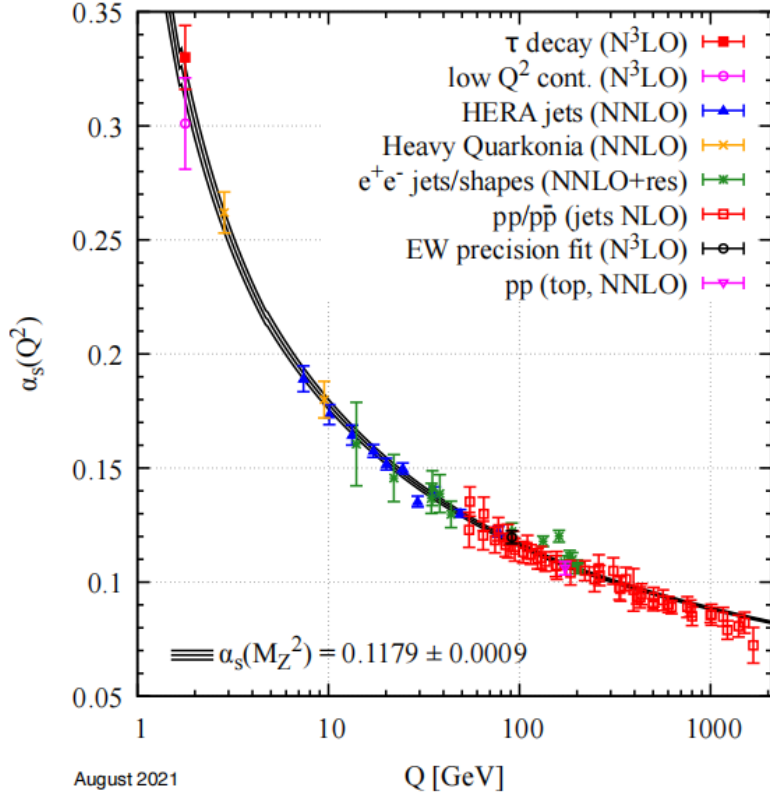


Figure 1.2 Theoretical predictions and various measurements for  $\alpha_s$  as function of  $Q^2$  and  $M_Z^2$ , taken from Ref<sup>[5]</sup>.

As shown in the figure, at low energies or long distances, quarks and gluons are strongly coupled (non-perturbative regime), and at high energies or short distances, they become weakly coupled. This phenomenon is known as asymptotic freedom. By this fact, we can expect that color charges will be free of strong force at an extremely high energy scale and be deconfined. The resulting hot and dense matter is called quark-gluon plasma. The lattice QCD have given the critical temperature at which the transition from hadron phase to quark-gluon plasma phase happen.

Lattice QCD<sup>[6]</sup>, grounded in the framework of lattice gauge theory, is a non-perturbative approach essential for comprehending the complexities of QCD. By discretizing space and time on a lattice, this approach forms the bridge to recover the continuous QCD in the infinite lattice size, rendering it mathematically well-defined. Within lattice QCD, quark fields are situated at lattice sites, leading to the issue of fermion doubling, while gluon fields exist on the links connecting these sites. As the lattice spacing shrinks to zero, this representation approaches continuous QCD. The execution of numerical lattice QCD calculations are predominantly performed numerically by Monte Carlo methods. Lattice QCD currently finds its primary applicability at low baryon densities, where the

numerical sign problem does not hinder calculations. Notably, Lattice QCD has aligned itself successfully with numerous experiments. For instance, it has theoretically determined the proton's mass with an accuracy better than 2 percent. Moreover, Lattice QCD predicts the transition from confined quarks to quark-gluon plasma at approximately 150 MeV, where the energy and pressure density increase rapidly.

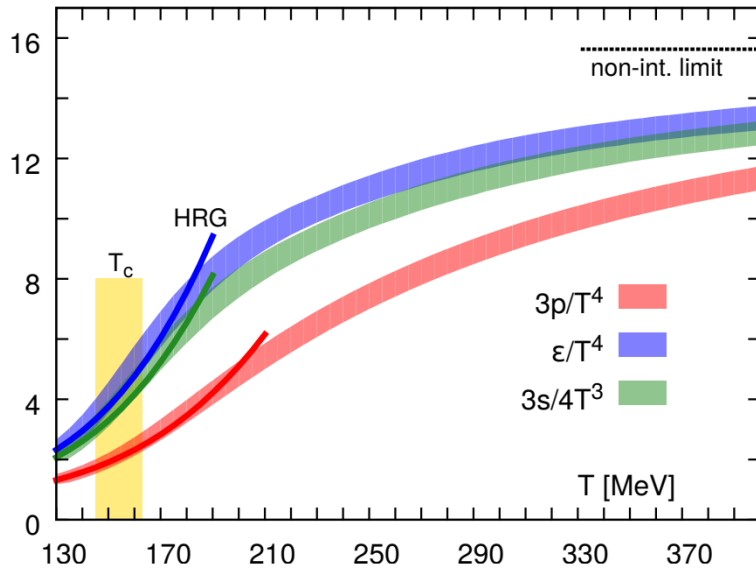


Figure 1.3 The normalized pressure, energy and entropy density as function of temperature, taken from Ref<sup>[7]</sup>.

### 1.3 Quark-gluon plasma

Quark-gluon plasma (QGP) is a state of matter with extremely high temperature and density. It is proposed and derived from the study of QCD in 1970s<sup>[8-9]</sup>. The proposal of QGP provided a theoretical framework for understanding the behavior of strongly interacting matter under such extreme conditions and has since been a subject of intense theoretical and experimental research in the interdisciplinary field of nuclear and particle physics.

In QGP, quarks and gluons are no longer confined in hadrons and free to propagate inside QGP. Although as a whole part, it manifests colorless. QGP state can be achieved either by increasing the temperature or the baryon density or chemical potential  $\mu_B$  of the system. The schematic phase diagram of QCD is shown in Fig 1.4.

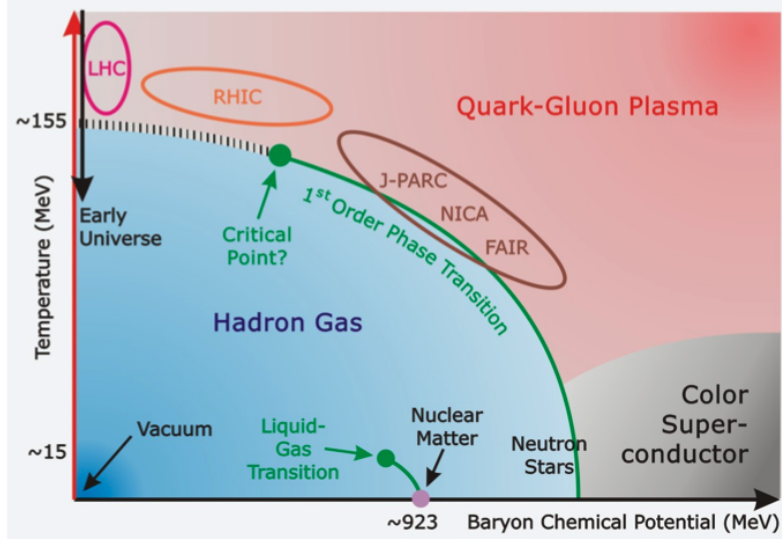


Figure 1.4 A schematic phase diagram of strongly interacting matter as a function of baryon chemical potential and temperature. (From A. Steidl, Frankfurt University)<sup>[10]</sup>.

The boundaries in the phase diagram suggest phase transformation. At high temperatures and low baryon densities, the transition from a hadron gas to the QGP marks a smooth crossover from confined hadrons to a deconfined state where quarks are free and color forces are screened. At the same time, restoration of chiral symmetry occurs. At finite densities and low temperatures, the diagram indicates a liquid-gas transition associated with nuclear matter's shift from condensed to gas-like states. At high densities and low temperatures, the diagram suggests the existence of a color superconducting phase which could exist in the core of cold neutron star. Finally, at finite net baryon densities, a first-order phase transition is expected. The endpoint of the first-order phase transition is called critical point, which offers insights into the QCD phase diagram's unique characteristics. These transitions provide a deep understanding of the behavior of strongly interacting matter under extreme conditions and guide experimental studies in heavy-ion collisions. QGP is expected to exist in the very early stage of universe and heavy-ion collisions, which are called "the Big Bang and the Little Bang". In Fig 1.5, the time-evolution of the little bang and universe after the Big Bang is presented.

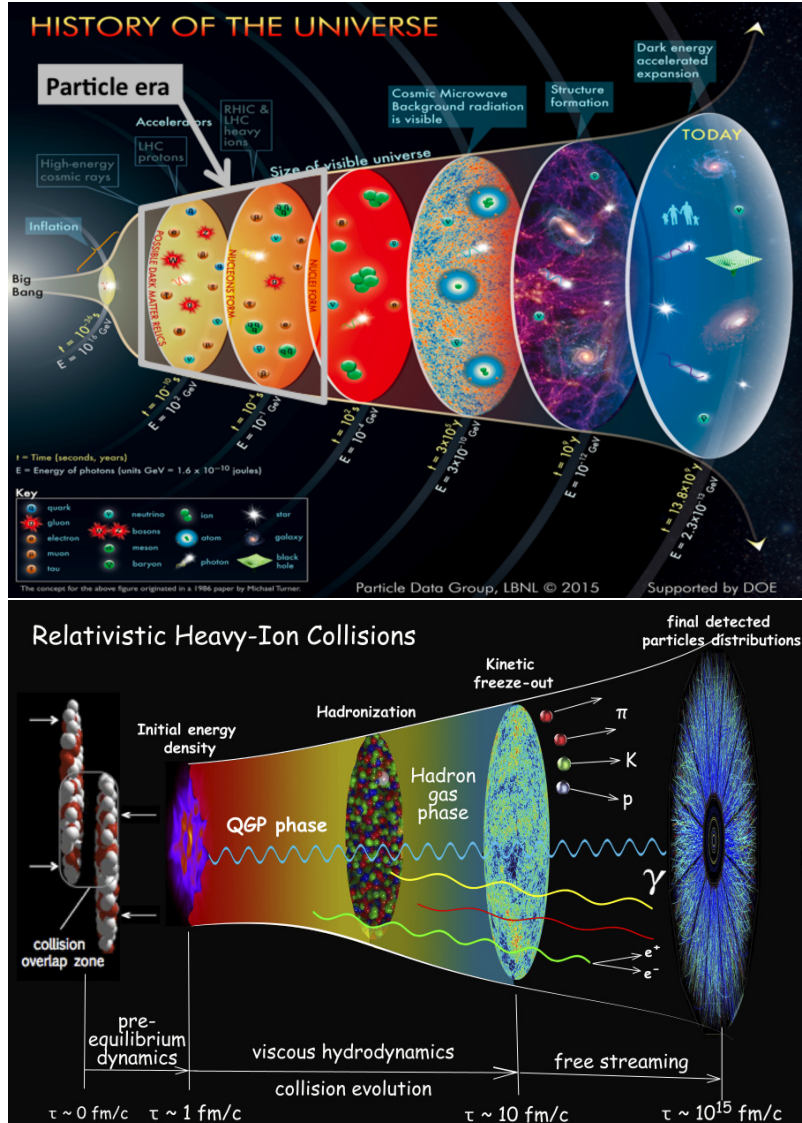


Figure 1.5 Time-evolution for the universe (up, taken from Particle Data Group<sup>[4]</sup>) and heavy-ion collisions (down, taken from Ref<sup>[11]</sup>).

## 1.4 Heavy-ion collisions

Heavy-ion collisions<sup>[12]</sup> provide a unique setting for investigating QGP due to the extreme conditions they create. For example, the simulated evolution of energy density done in Au+Au collisions at Relativistic Heavy Ion Collider (RHIC) energy  $\sqrt{s_{NN}} = 200 \text{ GeV}$ <sup>[13]</sup>, as shown in Fig 1.6, shows the temperature of the system could be larger than critical temperature  $T_c$  where the deconfinement phase transition happens.

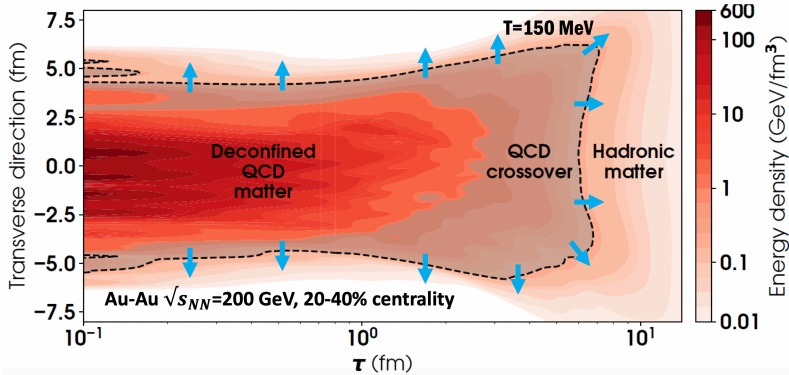


Figure 1.6 Contour plot of the evolution of the energy density in a midcentral Au+Au collision at the highest RHIC energy  $\sqrt{s_{NN}} = 200 \text{ GeV}$ . The horizontal axis shows the proper time  $\tau$ , the vertical axis shows one of the transverse coordinates. The black dashed line delineates the hadronization hypersurface  $T = T_c = 150 \text{ MeV}$ , taken from Ref<sup>[13]</sup>.

These collisions generate temperatures and energy densities comparable to those observed microseconds after the Big Bang. When heavy ions collide at relativistic speeds, they produce a relatively large volume of hot, dense matter, facilitating the formation of QGP. This state can persist for a limited time  $7\text{fm}/c$ , allowing researchers to examine its properties and evolution. Various experimental observables, such as particle spectra and correlations, offer insights into the characteristics of QGP. By comparing collisions with different energies and system sizes, one can explore the phase diagram of nuclear matter, improving our understanding of QGP and the underlying fundamental forces.

Time evolution in heavy-ion collisions refers to the dynamic progression of these collisions over time, encompassing various stages and processes. The time evolution can be divided into several key stages, see Fig 1.5:

- Pre-equilibrium stage: In the initial moments of a heavy-ion collision, the incoming nuclei undergo violent interactions, leading to the formation of a highly excited state known as the pre-equilibrium stage. During this phase, the colliding nucleons experience multiple scatterings and exchanges of energy, resulting in a rapid thermalization process. This stage is characterized by the dominance of partonic interactions, where quarks and gluons interact in a highly dense medium.
- QGP phase: As the system reaches sufficiently high energy densities and temperatures, quarks and gluons are deconfined from individual hadrons, forming the hot and dense QGP. Inside QGP, the system reaches a local thermal equilibrium. The QGP can be treated as perfect fluid and the evolution can be described by relativistic hydrodynamics<sup>[14-16]</sup>.
- Hadronization: As the QGP expands and cools down, it undergoes a phase tran-

sition known as hadronization. In this process, quarks and gluons recombine and form color-neutral hadrons such as protons, neutrons, mesons, and other baryons. Hadronization marks the transition from the deconfined partonic phase to the confined hadronic phase.

- Kinetic freeze-Out: Following hadronization, the system continues to expand and cool, eventually reaching a stage where the interactions between particles become so sparse that they effectively cease. This stage is referred to as kinetic freeze-out. Kinetic freeze-out is the moment when the final momentum distributions of the produced particles.
- Final-state particles: After kinetic freeze-out, the hadrons formed during the collision propagate freely to the detectors. These detected particles carry informations about the dynamics and properties of the collision, allowing us to study the underlying processes and properties of nuclear matter under extreme conditions.

## 1.5 QGP signatures in heavy-ion collisions

With the fact that QGP has a extremely short lifetime about a few fm/ $c$ , it can not be detected directly. But there are some experimental signatures that are considered highly sensitive to the QGP formation effect, also known as Hot Nuclear Matter (HNM) effects. Below are some typical signatures of QGP and their observations in heavy-ion collisions.

### 1.5.1 Parton energy loss

Parton energy loss is a phenomenon observed in heavy-ion collisions. When high-energy partons are produced in the initial stages of a heavy-ion collision, they propagate through the QGP. During this journey, they experience multiple scattering and interactions with the medium's constituents. These interactions lead to energy loss of the partons, resulting in the suppression of particle production in the high transverse momentum region, also known as 'jet quenching'. This effect has been observed at both RHIC<sup>[17-20]</sup> LHC<sup>[21-23]</sup>. As an example, the nuclear modification factor  $D$ -meson has been found suppressed in high- $p_T$  region, as shown in Fig 1.7.

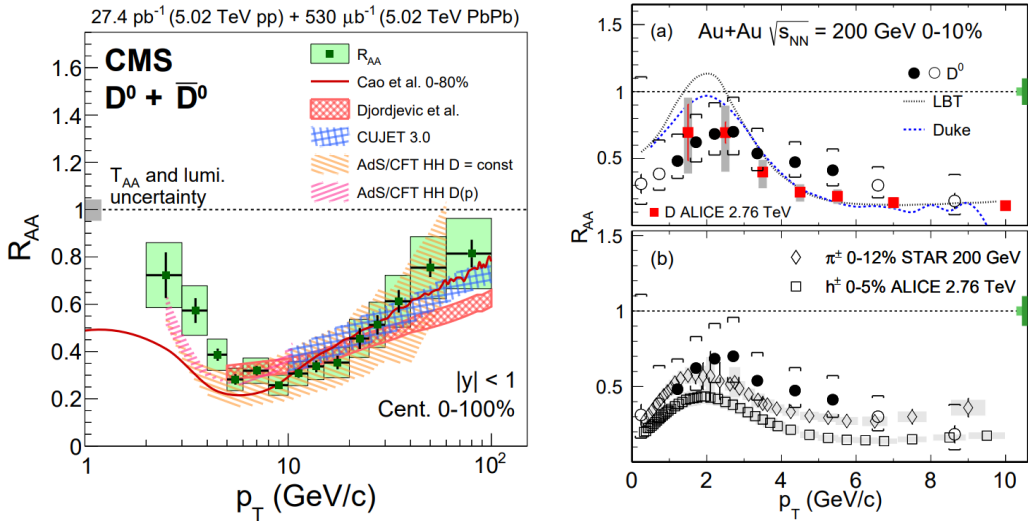


Figure 1.7 Nuclear modification factor  $R_{AA}$  as function of  $p_T$  for  $D$ -meson in (left) PbPb collisions<sup>[21]</sup> and (right) AuAu collisions in different centrality classes<sup>[20]</sup>. Theoretical model prediction comes from Ref<sup>[24-32]</sup>.

Nuclear modification factor is defined as follows

$$R_{AB} = \frac{d^2N_{AB}/dp_T dy}{\langle N_{coll} \rangle_{AB} d^2N_{pp}/dp_T dy}, \quad (1.4)$$

which is used to quantify the suppression or enhancement of particle production relative to that in a reference system, often  $pp$  collisions, with no QGP expected. Here  $\langle N_{coll} \rangle$  is average number of binary nucleon-nucleon collisions obtained by Galuber Model<sup>[33]</sup>. In the high- $p_T$  region, the nuclear modification factor is smaller than one, indicating the suppression of high- $p_T$   $D$ -meson production in PbPb and AuAu collisions compared to  $pp$  collisions, where charm quark loses significant energy when traversing the QGP medium<sup>[34]</sup>.

### 1.5.2 Collective flow

Collective flow refers to the collective motions of particles produced in heavy-ion collisions. It is a fundamental observable that provides insights into the dynamics and properties of the created medium. The anisotropy collective flow is characterized by Fourier coefficients  $v_n$  that describe the anisotropic distribution<sup>[35]</sup> of final particles in momentum space, with expression as follows,

$$E \frac{d^3N}{dp^3} = \frac{1}{2\pi} \frac{d^2N}{p_T dp_T dy} + \sum_{n=1}^{\infty} 2v_n \cos[n(\phi - \Phi_R)], \quad (1.5)$$

where  $\phi$  is the azimuthal angle of the emitted particle's momentum vector,  $\Phi_R$  represents the event plane angle and  $v_n$  quantifies the magnitude of the  $n$ -th harmonic term. One of the most extensively studied coefficients is  $v_2$ , often referred to as elliptic flow. Elliptic

flow results from the pressure gradients in the transverse plane during semi-central collisions. Initially, the almond-shaped geometry of the colliding nuclei in coordinate space is translated into momentum space due to hydrodynamic effects. Elliptic flow is particularly sensitive to the shear viscosity and the equation of state of the expanding medium, making it a valuable signature for investigating the transition from hadronic matter to the quark-gluon plasma<sup>[14-16,16]</sup>.

A high degree of non-zero elliptic flow has been observed in PbPb and AuAu collisions at LHC<sup>[36]</sup> and RHIC<sup>[37]</sup>. The  $v_2$  as function of  $p_T$  in different centrality classes, which corresponds to different multiplicity regions, are summarized in Fig 1.8.

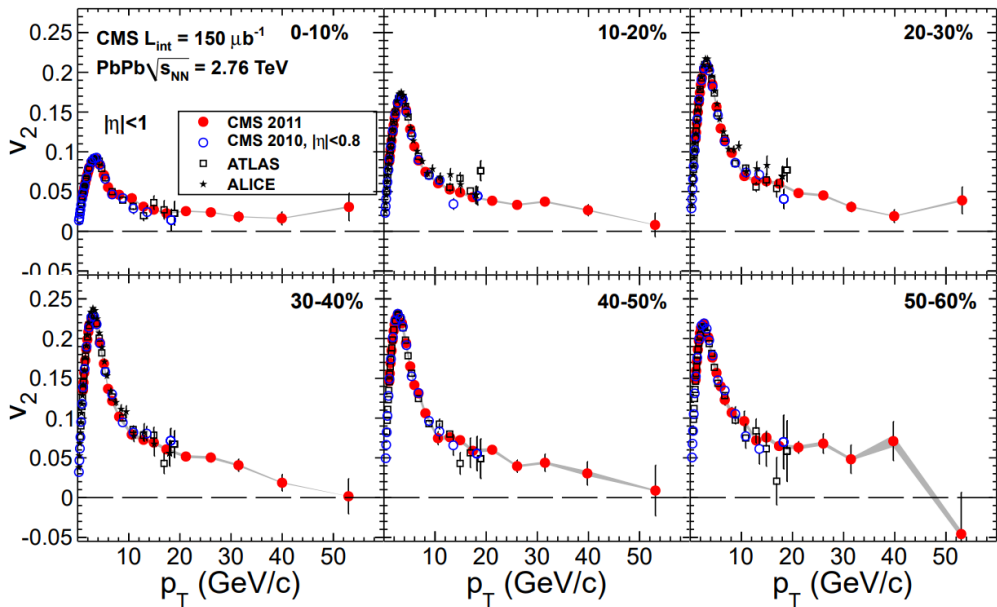


Figure 1.8 The azimuthal anisotropy parameter  $v_2$  in different centrality classes from CMS<sup>[36]</sup>.

### 1.5.3 Strangeness enhancement

In QGP, strange quark production will be enhanced, which is referred as strangeness enhancement<sup>[38]</sup>. Strange quarks are much heavier than up and down quarks, and they are not typically abundant in the initial colliding nuclei. However, due to the high temperature and energy density, and chiral symmetry restoration, strange quark mass will restore to lower than the temperature and hence, strange quark-antiquark pairs can be readily produced and become more prevalent. This increased strangeness production is a distinct feature of the deconfined phase of quarks and gluons<sup>[38]</sup>.

The strangeness enhancement has been observed at LHC, RHIC and Super Proton Synchrotron (SPS). The yield of strange hadrons in heavy-ion collisions relative to that in

$pp/p\text{Be}$  collisions is shown in Fig 1.9.

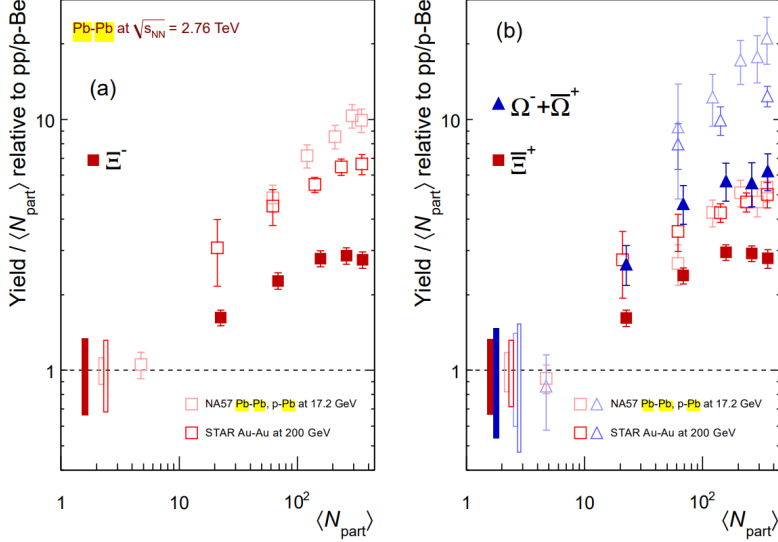


Figure 1.9 The relative yield of  $\Xi$  and  $\Omega$  as function of number of participant  $\langle N_{\text{part}} \rangle$ <sup>[39-41]</sup>.

The result in small system collisions like  $pp$  and  $p\text{Be}$  serve as baseline measurement in absence of QGP. Similarly, the strangeness enhancement is also multiplicity dependent within large collision systems.

### 1.5.4 Quarkonium suppression

The mechanism for quark deconfinement in hot and dense QGP is Debye color screening<sup>[42]</sup>. When the screening radius  $r_D$  is smaller than quark system, which is the hadron radius, the strong force which hold the quarks together can no longer function, which leads to the dissociation of hadron, and manifests as quarkonium suppression. Quarkonium with higher energy state and larger radius tend to dissociate first in QGP, which is known as sequential melting. Both quarkonium suppression and sequential melting has been observed in heavy-ion collisions.

Fig 1.10 shows the production of  $J/\psi$  and  $\psi(2S)$  as function of  $\eta = A^{1/3}(A - 1)/A + B^{1/3}(B - 1)/B$  in different collision systems measured by North Area (NA) experiments in SPS, where  $\eta$  is proportional to the average path length  $L$  for charmonia to pass through the nuclear matter.

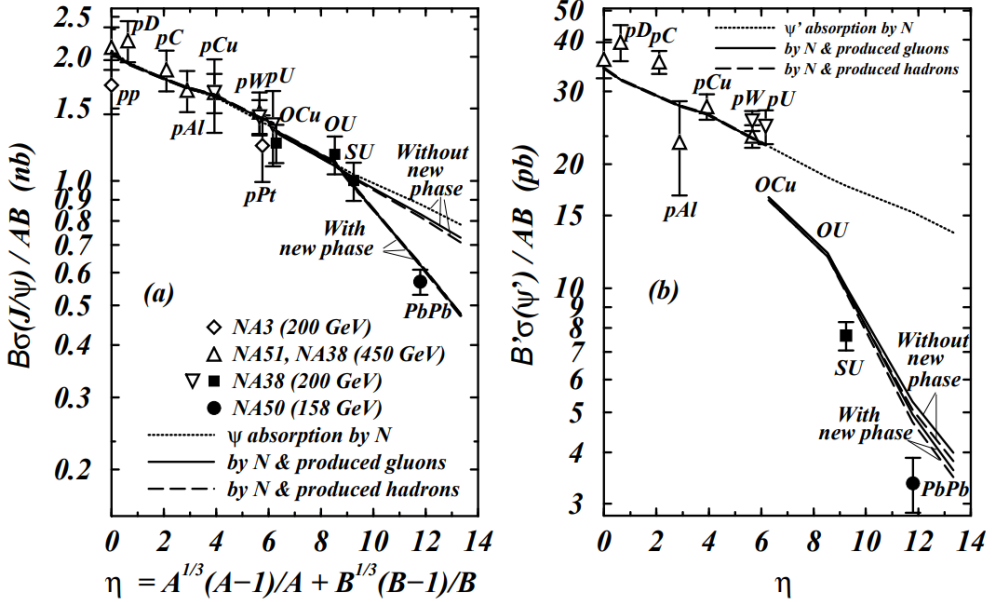


Figure 1.10  $B\sigma/AB$  as function of  $\eta$ , where  $B$  is branching ratio and  $\eta \propto L$ , the average path length. Data are taken from NA3<sup>[43]</sup>, NA51<sup>[44]</sup>, NA38<sup>[45-46]</sup>, and NA50<sup>[47-48]</sup>. Figure is taken from Ref<sup>[49]</sup>.

The production for  $J/\psi$  and  $\psi(2S)$  shows simply an exponential decay trend with  $L$  in  $pA$  collision systems, which is within expectation. However, the  $PbPb$  collisions results shows a clear deviation from the straight line in log-scale plot, which suggests the occurrence of QGP, a new phase of strong absorption of charmonia in  $PbPb$  collision, which can not be seen in  $pA$  collisions.

## 1.6 QGP signatures in small system collisions

Theoretically, the QGP are not expected in small system collisions (like  $pp$ ,  $pA$ ) with the relatively low particle density in a small volume. Nevertheless, QGP-like signatures have been observed in high-multiplicity small system collisions. Although unexpected, there are also some clues leading to this phenomenon. Most of the signatures of quark-gluon plasma (QGP) found in heavy-ion collisions, as listed in Sec 1.5, are multiplicity dependent. They collectively indicate that these signatures become more pronounced compared to the low-multiplicity region. Therefore, it is natural to investigate whether similar signatures can be observed in high-multiplicity small system collisions, where the environment is closer to that of heavy-ion collisions.

A high degree of collectivity in small system collisions has been observed by CMS<sup>[50]</sup>. In this study, the second-order azimuthal anisotropy harmonics  $v_2$  for two-

and multi-particle correlation is measured across  $pp$ ,  $p\text{Pb}$  and  $\text{PbPb}$  collisions. The findings illustrated in Fig 1.11 provide strong evidence supporting the presence of collectivity in high-multiplicity  $pp$  and  $p\text{Pb}$  collisions. Notably, this collectivity demonstrates a dependency on multiplicity, with a transition behavior towards increased collectivity as multiplicity rises across  $pp$ ,  $p\text{Pb}$ , and  $\text{PbPb}$  collision systems.

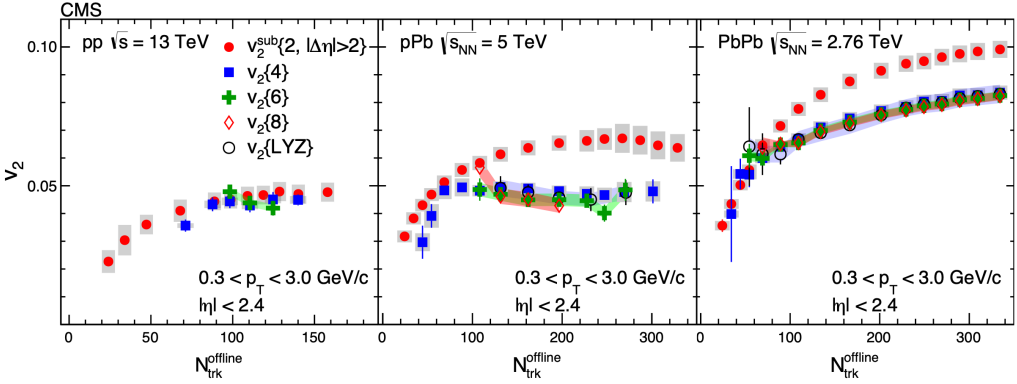


Figure 1.11 The  $v_2$  values as function of reconstructed charged tracks  $N_{\text{trk}}^{\text{offline}}$  [50].

A more clear comparison of the two-particle correlation between the low- and high-multiplicity samples is shown in Fig 1.12. The correlation is represented by the number of particle pairs with a unit phase space ( $\Delta\eta, \Delta\phi$ ) where  $\eta$  is pseudo-rapidity and  $\phi$  is the azimuthal angle. The peak around  $(0, 0)$  and  $\Delta\phi \approx \pi$  represents the particles originating from the same and back-to-back jets. The ridge structure observed in  $\Delta\phi \approx 0$  at large  $|\Delta\eta|$  is considered global collectivity, usually found in large systems and interpreted as signature of QGP formation. The subtle ridge found in high-multiplicity  $pp$  sample indicate a potential existence of QGP.

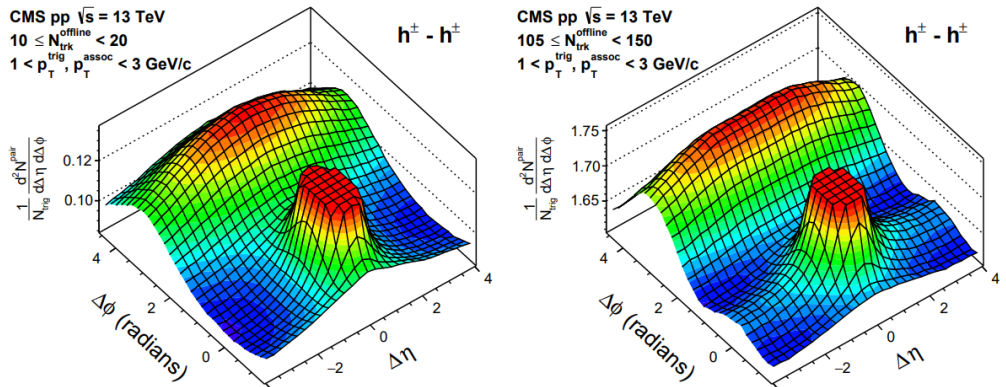


Figure 1.12 Two-particle correlation of low-multiplicity sample (left) and high-multiplicity sample in  $pp$  collisions [50].

Meanwhile, strangeness enhancement has been observed in high-multiplicity  $pp$  and  $p\text{Pb}$  collisions by ALICE<sup>[51]</sup>. As shown in Fig 1.13, the yield ratios of multi-strange hadrons to pion undergo different levels of increase with multiplicity. This phenomenon can not be reproduced by any of the Monte Carlo models commonly used, suggesting QGP-like effects in small system collisions.

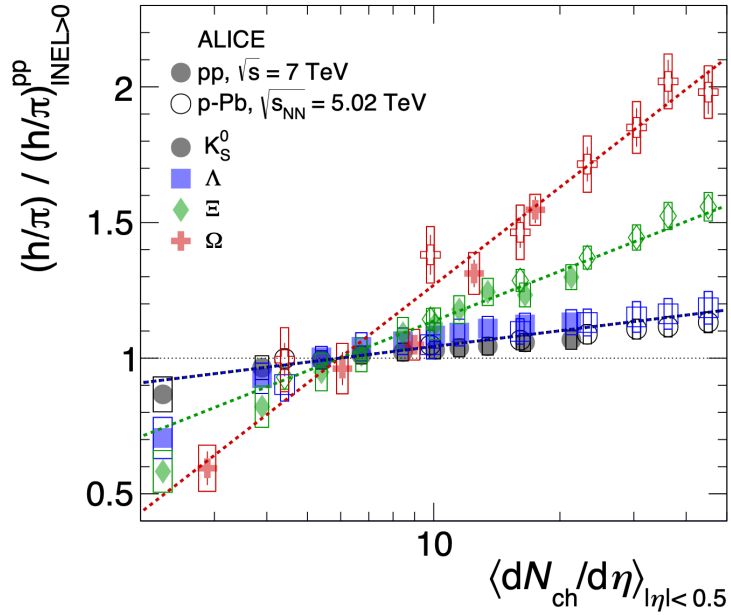


Figure 1.13 Yield ratios of multi-strange particles to pion as function of charged primary tracks density in  $pp$  and  $p\text{Pb}$  collisions<sup>[51]</sup>.

Additionally, an enhanced jet production in high-multiplicity  $pp$  collisions has been observed by ALICE<sup>[52]</sup>. Result in Fig 1.14 shows that, under different resolution parameter  $R$  defined by anti- $k_T$  clustering algorithm<sup>[53]</sup>, the jet yield increases with multiplicity.

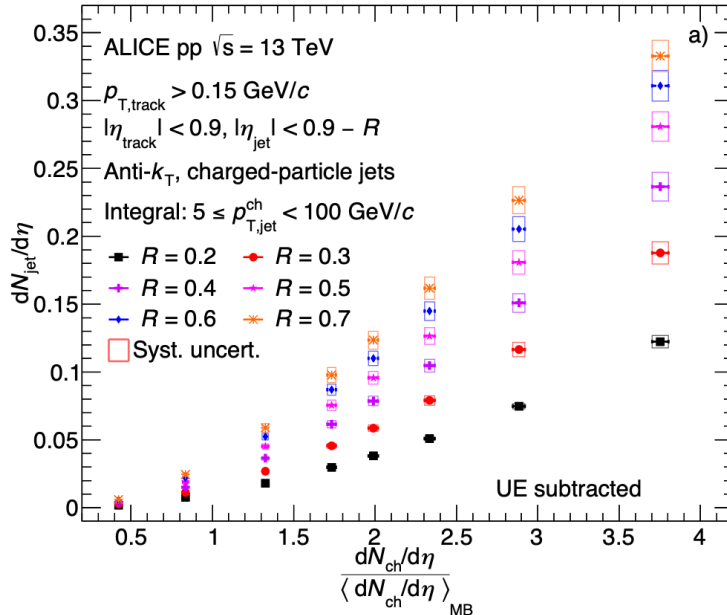


Figure 1.14 Integrated jet yield as function of self-normalized multiplicity for different resolution parameters  $R$ <sup>[52]</sup>.

With an increasing number of QGP-like signatures being observed, there is growing interest in investigating quarkonium suppression in high-multiplicity small system collisions as a means to probe the presence of QGP in such environments. This is the main topic of this thesis. Let us first review the current understanding of quarkonium production from small to large system collisions.

## 1.7 Quarkonium production in $pp$ collisions

### 1.7.1 Theoretical overview

Heavy quarkonium production can be factorized into two steps: First, quark and anti-quark pairs  $Q\bar{Q}$  with definite color and spin state are produced in hard parton scattering, which can be calculated perturbatively. Then, the produced  $Q\bar{Q}$  hadronize into quarkonium at a momentum scale smaller than the mass of quarkonium. The second step is in principle nonperturbative, and different models are proposed based on their different treatments for the nonperturbative part in  $pp$  collisions.

#### 1.7.1.1 Color-Singlet Model

The first model that are proposed for quarkonium production is Color-Singlet Model (CSM), which is based on the assumption that the quantum state does not evolve in the

hadronisation process, including color and spin. The hadronic cross section can be described as follows,

$$d\sigma_{Q+X} = \sum_{i,j} \int dx_i dx_j f_i(x_i, \mu_F) f_j(x_j, \mu_F) d\hat{\sigma}_{i+j \rightarrow (Q\bar{Q}+X)}(\mu_R, \mu_F) |R(0)|^2, \quad (1.6)$$

where  $Q$  denotes the quarkonium and  $f_{i,j}(x, \mu_F)$  denotes the parton  $i, j$  densities in the colliding hadrons. The  $R(0)$  is the radial wave function and the value of  $|R(0)|^2$  can be extracted from decay-width measurements. However, large discrepancy has been observed by CDF collaboration between  $J/\psi$  and  $\psi(2S)$  production at  $\sqrt{s} = 1.8$  TeV<sup>[54]</sup> and leading-order CSM, as shown in Fig 1.15. Now it is widely accepted that the next-and next-next-to-leading-order (NNLO) corrections are significantly larger than the LO contributions. Taking into account NLO and NNLO contributions has reduced the most apparent discrepancies in measurements of  $\psi(2S)$  production in  $pp$  collisions at RHIC, Tevatron and LHC energies<sup>[55]</sup>.

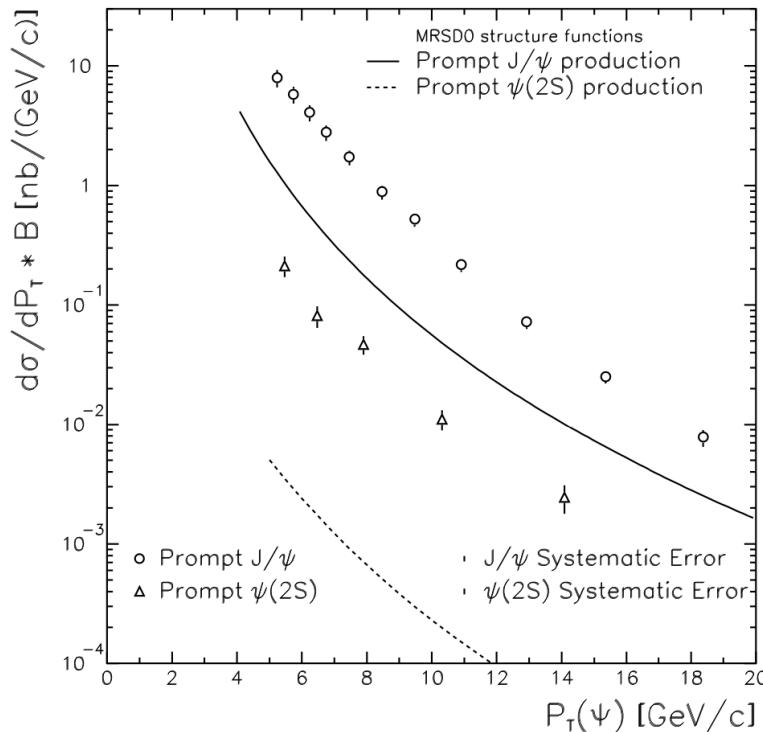


Figure 1.15 The  $p_T$  spectrum of  $J/\psi$  and  $\psi(2S)$  production in  $pp$  collisions at  $\sqrt{s} = 1.8$  TeV. The (dashed) curve is prediction by CSM. The cross section for  $J/\psi$  is  $\sim 6$  times higher and for  $\psi(2S)$  is  $\sim 50$  times higher than CSM prediction. Graph is taken from Ref<sup>[54]</sup>.

### 1.7.1.2 Color-Octet Model

Then a new Color-Octet Model (COM) is proposed where the quarkonium can also be produced via color-octet  $Q\bar{Q}$  pairs and higher order color-singlet contributions. Com-

pared to the CSM in Eq. 1.6, COM further takes into consideration additional quantum numbers like angular momentum, spin and colour, denoted as  $k$ . The equation for hadronic cross section can be expressed as

$$d\sigma_{Q+X} = \sum_{i,j} \int dx_i dx_j f_i(x_i, \mu_F) f_j(x_j, \mu_F) d\hat{\sigma}_{i+j \rightarrow Q\bar{Q}_k + X}(\mu_R, \mu_F, \mu_\Lambda) \langle \mathcal{O}_Q^k \rangle. \quad (1.7)$$

The  $\langle \mathcal{O}_Q^k \rangle$  are the non-perturbative NRQCD long distance matrix elements (LDMEs)<sup>[56]</sup>, that describes the hadronization from  $Q\bar{Q}$  in state  $k$  into quarkonium  $Q$ . The LDMEs can not be fixed by decay-width measurements nor through lattice calculations, and can only parameterized by experimental measurements. Via COM, the large discrepancy between the measurements of  $J/\psi$  and  $\psi(2S)$  by CDF is fixed, which unexplained by CSM.

### 1.7.1.3 NRQCD factorization

In NRQCD factorization formalism, the production of heavy quarkonium state can be expressed as

$$d\sigma_Q = \sum_k d\hat{\sigma}^k \langle \mathcal{O}_Q^k \rangle, \quad (1.8)$$

The LDME is characterized as the vacuum expectation value of a four-fermion operator within NRQCD, with each LDME exhibiting a recognized scaling pattern in powers of  $v$ , the traditional velocity of quark in a quarkonium rest frame. Consequently, the summation over can be systematically arranged in powers of  $v$ . Hence, Eq. 1.8 represents a two-dimensional expansion of  $\alpha_S$  and  $v$ . In practical applications, to achieve a specified level of precision, one typically truncates the summation and retains only a limited number of LDMEs for each production process. The effectiveness of the NRQCD factorization approach hinges on the convergence of this velocity expansion and the universality of LDMEs.

The NRQCD factorization encompasses contributions from both the color-singlet (CS) and color-octet (CO) channels. Disregarding the CO contributions allows the retrieval of the CSM for S-wave heavy quarkonium production. The inclusion of CO contributions in NRQCD can also addresses the infrared divergence issue encountered in the CSM<sup>[57]</sup>.

### 1.7.1.4 Color-Evaporation Model

Color-Evaporation Model (CEM)<sup>[58]</sup> introduce a quarkonium state parameter,  $F_Q$ , which is a process-independent probability that a  $Q\bar{Q}$  hadronize to the quarkonium state.

The production cross-section of a quarkonium state can be expressed as

$$\sigma_Q^{(N)LO} = F_Q \int_{2m_Q}^{2m_D} \frac{d\sigma_{Q\bar{Q}}^{(N)LO}}{dm_{Q\bar{Q}}} dQ\bar{Q}, \quad (1.9)$$

where  $2m_Q$  and  $2m_D$  are the kinematic threshold to produce the quark pair and the lightest open heavy-flavour quark. The main issue for CEM is the absence for polarisation observables. The CEM is successful in explaining the  $J/\psi$  production data. However, it predicts that the productions of quarkonium of different states do not depend on the kinematic variables, nor on the production process, which contradicts many experimental measurements. For example, the ratio of  $\psi(2S)$  to  $J/\psi$  is clearly dependent on  $p_T$ <sup>[59]</sup>. To overcome this, improved color evaporation model (ICEM) is proposed<sup>[60]</sup>, which just simply change the lower limit from  $2m_Q$  by  $m_Q$ , the mass of quarkonium. The ICEM can describe the production as well as the production ratio of  $\psi(2S)$  to  $J/\psi$  mesons<sup>[60]</sup>.

### 1.7.1.5 The Fragmentation Function Approach

In high-energy collisions, the NRQCD factorization Eq. 1.8 may go through a high-order  $\alpha_S$  correction at high  $p_T$  region, where the short-distance will receive an enhancement of order  $p_T^2/m_Q^2$  and correction in terms of  $\ln(p_T^2/m_Q^2)$ . To solve this problem, a new factorization is proposed to describe the quarkonium production in high- $p_T$  region, which is the Fragmentation Function Approach (FFs)<sup>[61]</sup>. In FFs, the LO and NLO terms of  $p_T^2/m_Q^2$  expansion can be factorized as

$$\begin{aligned} d\sigma_{Q+X}(p_T) &= \sum_{i,j,f} d\hat{\sigma}_{i+j \rightarrow f+X} \left( \frac{p_T}{z}, \mu_F \right) \otimes D_{f \rightarrow Q}(z, m_Q, \mu_F) \\ &\quad + \sum_{i,j,k} d\hat{\sigma}_{i+j \rightarrow Q\bar{Q}}(k) + X(P_{Q\bar{Q}(k)}) = \frac{p_T}{z}, \mu_F \\ &\quad \otimes D_{Q\bar{Q}(k) \rightarrow Q}(z, m_Q, \mu_F) + \mathcal{O}(m_Q^4/p_T^4), \end{aligned} \quad (1.10)$$

where the first and second terms represents for the LO and NLO terms,  $z$  is the light-cone momentum fraction, and  $D$  represents for the probability of finding  $Q$  hadronized from parton ( $D_{f \rightarrow Q}$ ) or heavy quarkonium state ( $D_{Q\bar{Q}(k) \rightarrow Q}$ ) instead of single parton. They can be expressed in terms of LDMEs as follows,

$$\begin{aligned} D_{f \rightarrow Q}(z, m_Q, \mu_0) &= \sum_n \hat{d}_{f \rightarrow Q\bar{Q}(n)}(z, m_Q, \mu_0, \mu_\Lambda) \langle \mathcal{O}_n^Q(\mu_\Lambda) \rangle, \\ D_{Q\bar{Q}(k) \rightarrow Q}(z, m_Q, \mu_0, \mu_\Lambda) &= \sum_n \hat{d}_{Q\bar{Q}(k) \rightarrow Q\bar{Q}(n)}(z, m_Q, \mu_0, \mu_\Lambda) \langle \mathcal{O}_n^Q(\mu_\Lambda) \rangle, \end{aligned} \quad (1.11)$$

where  $\hat{d}$  represents the perturbative evolution of a parton ( $\hat{d}_{f \rightarrow Q\bar{Q}(n)}$ ) and  $Q\bar{Q}$  in state  $k$  into quantum state  $n$ . The coefficients for FFs equation has been calculated to  $\mathcal{O}(\alpha_S^3)$ , summarized in Ref<sup>[62]</sup>. The FFs is expected to converge better than NRQCD factorization.

### 1.7.1.6 The Soft Gluon Factorization Approach

In Soft Gluon Factorization Approach (SGF) the cross-section of quarkonium production can be factorized as

$$(2\pi)^3 2P_Q^0 \frac{d\sigma_Q}{d^3 P_Q} \approx \sum_n \int \frac{d^4 P}{(2\pi)^4} Q_n(P) F_{n \rightarrow Q}(P, P_Q), \quad (1.12)$$

where  $P$  ( $P_Q$ ) is the momentum of  $Q\bar{Q}$  and quarkonium, and  $F_{n \rightarrow Q}$  is the soft gluon distribution. The Eq. 1.12 describe the hadronization from a  $Q\bar{Q}$  into a quarkonium by emitting soft gluons. The SGF resums relativistic corrections from kinematic effects and hence result in a better convergence in  $v$ .

### 1.7.1.7 FONLL for non-prompt charmonium

FONLL (Fixed-Order plus Next-to-Leading Logs)<sup>[63]</sup> for non-prompt charmonium refers to a theoretical framework used to calculate the production of charmonium particles originating from the  $b$ -hadron decay. Non-prompt charmonium production is particularly important in high-energy collisions where heavy-flavour hadrons are abundantly produced. FONLL is needed in this context because traditional fixed-order calculations fail to accurately describe the production of charmonium particles in high- $p_T$  regimes, where the charmonium's  $p_T$  is much larger than its mass. In such cases, the fixed-order calculations suffer from large logarithmic corrections that spoil the convergence of the perturbative expansion. FONLL addresses this issue by merging fixed-order calculations with resummed calculations, effectively including both leading-logarithmic (LL) and next-to-leading-logarithmic (NLL) terms in the perturbative expansion.

By incorporating both fixed-order and resummed calculations, FONLL provides a more accurate prediction for non-prompt charmonium production across a wide range of  $p_T$ , allowing for better agreement with experimental data from high-energy collider experiments. This is crucial for studying phenomena such as quarkonium suppression in heavy-ion collisions, as well as for testing the predictions of quantum chromodynamics (QCD) in the heavy-flavour sector.

### 1.7.2 Experimental results

The charmonium production has been measured in  $pp$  collisions at LHC<sup>[64-68]</sup> and RHIC<sup>[69-70]</sup>. As shown in Fig 1.16, with the production in high- $p_T$  region being well described by NLO NRQCD, the low- $p_T$  production can be described by CGC+NRQCD. The NLO NRQCD and CGC+NRQCD frame can provide good prediction for whole  $p_T$  spectrum and has been described the experimental data well.

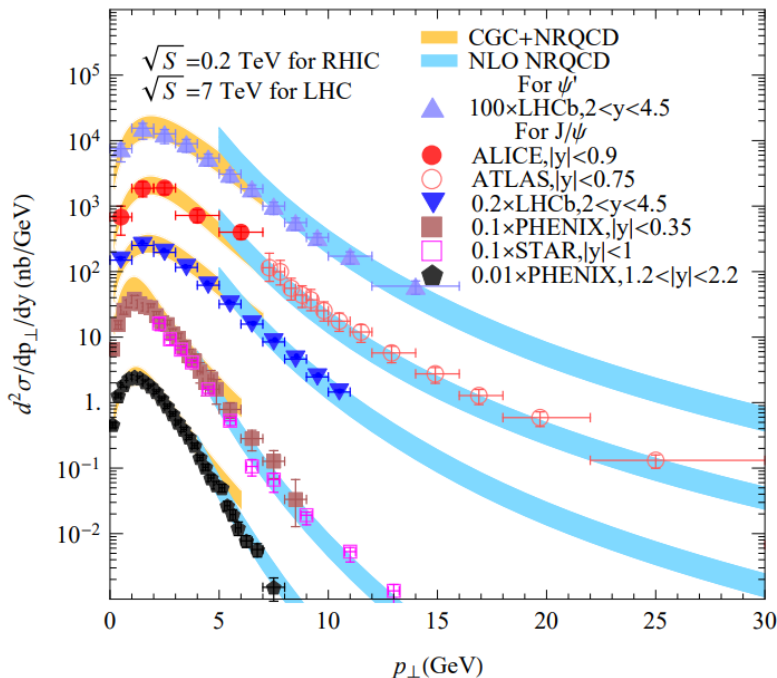


Figure 1.16 The  $\psi(2S)$  and  $J/\psi$  differential cross section as function of transverse momentum . Figure taken from<sup>[71]</sup>. Data is from Ref<sup>[67-70,72-73]</sup> and model prediction from Ref<sup>[74]</sup>.

LHCb has measured the non-prompt production for  $J/\psi$  and  $\psi(2S)$ . As an example, the result in 13 TeV  $pp$  collisions is shown in Fig 1.17. The prediction from FONLL aligns well with the  $p_T$ -spectrum of both  $J/\psi$  and  $\psi(2S)$ .

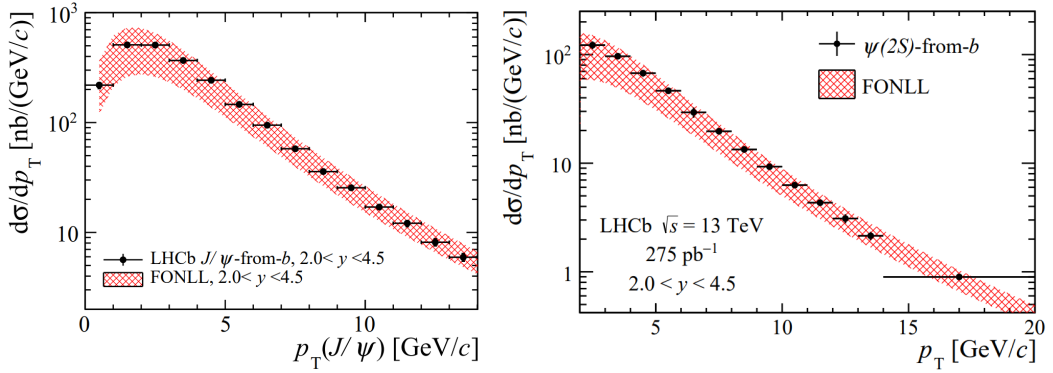


Figure 1.17 The  $p_T$ -spectrum for non-prompt (left)  $J/\psi$  and (right)  $\psi(2S)$  production in 13 TeV  $pp$  collisions, taken from Ref<sup>[64]</sup>

## 1.8 Quarkonium production in $pA$ collisions

### 1.8.1 Theoretical overview

The quarkonium production in  $pA$  collisions can be treated with a similar factorization as  $pp$  collisions. However, it can not be simply regarded as the simple superposition of nucleon-nucleon collisions. The quarkonium production is further affected by the so-called Cold Nuclear Matter (CNM) effects.

#### 1.8.1.1 Modification of nPDFs

Quarkonium production in nuclear collisions begins with the interaction of partons from the colliding nuclei. The nuclear Parton Distribution Function (nPDFs) determine the parton densities within the colliding nuclei, affecting the initial state of the collision. Variations in nPDFs, can modify the number of parton-parton collisions and the momentum fractions available for quarkonium production. The hard-process cross section for a final state in collisions involving hadron A, B can be expressed as:

$$d\sigma^{AB \rightarrow k+X} = \sum_{i,j,X'} f_i^A(Q^2) \otimes d\hat{\sigma}^{ij \rightarrow k+X'}(Q^2) f_j^B(Q^2) + \mathcal{O}(1/Q^2), \quad (1.13)$$

where  $d\hat{\sigma}^{ij \rightarrow k+X'}(Q^2)$  are coefficient functions that can be perturbatively calculated. While  $f_i^A, f_j^B$  contain long-range physics, hence can not be obtained by perturbative calculation. They are function of Bjorken  $x$  and momentum transfer  $Q^2$ . For a nucleus A, we can write nPDFs as

$$f_i^A(x, Q^2) = \frac{Z}{A} f_i^{p/A}(x, Q^2) + \frac{N}{A} f_i^{n/A}(x, A^2), \quad (1.14)$$

where  $f_i^{p/A}$  are PDFs of bound proton in the nucleus and  $f_i^{n/A}$  are that of bound neutron, which are derived from  $f_i^{p/A}$  via isospin symmetry. Then we can define the nuclear modification factors from the relation between the bound-proton and free-proton PDFs as follows,

$$R_i^A(x, Q^2) = \frac{f_i^{p/A}(x, Q^2)}{f_i^p(x, Q^2)}. \quad (1.15)$$

The  $Q^2$  evolution of  $R_i^A$  can be probed by DGLAP equation<sup>[75-77]</sup>. By fitting the experimental data to the DGLAP equation,  $f_i^p$  can be extracted. A schematic sketch for  $R_i^A(x, Q^2)$  is shown in Fig 1.18 from Ref<sup>[78]</sup>. According to the different shapes of the curve, the nuclear modifications are categorized as shadowing and anti-shadowing effects, EMC effect and Fermi motion smearing<sup>[79-82]</sup>.

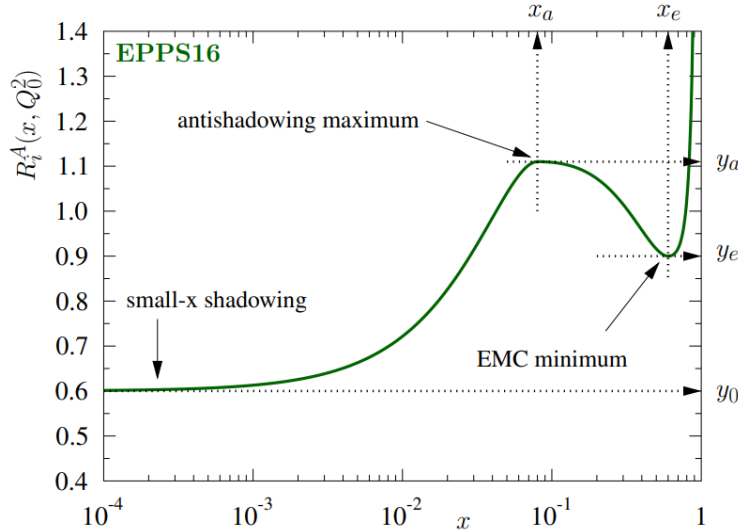


Figure 1.18 Illustration of the EPPS16 fit function  $R_i^A(x, Q^2)$ <sup>[78]</sup>.

### 1.8.1.2 Color-Glass Condensate

At low Bjorken  $x$ , the gluon density per unit transverse area in hadronic wavefunctions becomes very large. The large gluon density leads to a saturation of gluon distribution to a state of Color-Glass Condensate (CGC). The saturated gluon density may also affect the quarkonium production. At low  $x$ , the differential probability for the emission to the lowest order of  $\alpha_S$  is

$$dP_{brem} \approx \frac{\alpha_S C_R}{\pi^2} \frac{d^2 k_\perp}{k_\perp^2} \frac{dx}{x}, \quad (1.16)$$

where  $k_\perp$  is transverse momentum,  $C_R$  is  $SU(N_c)$  Casimir in the color representation,  $N_c$  for a gluon and  $(N_c^2 - 1)/2N_c$  for a quark. Eq. 1.16 describe the logarithmic enhancement of gluon emission at low transverse momentum. From Eq. 1.16 we can get the gluon number is

$$x \frac{dN_g}{dx}(Q^2) = \frac{\alpha_S C_R}{\pi^2} \int_{\Lambda_{QCD}^2}^{Q^2} \frac{d^2 k_\perp}{k_\perp^2} = \frac{\alpha_S C_R}{\pi^2} \ln \frac{Q^2}{\Lambda_{QCD}^2}. \quad (1.17)$$

When  $\alpha_S Y$  (where  $Y = \ln \frac{1}{x}$ ) at an order of unit, the correction for subsequent emissions of gluons to softer gluons modifying Eq. 1.17 as follows,

$$x \frac{dN_g}{dxdk_\perp^2} \sim \frac{\alpha_S C_R}{\pi} \frac{1}{k_\perp^2} e^{\omega \alpha_S Y}, \quad (1.18)$$

where  $\omega$  is an estimation number of order unity which is not fixed. And the quantity that controls gluon interaction is the occupation number given as follows,

$$n(Y, k_\perp, b_\perp) \equiv \frac{(2\pi)^3}{2(N_c^2 - 1)} \frac{dN_g}{dY d^2 k_\perp d^2 b_\perp}, \quad (1.19)$$

where  $b_\perp$  is the impact parameter of gluon in the transverse plane. When  $n \ll 1$ , the system is dilute where the gluon interaction is negligible. When  $n$  is at an order of unity, the gluons start overlapping and when it reaches an order of  $1/\alpha_S$ . Since the transverse area grows at a scale of  $A^{2/3}$ ,  $pp$  collisions tends to provide a dilute environment, except for the extremely small  $x$ , and in  $pA$  or  $AA$  collisions, the saturation effect becomes non-negligible. The Fig 1.19 represents a QCD evolution of gluon in phase space of  $Y = \ln \frac{1}{x}$  and  $\ln Q^2$ .

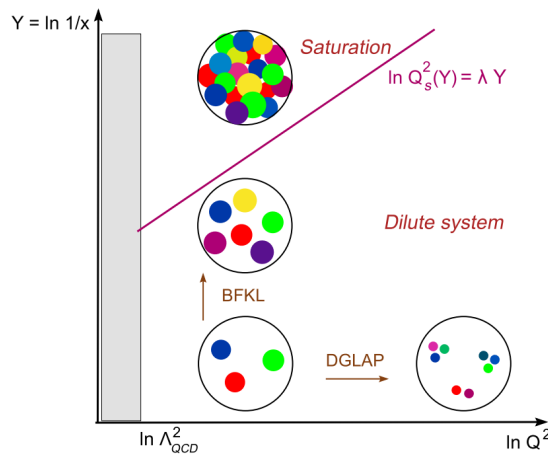


Figure 1.19 QCD evolution of gluons in phase space  $Y$  and  $\ln Q^2$ , taken from Ref<sup>[83]</sup>

### 1.8.1.3 Coherent energy loss

Coherent energy loss<sup>[84-85]</sup> refers to the phenomenon where the incident proton loses energy collectively as it interacts with the entire nucleus, rather than undergoing individual scatterings with individual nucleons within the nucleus. It is expected to happen in  $pA$  collisions, especially at high center-of-mass energy. The quarkonium production can be described as function of quarkonium energy  $E$ <sup>[84]</sup>

$$\frac{1}{A} \frac{d\sigma_{pA}}{dE} = \int_0^{\varepsilon^{max}} d\varepsilon \mathcal{P}(\varepsilon, E, \hat{q}L) \frac{d\sigma_{pp}}{dE}(E + \varepsilon), \quad (1.20)$$

where  $L$  is path length traveled across the target,  $\varepsilon$  denotes the energy loss incurred by the octet  $c\bar{c}$  pair propagating through the nucleus in the context of  $J/\psi$  production in  $p-A$  collisions, and  $\varepsilon^{max} = \min(E, E_p - E)$ , where  $E_p$  is the beam energy and the  $\mathcal{P}$  is the energy loss probability distribution, also called quenching weight is related to the coherent radiation spectrum for the process of gluon to quark and antiquark pair process. The quenching weight is dependent on the gluon nuclear broadening  $\sqrt{\hat{q}L}$  where

$$\hat{q} \equiv \hat{q}_0 \left( \frac{10^{-2}}{\min(x_0, x_2)} \right); x_0 \equiv \frac{1}{2m_p L}; x_2 \equiv M_\perp e^{-y}/\sqrt{s}. \quad (1.21)$$

The transport coefficient  $\hat{q}_0$  can be determined from experimental data, e.g.,  $\hat{q}_0 = 0.075^{+0.015}_{-0.005} \text{ GeV}^2/\text{fm}$  from the fitting  $J/\psi$  suppression measured by E866<sup>[86]</sup>.

### 1.8.1.4 Comover Interaction Model

Comover Interaction Model (CIM)<sup>[87]</sup> states that the quarkonium will dissociate when interacting with the produced particle "the comover" that travels along with quark and anti-quark pairs. This can explain the relative suppression of excited-state quarkonium compare to their ground state, which can not be explained by the initial-state effects. The CIM has been successfully describe the  $\psi$  production in LHC  $pp$ ,  $pA$  and  $AA$  collisions. The formalism, taking  $\psi$  as an example, is given as follows. The rate equation of charmonium density  $\rho^\psi$  in a given transverse coordinate  $s$ , rapidity  $y$  and impact parameter  $b$  is

$$\tau \frac{d\rho^\psi}{d\tau} = -\sigma^{co-\psi} \rho^{co}(b, s, y) \rho^\psi(b, s, y), \quad (1.22)$$

where  $\sigma^{co-\psi}$  is the charmonium dissociation cross-section due to interaction with comover of density  $\rho^{co}(b, s, y)$ . Integrating the equation we can get the survival probability of charmonium between initial time  $\tau_0$  and freeze-out time  $\tau_f$ . Assuming the interaction stops when its density reaches the same as  $pp$  density, and the density is inversely proportional

to the time,  $\tau_f/\tau_0 = \rho^{co}(b, s, y)/\rho_{pp}(y)$ , we can get the solution to be

$$S_\psi^{co}(b, s, y) = \exp(-\sigma^{co-\psi} \rho^{co}(b, s, y) \ln \frac{\rho^{co}(b, s, y)}{\rho_{pp}(y)}), \quad (1.23)$$

and comover density is thought to be proportional to the number of collisions,

$$\rho^{co}(b, s, y) = n(b, s) S_{co}^{sh} \frac{3}{2} (\mathrm{d}N_{ch}^{pp}/\mathrm{d}y), \quad (1.24)$$

where  $n(b, s)$  is the number of binary nucleon-nucleon collisions within unit transverse area and  $S_{co}^{sh}$  is the shadowing of nPDFs which will be unit in  $pp$  collisions. And the comover density in  $pp$  collisions is

$$\rho_{pp}(y) = \frac{3}{2} \mathrm{d}N_{ch}^{pp}/\mathrm{d}y / \pi R_p^2, \quad (1.25)$$

where  $R_p$  is the radius of proton. The nuclear modification factor is thus

$$R_{pA}^\psi(b) = \frac{\mathrm{d}N_{pA}^\psi/\mathrm{d}y}{n(b)\mathrm{d}N_{pp}^\psi/\mathrm{d}y} = \frac{\int \mathrm{d}^2s \sigma_{pA}(b) n(b, s) S_\psi^{sh} S_\psi^{co}}{\int \mathrm{d}^2s \sigma_{pp} n(b, s)}. \quad (1.26)$$

By introducing  $S^{sh}$  we take into account the shadowing effect of nPDFs, which may affect the charmonium production. The CIM has been successful at describing suppression of charmonia, bottomonia and  $X(3872)$  hadrons in various collision systems<sup>[88-91]</sup>.

## 1.8.2 Experimental results

The quarkonium production has been measured in  $p\text{Pb}$  and  $p\text{Au}$  collisions at RHIC<sup>[92]</sup> and LHC<sup>[93]</sup>. The modification due to CNM effects are quantified by nuclear modification factor which is defined as

$$R_{pA} = \frac{\mathrm{d}^2\sigma_{pA}/\mathrm{d}p_T\mathrm{d}y}{A\mathrm{d}^2\sigma_{pp}/\mathrm{d}p_T\mathrm{d}y} \quad (1.27)$$

The nuclear modification factor of  $J/\psi$  as function of rapidity and transverse momentum is shown in Fig 1.20. The result can be well described by the CEM model including the EPS09NLO set of nPDF<sup>[94]</sup>, two CGC-approached model<sup>[95-96]</sup>, the comover model<sup>[87]</sup> in their corresponding kinematic regions.

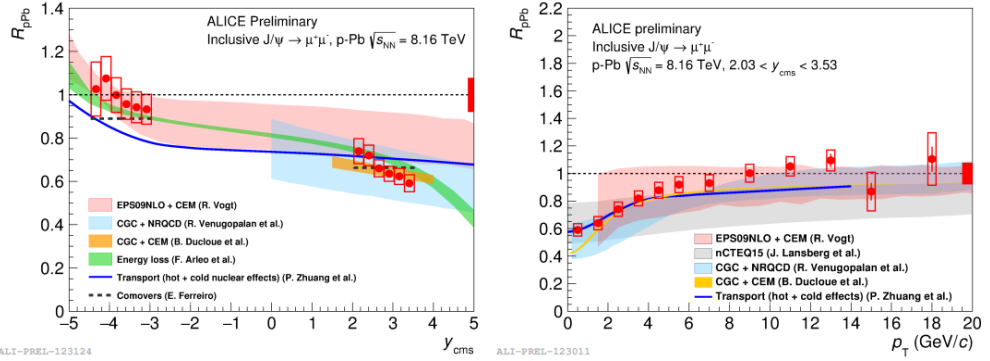


Figure 1.20 The rapidity dependence (left) and  $p_T$  dependence (right) of  $J/\psi$  nuclear modification factor  $R_{pA}$  by ALICE<sup>[93]</sup>, prediction model from Ref<sup>[87,94-99]</sup>.

The nuclear modification factor shows a positive  $p_T$  dependence. The production in  $p\text{Pb}$  collisions is less suppressed in high- $p_T$  region. This could be explained by less comover in high- $p_T$  region. The gluon saturation is likely to happen in low- $p_T$  region, which could also be an explanation for this observation. Besides, the model based on parton energy loss and FONLL with EPS09NLO set of nPDF make good prediction on the prompt and non-prompt nuclear modification factor, respectively, as shown in Fig 1.21. However, the model predictions do not align well with the  $\psi(2S)$  result.

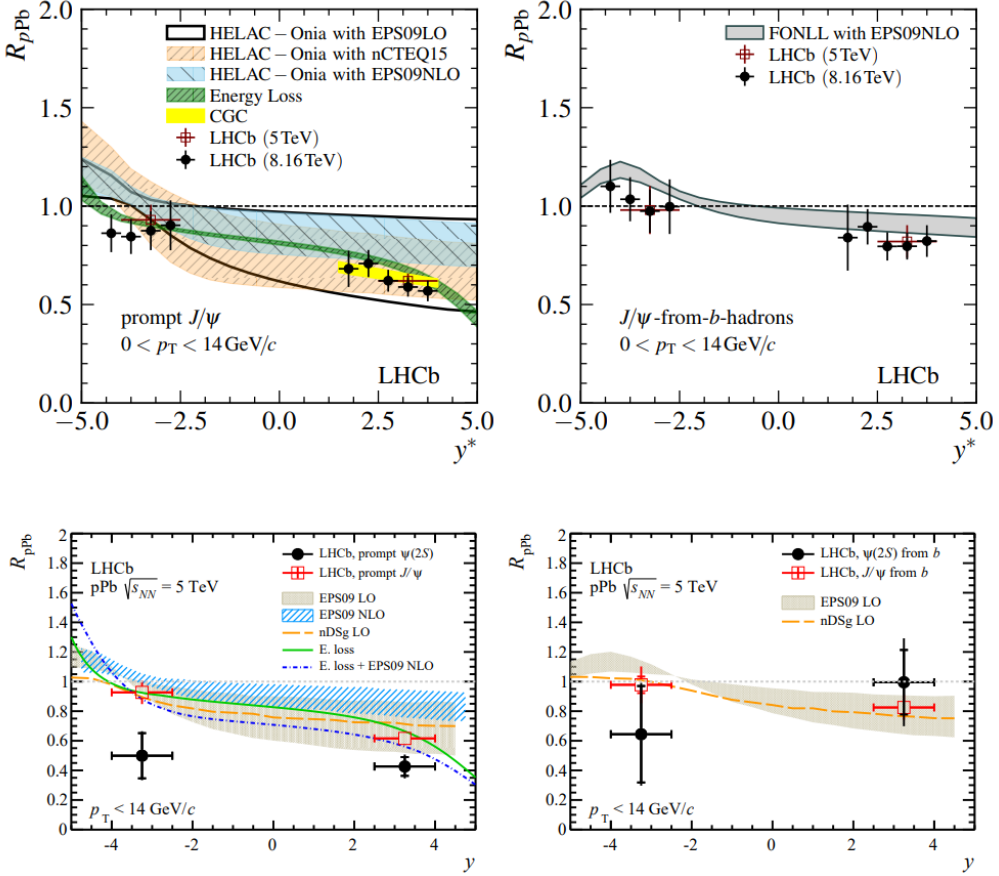


Figure 1.21 Nuclear modification factor in  $p\text{Pb}$  collisions at 5 TeV from LHCb for prompt (left) and non-prompt (right) charmonia, top row for  $J/\psi$  and bottom row for  $\psi(2S)$ <sup>[100]</sup>.

In the forward rapidity region, the nuclear modification factor is smaller than 1, which could result from the CNM effects like shadowing effect and saturation effect. And prompt  $\psi(2S)$  is more suppressed than prompt  $J/\psi$ , while the non-prompt  $\psi(2S)$  and  $J/\psi$  show a similar suppression in both forward and backward rapidity, which suggests the final-state effects is involved. The nuclear modification factor in  $p\text{Au}$  collisions measured by STAR shows a similar  $p_T$  dependence with result from ALICE, and different models describe the experimental results in certain kinematic ranges, as shown in Fig 1.22.

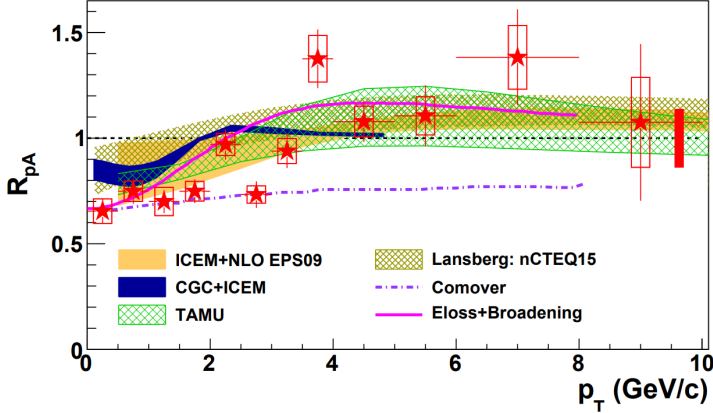


Figure 1.22 The  $J/\psi$  nuclear modification factor  $R_{pA}$  in  $p\text{Au}$  collisions<sup>[92]</sup>.

## 1.9 Quarkonium production in AA collisions

### 1.9.1 Theoretical overview

The quarkonium production in AA collisions is also affected by the existence of QGP or HNM effects. These effects mainly result from the interaction of quarkonium or its precursor with hot and dense QGP, or even cause the regeneration in QGP.

#### 1.9.1.1 Debye color screening

Quarkonium inside QGP may dissociate due to the color screening inside QGP. Take  $J/\psi$  as example. The radius of  $J/\psi$  is given by charmonium models in Ref<sup>[42]</sup>. The models suggest that the  $c\bar{c}$  has a non-relativistic interaction potential  $V(r)$  given as follows,

$$V(r) = \sigma r - \frac{\alpha_{eff}}{r}, \quad (1.28)$$

where  $\sigma$  represents for the string tension and  $\alpha_{eff}$  represents for the Coulombic interaction coupling. The typical value for isolated  $c\bar{c}$  systems are  $0.16 \text{ GeV}^2$  and  $\frac{1}{2}$  for  $\sigma$  and  $\alpha_{eff}$ . Minizing the bound state energy  $E(r)$ <sup>[101]</sup>,

$$E(r) = 2m + \frac{1}{2mr^2} + V(r) \quad (1.29)$$

gives us the equation

$$\frac{1}{mr_{J/\psi}^3} - \frac{\alpha_{eff}}{r_{J/\psi}^2} - \sigma = 0, \quad (1.30)$$

where  $m$  represents for the rest masses of  $c$ -quark. With increasing temperature,  $\sigma(T)$  decreases. At the critical temperature  $T_c$  where  $\sigma(T_c) = 0$ , the deconfinement happens.

And for  $T \geq T_c$ , the potential is expected [102] to be

$$V(r) = -\frac{\alpha_{eff}}{r} e^{-r/r_D(T)}. \quad (1.31)$$

Substitute the potential function into Eq. 1.29 and minimizing  $E(r)$  gives us the following equation,

$$\hat{r}(\hat{r} + 1)e^{-\hat{r}} = (m\alpha_{eff}r_D)^{-1} \quad (1.32)$$

where  $\hat{r} \equiv r/r_D$ . The restriction for Eq. 1.32 has solution only if  $(m\alpha_{eff}r_D)^{-1}$  won't exceed the maximum value for  $\hat{r}(\hat{r} + 1)e^{-\hat{r}}$ , which is around 0.84. So we can derive the smallest value of the screening radius permitting a bound state to be

$$r_D^{min}(T) = (0.84(m\alpha_{eff}(T))^{-1}). \quad (1.33)$$

With lattice QCD calculation<sup>[103]</sup>,  $\alpha_{eff}(T)$  decreases with temperature, in other words,  $r_D^{min}(T)$  increases with temperature, and as a lower limit for  $r_D$ ,  $r_D(T) < r_D^{min}(T)$  happens with increasing temperature. At  $T \approx 1.5T_c$ , the existence of  $J/\psi$  is excluded. The two determinants for Debye color screening effect are the binding energy and radius of quarkonium. Following the calculations above, we can calculate the temperature at which quarkonium of different states dissociates. When the temperature raised above the critical temperature  $T_c$ , first  $\psi(2S)$  and  $\Upsilon(3S)$  states melt, and when the temperature gets close to  $1.5 T_c$ ,  $J/\psi$  melts and when temperature gets slightly above  $2T_c$ ,  $\Upsilon(1S)$  state eventually melts. This is known as sequential melting, as shown in Fig 1.23.

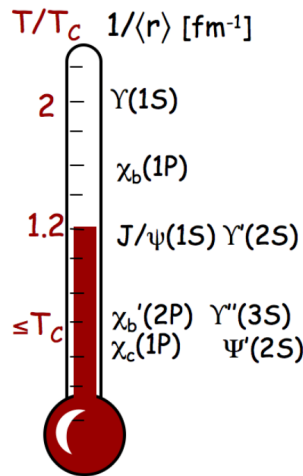


Figure 1.23 An illustrative sketch for sequential melting, figure taken from Ref<sup>[104]</sup>.

### 1.9.1.2 Dissociation and regeneration in QGP

The Debye screening phenomenon explains the dissociation of quarkonium in a static and uniform medium. However, in a dynamic and non-uniform environment like an inhomogeneous fireball, quarkonium can interact with medium particles leading to its dissociation<sup>[34]</sup>. There are two primary collision processes: gluon dissociation and inelastic parton scattering,

$$\text{Gluondissociation : } \psi + g \rightarrow Q + \bar{Q} \quad (1.34)$$

$$\text{Inelasticscattering : } \psi + p \rightarrow Q + \bar{Q} + p, p = g, q(\bar{q})$$

Gluon dissociation involves the breakup of quarkonium due to interactions with gluons. This process is often approached using theoretical methods like the Operator Production Expansion method<sup>[105-106]</sup>, which approximates the interaction between quarkonium and gluons. The OPE **method** is valid in the following cases:

- The binding energy of quarkonium is much larger than that of incoming gluon
- Quarkonium is tightly bound at low temperature
- Final-state interaction can be negligible

When the energy of incoming partons is comparable to or exceeds the binding energy of the quarkonium, inelastic parton scattering becomes important. Inelastic parton scattering occurs when incoming partons interact with constituent quarks within quarkonium, leading to its dissociation. The cross-section for this process is calculated considering thermal effects and parton-quarkonium interactions. To describe both the cases, potential NRQCD (pNRQCD) is used to study the quarkonium dissociate rate in QGP<sup>[107-108]</sup>.

In addition to this collisional dissociation of quarkonium, the regeneration of quarkonium need to be considered<sup>[109-112]</sup>. Regeneration refers to the process where quarkonium states are reformed from their constituent quarks or gluons. This process occurs as the inverse of quarkonium dissociation, following detailed balance principles, taking  $\psi$  as examples:

$$\begin{aligned} \text{Gluondissociation : } & \psi + g \rightarrow Q + \bar{Q} \\ \text{Inelasticscattering : } & \psi + p \rightarrow Q + \bar{Q} + p, p = g, q(\bar{q}) \\ & \downarrow \\ \text{Regeneration : } & Q + \bar{Q} \rightarrow \psi + g \\ & Q + \bar{Q} + p, p = g, q(\bar{q}) \rightarrow \psi + p \end{aligned} \quad (1.35)$$

This regeneration process is studied by Boltzmann equation based on perturbative

NRQCD<sup>[113]</sup>. The regeneration cross section for the gluon dissociation as function of collision energy  $s$  can be obtained as follows

$$\sigma_{Q+\bar{Q} \rightarrow J/\psi + g}(s) = \frac{4(s - m_{J/\psi}^2)^2}{3s(s - 4m_Q^2)} \sigma_{J/\psi + g \rightarrow Q+\bar{Q}}(s). \quad (1.36)$$

The open charm hadron  $R_{AA}$  and  $\nu_2$  measurements show that charm quark is almost thermalized in QGP. For calculating regeneration of charmonium in QGP, one need to couple the charm quark Langevin transport equation in QGP with the regeneration<sup>[114]</sup>.

## 1.9.2 Experimental results

The NA38 Collaboration provided the first evidence of  $J/\psi$  suppression in O-U collisions at 200 GeV/nucleon<sup>[115]</sup>. This suppression as shown in Fig 1.24 (left), indicated by a roughly 35% decrease in the ratio of  $J/\psi$  decays to muon pairs compared to continuum events, marked a significant finding in understanding deconfinement. Followed by NA50, who also find a decreasing trend on the ratio of  $J/\psi$  production to its Drell-Yan production with multiplicity, as shown in Fig 1.24 (right). Over the past four decades, advancements in theoretical models and experimental results have further solidified this understanding. The consensus on the qualitative interpretation of charmonium suppression, attributing it to a blend of color screening and recombination mechanisms, has emerged. However, achieving a quantitative description remains challenging, with ongoing debates surrounding spectral modifications of quarkonium states and their formation time relative to the QGP. More precise experimental data, particularly on excited quarkonium states and the open charm cross section, are crucial for refining model calculations.

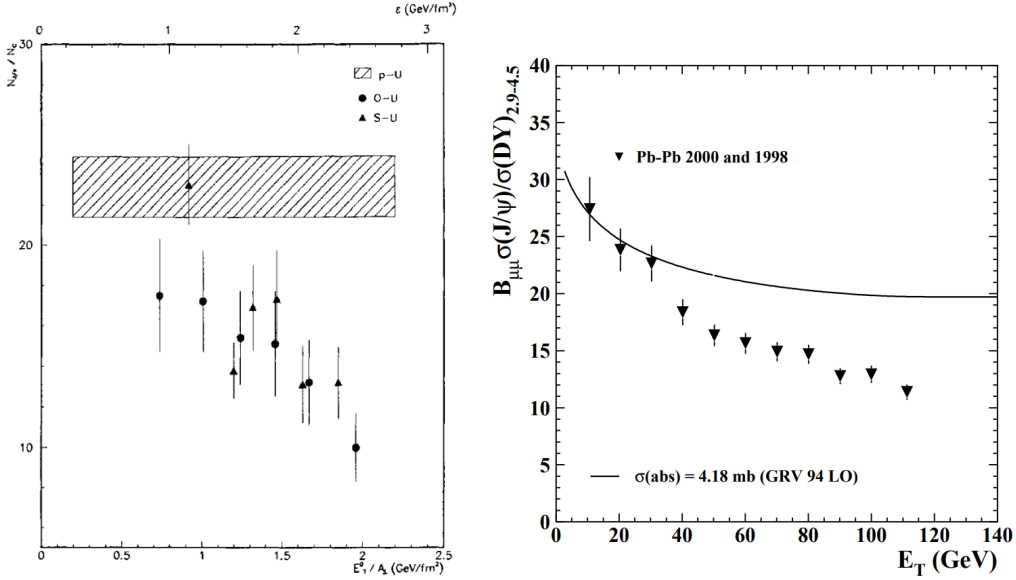


Figure 1.24 Ratio of (left) number of  $J/\psi$  to the number of continuum events, (right) production of  $J/\psi$  to its Drell-Yan production, as function of transverse energy<sup>[115]</sup>.

Experimental results have been presented, start from the fixed-target program at SPS, to RHIC and LHC. The  $J/\psi$  nuclear modification factor as function of centrality has been measured in PbPb and AuAu collisions, by ALICE<sup>[116-117]</sup>, PHENIX<sup>[118]</sup> and STAR<sup>[119]</sup>, respectively. As shown in Fig 1.25, measurements come to an agreement that  $J/\psi$  is suppressed in the high multiplicity region, which could result from the color screening and dissociation in QGP.

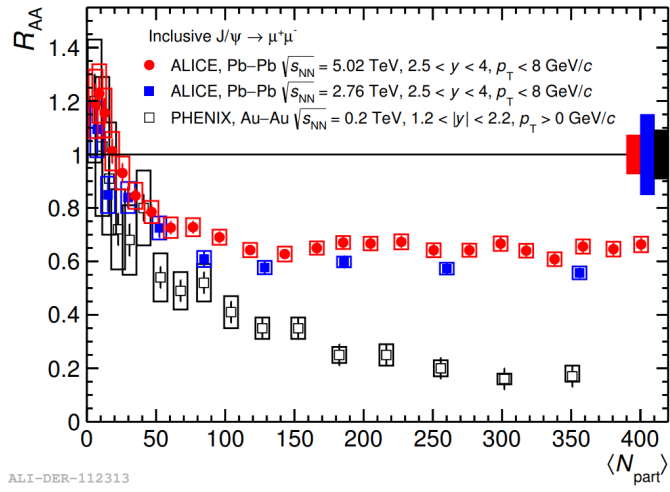


Figure 1.25 Centrality dependence of  $J/\psi$  nuclear modification factor<sup>[116-118]</sup>.

For bottomonium, the recombination effect are marginal. A very clear hierarchy in suppression between different  $\Upsilon$  states is found in PbPb collisions by CMS<sup>[120]</sup>, as shown

in Fig 1.26. This also support the sequential melting in QGP.

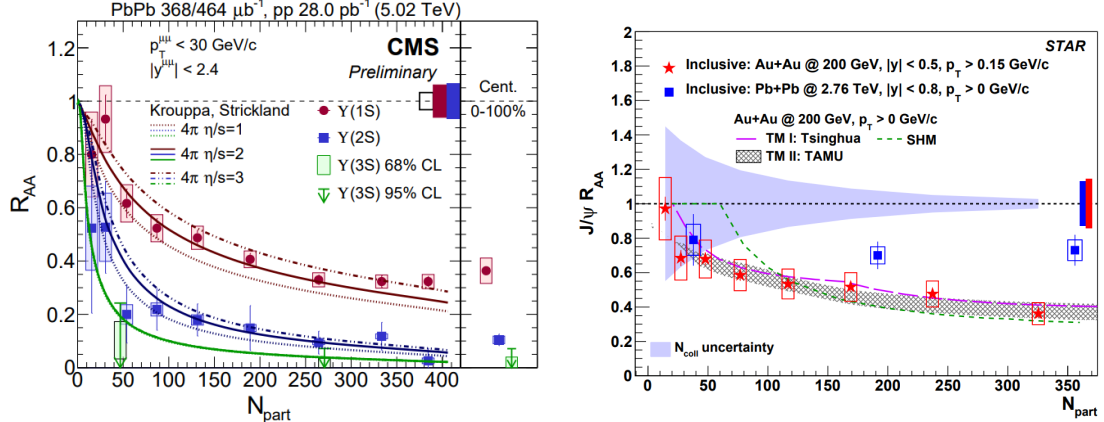


Figure 1.26 Multiplicity dependence of  $R_{AA}$  for (left) different  $\Upsilon$  states in PbPb collisions<sup>[120]</sup> and (right)  $J/\psi$  in AuAu collisions<sup>[119]</sup>.

## 1.10 Quarkonium production in high multiplicity small system collisions

The measurement of particle production yields in heavy-ion collisions, compared to those in  $pp$  collisions or across different collision centralities, aims to disentangle QGP effects. Recently, the representation of particle yields against collision charged-particle multiplicity has gained significant interests. Such studies in small system collisions, from  $pp$  to  $pPb$  collisions, offer insights into QGP creation and unexpected phenomena observed in high-multiplicity events, see Sec 1.6. These investigations raise questions about the mechanisms underlying collective behavior, whether QGP droplet is formed, and whether there are interactions of hard probes with small QGP droplets. In this section, recent measurements of quarkonium production as a function of charged-particle multiplicity in small system collisions at LHC energies are reviewed, focusing on charmonium and bottomonium yields and probing the nature of hadron production. These analyses typically present results as relative quantities, offering improved sensitivity to variations in particle yield with charged-particle multiplicity.

The production ratio of  $\Upsilon(2S)/\Upsilon(1S)$  and  $\Upsilon(3S)/\Upsilon(1S)$  as a function of charged track multiplicity in the midrapidity is reported by CMS<sup>[121-122]</sup>. Similar hierarchy of suppression has been found in  $pp$  and  $pPb$  collisions, where  $\Upsilon(2S)$  and  $\Upsilon(3S)$  production are more suppressed than  $\Upsilon(1S)$ , as shown in Fig 1.27.

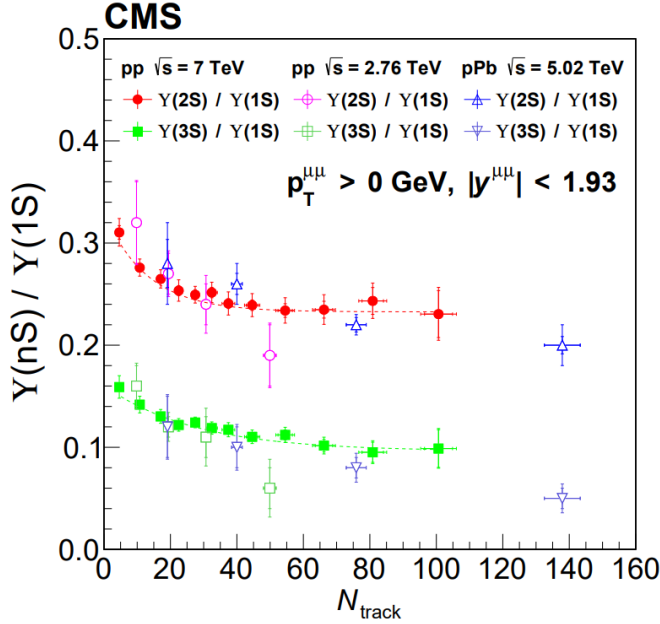


Figure 1.27 The  $\Upsilon(nS)/\Upsilon(1S)$  ratio as a function of charged track multiplicity in  $pp$  collisions at LHC energies from CMS<sup>[121-122]</sup>.

Similar phenomenon has been observed in the multiplicity dependence of  $\chi_{c1}(3872)/\psi(2S)$ , where the prompt ratio decreases with multiplicity and the non-prompt ratio does not, as shown in Fig 1.28. The non-prompt charmonium originated from  $b$ -hadron decay, usually farther from the collision center, and hence, farther from QGP or other produced final-state particles, are not affected by the nuclear matter effect. The decreasing trend in prompt ratio is in agreement with the observation on bottomonia by CMS.

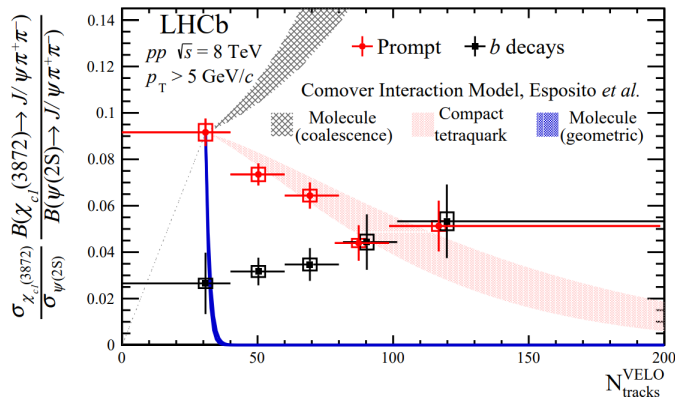


Figure 1.28 Multiplicity dependence of  $\chi_{c1}(3872)/\psi(2S)$  in 8 TeV  $pp$  collisions from LHCb<sup>[123]</sup>.

However, the  $\psi(2S)$ -to- $J/\psi$  ratio measured by ALICE does not exhibit a multiplicity dependence in  $pp$  or  $pPb$  collisions as shown in Fig 1.29. The error bars are relatively

large in  $p\text{Pb}$  result, making it difficult to draw conclusions.

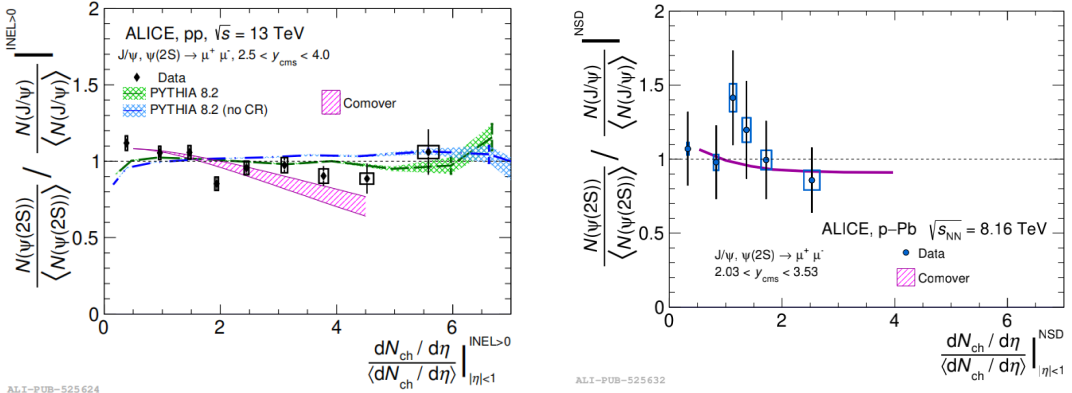


Figure 1.29 Self normalised  $\psi(2S)$ -to- $J/\psi$  yield ratio as function of self-normalised charged-particle multiplicity in  $pp$  (left) and  $p\text{Pb}$  collisions. Graph is taken from Ref<sup>[124]</sup>.

## 1.11 Motivation for this thesis

The results obtained from experiments conducted at SPS, RHIC and LHC and the related theory studies have established the following understanding about quarkonium production in heavy-ion collisions. In AA collisions, quarkonium production is strongly suppressed towards central or high-multiplicity collisions due to the creation of QGP, and the regeneration becomes more important at LHC energies for charmonium production. In  $pA$  collisions, quarkonia are less suppressed than in AA collisions, due to the lack of QGP effects. The excited quarkonium states is more suppressed in both AA and  $pA$  collisions, a hierarchy of suppression is observed for both charmonia and bottomonia. For small system  $pp$  and  $p\text{Pb}$  collisions, the excited  $\Upsilon$  states seem to be less produced relative to ground state in high multiplicity events. However, this is not observed for charmonia states yet.

This study focuses on exploring charmonia production in high-multiplicity  $pp$  and  $p\text{Pb}$  collisions, as a probe for the potential existence of QGP droplet in these collisions, with the fact that more and more QGP signatures are found in high-multiplicity small system collisions.

Firstly, the multiplicity dependence of  $\psi(2S)$ -to- $J/\psi$  ratio in  $pp$  collisions at center-of-mass energy  $\sqrt{s} = 13 \text{ TeV}$  is measured. By presenting the  $\psi(2S)$ -to- $J/\psi$  production ratio as function of different multiplicity variables, which are measured in different kinematic region, the suppression due to comover effect and potential existence of QGP can be disentangled, and the discrepancy observed in different measurements may be explained

by different choices of multiplicity measurements. By measuring the production ratio, the initial-state effects like modification of nPDFs and initial-state energy loss cancel, and make the ratio a good indicator for final-state effects.

Then the  $\psi(2S)$ -to- $J/\psi$  ratio as a function of multiplicity is also measured in  $p\text{Pb}$  collisions at  $\sqrt{s_{NN}} = 8.16 \text{ TeV}$  in forward ( $p-$  going) and backward ( $\text{Pb}-$ going) direction. It completes the missing piece on multiplicity dependence of charmonia in small system collisions, as a transition between small system collisions to large systems. By comparing the result in  $pp$ ,  $p\text{Pb}$  forward and backward measurements, where the mean charged particle multiplicity increases in sequence, the properties for charmonium production is probed in an environment approaching to the high-density AA collisions.

The data sample used is collected by LHCb experiment, which is introduced in Chapter 2. With its excellent ability in primary vertex (PV) reconstruction, the decay time of charmonium can be obtained with high precision. Therefore, the prompt production for charmonium, that are directly from the collisions, can be separated from the production from  $b$ -hadron decay. Take advantage of the high muon identification and dimuon trigger efficiency in LHCb detector, large statistics of  $J/\psi$  and  $\psi(2S)$  can be reconstructed through  $J/\psi \rightarrow \mu^+ \mu^-$  ( $\psi(2S) \rightarrow \mu^+ \mu^-$ ) decay channel to perform this study.

## CHAPTER 2 LHCb EXPERIMENT

The LHCb experiment is one of the four main particle physics experiments located at the Large Hadron Collider (LHC). The LHC, operated at the highest energy in the world, is a circular tunnel with a 27 km circumference near Geneva, straddling the French-Swiss border. The acceleration process of protons at the LHC involves multiple stages, starting with a linear accelerator and progressing through various synchrotrons to reach energies up to 7 TeV. Additionally, heavy ions can also be accelerated through a separate process in the low energy ion ring (LEIR) and get further accelerated reach the energy of 2.56 TeV before reaching the LHC.

The LHC consists of two independent vacuum pipes where two beams circulate in opposite directions, with four beam intersection points hosting the main experiments: ATLAS, CMS, ALICE, and LHCb, shown in Fig 2.1. While ATLAS and CMS are general-purpose experiments, ALICE focuses on heavy ion physics, and LHCb is specialized for heavy flavor physics . These experiments contribute significantly to the study of charmonium production.

The LHC operates with high instantaneous luminosity, which is crucial for obtaining a large number of events of interest. The designed instantaneous luminosity of the LHC is  $10^{34} \text{ cm}^{-2} \text{ s}^{-1}$ , achieved in 2016, while the LHCb experiment aims for a reduced luminosity of  $2\text{--}4 \times 10^{32} \text{ cm}^{-2} \text{ s}^{-1}$  for precise heavy-flavor measurements. Data from proton-proton collisions at different energies have been collected at the LHC, with the center-of-mass energy reaching 13 TeV during Run2. Short runs at lower energies, such as  $\sqrt{s} = 2.76 \text{ TeV}$  and 5 TeV, were also conducted to provide references for heavy ion collisions and complement measurements on charmonium production in proton-proton collisions.

LHCb<sup>[125-126]</sup> is the Large Hadron Collider beauty experiment. It is one of the four main experiments conducted at the Large Hadron Collider (LHC). The primary goal of LHCb is to study the phenomenon known as CP violation, which stands for charge-conjugation and parity symmetry violation, and rare decays of  $b$  and  $c$  quarks, with the aim of identifying indirect evidence of new physics. The observed level of CP violation in the weak interactions is insufficient to explain the matter-antimatter asymmetry in the universe, indicating the need for new sources of CP violation beyond the SM. To address this, LHCb focuses on studying heavy flavor physics, where many models of new physics

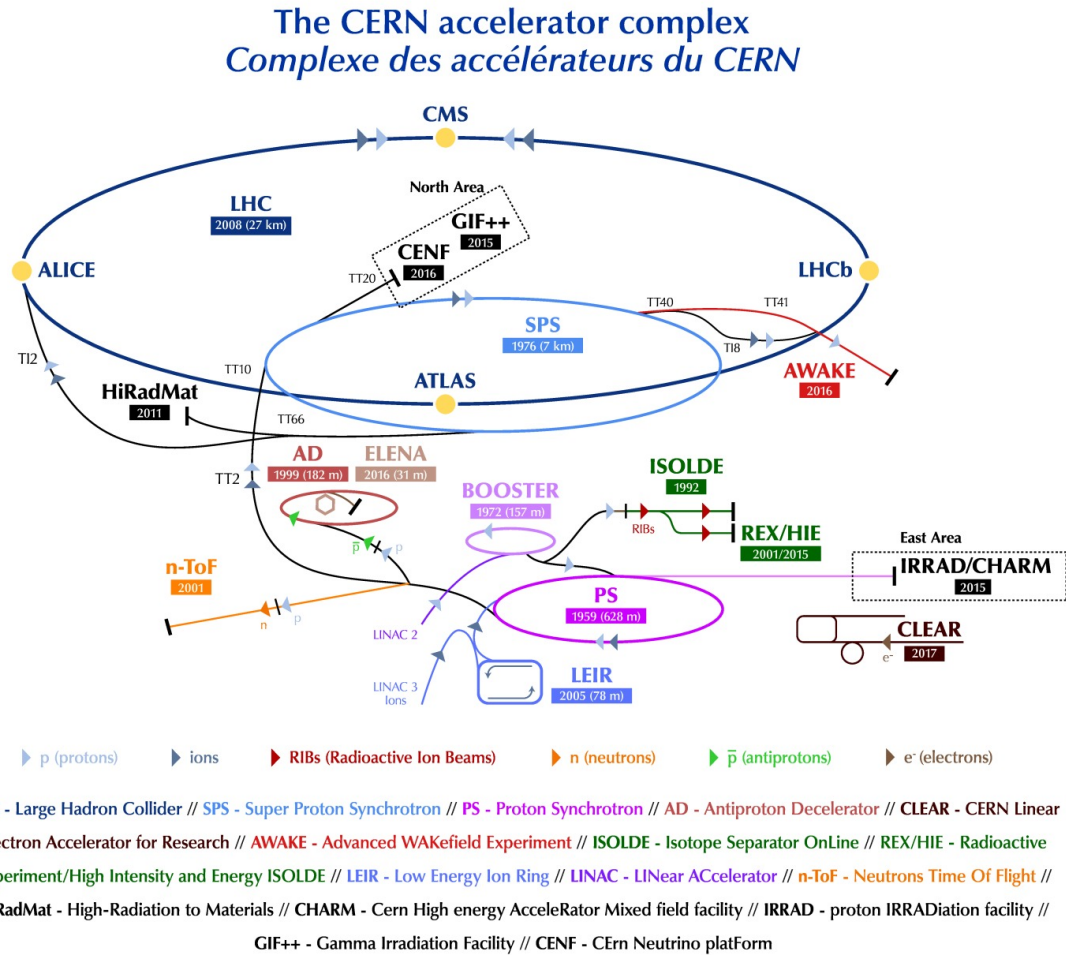


Figure 2.1 An illustrative schematic for LHC.

predict contributions that alter the expected values of CP violating phases or the branching fractions of rare decays. The experiment utilizes large data samples, collected thanks to the high beauty and charm production cross-sections at the LHC. Despite the challenges posed by increased background levels in hadronic collisions, LHCb has distinct advantages, such as a higher cross-section, larger boost, and the production of all species of  $b$  hadrons.

## 2.1 LHCb detector

LHCb detector<sup>[126]</sup> is a single-arm spectrometer covering the forward pseudorapidity range  $2 < \eta < 5$ , where  $b$ -hadrons are predominately produced in the cone. LHCb detector can ideally accept about 25% of  $b$ -hadron with less than 2% of the angle coverage. The layout of LHCb detector is shown in Fig 2.2.

Within the LHCb detector, a diverse array of subdetectors fulfills critical roles in

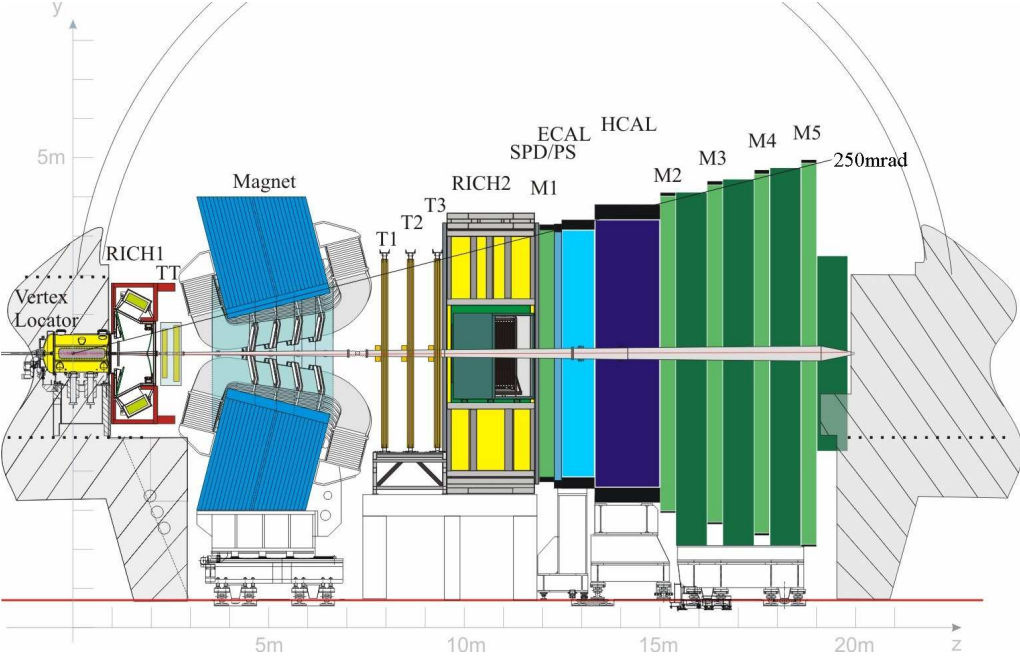


Figure 2.2 View of LHCb detector along the beam-going axis. The  $z$ -axis is the beam-going direction, and the horizontal  $x$ -axis and vertical  $y$ -axis form a right-hand coordinate system. Figure is taken from Ref<sup>[127]</sup>, figure is taken from Ref<sup>[126]</sup>.

particle detection and identification. These encompass the VELO (Vertex Locator), TT (Tracker Turicensis), T1-T3 tracking stations, RICH1 and RICH2 (Ring Imaging Cherenkov detectors), a comprehensive calorimeter system (SPD, PS, ECAL, HCAL), and a muon detection system comprising M1-M5 stations. In the following sections, we will delve into each of these components, detailing their functionalities.

## 2.2 Tracking system

The tracking system<sup>[128]</sup> that reconstruct the tracks of charged particles is composed of VErtex LOcater (VELO), Tracker Turicensis (TT), Inner Tracker (IT) and Outer Tracker (OT). The IT and OT are inner and outer part of T-stations (T1 to T3 in as shown in Fig 2.2), which are composed of silicon micro-strip detectors and straw tubes, respectively. The IT is closer to the beam pipe.

### 2.2.1 Vertex Locator

The VELO<sup>[129-130]</sup> consists of 21 stations arranged along the beam axis ( $z$ -axis). Consisting of 42 silicon modules, each station is assembled in two halves, forming semicircular modules. The cross-sectional view in the  $(x, z)$  and  $(x, y)$  planes illustrates the VELO's design in Fig 2.3, with the two halves fully closed during stable beams for safety. Each

module consists of  $r$  and  $\phi$  sensors, measuring radial and azimuthal coordinates, respectively, with a linearly increasing pitch. The VELO enables the precise reconstruction of

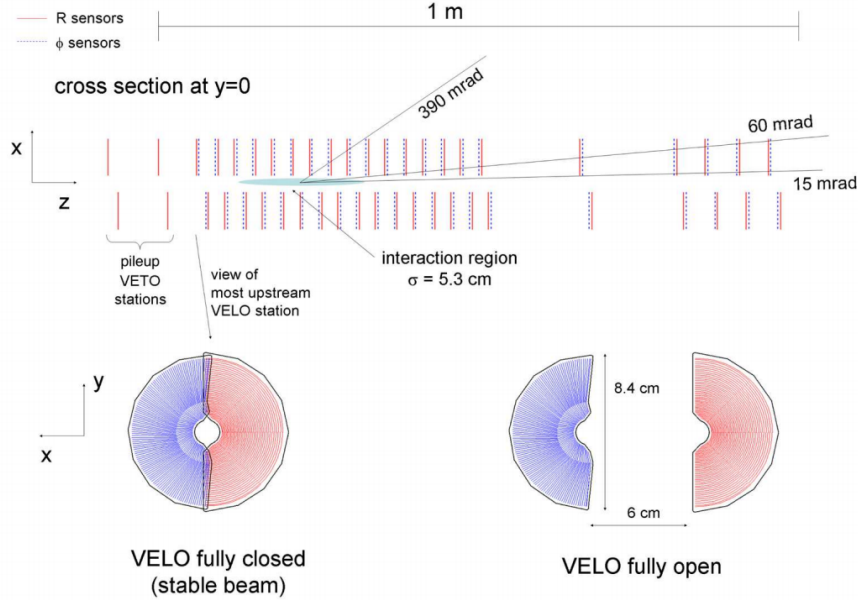


Figure 2.3 Cross-sectional view of VELO, figure is taken from Ref<sup>[126]</sup>.

production and decay vertices for  $b$ - and  $c$ -hadrons. The detector's geometry covers the angular acceptance of downstream sub-detectors, ensuring that tracks crossing at least three VELO stations emerge from the interaction region. The VELO plays a key role in flavor tagging by providing accurate impact parameters and decay lifetimes.

The VELO is retractable for safety during beam injection, with an automated procedure initiated during injection and reversed under stable conditions. The spatial resolution for VELO can reach to about  $13\mu\text{m}$  in the  $(x, y)$  plane and  $50\mu\text{m}$  along  $z$ -axis, with enough number of charged tracks to reconstructing PV. The resolution as function of charged tracks is shown in Fig 2.4. The proper time resolution of the VELO is approxi-

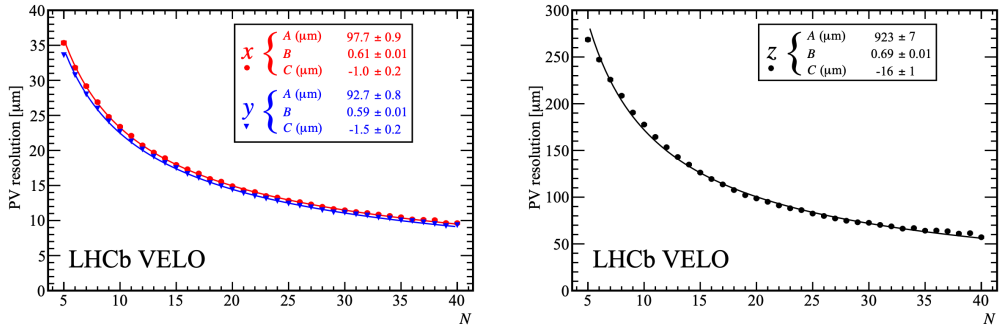


Figure 2.4 PV resolution for one PV reconstructed as function of charged tracks Ref<sup>[126]</sup>.

mately 50 fs, significantly smaller than the lifetime of  $b$ -hadrons in the ground state. This resolution is vital for distinguishing prompt and non-prompt charmonium in production measurements. Overall, the VELO's tracking efficiency exceeds 98%, with impressive spatial resolutions and impact parameter measurements, making it a crucial and high-performing component of the LHCb experiment.

A more detailed review for VELO performance can be found in Ref<sup>[129]</sup> and the layout of modules for VELO can be found in Ref<sup>[126]</sup>.

## 2.2.2 Tracker Turicensis

The TT is a critical tracking station within the LHCb experiment, positioned upstream of the dipole magnet with dimensions of approximately 150 cm in width and 130 cm in height. The TT employs silicon micro-strip sensors with a fine strip pitch of 183  $\mu\text{m}$ . It consists of four detection layers arranged in an  $x - u - v - x$  layer configuration, where the first and last layers ( $x$ ) are organized with vertical strips, while the middle two layers ( $u$  and  $v$ ) are rotated by an angle of  $\pm 5$  deg with respect to the  $y$ -axis. This unique arrangement allows for three-dimensional hit position measurements. The TT achieves an exceptional overall hit efficiency exceeding 99.7%. The schematic layout for TT can be found in Fig 2.5.

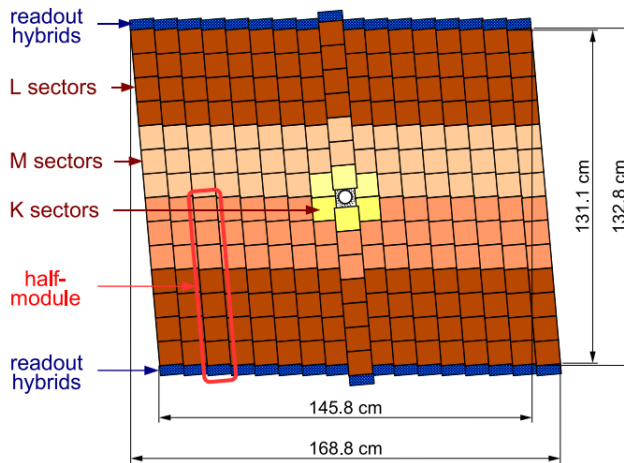


Figure 2.5 Layout of Tracker Turicensis, figure is taken from Ref<sup>[126]</sup>.

## 2.2.3 T-stations

The T-stations T1-T3 are located in the downstream of magnet, each station has similar layers as TT. The T-stations can be divided into inner tracker and outer tracker.

The Inner Tracker<sup>[131]</sup> (IT) within the T-stations plays a critical role, featuring three

stations, each housing four detector boxes strategically arranged around the beam pipe. These boxes, designed to be light-tight and electrically insulated, and undergo continuous nitrogen flushing to prevent condensation. Each box is equipped with four detection layers, and the modules within them vary based on their location (top, bottom, left, or right). IT detector modules consist of either single or dual silicon sensors connected to a front-end readout hybrid, contributing to precise tracking and accurate hit position measurements.

The layout of IT is shown in Fig 2.6.

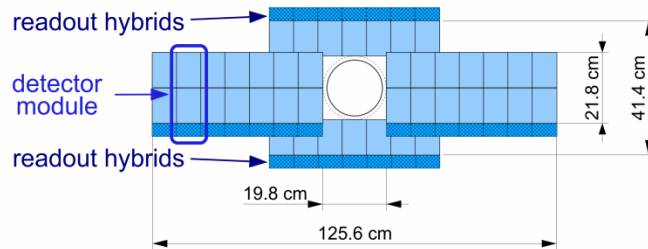


Figure 2.6 Layout of IT, figure is taken from Ref<sup>[126]</sup>.

The Outer Tracker (OT)<sup>[132]</sup> in the T-stations serves as a drift-time detector, playing a crucial role in tracking charged particles and accurately measuring their momentum. Consisting of an array of gas-tight straw-tube modules with length 2.4 m and inner diameter 4.9 mm, the OT features a unique design with staggered layers in an  $x - u - v - x$  geometry similar to TT. The counting gas mixture, a combination of Argon (70%) and CO<sub>2</sub> (30%), ensures fast drift times less than 50 ns and sufficient drift-coordinate resolution approximately 200 $\mu$ m. The OT consists of three stations, each with four layers, providing excellent momentum resolution for precise mass determinations of reconstructed  $b$ -hadrons. The modular design, radiation resistance, and material constraints make the OT an indispensable component for achieving high tracking efficiency and low reconstruction errors in the LHCb experiment. The layout of TT is shown in Fig 2.7.

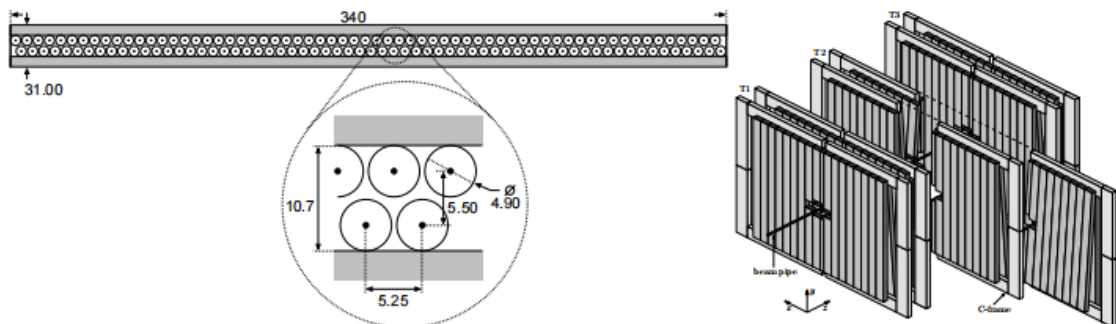


Figure 2.7 (left) Cross-sectional view of straw-tube and (right) layout for OT, figure is taken from Ref<sup>[133]</sup>.

## 2.2.4 Magnet

The magnet system<sup>[134]</sup> is composed of a warm magnet with saddle-shaped coils, integrated into a yoke made of laminated low carbon steel plates. These plates, 100 mm thick, form identical horizontal bottom and top parts and two mirror-symmetrical vertical parts (uprights) of the magnet yoke. The yoke's total weight is 1500 tons, and the two coils, each of conical saddle shape, weigh 54 tons, making up a total weight of 1600 tons. The perspective view for the LHCb dipole magnet is shown in Fig 2.8.

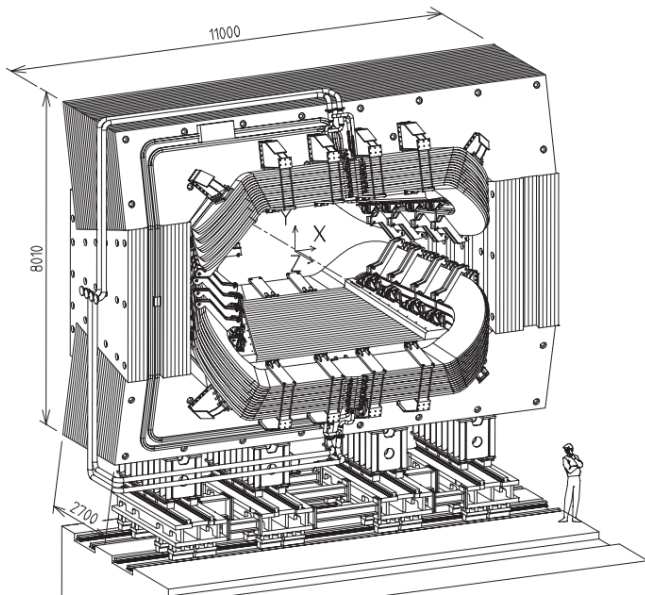


Figure 2.8 Perspective view of magnet system in LHCb, figure is taken from Ref<sup>[126]</sup>.

Each coil comprises fifteen pancakes arranged in five triplets, made of pure Al-99.7 hollow conductor with a central cooling channel. The conductor is designed for a specific ohmic resistance below  $28 \Omega \cdot \text{m}$  at  $20^\circ\text{C}$ . The coils are conically shaped and placed mirror-symmetrically to each other in the yoke, with cast aluminum clamps holding together the triplets. Finite element models have been extensively used to analyze the coil support system, ensuring stability under electromagnetic and thermal stresses.

The magnet system is designed to generate an integrated magnetic field of  $4 \text{ T} \cdot \text{m}$  for tracks of 10 m length, accommodating varying field levels inside the RICHs envelope and regions between the vertex locator and the Trigger Tracker tracking station. The magnetic field distribution along  $z$  direction is shown in Fig 2.9. The design also considers the need for the magnet to be assembled in a temporary position and divided into two relatively light elements for practical construction. The magnet has capability for the reversal of the magnetic field in  $y$  direction within the detector, up for positive  $y$  and down for negative

y. Changing the polarity is essential for studying the properties of particles with opposite charges or for controlling the trajectories of charged particles within the detector.

### 2.2.5 Track reconstruction

According to the track reconstructed from different hits in different sub-detectors, the tracks can be categorized into different types as shown in Fig 2.9:

- Long Tracks: long tracks<sup>[135]</sup> requires hits from both VELO and T stations, and optionally in TT. As they traverse the whole magnetic region, they have the most precise estimation for momentum. Therefore, they are most important set of tracks for analysis.
- Upstream Tracks: upstream tracks pass through VELO and TT only, their momentum are usually too small to pass the whole tracking system. But they will pass through Ring-Imaging CHerenkov detector 1 (RICH1) which contributes to the understanding of the particle identification (PID) algorithm of the RICH.
- Downstream Tracks: downstream tracks require hits from TT and T-stations only. They represents the long-lived particles that decay outside the VELO, hence, are important for the reconstructions of long-lived particles like  $K_S^0$  and  $\Lambda$ .
- VELO Tracks: VELO tracks pass only VELO, including both forward and backward tracks. They are typically large angle and are useful for primary vertex (PV) reconstruction. Also, the number of VELO tracks can represent the local charged particle multiplicity in a collision event.
- T Tracks: T tracks pass only through T-stations, which are typically produced in secondary interactions. They can contribute to the PID algorithm for RICH2.

The tracks used in this analysis are Long Tracks and the multiplicity variable is the number of tracks used in reconstructing PV.

The track finding efficiency<sup>[136]</sup> is defined as the probability that the trajectory of a charged particle passing through the tracking system is successfully reconstructed. It is assessed using a tag-and-probe technique with  $J/\psi \rightarrow \mu^+ \mu^-$  decays. In this method, one daughter particle is fully reconstructed (tag leg), while the other (probe leg) is only partially reconstructed. The efficiency is determined by matching the partially reconstructed probe leg to a fully reconstructed long track. The tracking efficiency remains consistently above 96% in the momentum range of 5 GeV/c to 200 GeV/c and pseudorapidity range of  $2 < \eta < 5$ , covering LHCb's phase space. The track efficiency determined by samples collected in 2011 and 2012 is shown in Fig 2.10.

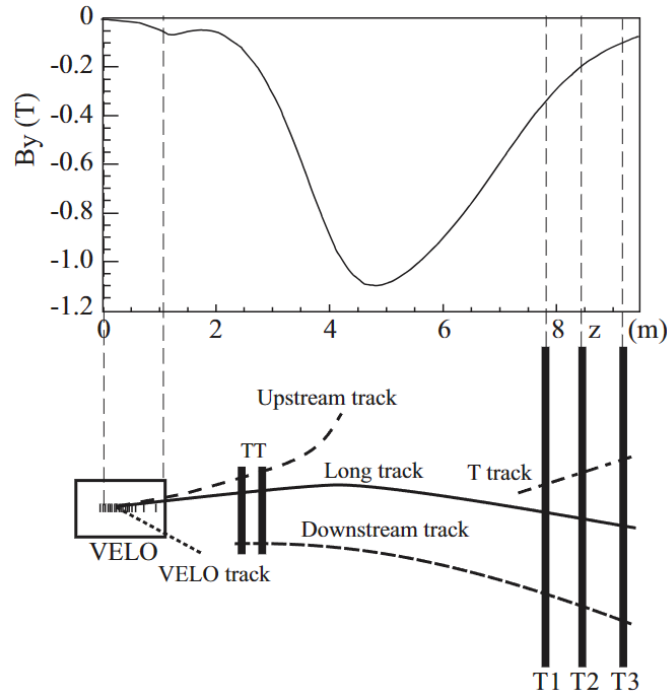


Figure 2.9 Illustration for different track types, figure is taken from Ref<sup>[125]</sup>.

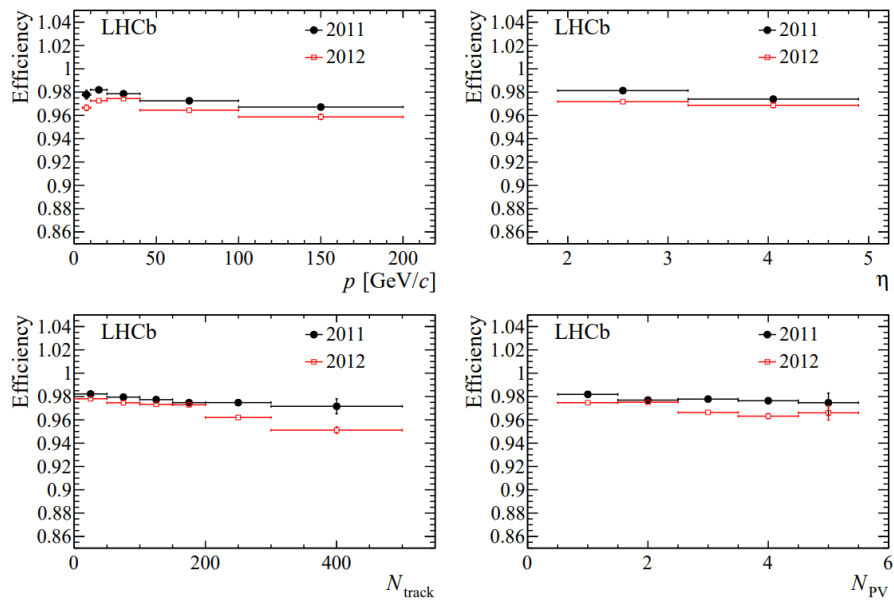


Figure 2.10 Tracking efficiency as functions of momentum  $p$ , pseudorapidity  $\eta$ , number of tracks  $N_{\text{tracks}}$  and number of PV reconstructed  $N_{\text{PV}}$ , figure is taken from Ref<sup>[125]</sup>.

## 2.3 Particle identification

The Particle Identification (PID) system<sup>[137]</sup> in the LHCb experiment incorporates three essential sub-detectors: Cherenkov detectors (RICH1 and RICH2)<sup>[138-139]</sup>, calorimeters (including the Preshower Detector (PS), Scintillating Pad Detector (SPD)<sup>[140]</sup>, Hadronic Calorimeter (HCAL)), and Electromagnetic Calorimeter (ECAL)<sup>[141]</sup>, and dedicated muon stations (M1–M5). The Cherenkov detectors exploit the production of Cherenkov radiation to identify charged hadrons (such as  $\pi$ ,  $k$  and  $p$ ) while the calorimeter system, consisting of various components, plays a pivotal role in the identification of electrons, photons, and hadrons. The muon stations are specifically designed for muon identification. This comprehensive PID system not only provides excellent capabilities for discriminating between different types of charged particles but also enables the reconstruction and identification of neutral particles, including photons and  $\pi^0$  mesons, through the calorimeter systems. The collaboration of these sub-detectors allows for precise particle identification and contributes significantly to the comprehensive study of particle properties and interactions at the LHCb experiment.

### 2.3.1 Cherenkov detectors

The Ring Imaging Cherenkov detector (RICH) operates on the principle of Cherenkov radiation, wherein charged particles, moving through a transparent medium at speeds exceeding the local speed of light, emit photons in a cone-shaped pattern. RICH distinguishes between different charged particles by precisely measuring the Cherenkov angle, which is related to the particle's velocity  $v$  and the refractive index of the medium. Utilizing the relationship

$$\cos \theta_c = \frac{c}{nv}, \quad (2.1)$$

where  $c$  is the speed of light in vacuum and  $n$  the refractive index. RICH identifies particles by combining momentum information from the tracking system, inferring particle mass, and enabling species discrimination. With its ability to provide ring-shaped images based on Cherenkov radiation, RICH allows for the precise localization of particle trajectories. There are two RICH's in the LHCb detector:

- RICH1<sup>[138]</sup>: the upstream Cherenkov detector in the LHCb experiment, is strategically positioned between the VELO (Vertex Locator) and the Trigger Tracker, covering the low-momentum charged particle range of approximately 1–60 GeV/c. This detector utilizes a combination of aerogel and fluorobutane ( $C_4F_{10}$ ) gas ra-

diators to achieve Particle Identification goals, particularly separating pions from kaons in selected  $b$  hadron decays. The design of RICH1 incorporates a wide angular acceptance, spanning from  $\pm 25$  mrad to  $\pm 300$  mrad horizontally and  $\pm 250$  mrad vertically. Its placement upstream of the LHCb dipole magnet allows for the detection of low-momentum particles. The Cherenkov light produced in RICH1 is focused using a combination of spherical and flat mirrors, and Hybrid Photon Detectors (HPDs) are employed to detect Cherenkov photons in the wavelength range of 200–600 nm. The overall design of RICH1 prioritizes minimizing material within the particle acceptance, employing lightweight spherical mirrors, and addressing constraints such as the presence of the LHCb beryllium beampipe and shielding from the fringe field of the dipole magnet.

- RICH2<sup>[139]</sup>: In contrast, RICH2, the downstream Cherenkov detector, is positioned downstream of the LHCb dipole magnet and is specifically designed to cover the high-momentum range from approximately 15 GeV/c up to and beyond 100 GeV/c, utilizing a CF<sub>4</sub> radiator. While RICH2 has a more limited angular acceptance compared to RICH1, spanning  $\pm 15$  mrad to  $\pm 120$  mrad horizontally and  $\pm 100$  mrad vertically, it strategically covers the region where high-momentum particles are produced. Similar to RICH1, RICH2 employs a combination of spherical and flat mirrors to focus Cherenkov light, and HPDs are used for detecting Cherenkov photons within the wavelength range of 200–600 nm. The design of RICH2 also takes into account constraints such as minimizing material within the particle acceptance and providing effective shielding for the HPDs from the fringe field of the LHCb dipole magnet. Together, RICH1 and RICH2 contribute to the comprehensive PID system at LHCb, allowing for precise identification of charged particles across a broad momentum spectrum.

The Side view for RICH1 and RICH2 is shown in Fig 2.11. The cherenkov angle versus particle momentum for RICH is shown in Fig 2.12. In the low momentum region, Aerogel can separate kaons from pions and in the high momentum region, CF<sub>4</sub> will be a good medium that separates them.

The detailed information for RICH detector performance in LHC run 2 can be found in Ref<sup>[142]</sup>

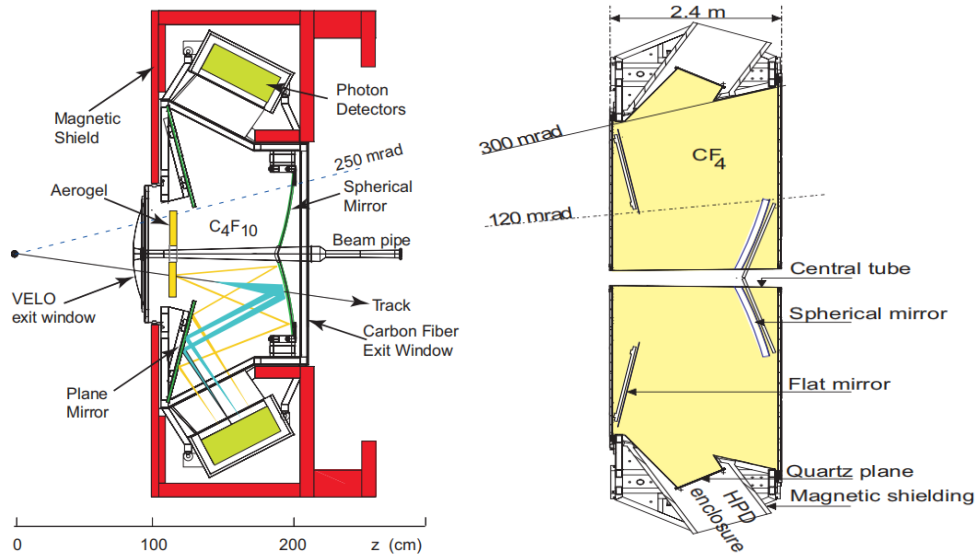


Figure 2.11 Side view for (left) RICH1 and (right) RICH2, figure is taken from Ref<sup>[133]</sup>.

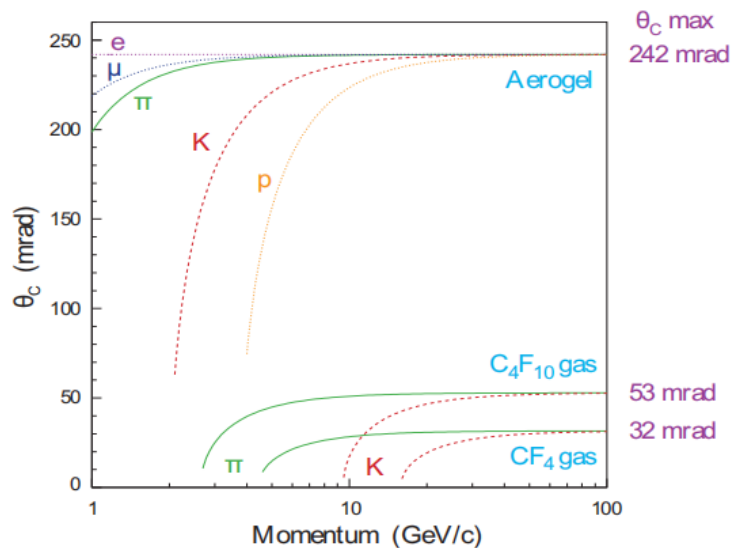


Figure 2.12 Cherenkov angle versus particle momentum in different media, figure is taken from Ref<sup>[133]</sup>.

### 2.3.2 Calorimeter

The calorimeter system<sup>[141]</sup> in the LHCb experiment plays a crucial role in identifying and measuring the energies of particles produced in high-energy collisions. Consisting of the SPD, PS, ECAL and HCAL, this system is strategically positioned downstream of the tracking stations and Cherenkov detectors along the beam axis. The calorimeter system aims to provide precise information on charged particles, electrons, photons, and hadrons. The SPD and PS, consisting of scintillating pads and a lead absorber, aid in distinguishing charged particles and contribute to initiating electromagnetic showers. The ECAL, employing a shashlik-type calorimeter structure, and the HCAL, utilizing iron plates and scintillating tiles, focus on detecting electromagnetic and hadronic showers, respectively. The cell segmentation and the layout for calorimeter system can be found in Fig 2.13.

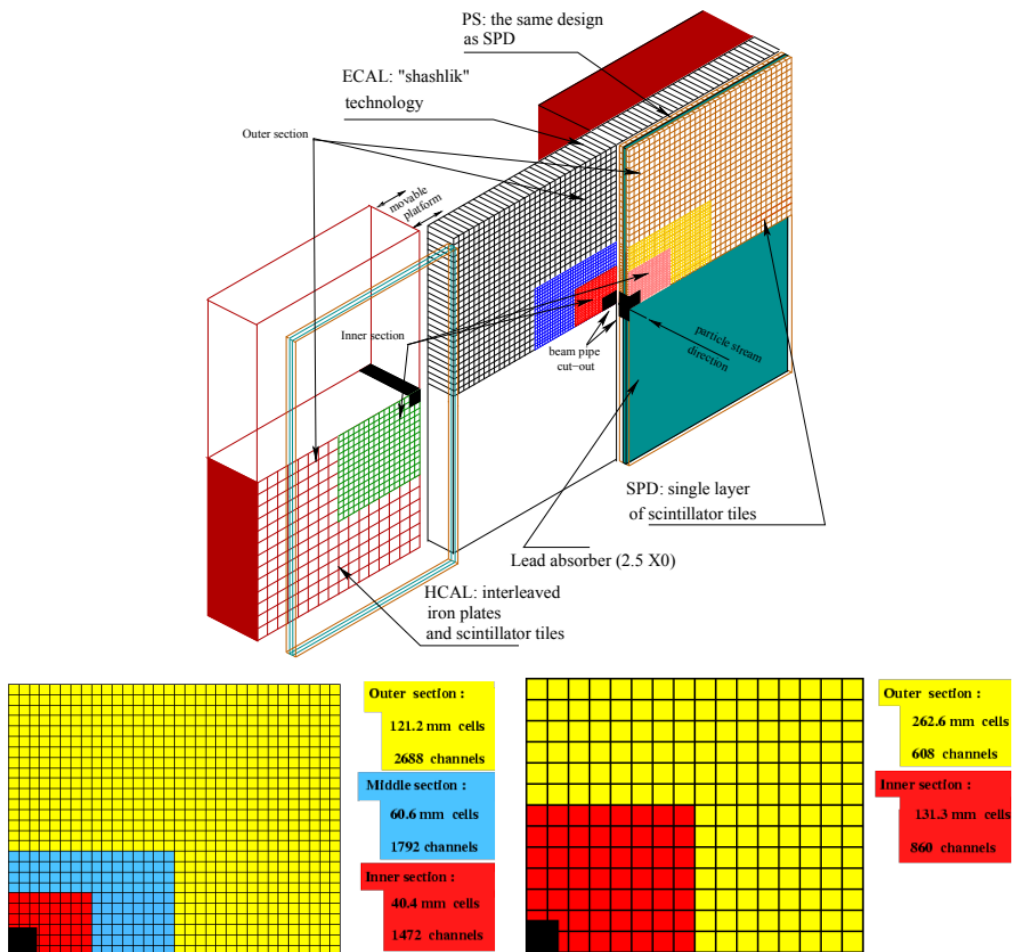


Figure 2.13 The (upper) layout and cell segmentation for calorimeter system in LHCb detector, figure is taken from Ref<sup>[141]</sup>.

The design of the calorimeter system ensures efficient trigger capabilities and accu-

rate reconstruction of particles' energies and positions. Specifically, the SPD signals the presence of charged particles, aiding in electron-photon discrimination. The ECAL, with a thickness of 25 radiation lengths, achieves full containment of electromagnetic showers, while the 5.6 nuclear interaction lengths thick HCAL, limited by space constraints, plays a crucial role in triggering decays with hadronic final states. Moreover, the calorimeter system facilitates the identification of electrons, photons, and hadrons, contributing to the experiment's physics program. Robust  $e/\pi$  and  $\gamma/\pi^0$  identification is achieved, with high reconstruction efficiencies and signal purity.

The calorimeter system can achieve an electron reconstruction efficiency more than 90%<sup>[141]</sup> with a mis-identification (misID) of around 4.5%, and an efficiency of 95% for non-converted photons while rejecting 50%  $\pi^0$  containminations. More parameters can be found in Ref<sup>[141]</sup>.

### 2.3.3 Muon stations

The muon system<sup>[143]</sup> is designed to facilitate the trigger, identification, and track reconstruction of muons. Consisting of five distinct stations denoted as M1-M5, strategically positioned along the beam axis, the muon system employs advanced instrumentation, primarily multi-wire proportional chambers (MWPC), to achieve its objectives. The side view for the layout of muon stations is shown in Fig 2.14.

Starting with M1, strategically located upstream of the calorimeter system, this station plays a crucial role in improving the  $p_T$  resolution for muons during the hardware trigger process. Meanwhile, M2-M5, positioned as the most downstream sub-detectors, are interleaved with iron absorbers, serving to capture penetrating muons and allowing the system to discern particles from various species. The minimum momentum requirement of approximately 6 GeV/c ensures that muons traversing all five stations undergo a comprehensive measurement, considering the total absorber thickness including calorimeters. The geometry of the muon stations is noteworthy, exhibiting a projective design where transverse dimensions scale proportionally with the distance from the interaction point. This layout ensures optimal performance and adaptability in various scenarios, making the muon system a versatile tool for capturing and analyzing muon tracks.

Muon identification is achieved through intricate selection processes, including a binary selection called IsMuon, based on hits in muon stations and calorimeters. It is a decision-making process used to determine whether a given particle track is likely to be a muon. The selection is based on the number of muon stations where a hit is detected

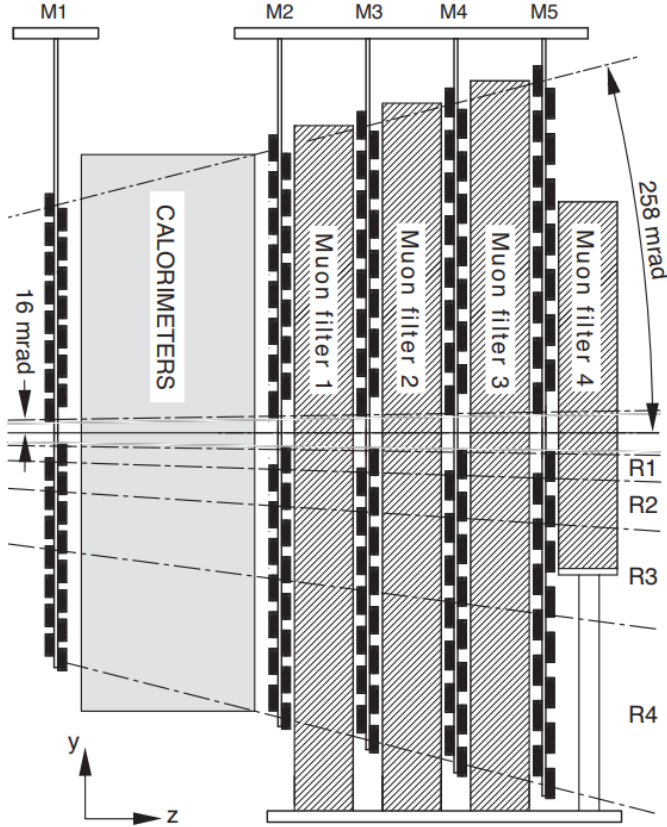


Figure 2.14 Side view of muon system, figure is taken from Ref<sup>[141]</sup>.

within a defined field of interest (FOI) around the track extrapolation. The detailed information for IsMuon can be found in Ref<sup>[144]</sup>. The PID efficiency and the misID rate for IsMuon is shown in Fig 2.15.

Additional discriminating variables, such as  $DLL\mu$  and  $ProbNN\mu$ , which obtained from the log-likelihood of muon and pion hypothesis and from multivariate analyses<sup>[145]</sup>, respectively, contribute to refining the muon particle identification, striking a balance between efficiency and purity in specific analyses. In this analysis, IsMuon,  $DLL\mu$  and  $ProbNN\mu$  are all applied.

The muon system's efficiency and performance are underscored by its extensive coverage, comprising 1380 chambers across a total area of  $435 \text{ m}^2$ . Most of the regions in M1 to M5 muon stations have an efficiency over 99%, resulting a muon identification efficiency over 95% for the combined response of the five stations.

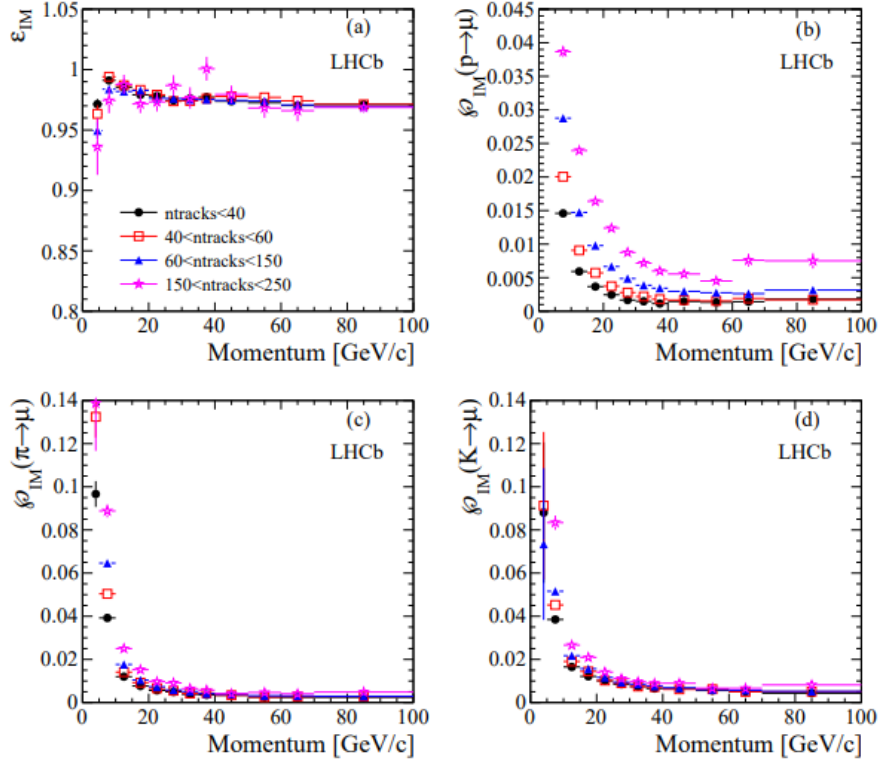


Figure 2.15 PID efficiency and misID rate of IsMuon as a function of momentum in different transverse momentum regions, figure is taken from Ref<sup>[144]</sup>.

## 2.4 Trigger

To navigate the vast amount of data generated by proton-proton collisions, the LHCb employs a sophisticated trigger system<sup>[146]</sup>. This system, consisting of two crucial levels – L0 and High-Level Trigger (HLT) – serves as the gatekeeper, selecting events of particular interest for in-depth analysis. The LHCb trigger scheme is shown in Fig 2.16. First a hardware level L0 trigger will be applied to reducing the collision rate from a staggering 10 MHz to a more manageable frequency around 1 MHz, then according to the L0 trigger line, only a subset of HLT first (HLT1) trigger will be applied. Then the HLT second (HLT2) selections are run for all the events accepted from previous levels, independent of the L0 and HLT1 trigger. In the following subsections we may introduce L0 and HLT trigger.

### 2.4.1 L0 trigger

The L0 trigger in the LHCb experiment plays a pivotal role as the first level of event selection, swiftly and efficiently reducing the collision rate to approximately 1 MHz. This critical reduction is achieved through the integration of information from the calorimeter

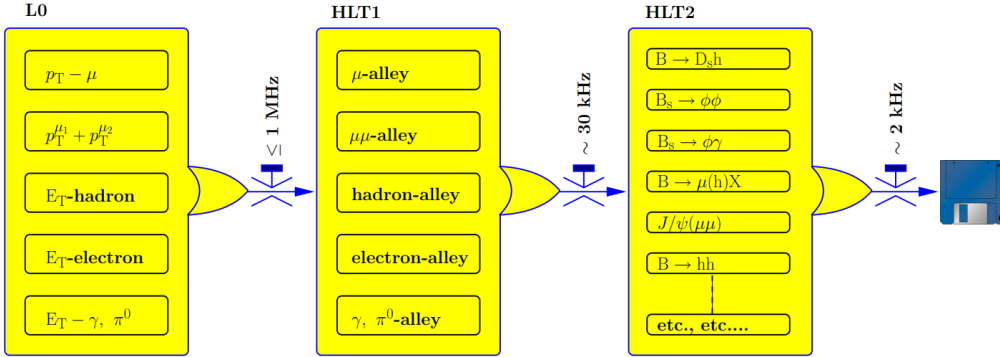


Figure 2.16 Trigger scheme for LHCb detector, figure is taken from Ref<sup>[147]</sup>.

system and muon stations, enabling rapid decision-making with a latency of 4 s.

The L0 calorimeter trigger focuses on clusters exhibiting high transverse energy ( $E_T$ ), a quantity measured by the ECAL and HCAL. These clusters are identified as hadron, electron, or photon candidates based on the calorimeter system's classification capabilities. Simultaneously, the total number of hits in the Scintillating Pad Detector (SPD), denoted as nSPDHits, serves as a proxy for charged track multiplicity. This information is crucial for vetoing events with excessively high multiplicities, expediting subsequent reconstruction in higher trigger levels. The L0 muon trigger is dedicated to identifying muon tracks with elevated transverse momentum ( $p_T$ ). Utilizing a stand-alone algorithm for muon track reconstruction, this trigger requires aligned hits in all five muon stations. The algorithm assumes the muon track originates from the interaction point, determining its  $p_T$  by analyzing hit positions in the first two stations (M1 and M2) with a relative resolution of approximately 20%. The L0 muon trigger selects up to eight muon candidates by choosing two tracks with the highest  $p_T$  in each quadrant. The trigger line L0Muon establishes a threshold on the highest  $p_T$  among these candidates, while the line L0DiMuon imposes a requirement on the product of the two largest  $p_T$  values.

## 2.4.2 HLT

Consisting of two stages, HLT1 and HLT2, the HLT system utilizes information from all sub-detectors to perform delicate online selections. HLT1 focuses on partial event reconstruction, reconstructing long tracks and primary vertices using simplified algorithms within the constraints of time and storage. This stage enables the rejection of fake tracks and the selection of particles with  $p_T$  and large impact parameters (IP). Following this, HLT2 performs a comprehensive event reconstruction, incorporating detailed information from all LHCb sub-detectors. This includes intricate track reconstruction processes, con-

sideration for all types of tracks, and the incorporation of PID information from detectors such as RICH, calorimeters, and muon stations.

Since an event is composed of many tracks and a certain number of them are combined as a signal, the event is classified into different types:

- Trigger on signal (TOS): signal candidate can trigger this event
- Trigger independent of signals: the rest of the event (subtract the signal candidate) can trigger this event
- Trigger on both (TOB): both signal candidate and the rest can trigger this event

The TIS and TOS decisions are used in this analysis.

## CHAPTER 3 MULTIPLICITY DEPENDENCE OF $\sigma_{\psi(2S)}/\sigma_{J/\psi}$ IN $pp$ COLLISIONS

In this chapter, the study of multiplicity-dependence of  $\sigma_{\psi(2S)}/\sigma_{J/\psi}$  in  $pp$  collisions at  $\sqrt{s} = 13$  TeV under different multiplicity schemes with the LHCb experiment is reported. The measurements are done for prompt and non-prompt parts separately. The results are compared to theory predictions<sup>[148]</sup>. And the multiplicity dependence of the ratio in different  $p_T$  and  $y$  regions is also reported. The overall ratio and its  $p_T$  dependence are compared to world data, which shows good agreements.

### 3.1 Data and Monte Carlo samples

This study uses  $pp$  collisions data at a center-of-mass energy of 13 TeV collected by the LHCb detector in 2016 with a corresponding luminosity of  $658 \pm 13 \text{ pb}^{-1}$ <sup>[149]</sup>. The data were taken under magnetic field in both MagDown and MagUp directions. The muons from charmonia decays are tracked and identified by the LHCb tracking and PID systems. Finally, the events that satisfying certain criteria will trigger the L0 and HLT selections and be recorded.

In simulation,  $pp$  collisions are generated using Pythia<sup>[150]</sup> with a specific LHCb configuration<sup>[151]</sup>. The prompt charmonium production is simulated in Pythia with contributions from both the leading order color-singlet and color-octet mechanisms<sup>[151-152]</sup>, and the charmonium is generated without polarization. Decays of hadronic particles are described by EvtGen<sup>[153]</sup>, in which final state radiation is generated using Photos<sup>[154]</sup>. The interaction of the generated particles with the detector and its response are implemented using the Geant4 toolkit<sup>[155]</sup> as described in Ref<sup>[156]</sup>. To study the efficiencies, 10 M full simulation samples for  $J/\psi$  and  $\psi(2S)$  are generated respectively, and for the geometrical acceptance, generator level Monte Carlo samples of 1 M candidates are produced for both  $J/\psi$  and  $\psi(2S)$  respectively. Since the acceptance is only a function of kinematic variables, hence, it is universal for all multiplicity regions. The generator-level and full-simulation samples contain both prompt and non-prompt charmonia, so that the acceptance and efficiencies can be estimated separately for prompt and non-prompt charmonia. The charmonia is generated without polarization.

### 3.2 Analysis strategy

The double differential cross-section for prompt and non-prompt production of  $J/\psi$  and  $\psi(2S)$  in a given ( $p_T$ ,  $y$ ) bin with multiplicity in a certain range is defined as

$$\frac{d^2\sigma}{dydp_T} = \frac{N(p_T, y)}{\mathcal{L} \times \epsilon_{\text{tot}}(p_T, y) \times \mathcal{B} \times \Delta y \times \Delta p_T}, \quad (3.1)$$

where

- $N$  is the number of prompt or non-prompt  $J/\psi$  or  $\psi(2S)$  reconstructed through the dimuon decay channel, obtained by the signal extraction in Section 3.4;
- $\mathcal{L} = 658 \pm 13 \text{ pb}^{-1}$  is the integrated luminosity;
- $\epsilon_{\text{tot}}$  is the total efficiency for prompt or non-prompt  $J/\psi$  or  $\psi(2S)$  in a particular  $p_T$ - $y$  bin with multiplicity in a certain range, described in Section 3.5;
- $\mathcal{B}(J/\psi \rightarrow \mu^+ \mu^-) = (5.961 \pm 0.033)\%$  is the branching fraction of the decay  $J/\psi \rightarrow \mu^+ \mu^-$ , quoted from the PDG 2022 review<sup>[5]</sup>.
- $\mathcal{B}(\psi(2S) \rightarrow e^+ e^-) = (7.93 \pm 0.17) \times 10^{-3}$  is the branching fraction of the decay  $\psi(2S) \rightarrow e^+ e^-$ , quoted from the PDG 2022 review<sup>[5]</sup>. The dielectron branching fraction is used since it has a much smaller uncertainty than the dimuon one;
- $\Delta p_T$  is the bin width of the transverse momentum;
- $\Delta y$  is the bin width of the rapidity.

In considering that  $\psi(2S)$  has much less yields than  $J/\psi$ , for the cross section ratio  $\sigma_{\psi(2S)}/\sigma_{J/\psi}$ , ( $p_T$ ,  $y$ ) binning scheme and multiplicity schemes are used as follows:

- $p_T$  boundaries [ GeV/c ]: 0.3, 2, 4, 6, 8, 20;
- $y$  boundaries: 2.0, 2.8, 3.5, 4.5;
- For multiplicity (boundaries each at a time)
  - $N_{\text{tracks}}^{\text{PV}}$ : 4, 20, 45, 70, 95, 200.
  - $N_{\text{bwd}}^{\text{PV}}$ : 0, 8, 15, 22, 30, 80.
  - $N_{\text{fwd}}^{\text{PV}}$ : 0, 12, 24, 36, 48, 130.

The details for multiplicity variables can be found in Sec 3.2.1. There is a wider bin in high  $p_T$  and multiplicity region, and the scheme of  $y$  is not exactly evenly distributed for the sake of significant signal numbers for fitting in each bin. And a common binning scheme is used for both  $J/\psi$  and  $\psi(2S)$ .

Then the double-differential production ratio of  $\psi(2S)$  to  $J/\psi$  is defined as

$$\frac{\sigma_{\psi(2S)}(p_T, y)}{\sigma_{J/\psi}(p_T, y)} = \frac{N_{\psi(2S)}(p_T, y)}{N_{J/\psi}(p_T, y)} \times \frac{\epsilon_{\text{tot}, J/\psi}(p_T, y)}{\epsilon_{\text{tot}, \psi(2S)}(p_T, y)} \times \frac{\mathcal{B}_{J/\psi \rightarrow \mu^+ \mu^-}}{\mathcal{B}_{\psi(2S) \rightarrow e^+ e^-}}. \quad (3.2)$$

And the ratio over an integrated kinematic bins is defined by

$$\frac{\sum_{i \in I} \sigma_{\psi(2S),i}}{\sum_{i \in I} \sigma_{J/\psi,i}} = \frac{\sum_{i \in I} (\Delta p_T \times \Delta y)_i \times N_{\psi(2S),i}/\epsilon_{\psi(2S),i}}{\sum_{i \in I} (\Delta p_T \times \Delta y)_i \times N_{J/\psi,i}/\epsilon_{J/\psi,i}} \times \frac{\mathcal{B}_{J/\psi \rightarrow \mu^+ \mu^-}}{\mathcal{B}_{\psi(2S) \rightarrow e^+ e^-}}, \quad (3.3)$$

where the widths for  $p_T$  and  $y$  are no longer canceled and  $I$  denotes a certain set of ( $p_T$ ,  $y$ ) bins.

To separate the prompt and non-prompt productions, the pseudo-proper time defined as

$$t_z = \frac{(z_X - z_{PV}) \times m_X}{p_z}, \quad (3.4)$$

is introduced, where  $X$  is  $J/\psi$  or  $\psi(2S)$ ,  $z_X$  is the  $z$  position of the decay vertex,  $z_{PV}$  that of the primary vertex,  $p_z$  the measured momentum along the beam axis  $z$ , and  $m_X$  the known mass for  $J/\psi$  and  $\psi(2S)$ <sup>[5]</sup>. Given that  $b$ -hadrons have lifetimes that much larger than the time resolution of VELO, the prompt and non-prompt production can be separated by a two-dimensional (2D) fit to the invariant mass and pseudo-proper time, see Section 3.4 for details. Then the production ratio as function of different multiplicity variables is obtained.

### 3.2.1 Multiplicity variables

The multiplicity variables under investigation are defined as follows. The variable  $N_{\text{tracks}}^{\text{PV}}$  represents the number of tracks utilized in reconstructing the primary vertex (PV), where a minimum of four tracks is necessitated to establish a high-quality PV. Meanwhile,  $N_{\text{bwd}}^{\text{PV}}$  and  $N_{\text{fwd}}^{\text{PV}}$  denote the number of tracks situated in the backward ( $-5.2 < \eta < -1.5$ ) and forward ( $1.5 < \eta < 5.2$ ) pseudorapidity regions, respectively. The forward region approximately aligns with the LHCb acceptance. The two muon tracks are included within  $N_{\text{tracks}}^{\text{PV}}$  and  $N_{\text{fwd}}^{\text{PV}}$  but are not counted within  $N_{\text{bwd}}^{\text{PV}}$ . For each of the three multiplicity variables, we define a dimensionless quantity as the ratio of the measured multiplicity to the corresponding mean values in no-bias data, as listed in Table 3.1, and the distribution of the multiplicity variables is shown in Fig 3.1. The no-bias data are recorded with random trigger decisions; therefore, the mean value of multiplicity in the no-bias data serves as a suitable reference for the mean multiplicity.

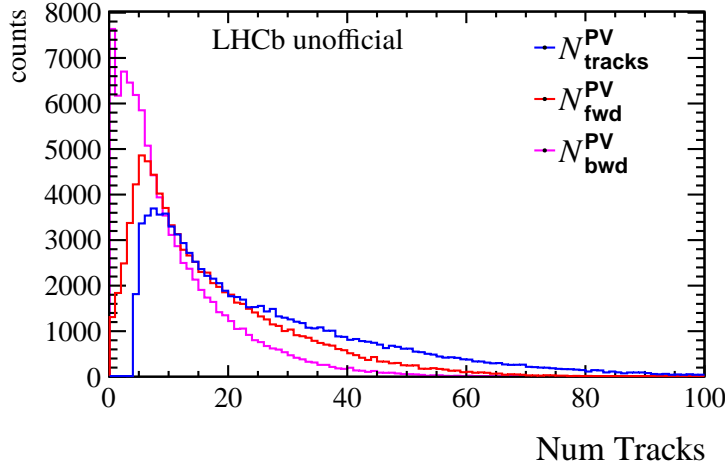


Figure 3.1 Multiplicity distribution in no-bias data.

Table 3.1 Mean values of the three multiplicity variables in no-bias data.

Variable	mean value
$N_{\text{tracks}}^{\text{PV}}$	25.88
$N_{\text{fwd}}^{\text{PV}}$	16.14
$N_{\text{bwd}}^{\text{PV}}$	9.74

In addition to the local, forward, and backward multiplicity variables, the number of primary charged particles  $N_{\text{ch}}$  is also derived by correcting  $N_{\text{tracks}}^{\text{PV}}$  within the LHCb acceptance using Monte Carlo simulation samples as described in Sec. 3.1. The distribution of  $N_{\text{tracks}}^{\text{PV}}$  in the simulated sample is weighted to match the (non-)prompt data to correct any bias between the simulated sample and the data. Subsequently, a second-order polynomial  $f_2$  is employed to characterize the correlation between  $N_{\text{tracks}}^{\text{PV}}$  and  $N_{\text{ch}}$  across the full  $N_{\text{tracks}}^{\text{PV}}$  range. The charged-particle multiplicity density in the  $N_{\text{tracks}}^{\text{PV}}$  interval  $i$  is then calculated as follows:

$$\frac{dN_{\text{ch}}^i}{d\eta} = \frac{1}{\Delta\eta} f_2(N_{\text{tracks}}^{\text{PV},i}), \quad (3.5)$$

where  $\Delta\eta$  represents the pseudorapidity coverage of the LHCb detector. The systematic uncertainty for  $dN_{\text{ch}}/d\eta$  encompasses uncertainties from the fit for the correction function and variations from results obtained using a power-function correction instead of  $f_2$ . The two-dimensional distribution of  $(N_{\text{tracks}}^{\text{PV}}, N_{\text{ch}})$  and the fit for the correction functions is shown in Fig 3.2, taking prompt  $J/\psi$  as an example.

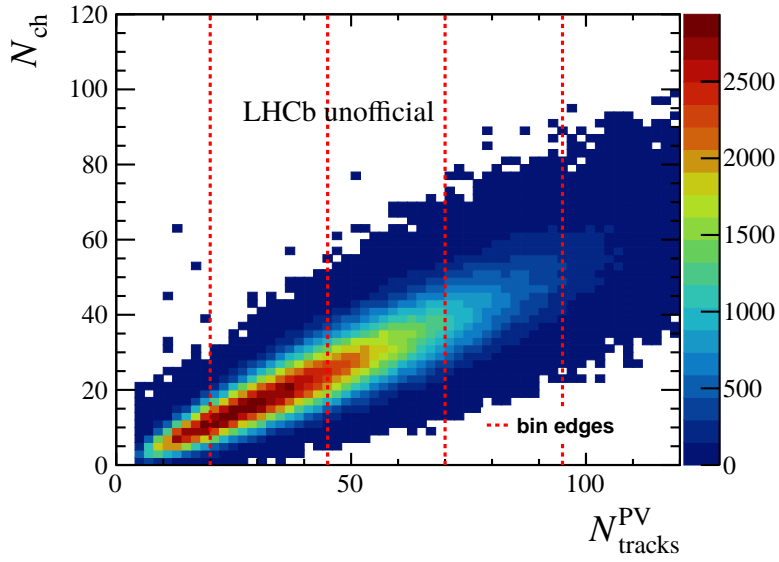


Figure 3.2 The two-dimensional distribution of  $(N_{\text{tracks}}^{\text{PV}}, N_{\text{ch}})$  for prompt  $J/\psi$ .

This uncertainty is determined using (non-)prompt  $J/\psi$  Monte Carlo and data samples, considering the negligible difference between the  $\psi(2S)$  and  $J/\psi$  multiplicity distributions compared to the statistical uncertainty from the fit. As there is currently no correction for efficiency in the no-bias data,  $dN_{\text{ch}}/d\eta$  is not self-normalised by dividing by the mean value of  $\langle dN_{\text{ch}}/d\eta \rangle_{\text{NB}}$ .

### 3.3 Online and offline selections

#### 3.3.1 Trigger and Turbo stream selections

The reconstruction of  $J/\psi$  and  $\psi(2S)$  candidates involves the dimuon decay channel, with selection criteria applied at two trigger stages. The initial hardware L0 trigger line, named L0Muon, identifies events featuring at least one muon candidate possessing a transverse momentum  $p_T$  greater than 0.9 GeV/ $c$ . For subsequent stages, the HLT1 and HLT2 trigger lines, specifically HLT1DiMuonHighMass and HLT2DiMuonJpsiTurbo, are utilized. In combination, the software trigger necessitates the presence of two loosely identified muons, each with  $p_T > 0.3$  GeV/ $c$  and total momentum  $p > 6$  GeV/ $c$ , to establish a high-quality vertex. Additionally, it employs a preliminary mass window for the invariant mass of each candidate. The online selections in the high level trigger lines are summarized in Table 3.2 for both  $J/\psi$  and  $\psi(2S)$ .

Table 3.2 Selection criteria in the high level trigger lines

trigger line	main cuts
<i>Hlt1DiMuonHighMass</i>	track $p_T > 300$ MeV/ $c$ track $p > 6000$ MeV/ $c$ $M_{\mu^+\mu^-} > 2700$ MeV/ $c^2$ Muon ID: IsMuon
<i>Hlt2DiMuonJPsiTurbo</i>	$(3096.9 - 120) \text{ MeV}/c^2 < m_{J/\psi} < (3096.9 + 120) \text{ MeV}/c^2$
<i>Hlt2DiMuonPsi2STurbo</i>	$(3686.09 - 120) \text{ MeV}/c^2 < m_{\psi(2S)} < (3686.09 + 120) \text{ MeV}/c^2$ track $\chi^2/\text{ndf} < 4$ vertex $\chi^2/\text{ndf} < 25$

### 3.3.2 Offline selections

The offline selections are applied to both  $J/\psi$  and  $\psi(2S)$  candidates to reduce the combinatorial background to a reasonable level and ensure the good quality of the signal-extraction fit. First, each event is required to have exactly one primary vertex (PV) reconstructed to avoid track contributions to multiplicity from multiple PVs that occur in the same beam crossing (pile-up).  $J/\psi$  and  $\psi(2S)$  candidates are reconstructed with pairs of oppositely charged tracks reconstructed in the full tracking system (long tracks). The ghost probability for each track ( $\mu^+$  and  $\mu^-$ ) to be less than 0.3. Both two tracks must have a transverse momentum  $p_T$  above 1200 MeV/ $c$ , pass muon identification, and have a good quality of the track fit ( $\chi^2/\text{ndf} < 3$ ). The pseudo-rapidity of each muon is required to be in the range  $2.0 < \eta < 4.9$ . Particle identification (PID) selections are performed to identify muon candidates. The two muons are required to form a good vertex by restricting the vertex fit quality  $\text{Prob}(\chi^2/\text{ndf}) > 0.5\%$ .

The full offline selection criteria are summarized in Table 3.3.

Table 3.3 Summary of Offline Selections

Quantity	Requirement
nPVs	= 1
$z_{\text{PV}}$	$> -60 \text{ mm}$ (for $N_{\text{tracks}}^{\text{PV}}$ as multiplicity variable) $> -30 \text{ mm}$ (for $N_{\text{bwd}}^{\text{PV}}$ as multiplicity variable)
vertex $\chi^2/\text{ndf}$	$< 7.8794$
mass window	$m_{J/\psi} \pm 120 \text{ MeV}/c^2$ $m_{\psi(2S)} \pm 120 \text{ MeV}/c^2$
PID	IsMuon, $\text{DLLmu} > 2$ $\text{probNNmu} > 0.8$
muon $\eta$	$2 < \eta < 4.9$
track ghost prob.	$< 0.3$
$t_z$	$-10 \text{ ps} < t_z < 10 \text{ ps}$
$t_z$ uncertainty	$< 0.3 \text{ ps}$

The restriction of vertex  $\chi^2/\text{ndf} < 7.8794$  is chosen so that the P-Value is exactly 0.005. For PID selection, we set  $\text{DLLmu} > 2$  to reduce combinatorial background for both  $J/\psi$  and  $\psi(2S)$ . And  $\text{probNNmu} > 0.8$  is further applied since it can largely reduce the combinatorial background for  $\psi(2S)$  at high multiplicity and low  $p_T$  bins.

Here we restrict  $z_{\text{PV}}$  to be larger than -60 mm in order to maintain uniform VELO acceptance. From Figure 3.3 we can see that for  $z_{\text{PV}} < -60 \text{ mm}$  (as indicated by the black, red, and green points), there is a clear shift from the other curves toward lower track multiplicity. This is because many events producing tracks that can not enter the VELO acceptance. Therefore, in this analysis, we restrict our primary vertex  $z$  range to  $z_{\text{PV}} > -60 \text{ mm}$ . If  $N_{\text{bwd}}^{\text{PV}}$  is used as multiplicity variables, the restriction is further modified to  $z_{\text{PV}} > -30 \text{ mm}$ , and no restriction needs to be made for  $N_{\text{fwd}}^{\text{PV}}$  as multiplicity variable, which can be seen in Fig. 3.3.

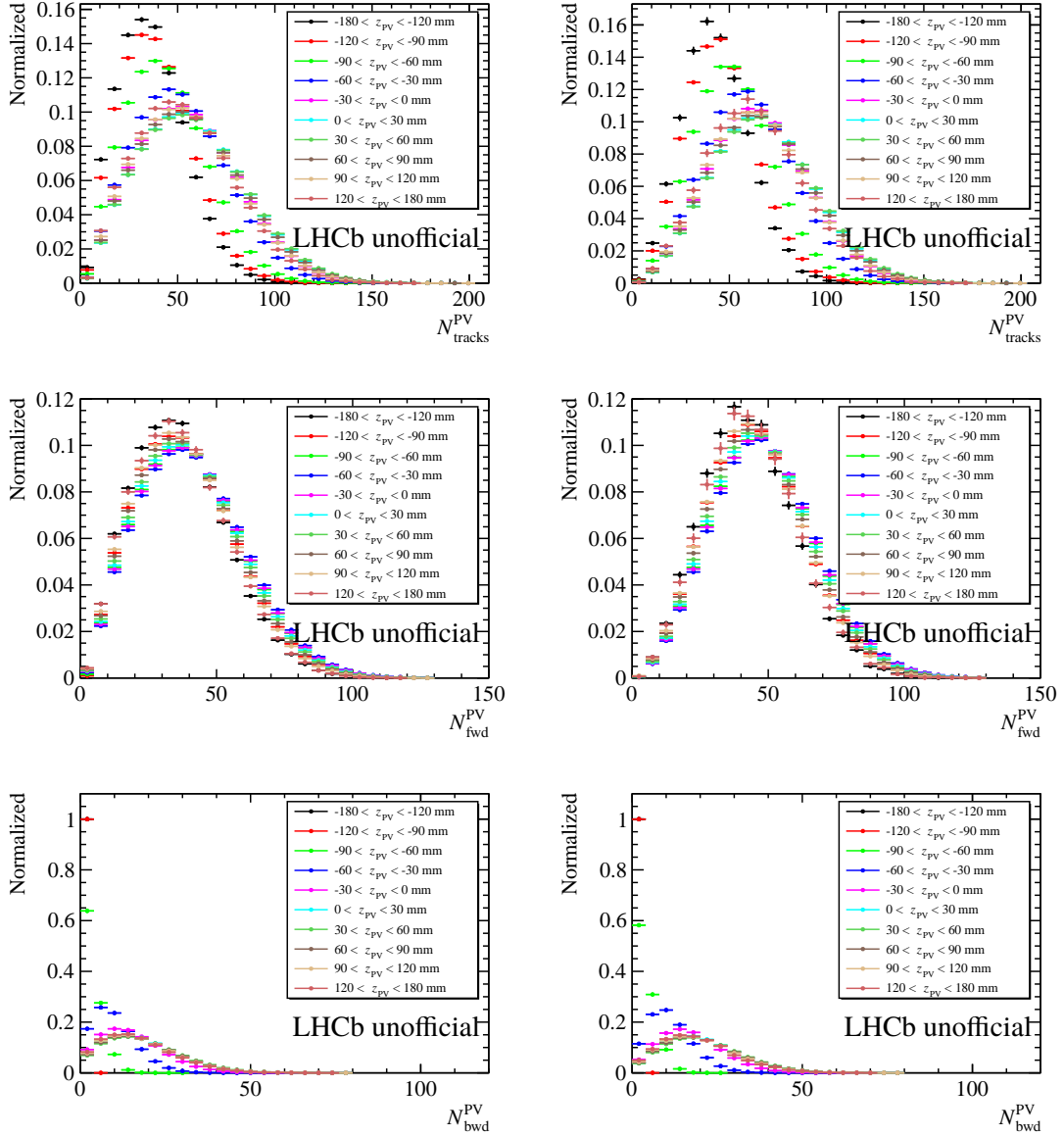


Figure 3.3 Distribution of  $N_{\text{tracks}}^{\text{PV}}$ ,  $N_{\text{bwd}}^{\text{PV}}$  and  $N_{\text{fwd}}^{\text{PV}}$  under  $n_{\text{PVs}} = 1$  for  $J/\psi$  (left) and  $\psi(2S)$  (right) data samples. The events with  $z_{\text{PV}}$  smaller than a certain range show clear deviation, hence are rejected to guarantee a uniform VELO acceptance for charged tracks.

### 3.4 Signal extraction

The total number of  $J/\psi$  and  $\psi(2S)$  signals is determined from an extended unbinned maximum likelihood fit to the invariant mass distribution of the selected candidates. The fit models for both  $J/\psi$  and  $\psi(2S)$  are the same, which are selected in accordance with the previous studies of  $J/\psi$ <sup>[157]</sup> and  $\psi(2S)$ <sup>[65]</sup> production at 13 TeV. The only strategy for both is as follows.

In the fit the background component is modelled with an exponential function

$$f_{\text{bkg}}(m) = a_0 e^{-p_0 \cdot m}. \quad (3.6)$$

The signal component is described by the sum of two Crystal Ball (CB) functions<sup>[158]</sup>.

The CB function is defined as:

$$f_{\text{CB}}(m; \mu, \sigma, \alpha, n) = \begin{cases} \left(\frac{n}{|\alpha|}\right)^n e^{-\frac{1}{2}\alpha^2} \left(\frac{n}{|\alpha|} - |\alpha| - \frac{m-\mu}{\sigma}\right)^{-n} & \frac{m-\mu}{\sigma} < -|\alpha| \\ \exp\left(-\frac{1}{2}\left(\frac{m-\mu}{\sigma}\right)^2\right) & \frac{m-\mu}{\sigma} > -|\alpha|. \end{cases}, \quad (3.7)$$

which combines a Gaussian core (described by the parameters  $\mu$  and  $\sigma$ ) and one tail on the left (described by the parameters  $\alpha$  and  $n$ ). The tails in CB functions are used to model the radiative effects, which leads to more candidates with lower invariant mass. Not all parameters of the CB functions are left free when fitting data. Some parameters are fixed or parameterized. For both  $J/\psi$  and  $\psi(2S)$ , the two CB functions share one common mean value  $\mu$  and have different widths  $\sigma_1$  and  $\sigma_2$ , and  $\alpha$  is parameterized from simulation as a function of the  $\sigma$ :  $\alpha = 2.066 \pm 0.0085\sigma - 0.00011\sigma^2$ , which applies to both CB functions. Furthermore, for  $\psi(2S)$  only,  $\sigma_1$  and  $\sigma_2$  are parameterized as a linear function:  $\sigma_2 = 25.7 + \sigma_1$  and the fraction of the narrower CB function is fixed at 0.96, both determined from simulation. For the tail parameters,  $n$  is fixed to unity from physics<sup>[159]</sup>. Therefore, there are merely three (two) free parameters for the  $J/\psi$  ( $\psi(2S)$ ) signal shape,  $\mu$  and  $\sigma_1$ . The invariant mass fit is performed in each  $p_T$ - $y$  bin and  $N_{\text{tracks}}^{\text{PV}}$  bin of the candidate.

To determine the signal yields of prompt and from- $b$  components separately, the  $t_z$  distribution is used. In each kinematic and multiplicity bin, an unbinned extended maximum likelihood fit to the two-dimension distributions of invariant mass  $m(\mu^+ \mu^-)$  and  $t_z$  is performed to separate the prompt and non-prompt components.

At the generator level, the  $t_z$  distribution of the prompt component is a Dirac delta function,  $\delta(t_z)$ , while that from  $b$  follows an exponential function as seen from simulation. For  $J/\psi$  and  $\psi(2S)$  signals, the detector resolution is taken into account by convolving a resolution function, which is described by the sum of two Gaussian functions,

$$f_{\text{resolution}}(t_z; \mu, S_1, S_2, \beta) = \frac{\beta}{\sqrt{2\pi} S_1 \sigma} e^{-\frac{(t_z-\mu)^2}{2S_1^2 \sigma^2}} + \frac{1-\beta}{\sqrt{2\pi} S_2 \sigma} e^{-\frac{(t_z-\mu)^2}{2S_2^2 \sigma^2}}. \quad (3.8)$$

The parameter  $\sigma$  is the event-by-event uncertainty of  $t_z$ , with  $S_1$  and  $S_2$  are two scale factors to correct the non-perfect estimation of the  $t_z$  uncertainty. The parameter  $\mu$  is the bias of the  $t_z$  measurement, and  $\beta$  is the fraction of one of the two Gaussians. In the fitting

procedure, all the resolution parameters are floated. For some ( $p_T, y, N_{\text{tracks}}^{\text{PV}}$ ) bin, the count for signal yield for  $\psi(2S)$  or  $J/\psi$  is significantly low then the fit will fail due to too many free parameters. In this case we may set  $\beta = 0$ , i.e., only one Gaussian function is used to describe the resolution.

It is possible that the reconstructed candidate is associated with a "wrong" PV. This can happen either because the real PV that produces the candidate failed to be reconstructed, and the candidate was associated with the nearest reconstructed PV in the event, or because a wrong PV is accidentally close to the candidate. For the latter case, the positions of the reconstructed and the true PV are correlated, which results in a Gaussian-like  $t_z$  distribution with a width much larger than the detector resolution. This effect can be described by adding a third Gaussian with a much larger width than the resolution function. However, it is found from simulation that including the wide Gaussian in the resolution does not change the fitted parameters significantly because the fraction of this component is quite small,  $\leq 1\%$  as seen from studies in Ref<sup>[157]</sup>. Therefore, the third wide Gaussian is not used in the fit function. For the former case that the true PV is not reconstructed, the true PV and wrongly associated PV are not correlated, which results in a long tail in the  $t_z$  distribution that can be modeled using the next-event method for both  $J/\psi$  and  $\psi(2S)$ . The next-event method is applied directly on data sample. The next-event pseudo-proper time,  $t_z^{\text{next}}$ , for each candidate, is calculated combining the candidate with the closest PV of another (next) event as

$$t_z^{\text{next}} = \frac{(z_{\mu\mu} - z_{\text{PV}}^{\text{next}}) \times m_{\mu\mu}}{p_z}, \quad (3.9)$$

where  $z_{\text{PV}}^{\text{next}}$  is the  $z$ -coordinate of the nearest PV of the next selected event. The tail distribution  $f_{tail}(t_z)$  is extracted in each bin separately and not convolved with resolution functions since the distribution is much wider than the resolution and very smooth in the whole  $t_z$  region. It should be noted that since the requirement of PV reconstruction is loose, using at least 4 VELO tracks, the probability to reconstruct the true PV is very high ( $> 99\%$ ).

The candidates in the mass sidebands, where  $m_{\mu^+\mu^-}$  is at least  $60 \text{ MeV}/c^2$  away from the mass of  $J/\psi$  and  $\psi(2S)$ , are used as the background control sample to model the  $t_z$  distribution of the background. The background control sample consists of random combinations of muons from semi-leptonic  $b$  and  $c$  decays, which tend to produce positive  $t_z$  values, as well as mis-reconstructed tracks from decays-in-flight of kaons and pions, which contribute both to positive and negative  $t_z$  values. The  $t_z$  distribution of the background

is therefore modeled with an empirical function, composed of a Dirac delta function and five exponentials (three for positive  $t_z$  and two for negative  $t_z$ , with one positive  $t_z$  and one negative sharing the same slope parameter). This function is convolved with the sum of two Gaussian functions as a resolution function, which has different parameters as for signals,<sup>①</sup>,

$$f_{\text{background}} = \left[ (1 - f_1 - f_2 - f_3 - f_4)\delta(t_z) + \theta(t_z)\left(\frac{f_1}{\tau_1}e^{-t_z/\tau_1} + \frac{f_2}{\tau_2}e^{-t_z/\tau_2}\right) + \theta(-t_z)\left(\frac{f_3}{\tau_3}e^{t_z/\tau_3} + \frac{f_4}{2\tau_4}e^{-|t_z|/\tau_4}\right) \right] \otimes \left( \frac{\beta'}{\sqrt{2\pi}S'_1\sigma} e^{-\frac{(t_z-\mu)^2}{2S'^2_1\sigma^2}} + \frac{1-\beta'}{\sqrt{2\pi}S'_2\sigma} e^{-\frac{(t_z-\mu)^2}{2S'^2_2\sigma^2}} \right). \quad (3.10)$$

The parameters in Eq. 3.10 are determined by fitting the  $t_z$  distribution of background control sample defined above (in each kinematical bin of  $J/\psi$  and  $\psi(2S)$ ), and are fixed for the final fits. In Fig. 3.4, the  $t_z$  distribution of the background in the kinematic range  $p_T \in [2, 4] \text{ GeV}/c$ ,  $y \in [2.0, 2.8]$  and  $N_{\text{tracks}}^{\text{PV}} \in [20, 40]$  is shown, superposed by a fit using Eq. 3.10.

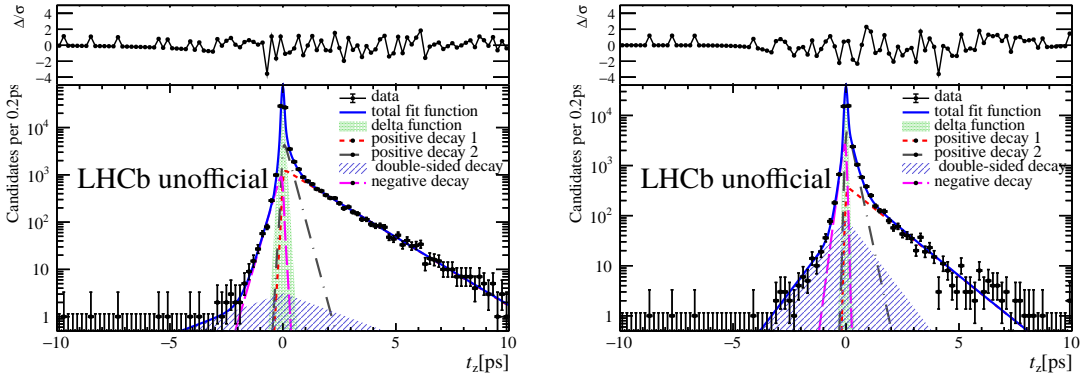


Figure 3.4 The background  $t_z$  fit for  $20 \leq N_{\text{tracks}}^{\text{PV}} < 45$ ,  $2 < y < 2.8$  and  $2 < p_T < 4 \text{ GeV}/c$ . The left is for  $J/\psi$  and the right is for  $\psi(2S)$ .

In total, the eventual function for the  $t_z$  fit is:

$$F_{t_z}(t_z; n_{\text{prompt}}, n_{\text{tail}}, n_{\text{bdecay}}, n_{\text{bkg}}, \mu, S_1, S_2, \beta, \tau_b) = \left( n_{\text{prompt}}\delta(t_z) + \frac{n_{\text{bdecay}}}{\tau_b}e^{-t_z/\tau_b} \right) * f_{\text{resolution}}(t_z; \mu, S_1, S_2, \beta) + n_{\text{tail}}f_{\text{tail}}(t_z) + n_{\text{bkg}}f_{\text{background}}(t_z), \quad (3.11)$$

where  $n_{\text{bkg}}$ ,  $n_{\text{prompt}}$ ,  $n_{\text{bdecay}}$  and  $n_{\text{tail}}$  are the number of background, prompt components, non-prompt component decay and wrong PV events, respectively.

<sup>①</sup> The uncertainty on the background vertex is usually worse than that for the signal vertex.

Because the requirement of the PV reconstruction is loose, and the PV is not refitted by removing the VELO segments of the muon tracks, it is reasonable to assume that prompt components and non-prompt component decay have equal probability to be assigned with a wrong PV. Therefore, the fractions of the prompt and from  $b$  components in  $n_{tail}$  is equal to the fraction  $\frac{n_{prompt}}{n_{bdecay}+n_{prompt}}$  and  $\frac{n_{bdecay}}{n_{bdecay}+n_{prompt}}$ . Even if the shape is extracted from data including the background candidate, the fit result  $n_{tail}$  should only contain prompt and non-prompt components. First, the shape of the PDF due to the wrong-PV effect should be the same no matter from which sample we extract it. Then, the wrong-PV effect for background candidates should be merged in the background PDF, which means the  $n_{tail}$  part in the total PDF should be specifically for signal candidates. And in this analysis, we only care about the ratio of the prompt and the non-prompt, where  $n_{tail}$  in each kinematic bin and multiplicity bin accounts for about 0.1% of  $n_{bdecay} + n_{prompt}$ , which results in an even more negligible influence on the ratio in Eq 3.2. In this case, we can ignore the subtle contribution to  $n_{bdecay}$  and  $n_{prompt}$  from  $n_{tail}$ .

The two-dimensional fit to the invariant mass and the lifetime in the kinematic range  $4 < p_T < 6 \text{ GeV}/c$ ,  $2.0 < y < 2.8$  and multiplicity bin  $20 \leq N_{\text{tracks}}^{\text{PV}} < 45$  is shown in Fig. 3.5, with the red shaded area being prompt components, and the cyan shaded area being non-prompt component, the dots with vertical error bar are data points, the violet dashed lines are the combinatorial background, the green dashed lines are the components by wrong PV (which are invisible in the graph of projection on mass) and the blue lines are the total fit functions. During the  $t_z$ -mass combined fitting procedure, the parameters of mass signal shape ( $\mu_{mass}, \sigma_{mass}, p_0$ ) are floated within a certain times of their uncertainties from the 1D mass fit for the final fits of  $J/\psi$ . While for  $\psi(2S)$ , due to the limitation of number of candidates, the parameters are fixed. According to the comparison of this two fitting strategies upon  $J/\psi$ , no significant difference between errors of prompt and non-prompt components are observed ( 0.1%).

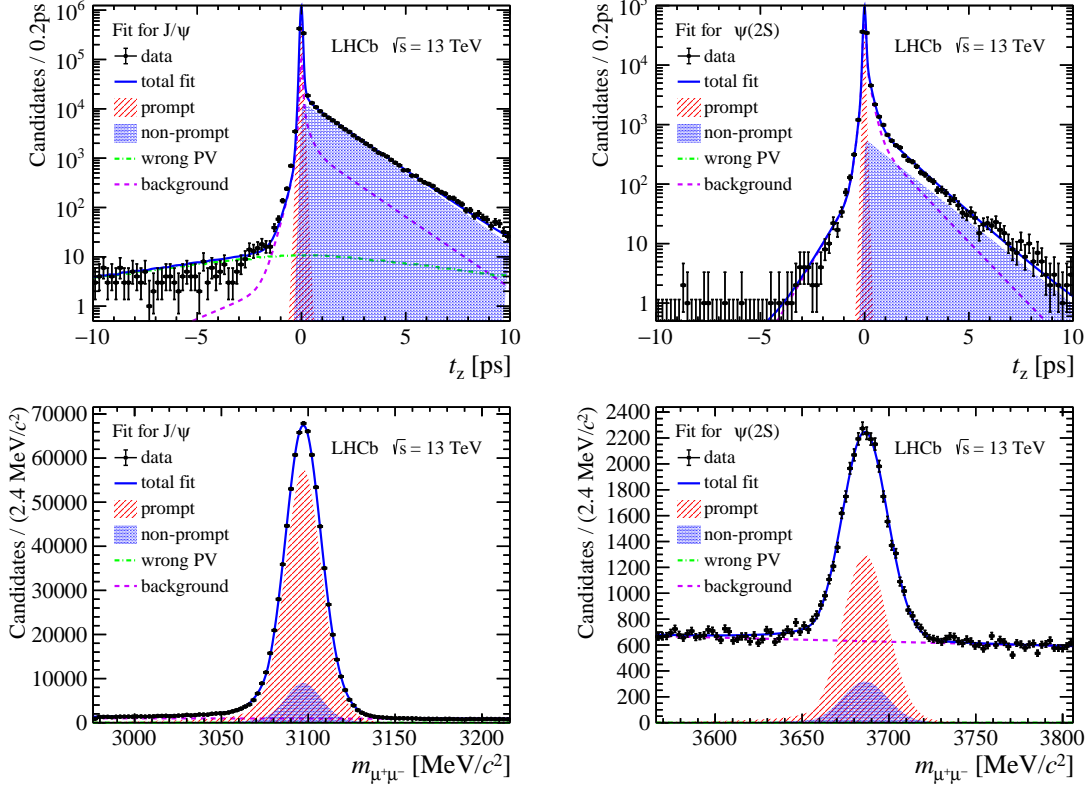


Figure 3.5 Projection in (top)  $t_z$  and (bottom) mass spectrum of  $t_z$ -mass fit for  $20 \leq N_{\text{tracks}}^{\text{PV}} < 40, 2 < y < 2.8$  and  $2 < p_T < 4 \text{ GeV}/c$ , with left column for  $J/\psi$  and right column for  $\psi(2S)$ .

After fitting all the kinematic and multiplicity bins, the prompt and non-prompt yields for  $J/\psi$  and  $\psi(2S)$  in  $4 \leq N_{\text{tracks}}^{\text{PV}}$  is shown in Fig 3.6 as an example.

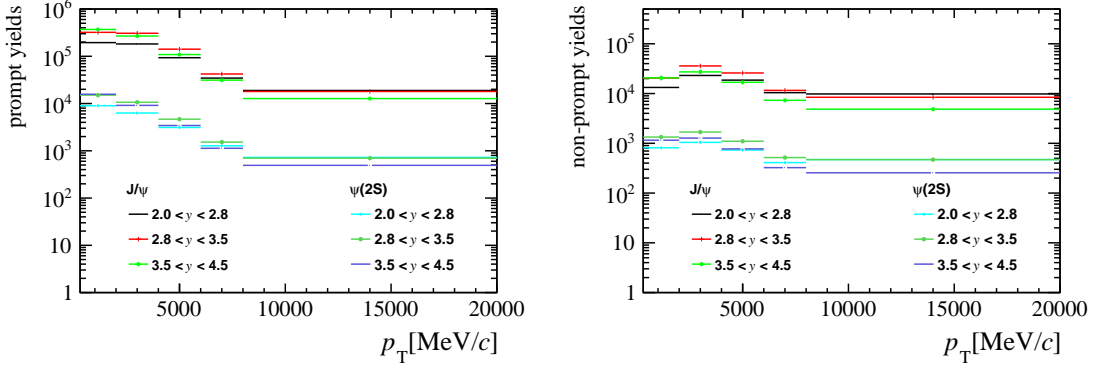


Figure 3.6 The (left) prompt and (right) non-prompt yields for  $J/\psi$  and  $\psi(2S)$  in  $4 \leq N_{\text{tracks}}^{\text{PV}}$ .

### 3.5 Efficiency determination

The total efficiency  $\epsilon_{\text{tot}}$  is determined independently in each kinematic bin and multiplicity bin. The expression is as follows,

$$\epsilon_{\text{tot}} = \epsilon_{\text{acc}} \times \epsilon_{\text{Reco\&Sel}} \times \epsilon_{\text{MuonID}} \times \epsilon_{\text{Trigger}}. \quad (3.12)$$

The efficiency is calculated truth matched candidates, with truth-matching inefficiency around 0.3%, which is negligible. The Monte Carlo samples for both prompt and non-prompt components of  $J/\psi$  and  $\psi(2S)$  are divided according to the multiplicity binning schemes in Sec 3.2. For different multiplicity regions based on division upon different multiplicity variables, efficiencies are calculated in the same way in the same binning scheme for kinematic variables  $p_T$  and  $y$ . Since we have already separated the data and MC in a multiplicity bin, and the bin width of  $p_T$  and  $y$  is not so small that the efficiency can be treated as constant in a certain kinematic bin. All the efficiencies are corrected by reweighting the distribution of  $p_T$ - $y$  spectrum of MC to that of s-weighted data which contains only signals and is obtained with the sPlot method<sup>[160]</sup>. Also, the effect caused by the difference in the distribution of multiplicity is corrected by reweighting the distribution of multiplicity variables of MC to that of s-weighted data which contains only signals. Since the prompt and non-prompt components have different distributions in  $p_T$ - $y$  and multiplicity variables, before calculating efficiencies, the  $p_T$ - $y$  and multiplicity distributions of MC are reweighted separately for prompt and non-prompt components, as shown in Fig 3.7 and Fig 3.8. The reweight on multiplicity is done only once, according to which multiplicity variable is used.

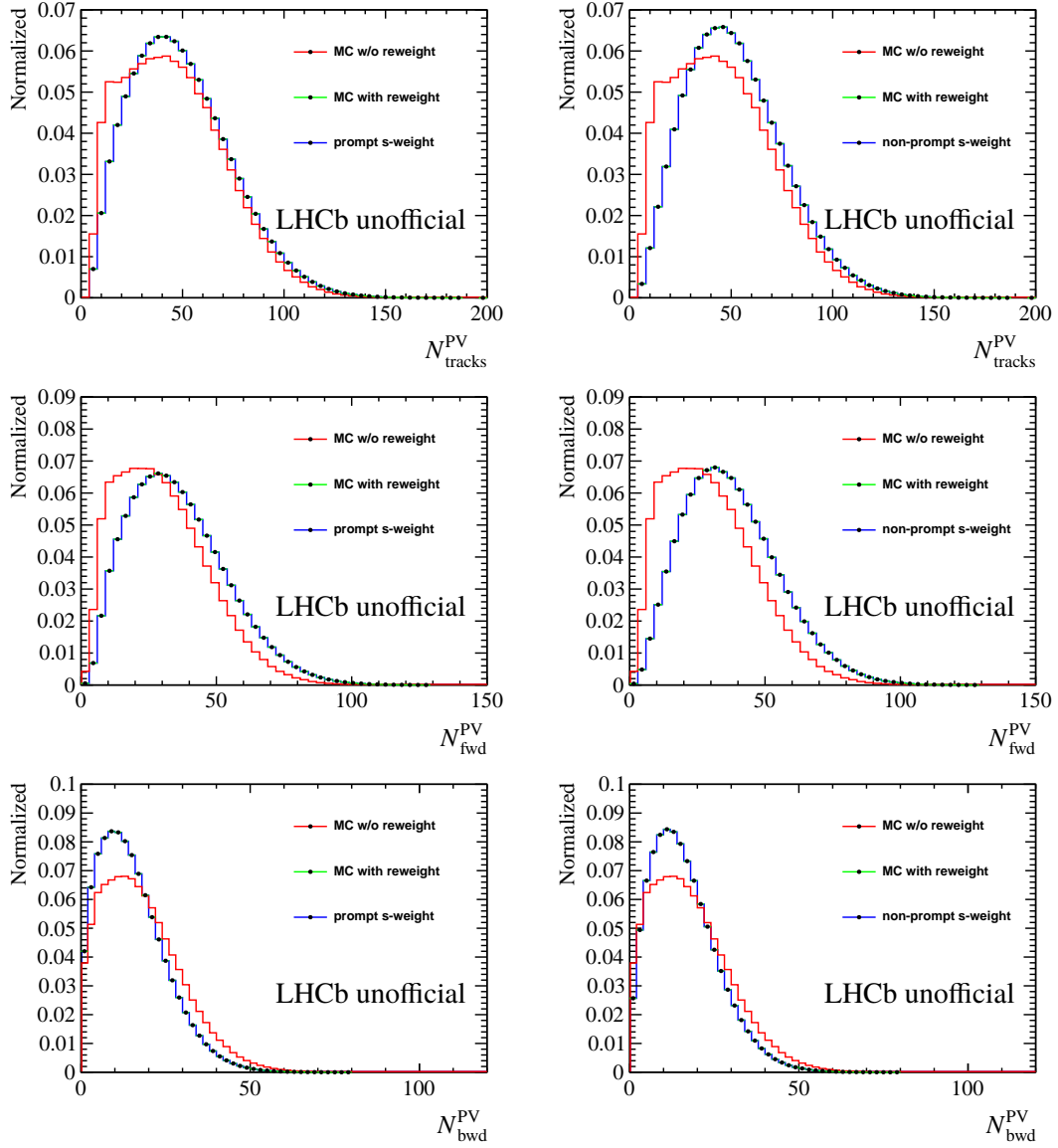


Figure 3.7 Reweighting the multiplicity distribution to match MC to s-weighted data, the left column is for prompt  $J/\psi$  and the right column is for non-prompt  $J/\psi$ .

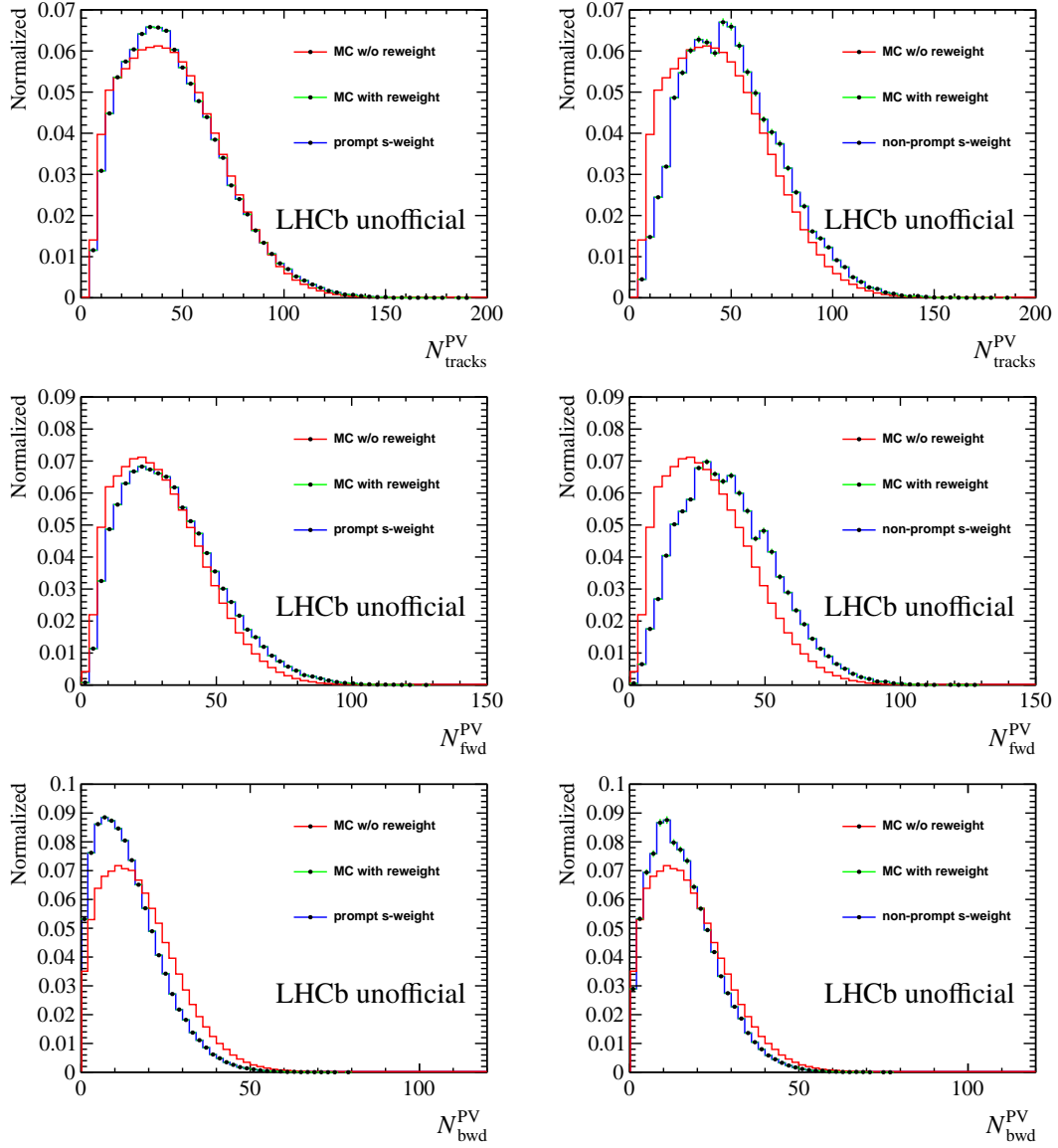


Figure 3.8 Reweighting the multiplicity distribution to match MC to s-weighted data, the left column is for prompt  $\psi(2S)$  and the right column is for non-prompt  $\psi(2S)$ .

The  $J/\psi$   $p_{\text{T}}\text{-}y$  reweight is done in two dimensions simultaneously, with 10 grids in  $y$  and 20 grids in  $p_{\text{T}}$ . The result is presented as the  $p_{\text{T}}$ -reweight in each  $y$  bin, and result for prompt  $J/\psi$  and  $\psi(2S)$  in the first  $y$  bin is shown in Fig 3.9, the result for prompt and non-prompt in all  $y$  bins can be found in Fig 3.10 and Fig 3.11.

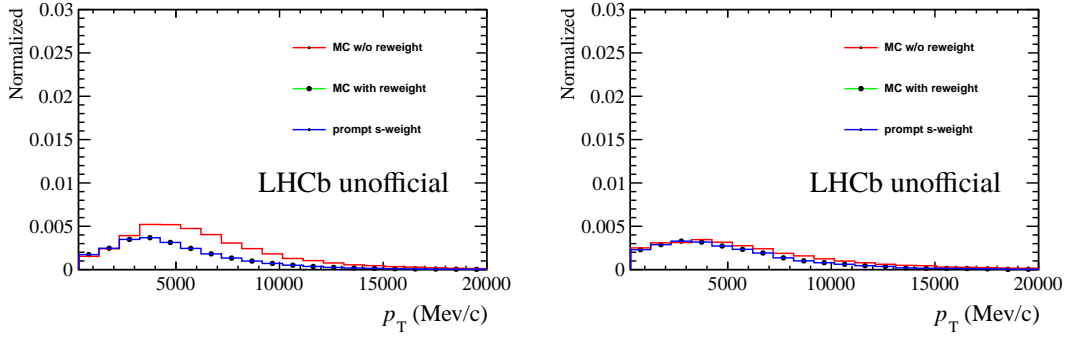


Figure 3.9 The  $p_T$ - $y$  reweight in rapidity range  $2 < y < 2.25$  for prompt  $J/\psi$  (left) and prompt  $\psi(2S)$  (right).

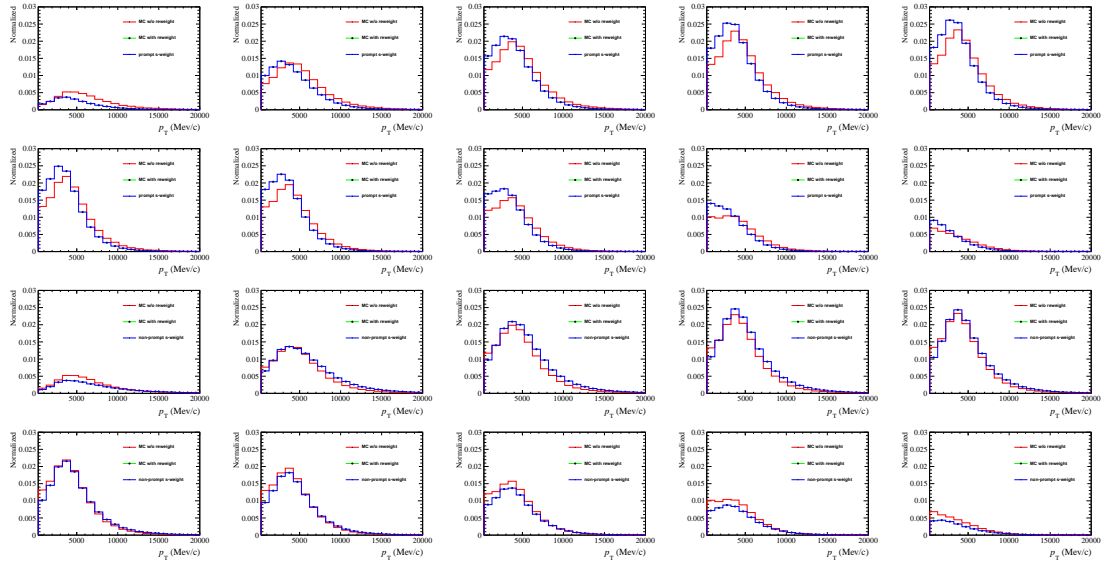


Figure 3.10 The  $p_T$ - $y$  reweight in  $2 < y < 4.5$  and  $0 < p_T < 20 \text{ GeV}/c$  for  $J/\psi$ , each subplot represents the  $p_T$  reweight in each  $y$  bin of width 0.25. The top two rows are for prompt  $J/\psi$  and the bottom two rows are for non-prompt  $J/\psi$ .

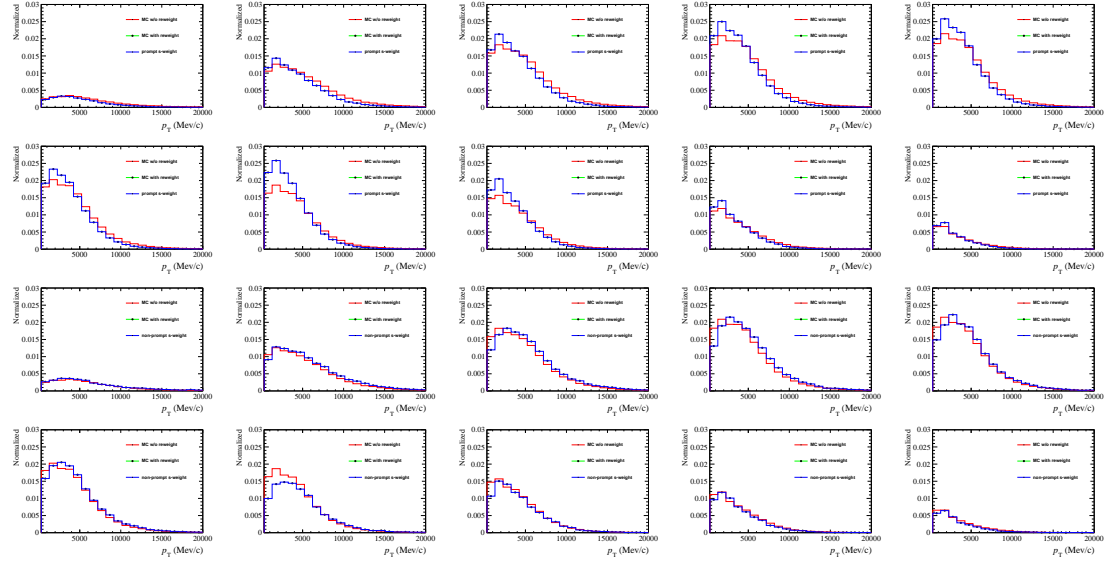


Figure 3.11 The  $p_T$ - $y$  reweight in  $2 < y < 4.5$  and  $0 < p_T < 20 \text{ GeV}/c$  for  $\psi(2S)$ , each subplot represents the  $p_T$  reweight in each  $y$  bin of width 0.25. The top two rows are for prompt  $\psi(2S)$  and the bottom two rows are for non-prompt  $\psi(2S)$ .

### 3.5.1 Geometrical acceptance

The geometrical acceptance in each kinematic bin is defined as

$$\epsilon_{\text{acc}} \equiv \frac{N(p_T, y) \text{ with both } \mu \text{ in LHCb acceptance}}{N(p_T, y)}. \quad (3.13)$$

The LHCb acceptance means the polar angle  $[10, 400]$  mrad defined with respect to the direction of LHCb  $z$ -axis, before the effect of the magnetic field. The efficiency  $\epsilon_{\text{acc}}$  is determined using a simulated sample at the generator level. In Fig. 3.12, the efficiency in each  $p_T$  and  $y$  bin of  $J/\psi$  and  $\psi(2S)$  mesons for  $z_{\text{PV}} > -60 \text{ mm}$  and  $n\text{PVs}=1$  are presented. The geometrical acceptances for prompt production and production from  $b$ -hadron decay are calculated separately for both  $J/\psi$  and  $\psi(2S)$ . Since the geometrical acceptance is only a function of kinematic variables, and the  $p_T$ - $y$  binning is fine enough, the same geometrical acceptance efficiencies are used in different multiplicity regions.

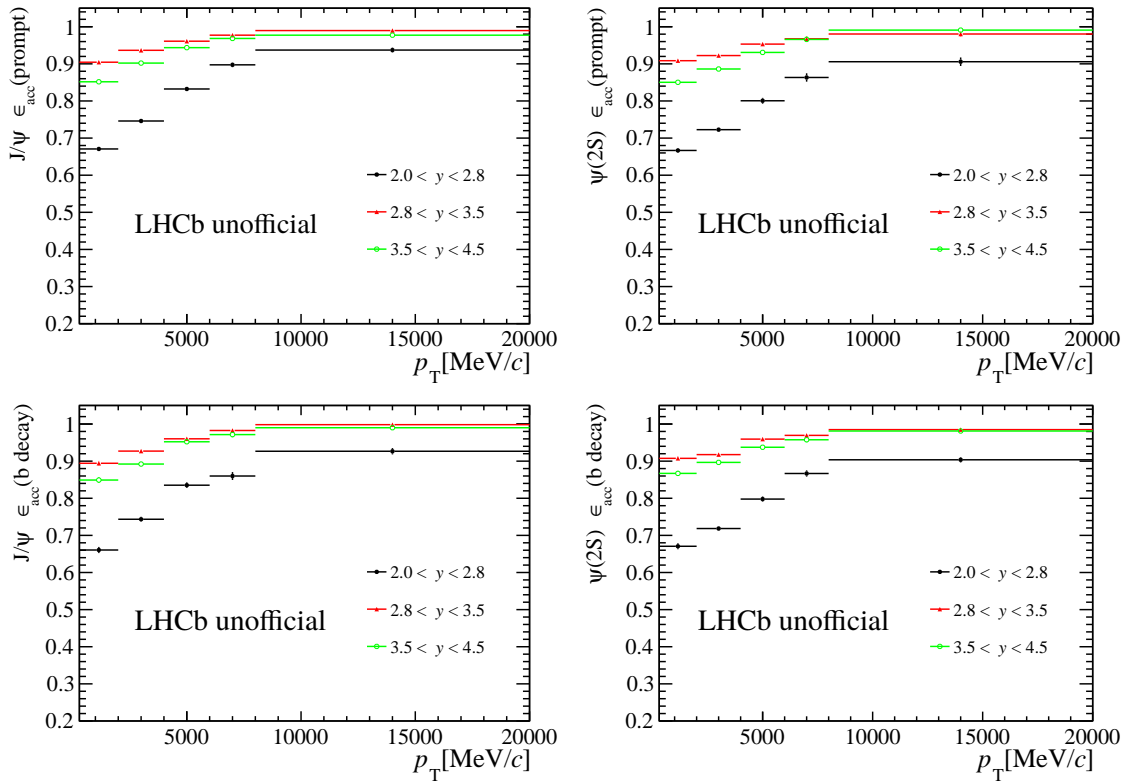


Figure 3.12 Geometrical acceptance efficiency for (left)  $J/\psi$  and (right)  $\psi(2S)$  in multiplicity bin  $4 \leq N_{\text{tracks}}^{\text{PV}} < 20$ , the top row is for prompt and the bottom row is for non-prompt components.

### 3.5.2 Reconstruction-selection efficiency

The reconstruction and selection efficiency in each kinematic bin is estimated as

$$\epsilon_{\text{Reco\&Sel}} \equiv \frac{N(p_T, y) \text{ reconstructed and selected (w/o } \mu \text{ ID and trigger)}}{N(p_T, y) \text{ with both } \mu \text{ in LHCb acceptance}}. \quad (3.14)$$

It includes the efficiency of reconstructing the two muon tracks and the selection of the signals, with the selection criteria listed in Table 3.3 (excluding muon identification and the trigger). Then the track reconstruction efficiency in the simulation need to be further corrected using the data tracking efficiency. The ratio of tracking efficiencies for a single track in data and simulation determined with the Long Tag-Probe method<sup>[161]</sup> is shown in Fig. 3.13. In Tag-Probe method, a fully reconstructed long track is used as a tag and a partially reconstructed track is treated as probe. Then the probe track is used to match a fully reconstructed one, with the successfully matched fraction being track finding efficiencies. The calibration sample used is  $J/\psi \rightarrow \mu^+ \mu^-$  sample.

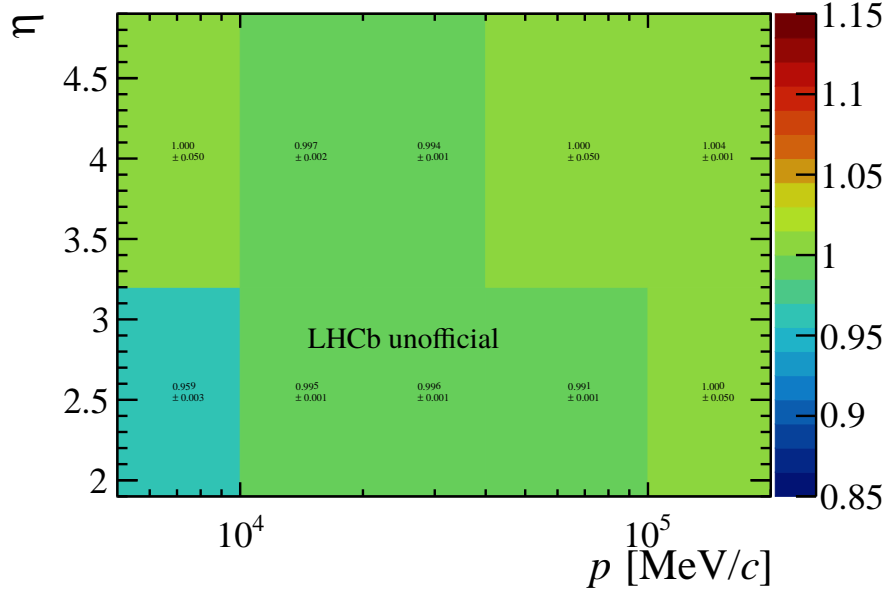


Figure 3.13 Tracking efficiency ratio between data and MC2016 simulation in bins of  $p_\mu$  and  $\eta_\mu$  of the muon.

For a given event the correction factor is determined by multiplying the efficiency ratios for each of the tracks in the final state. The factor is further corrected by the weight from the multiplicity and  $p_T$ - $y$  reweight discussed in Sec 3.5. For each  $p_T$  and  $y$  bin, the efficiency of  $\epsilon_{\text{Reco\&Sel}}$  is shown in Fig. 3.14 for  $N_{\text{tracks}}^{\text{PV}}$  from 4 to 20.

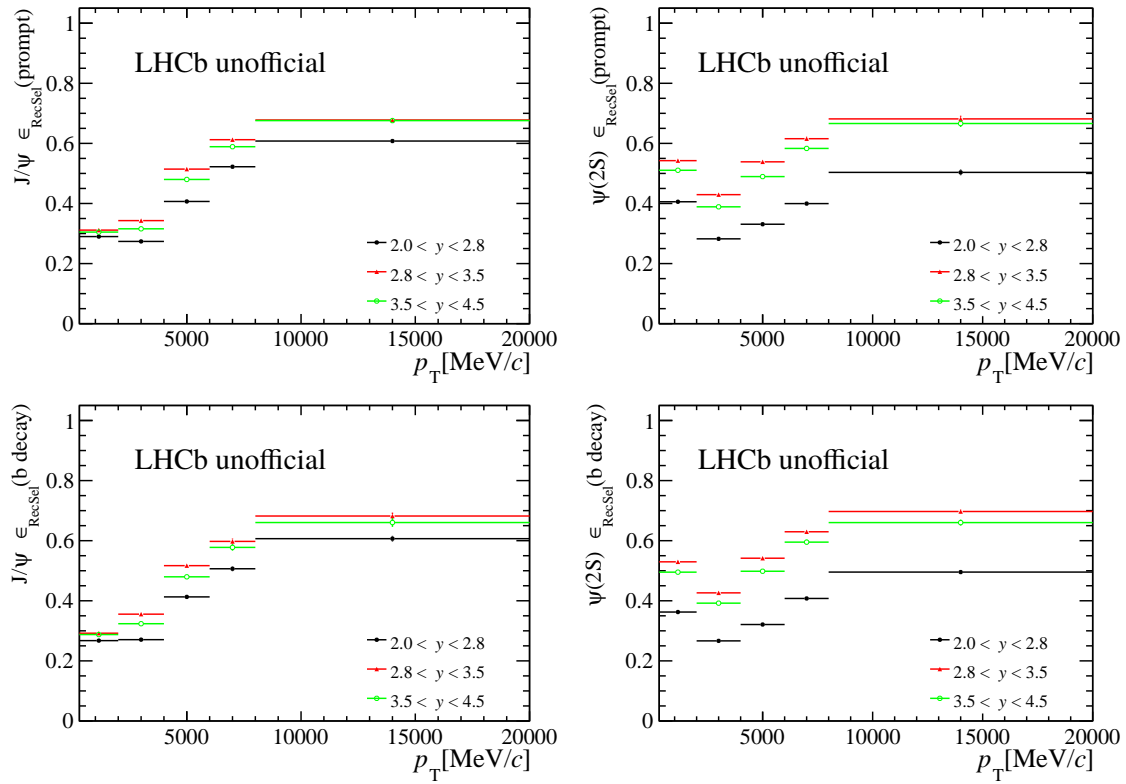


Figure 3.14 Reconstruction and selection efficiency for (left)  $J/\psi$  and (right)  $\psi(2S)$  in multiplicity bin  $4 \leq N_{\text{tracks}}^{\text{PV}} < 20$ . The top row is for prompt and the bottom row is for non-prompt components.

### 3.5.3 Muon identification efficiency

The muon identification requirement used in this analysis is listed in Table 3.2. The efficiency is introduced by

$$\epsilon_{\text{MuonID}} \equiv \frac{N(p_T, y) \text{ selected with } \mu\text{ID but w/o trigger}}{N(p_T, y) \text{ reconstructed and selected (w/o } \mu\text{ID \& trigger)}}. \quad (3.15)$$

The Muon ID efficiency is obtained using full simulated samples and single track muon ID efficiency obtained with the data using the PIDCalib package<sup>[162]</sup>. The full simulated samples used here pass all the selections except the muon ID and the trigger. The selected samples are the same one is used in the reconstruction and selection efficiency study. The muon ID efficiency in each  $(p_T, y)$  bin is then calculated by averaging the muon ID efficiency of each candidate in the bin, which is the product of the muon ID efficiencies of the two muons from the efficiency table, obtained from the PIDCalib package, according to their  $(p, \eta, \text{nSPDHits})$  values. The formula is

$$\bar{\epsilon}(p_T, y) = \frac{\sum_{i=1}^N \epsilon_{\mu^+}(p_{\mu^+}, \eta_{\mu^+}, \text{nSPDHits}) \epsilon_{\mu^-}(p_{\mu^-}, \eta_{\mu^-}, \text{nSPDHits})}{N_{\text{res\&sel}}}. \quad (3.16)$$

where  $\epsilon_{\mu^+}(p_{\mu^+}, \eta_{\mu^+}, \text{nSPDHits})$  and  $\epsilon_{\mu^-}(p_{\mu^-}, \eta_{\mu^-}, \text{nSPDHits})$  are the muon ID efficiencies

obtained from the efficiency table. The efficiency table used here is from the calibration sample which contains  $J/\psi$  candidates taken in the same period and the average efficiency over the whole period is used. One 3-Dimensional efficiency table dedicated to the muon ID selection is obtained from this calibration sample in bins of the muon ( $p, \eta, n_{SPD}\text{Hits}$ ) using the tag-and-probe method. The MagDown and MagUp efficiencies are calculated separately. For the muon candidates whose  $(p, \eta, n_{SPD}\text{Hits})$  are out of the range of the calibration sample, we simply set the value to be one due to the fact that the production in those bins is significantly small. For each  $p_T$  and  $y$  bin, the efficiency of  $\epsilon_{\text{MuonID}}$  is shown in Fig. 3.15.

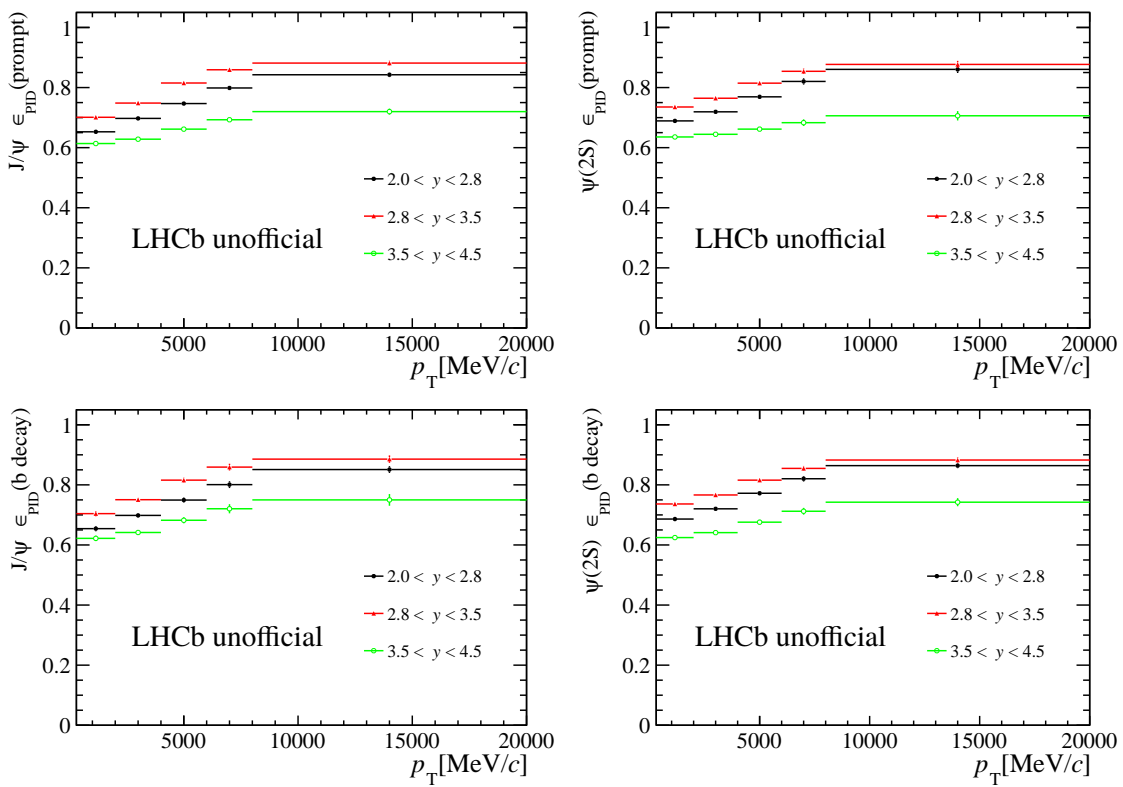


Figure 3.15 PID efficiency for (left)  $J/\psi$  and (right)  $\psi(2S)$  in multiplicity bin  $4 \leq N_{\text{tracks}}^{\text{PV}} < 20$ . The top row is for prompt and the bottom row is for non-prompt components.

### 3.5.4 Trigger efficiency

The trigger efficiency in each kinematic bin is defined as

$$\epsilon_{\text{Trigger}} \equiv \frac{N(p_T, y) \text{ selected with } \mu\text{ID \& trigger}}{N(p_T, y) \text{ selected with } \mu\text{ID but w/o trigger}} \quad (3.17)$$

Here the triggers include both TOS requirements of L0DiMuon, Hlt1DiMuonHighMass for both, and Hlt2DiMuonJPsiTurbo for  $J/\psi$  and Hlt2DiMuonPsi2STurbo for  $\psi(2S)$ , respectively. Only L0DiMuon and Hlt1DiMuonHighMass contribute actually to the effi-

ciency because the Hlt2DiMuonJPsiTurbo and Hlt2DiMuonPsi2STurbo is almost fully efficient due to the facts that the offline selections are more strict. For each  $p_T$  and  $y$  bin, the efficiencies of  $\epsilon_{\text{Trigger}}$  for both  $J/\psi$  and  $\psi(2S)$  from different sources for  $N_{\text{tracks}}^{\text{PV}}$  from 4 to 20 are shown in Fig. 3.16.

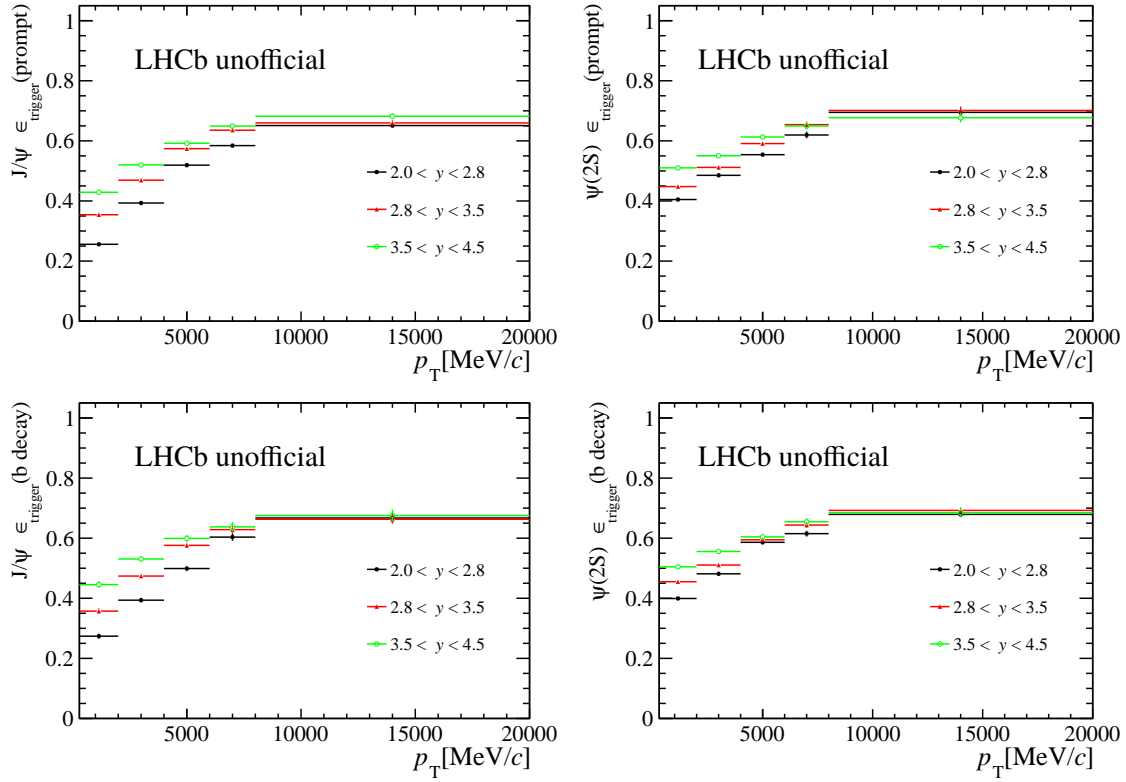


Figure 3.16 Trigger efficiency for (left)  $J/\psi$  and (right)  $\psi(2S)$  in multiplicity bin  $4 \leq N_{\text{tracks}}^{\text{PV}} < 20$ . The top row is for prompt and the bottom row is for non-prompt components.

### 3.5.5 Total efficiency

The total efficiencies  $\epsilon_{\text{tot}}$  for  $J/\psi$  and  $\psi(2S)$  from different sources for  $N_{\text{tracks}}^{\text{PV}}$  from 4 to 20 are shown in Fig. 3.17. The efficiencies for prompt and non-prompt components are used to calculate the corresponding final cross-section.

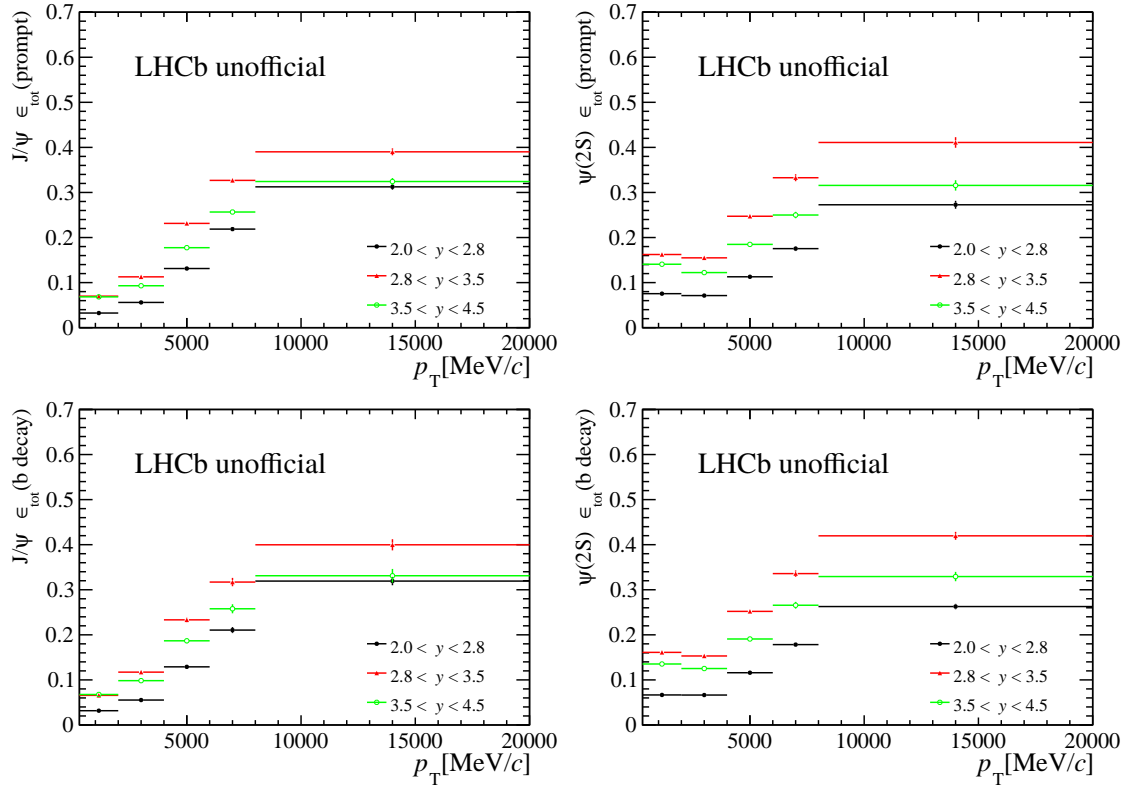


Figure 3.17 Total efficiency for (left)  $J/\psi$  and (right)  $\psi(2S)$  in multiplicity bin  $4 \leq N_{\text{tracks}}^{\text{PV}} < 20$ . The top row is for prompt and the bottom row is for non-prompt components.

The total efficiencies are also determined separately in each multiplicity bins. Except for the total efficiency in lowest multiplicity shown in Fig 3.17, an example of total efficiency in the highest multiplicity bins  $95 \leq N_{\text{tracks}}^{\text{PV}} < 200$  is shown in Fig 3.18. Difference can be seen between the total efficiencies in lowest and highest multiplicity bin, highlighting the necessity for calculating efficiency separately in different multiplicity bins. And conclusion can be draw that the total efficiencies for prompt and non-prompt components are almost the same.

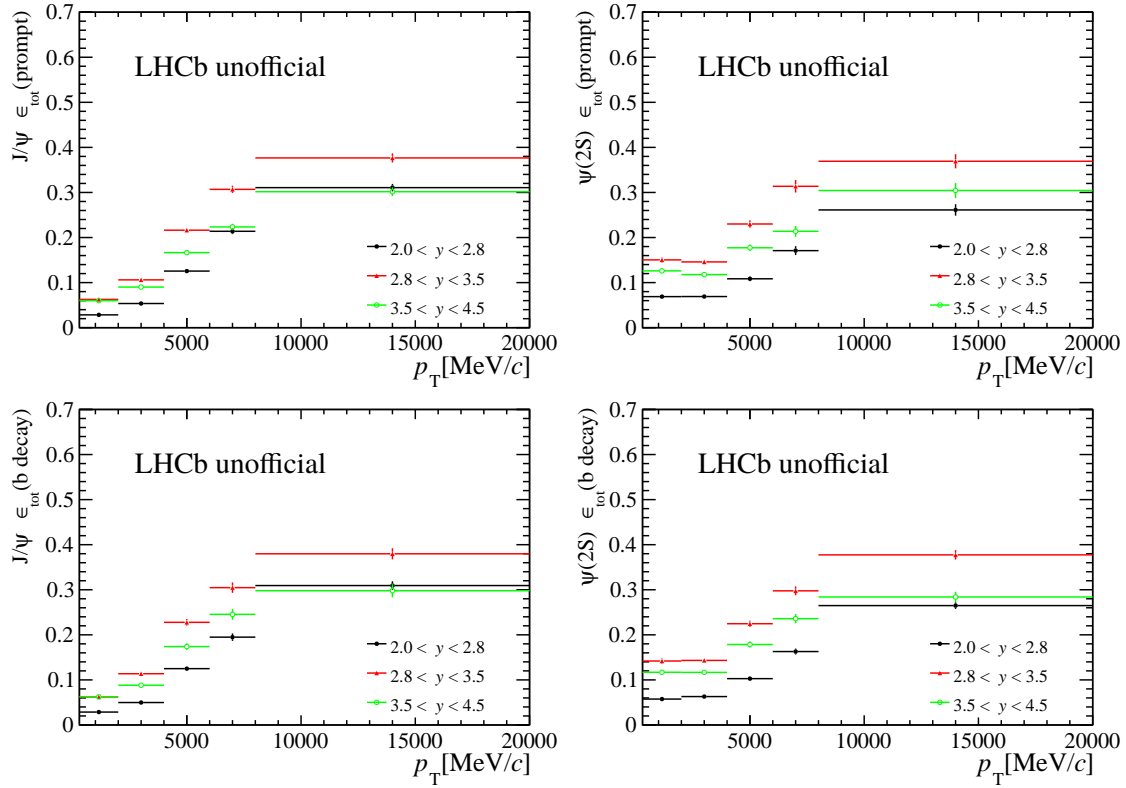


Figure 3.18 Total efficiency for (left)  $J/\psi$  and (right)  $\psi(2S)$  in multiplicity bin  $95 \leq N_{\text{tracks}}^{\text{PV}} < 200$ . The top row is for prompt and the bottom row is for non-prompt components.

### 3.5.6 Variation due to different reweight samples

Since the potential multiplicity-dependent comover breakup effects may vary with charmonium kinematic variables like  $(p_T, y)$ , their two-dimensional  $(p_T, y)$  distributions may differ in different multiplicity region. To study this effect on efficiencies, the  $(p_T, y)$  spectra are prepared for three different multiplicity classes:

- Data sample with all  $N_{\text{tracks}}^{\text{PV}}$  values.
- Data sample with  $N_{\text{tracks}}^{\text{PV}} \geq 70$  as high-multiplicity sample, where 70 is the bin edge of the second to last  $p_T$  bin in  $p_T$  binning scheme.
- Data sample with  $N_{\text{tracks}}^{\text{PV}} < 70$  as low-multiplicity sample.

The  $(p_T, y)$  distributions of high- and low-multiplicity samples are shown in Fig. 3.19. Using these two distributions for  $(p_T, y)$  reweight alternatively, we can calculate the resulting  $\psi(2S)$  to  $J/\psi$  total efficiency ratios for both prompt and non-prompt components in each multiplicity region. Comparing the newly calculated ratio of total efficiencies with the original one, where the center values and uncertainties for ratio of efficiencies are from the results reweighted by the full-multiplicity sample, we record the variation in each  $(p_T, y, N_{\text{tracks}}^{\text{PV}})$  bin in form of a certain time of statistical uncertainty in that bin. And the result

is shown in Fig 3.20. It's clearly shown that all the variations are within uncertainties. Therefore, the variation caused by reweight samples in different multiplicity regions is negligible.

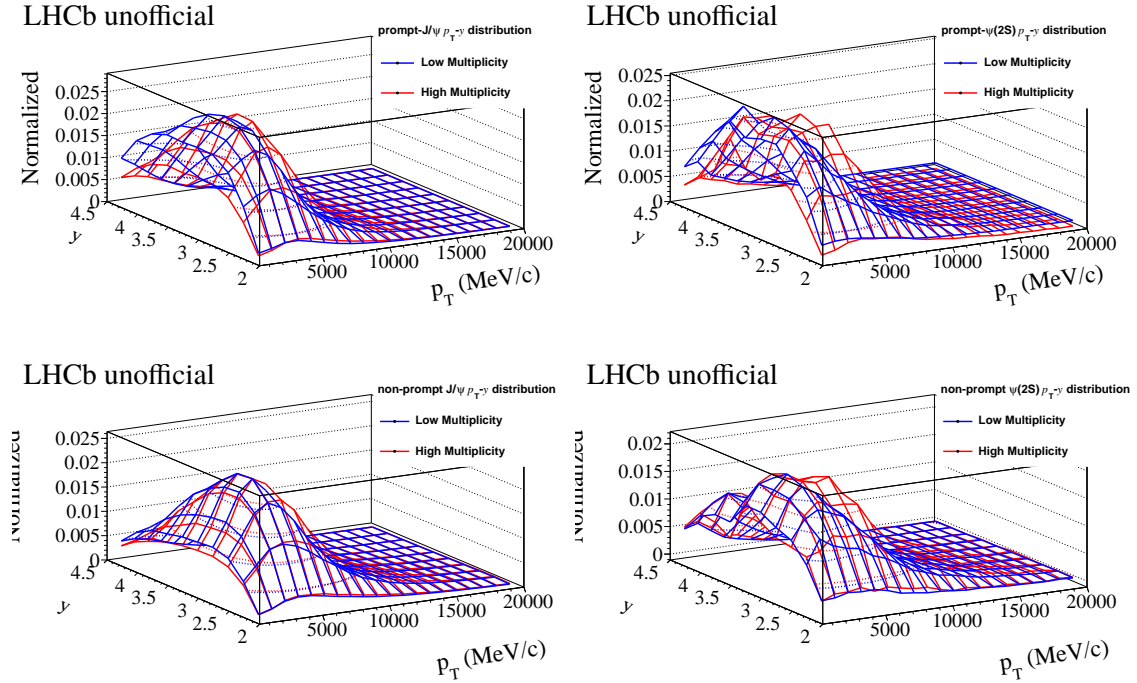


Figure 3.19 Two-dimensional ( $p_T$ ,  $y$ ) distribution for prompt and non-prompt components of different samples (high-multiplicity sample in red).

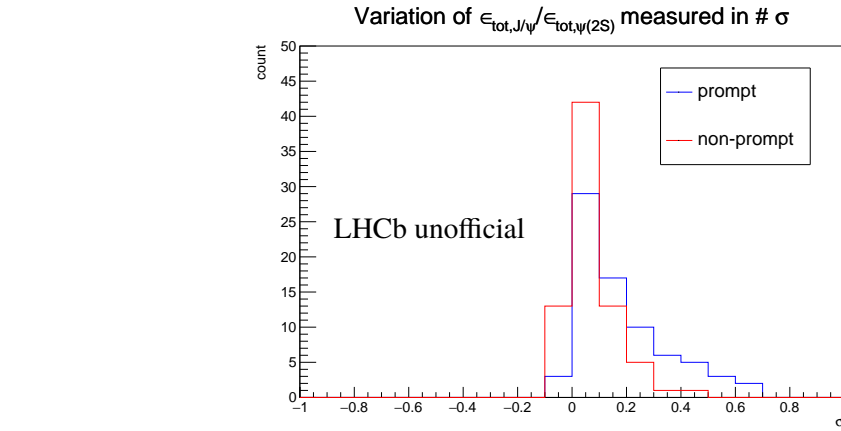


Figure 3.20 Distribution of the variation due to different reweight samples recorded in times of the statistical uncertainty.

### 3.6 Systematic uncertainties

The production ratio of  $\psi(2S)$  to  $J/\psi$  in a certain ( $p_T$ ,  $y$ ) interval is defined in Eq 3.2, which is universal for both prompt components and components from  $b$ -hadron decay

in each multiplicity bin. The systematic uncertainties of various sources are combined through the error propagation formula in each bin. When calculating the systematic uncertainties of the ratio of integrated production, the bin size is no more canceled and we need to take into account the production as weight in each bin. The ratio of integrated production is defined in Eq 3.3. When studying its systematic uncertainties, a simple and straightforward way is to calculate the uncertainties of  $\frac{\Sigma_{(p_T,y)}\sigma_{\psi(2S)}(p_T,y)}{\Sigma_{(p_T,y)}\sigma_{J/\psi}(p_T,y)}$  itself. For example, if we calculate the uncertainty of the fit model, instead of combining the uncertainties from different bins, we directly calculate how much  $\frac{\Sigma_{(p_T,y)}\sigma_{\psi(2S)}(p_T,y)}{\Sigma_{(p_T,y)}\sigma_{J/\psi}(p_T,y)}$  would vary when we change the fit model. For the uncertainties which are independent of bins, we can combine them through the error propagation formula, for example, the Systematic uncertainty due to MC sample size. Several sources of systematic uncertainties are considered. And the systematic uncertainties are calculated separately in each multiplicity bin. In this section, we only show the results for the first multiplicity bin, which is  $4 \leq N_{\text{tracks}}^{\text{PV}} < 20$ , as an example.

### 3.6.1 Uncertainty from signal extraction

#### 3.6.1.1 Signal mass shape

Using the sum of two Crystal Ball functions parametrized as described in Section 3.4 could bias the signal yields. For an alternative, the signal invariant mass is also fitted with the model which is extracted from the kernel-estimated distribution from the simulated sample bin by bin. In order to account for the resolution difference between data and simulation, a Gaussian function (all the parameters float during the fit procedure) is used to smear the shape of the signals. The study is performed in each kinematic bin, and the signal yields from the default fit and alternative fit are compared. For both  $J/\psi$  and  $\psi(2S)$ , we change the fit model to get their uncertainties then calculate the uncertainties of ratio through the error propagation formula. The detailed results of systematic uncertainty for ratio in each  $p_T$  and  $y$  bin in the  $N_{\text{tracks}}^{\text{PV}}$  bin of 4 to 20 are shown in Fig. 3.21. The result is common for both prompt components and components from  $b$ -hadron decay since when we fit the mass spectrum, we fit both components simultaneously.

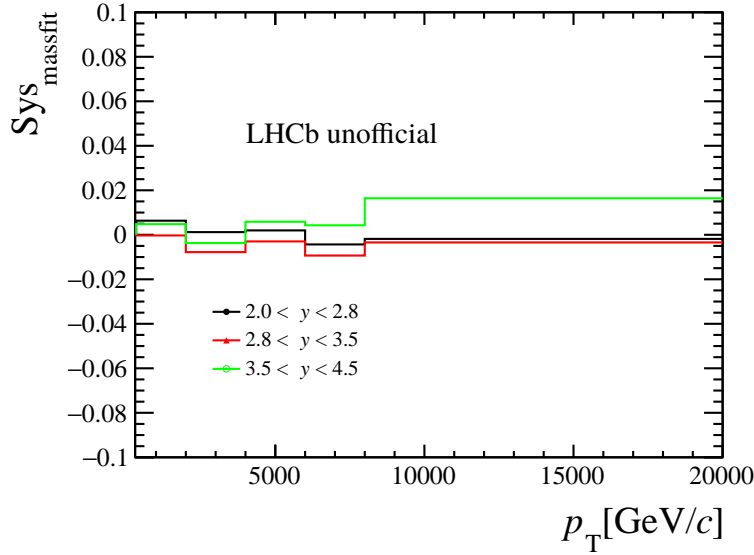


Figure 3.21 The systematic uncertainty of  $\psi(2S)$  to  $J/\psi$  production ratio due to the fit model in multiplicity bin  $4 \leq N_{\text{tracks}}^{\text{PV}} < 20$ .

For the ratio of integrated production, we change the fit model and calculate a new value with Eq 3.3. The variation between the new ratio and the original one is quoted as systematic uncertainty for ratio of integrated production due to mass fit model.

### 3.6.1.2 Fit to $t_z$ background

There are several scenarios that could deviate the fitted non-prompt fraction  $F_b$  from its true value.

The first is the imperfect modeling of the detector resolution of  $t_z$ . Since the shape of prompt  $\psi(2S)$  is dominated by the resolution, a defective description of the resolution could make the prompt  $J/\psi$  and  $\psi(2S)$  distribution not fitted very well, and thus will affect the fitted fraction of non-prompt component. To study this effect, a third wide Gaussian is added to the resolution function. It is found that the difference of the fitted  $F_b$  between the default fit and the new fit is negligible ( $< 0.1\%$ ).

The second is the systematic uncertainty related to the background description. In the nominal procedure, the fit explicitly models the background distribution using the candidates in the mass sidebands. As an alternative, the parameters of the  $t_z$  distribution for the background are obtained by the sPlot technique for both  $J/\psi$  and  $\psi(2S)$  and are fixed in the  $t_z$  fit.

For each  $p_T$  and  $y$  bin, the systematic uncertainties of the ratio are calculated by propagating the uncertainties from  $J/\psi$  and  $\psi(2S)$ . For the ratio of integrated production, similarly, as above, we change the fit model for  $t_z$  background for both  $J/\psi$  and  $\psi(2S)$  to

calculate a new value and quote the variation of ratio as a systematic uncertainty. The uncertainties for prompt and non-prompt components are calculated separately. The results in a single bin are shown in Fig 3.22.

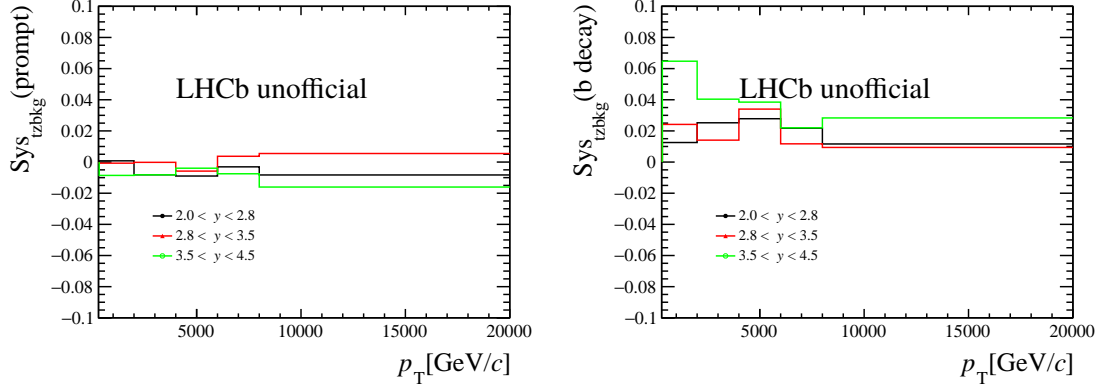


Figure 3.22 The systematic uncertainty of (left) prompt and (right) non-prompt production ratio due to  $t_z$  background fit model in multiplicity bin  $4 \leq N_{\text{tracks}}^{\text{PV}} < 20$ .

### 3.6.1.3 Fit to $t_z$ signal

For the imperfect modeling of detector resolution, we fit the  $t_z$  spectrum on MC and then compare the yields of prompt components to the real counts in MC. The variation in the ratio is quoted as systematic uncertainty due to imperfect modeling of the  $t_z$  signal model. The fitting strategy in each bin should be the same as is applied in the data, for example, in some kinematic and multiplicity bin of  $\psi(2S)$  data, the resolution function is described by only one gaussian function due to the limit size, then we should also use only one gaussian function to describe the resolution for MC in the same bin. The systematic uncertainties of ratio in different kinematic bins for  $4 \leq N_{\text{tracks}}^{\text{PV}} < 20$  are shown in Fig 3.23.

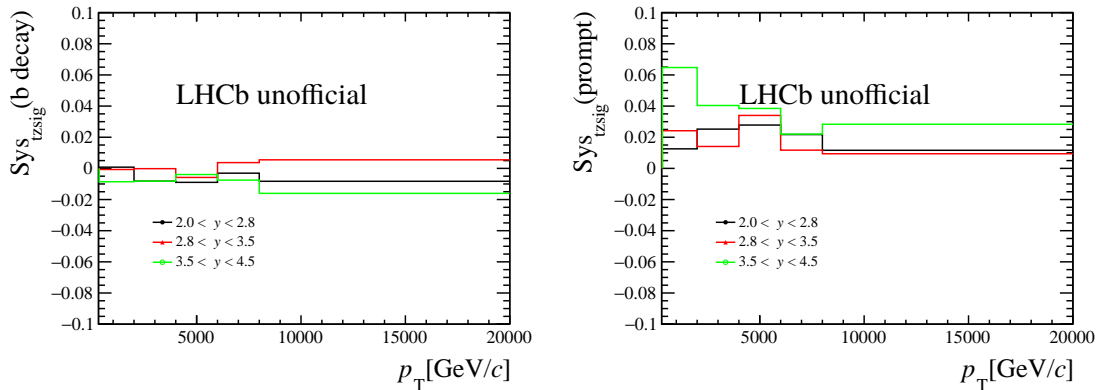


Figure 3.23 The systematic uncertainty of (left) prompt and (right) non-prompt production ratio due to  $t_z$  signal fit model in multiplicity bin  $4 \leq N_{\text{tracks}}^{\text{PV}} < 20$ .

### 3.6.2 Uncertainty from trigger efficiency

The trigger efficiency in simulation is cross-checked with data, and the resulting difference in the production ratio between simulation and data is quoted as a systematic uncertainty. For both L0DiMuon and Hlt1DiMuonHighMass the TISTOS method<sup>[163]</sup> is used to evaluate the efficiency for L0DiMuon&&Hlt1DiMuonHighMass both in simulation and data. We use L0Global and Hlt1Global as the TIS line. As the data sample size is limited by the number of the TIS events of  $\psi(2S)$  sample, we only consider the uncertainty in different multiplicity bins. By comparing the calculated efficiencies using TISTOS method in data and MC, we estimate the difference in trigger efficiency calculated by MC and the true trigger efficiency. It is shown in Fig. 3.24.

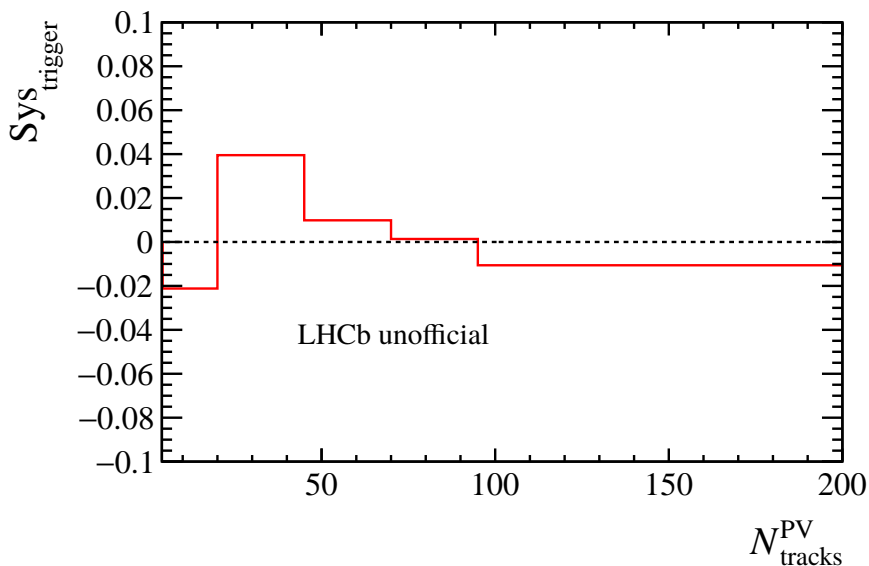


Figure 3.24 Summary of Systematic Uncertainties of ratio due to uncertainty of  $\epsilon_{\text{trigger}}$  in different multiplicity region.

To compare the ratio as a function of  $p_{\text{T}}$  with other measurements in different collision systems, we also calculate the systematic uncertainties in different  $p_{\text{T}}$  bins, where we integrate over the multiplicity and rapidity dimensions due to the limit in TIS sample size. It is shown in Fig. 3.25.

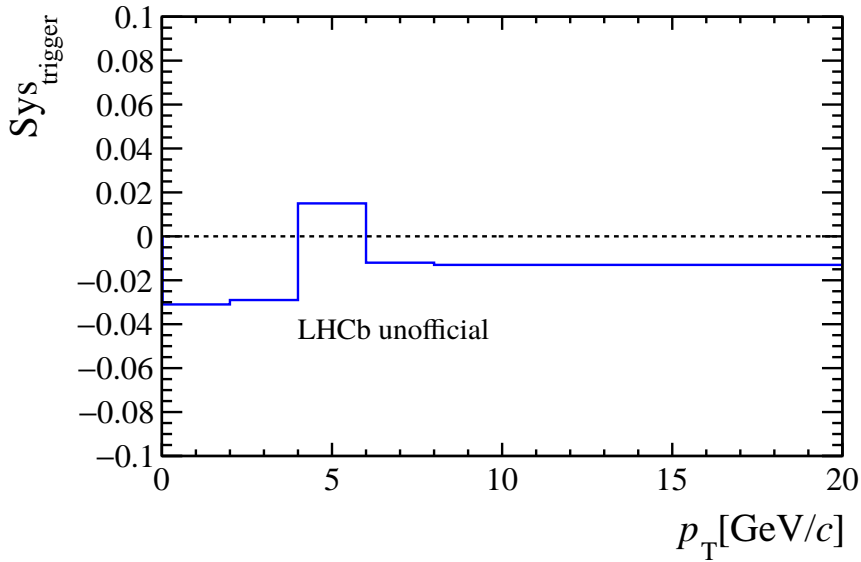


Figure 3.25 Systematic uncertainties of ratio due to uncertainty of  $\epsilon_{\text{trigger}}$  in different  $p_T$  regions.

### 3.6.3 Uncertainty from tracking efficiency

There are two sources of systematic uncertainties associated with the track reconstruction efficiency.

One is the statistical uncertainty of the ratios due to the limited sample size used to obtain the tracking correction table. This part could be obtained by toy studies: Two hundred experiments were performed where the efficiency for each bin in the  $p$  and  $\eta$  was sampled from Fig. 3.13 by Gaussian distributions with the corresponding central value as the mean and the uncertainty as the width; For each experiment, the reconstruction and selection efficiency of prompt and non-prompt components in different bins could be obtained with the sampled efficiency correction table, and hence we can calculate two hundred values for ratio in a single bin or any integrated region; Finally, using a gaussian function to fit the two hundred of results, and the sigma divided by the mean value of the fit result is quoted as the relative uncertainty. The relative uncertainty in each bin for prompt and non-prompt components for  $N_{\text{tracks}}^{\text{PV}}$  from 4 to 20 is shown in figure 3.26.

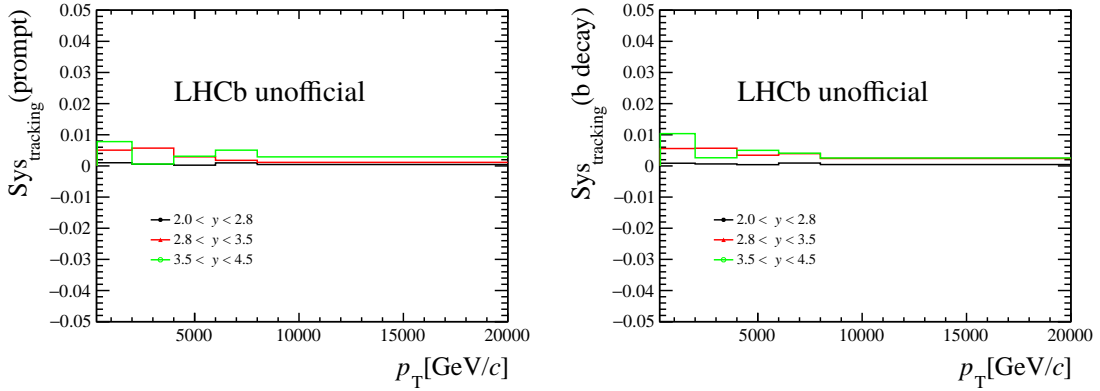


Figure 3.26 The systematic uncertainty of (left) prompt and (right) non-prompt production ratio due to the uncertainty of track table in multiplicity bin  $4 \leq N_{\text{tracks}}^{\text{PV}} < 20$ .

Another one is the choice of event multiplicity variable. It is found that the choice of the multiplicity variable (nTracks, nSPDHits, or others) can affect the single track reconstruction efficiency slightly. Systematic uncertainty due to this effect has been studied and suggest to be 0.8% per track, as detailed in Ref<sup>[164]</sup>. But when we calculate the ratio between  $J/\psi$  and  $\psi(2S)$ , the uncertainty due to the choice of multiplicity variable is canceled out since we use the same table for calculating both  $J/\psi$  and  $\psi(2S)$ .

### 3.6.4 Uncertainty from muonID efficiency

The systematic uncertainty due to MuonID includes the following contributions: The first is the statistical uncertainty is due to the finite size of the calibration sample. To estimate the systematic uncertainty, we first generate two hundred tables of efficiencies from the original table, where the efficiency in each bin of each table is randomly sampled from a Gaussian distribution using the central value as the mean and the uncertainty as the width. Then, we obtain two hundred efficiency values from the generated efficiency tables, hence, we calculated two hundred productions of  $J/\psi$  and  $\psi(2S)$  in each  $p_T$ - $y$  bin in different multiplicity region and their ratios. Finally, we fit the distribution of the two hundred ratios (in a single bin and integrated region) with a Gaussian function. The ratio between the width and the mean value of the fitted Gaussian function is quoted as a systematic uncertainty, which is summarized in Fig 3.27.

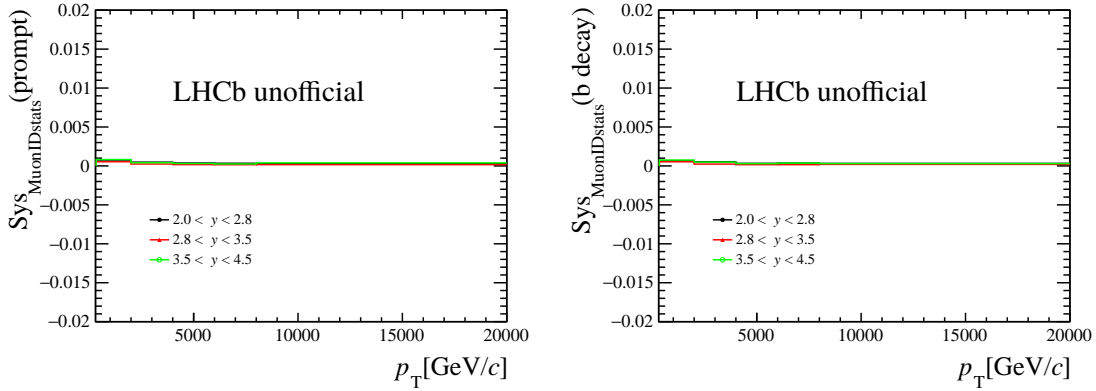


Figure 3.27 The systematic uncertainty of (left) prompt and (right) non-prompt production ratio due to the statistical uncertainty of PID efficiency in multiplicity bin  $4 \leq N_{\text{tracks}}^{\text{PV}} < 20$ .

The second source is the uncertainty due to binning scheme of the calibration sample. This can be studied by varying the binning method in  $p_\mu$ ,  $\eta_\mu$ , and nSPDHits respectively. The default one and the two alternative binning schemes could be found below. The nominal binning scheme of the muon ID efficiency for muons used to calculate the muon ID efficiency of  $J/\psi$  and  $\psi(2S)$  mesons is defined:

- $p_\mu$  boundaries [ GeV/c ]: 3, 6, 8, 10, 12, 13, 14, 15, 16, 18, 20, 24, 28, 32, 40, 60, 70, 80, 90, 100, 200, 1000
- $\eta$  boundaries: 2.0, 2.5, 3.0, 3.5, 4.0, 4.5, 4.9
- nSPDHits boundaries: 0, 200, 400, 1000.

One of the two alternative binning schemes is defined:

- $p_\mu$  boundaries [ GeV/c ]: 5, 7, 9, 11, 12, 13, 14, 15, 17, 19, 23, 27, 32, 40, 55, 65, 75, 85, 95, 150, 200, 1000
- $\eta$  boundaries: 2.0, 2.4, 2.9, 3.4, 3.9, 4.4, 4.9
- nSPDHits boundaries: 0, 300, 500, 1000.

The other one binning schemes is defined:

- $p_\mu$  boundaries [ GeV/c ]: 3, 5.5, 7.5, 9.5, 11.5, 12.5, 13.5, 14.5, 15.5, 17.5, 19.5, 23.5, 27.5, 32, 38, 48, 58, 68, 78, 88, 98, 198, 1000
- $\eta$  boundaries: 2.0, 2.6, 3.1, 3.6, 4.1, 4.6, 4.9
- nSPDHits boundaries: 0, 150, 480, 1000.

The maximum difference between the two new ratios calculated by new efficiency and the original ratio is quoted as the systematic uncertainty. The relative uncertainties for the ratio in each bin for  $N_{\text{tracks}}^{\text{PV}}$  from 4 to 20 are summarized in Fig 3.28.

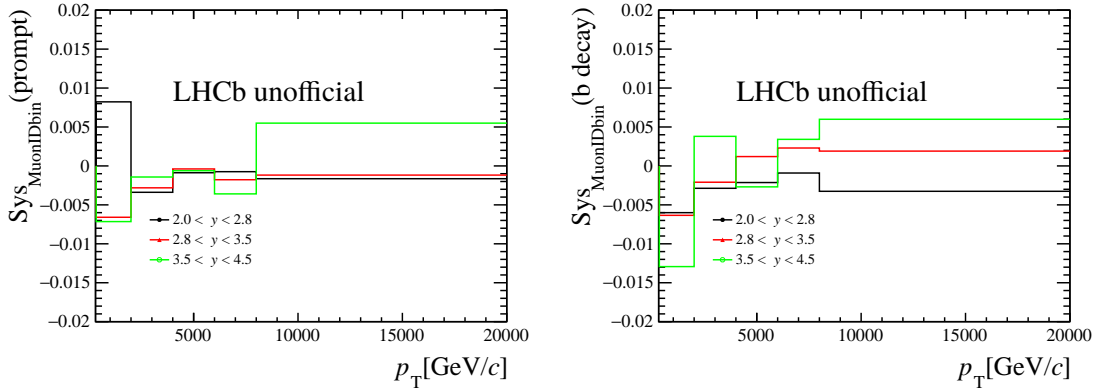


Figure 3.28 The systematic uncertainty of (left) prompt and (right) non-prompt production ratio due to the binning scheme of calibration sample in multiplicity bin  $4 \leq N_{\text{tracks}}^{\text{PV}} < 20$ .

### 3.6.5 Uncertainty due to limit MC sample size

The limited size of the simulation sample used to determine the efficiencies is a source of systematic uncertainties. The uncertainty of ratio due to MC sample size in different bin for  $N_{\text{tracks}}^{\text{PV}}$  from 4 to 20 are summarized in Fig 3.29.

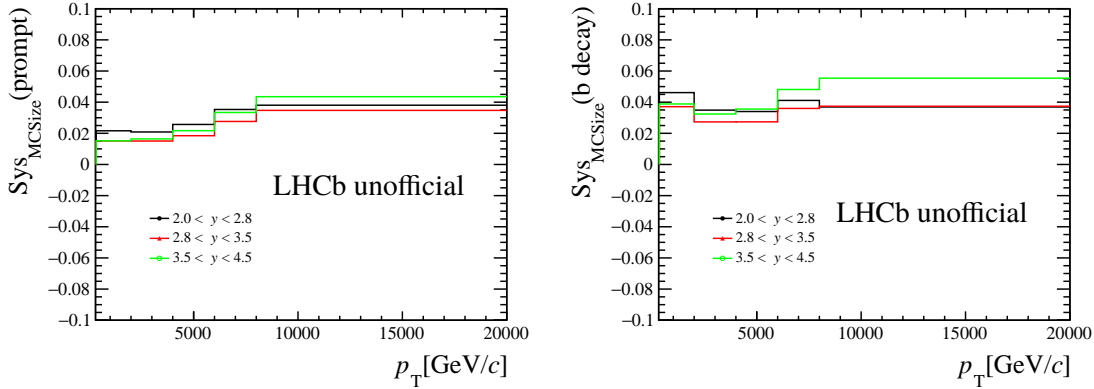


Figure 3.29 The systematic uncertainty of (left) prompt and (right) non-prompt production ratio due to limit sample size in multiplicity bin  $4 \leq N_{\text{tracks}}^{\text{PV}} < 20$ .

The uncertainty due to limited size of the simulated sample used to determine the efficiencies is propagated to the final result. The trigger efficiency is estimated from simulation and is cross-checked by a data-driven method using a fully reconstructed sample. The trigger efficiency in data is determined using a subset of events that would have triggered independently of the  $J/\psi$  and  $\psi(2S)$  signal candidates<sup>[165]</sup>. The relative difference between data and simulation in different multiplicity bins is taken as a systematic uncertainty. The uncertainties in the charmonium branching ratios and luminosity cancel in the normalised ratios, defined as the ratios in different multiplicity regions divided by the total ratio over all multiplicity regions. The systematic uncertainties for the ratios in different

$N_{\text{tracks}}^{\text{PV}}$  bins are summarized in Table 3.4.

Table 3.4 Summary of systematic uncertainties for the double-differential  $\psi(2S)$ -to- $J/\psi$  cross-section ratio in different multiplicity bins (in %). Sources marked with  $\dagger$  are considered to be correlated between bins.

Source	Interval of $N_{\text{tracks}}^{\text{PV}}$				
	4–20	20–45	45–70	70–95	95–200
Signal mass shape $\dagger$					
prompt & non-prompt	0.1–1.6	0.1–1.3	0.1–1.1	0.1–1.8	0.1–3.2
Signal $t_z$ shape $\dagger$					
prompt	0.2–1.8	0.2–1.2	0.0–1.4	0.0–1.8	0.1–9.7
non-prompt	0.0–1.8	0.2–2.0	0.0–2.3	0.1–1.7	0.0–4.0
Background $t_z$ shape $\dagger$					
prompt	0.0–1.6	0.2–3.1	0.0–2.2	0.2–6.2	0.4–6.4
non-prompt	1.2–6.5	0.2–5.1	0.2–3.4	0.6–3.7	0.0–9.7
Tracking efficiency $\dagger$					
prompt	0.0–0.8	0.0–0.7	0.0–0.7	0.0–0.7	0.0–0.8
non-prompt	0.0–1.0	0.0–1.1	0.0–1.2	0.0–1.1	0.0–1.1
Trigger efficiency $\dagger$					
prompt & non-prompt	2.1	4.0	1.0	0.0	1.1
Muon ID sample size $\dagger$					
prompt	0.0–0.1	0.0–0.1	0.0–0.1	0.0–0.1	0.0–0.1
non-prompt	0.0–0.1	0.0–0.1	0.0–0.1	0.0–0.1	0.0–0.1
Muon ID binning $\dagger$					
prompt	0.1–0.8	0.1–0.8	0.1–0.9	0.1–0.7	0.1–0.9
non-prompt	0.0–0.9	0.0–0.8	0.1–0.7	0.1–0.8	0.1–1.0
Simulated sample size					
prompt	1.5–4.4	1.1–2.4	1.3–2.5	2.0–3.4	4.0–6.4
non-prompt	2.7–5.5	1.6–3.2	1.6–3.4	2.3–4.7	4.1–8.9
Total					
prompt	3.1–7.7	4.3–5.5	2.2–3.9	2.9–7.7	6.1–13
non-prompt	5.2–10.2	5.0–7.6	3.3–5.3	3.9–8.4	7.4–17

### 3.6.6 Other systematic uncertainties

- The uncertainty of  $\mathcal{B}(J/\psi \rightarrow \mu^+ \mu^-) = (5.961 \pm 0.033)\%$  and  $\mathcal{B}(\psi(2S) \rightarrow e^+ e^-) = (7.93 \pm 0.17) \times 10^{-3}$  are canceled when the normalised ratio is calculated.

- The relative uncertainty of the luminosity is canceled out when calculating the production ratio cross-section, with the datasets for  $J/\psi$  and  $\psi(2S)$  taken in the same period.
- A fraction of events (less than 1%) is lost because of the long QED radiative tail. But when calculating the production ratio, the effects for  $J/\psi$  and  $\psi(2S)$  are canceled out.

## 3.7 Results

### 3.7.1 Multiplicity dependence of integrated production ratio

The recorded  $\psi(2S)$ -to- $J/\psi$  production cross-section ratios are displayed across various kinematic and multiplicity bins. The complete numerical data details are available in Appendix A 5.2.

The  $\psi(2S)$ -to- $J/\psi$  ratio in each multiplicity bin is normalised to the ratio of total cross-section of  $J/\psi$  and  $\psi(2S)$  mesons as

$$\text{Normalised } \sigma_{\psi(2S),n}/\sigma_{J/\psi,n} = \frac{\sigma_{\psi(2S),n}/\sigma_{J/\psi,n}}{\sum_n \sigma_{\psi(2S),n}/\sum_n \sigma_{J/\psi,n}}, \quad (3.18)$$

where  $n$  is the bin index for multiplicity. The ratio of integrated production over  $p_T$  and  $y$  relative to the normalised  $N_{\text{tracks}}^{\text{PV}}$  is shown in Fig. 3.30, and the ratios are investigated in terms of the normalised  $N_{\text{bwd}}^{\text{PV}}$  and  $N_{\text{fwd}}^{\text{PV}}$  in Fig. 3.31.

The production ratio from  $b$ -hadron decays displays minimal dependence on multiplicity, regardless of the selected multiplicity variable. For prompt  $\psi(2S)$  and  $J/\psi$ , a distinct reduction in the ratio with  $N_{\text{tracks}}^{\text{PV}}$  is observed (a negative value for decreasing slope with P-value less than 0.05% under zero hypothesis), consistent with the predictions of the co-mover model, except in the low multiplicity region.

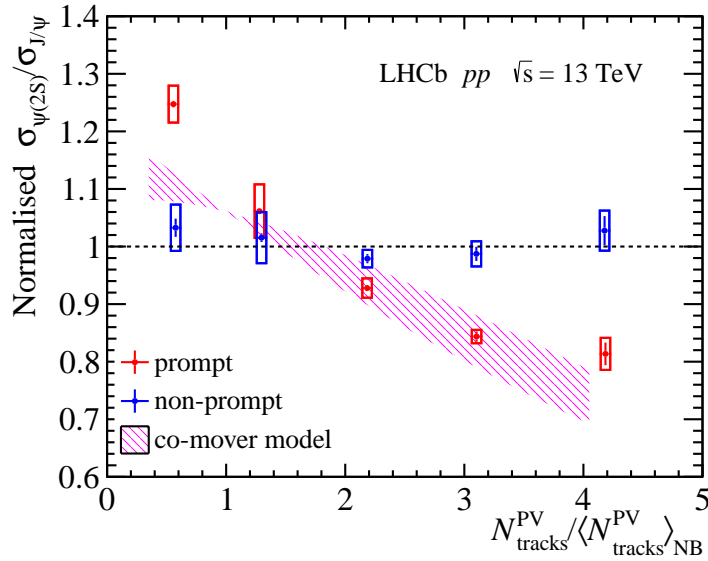


Figure 3.30 Normalised production ratio as a function of  $N_{\text{tracks}}^{\text{PV}}/\langle N_{\text{tracks}}^{\text{PV}} \rangle_{\text{NB}}$ , integrated over the full  $p_{\text{T}}\text{-}y$  range of  $2.0 < y < 4.5$  and  $0.3 < p_{\text{T}} < 20$  GeV/ $c$  with  $-60 < z_{\text{PV}} < 180$  mm. The error bars represent statistical uncertainties and the boxes represent systematical uncertainties.

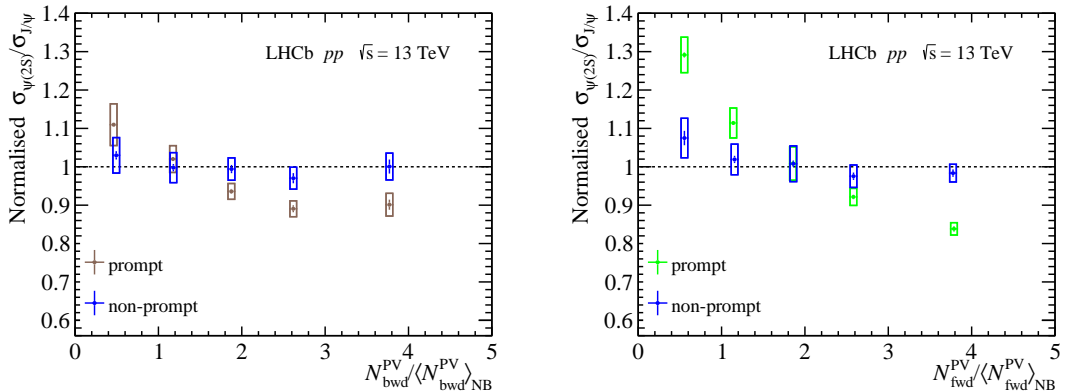


Figure 3.31 Normalised production ratio as a function of  $N_{\text{bwd}}^{\text{PV}}/\langle N_{\text{bwd}}^{\text{PV}} \rangle_{\text{NB}}$  (left, with  $-30 < z_{\text{PV}} < 180$  mm) and  $N_{\text{fwd}}^{\text{PV}}/\langle N_{\text{fwd}}^{\text{PV}} \rangle_{\text{NB}}$  (right, with  $-180 < z_{\text{PV}} < 180$  mm), integrated over the full  $p_{\text{T}}\text{-}y$  range of  $2.0 < y < 4.5$  and  $0.3 < p_{\text{T}} < 20$  GeV/ $c$ .

Notably, the decreasing trend is more slight as a function of  $N_{\text{bwd}}^{\text{PV}}$  compared to both  $N_{\text{fwd}}^{\text{PV}}$  and  $N_{\text{tracks}}^{\text{PV}}$ . This implies a connection between the relative suppression and local particle multiplicity, since  $N_{\text{bwd}}^{\text{PV}}$  is measured in a distinct rapidity range from the region of charmonia production. According to the comover effect<sup>[148]</sup>, this suggests that the ratio should remain constant across various  $N_{\text{bwd}}^{\text{PV}}$  regions. However, it's worth noting that  $N_{\text{bwd}}^{\text{PV}}$  is not entirely independent from  $N_{\text{fwd}}^{\text{PV}}$ , which shows a correlation factor with  $N_{\text{fwd}}^{\text{PV}}$  of 0.54 for  $J/\psi$  and 0.51 for  $\psi(2S)$ . Fig 3.32 shows an example of  $(N_{\text{fwd}}^{\text{PV}}, N_{\text{bwd}}^{\text{PV}})$  distribution for prompt  $\psi(2S)$ .

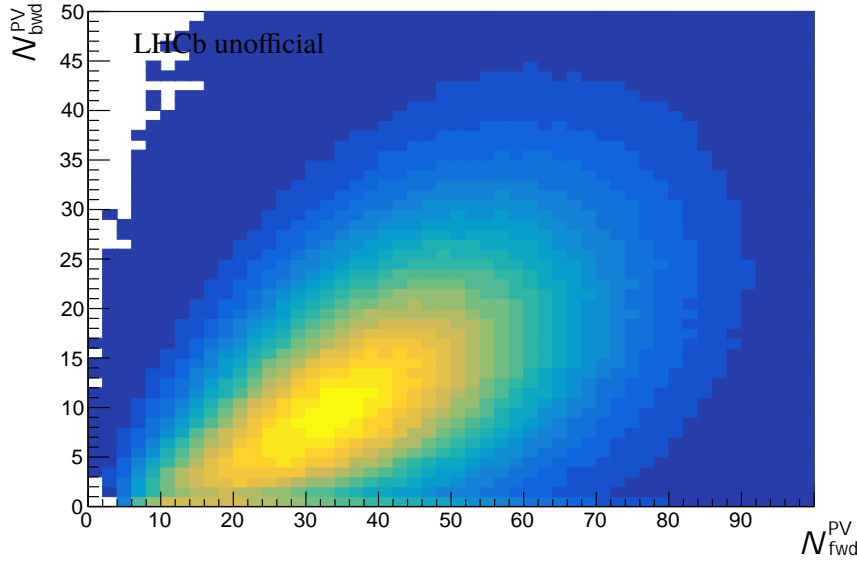


Figure 3.32 The two-dimensional distribution of  $(N_{\text{fwd}}^{\text{PV}}, N_{\text{bwd}}^{\text{PV}})$  for prompt  $\psi(2S)$ .

To assess the impact of the correlation between  $N_{\text{bwd}}^{\text{PV}}$  and  $N_{\text{fwd}}^{\text{PV}}$ , the mean  $N_{\text{fwd}}^{\text{PV}}$  value within each  $N_{\text{bwd}}^{\text{PV}}$  bin for prompt  $J/\psi$  and  $\psi(2S)$  is computed. Subsequently, the normalised ratios across different  $N_{\text{bwd}}^{\text{PV}}$  bins are plotted as a function of  $N_{\text{fwd}}^{\text{PV}}$ , as depicted in Fig. 3.33. The consistent alignment in the decreasing trend supports the hypothesis that the dependency of the normalised  $\psi(2S)$ -to- $J/\psi$  ratio on  $N_{\text{bwd}}^{\text{PV}}$  arises from the correlation between  $N_{\text{bwd}}^{\text{PV}}$  and  $N_{\text{fwd}}^{\text{PV}}$ .

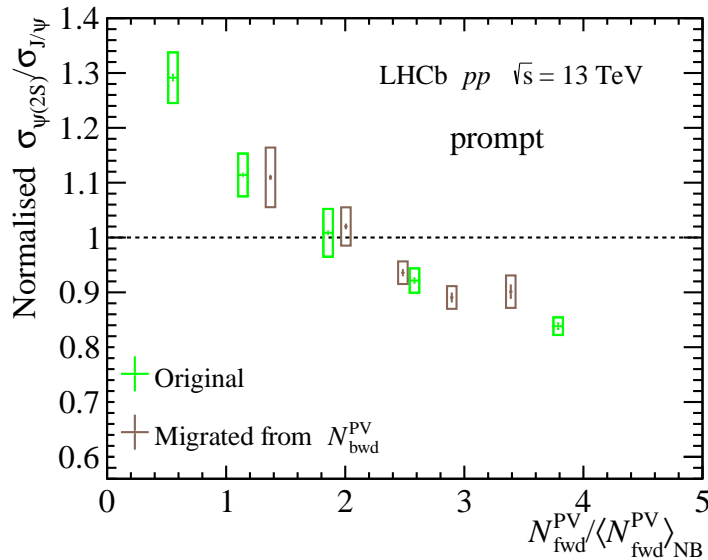


Figure 3.33 Normalised production ratio as a function of  $N_{\text{fwd}}^{\text{PV}} / \langle N_{\text{fwd}}^{\text{PV}} \rangle_{\text{NB}}$ , compared to a translation of the ratio as a function of  $N_{\text{bwd}}^{\text{PV}} / \langle N_{\text{bwd}}^{\text{PV}} \rangle_{\text{NB}}$ .

The ratio as function of  $dN_{ch}/d\eta$  is shown in Fig. 3.34. It shows consistency with the result in Fig. 3.30.

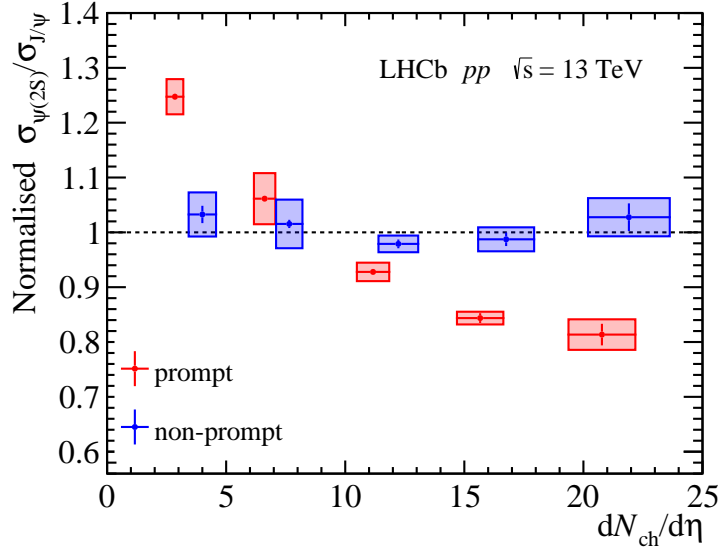


Figure 3.34 Normalised production ratio as a function of  $dN_{ch}/d\eta$ . The width for the shaded box is the systematic uncertainty for  $dN_{ch}/d\eta$ .

### 3.7.2 Multiplicity dependence in different kinematic regions

Figures 3.35, 3.36, and 3.37 display the normalised production ratios as a function of multiplicity in various  $p_T$  ranges. For non-prompt production, the ratio almost stay constant in all  $p_T$  ranges. The relative suppression of  $\psi(2S)$  meson production is more evident in the lower  $p_T$  region. For high- $p_T$  regions, the relative suppression is much less significant. This is qualitatively consistent with the picture that much less comoving particles can be found at higher  $p_T$ . This is consistent with what has been observed in  $\Upsilon(nS)$  by CMS<sup>[122]</sup>.

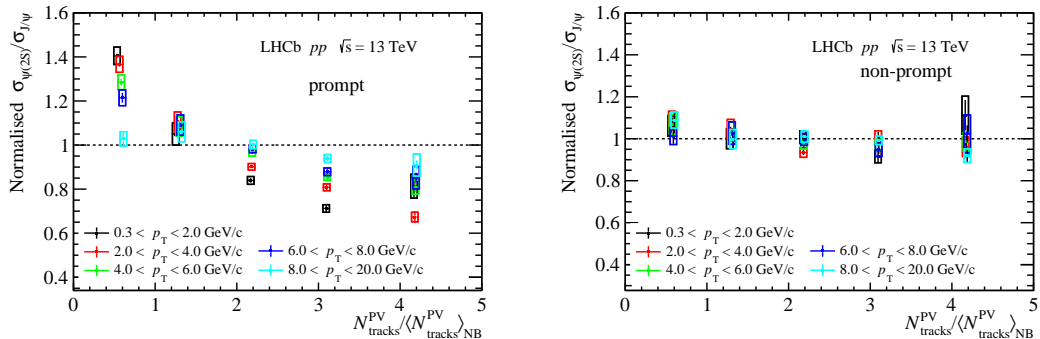


Figure 3.35 Normalised production ratio for (left) prompt and (right) non-prompt charmonia as a function of  $N_{tracks}^{PV}/\langle N_{tracks}^{PV} \rangle_{NB}$  in different  $p_T$  intervals, integrated over  $y$  range of 2 to 4.5.

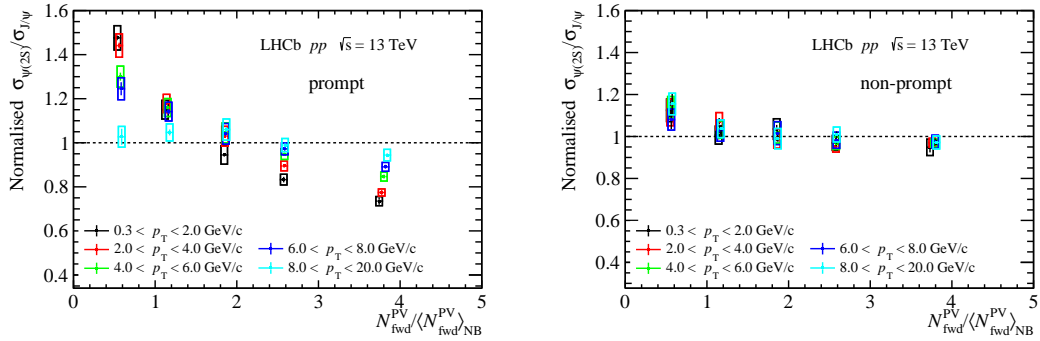


Figure 3.36 Normalised production ratio for (left) prompt and (right) non-prompt charmonia as a function of  $N_{\text{fwd}}^{\text{PV}} / \langle N_{\text{fwd}}^{\text{PV}} \rangle_{\text{NB}}$  in different  $p_T$  intervals, integrated over  $y$  range of 2 to 4.5.

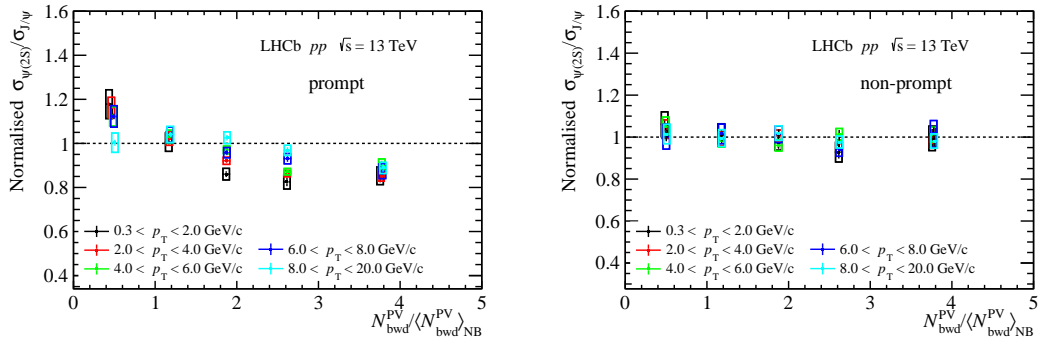


Figure 3.37 Normalised production ratio for (left) prompt and (right) non-prompt charmonia as a function of  $N_{\text{bwd}}^{\text{PV}} / \langle N_{\text{bwd}}^{\text{PV}} \rangle_{\text{NB}}$  in different  $p_T$  intervals, integrated over  $y$  range of 2 to 4.5.

The results in different rapidity bins are shown in Fig. 3.38, 3.39 and 3.40. Notably, there is small difference across different rapidity regions, for both prompt and non-prompt components.

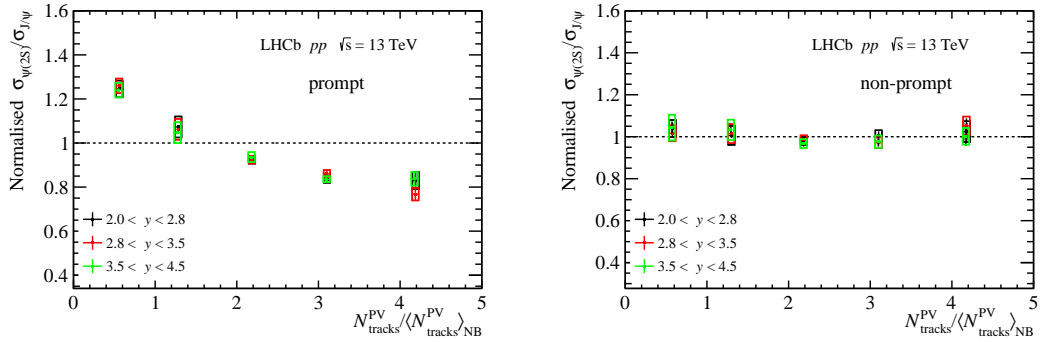


Figure 3.38 Normalised production ratio for (left) prompt and (right) non-prompt charmonia as a function of  $N_{\text{tracks}}^{\text{PV}} / \langle N_{\text{tracks}}^{\text{PV}} \rangle_{\text{NB}}$  in different  $y$  intervals.

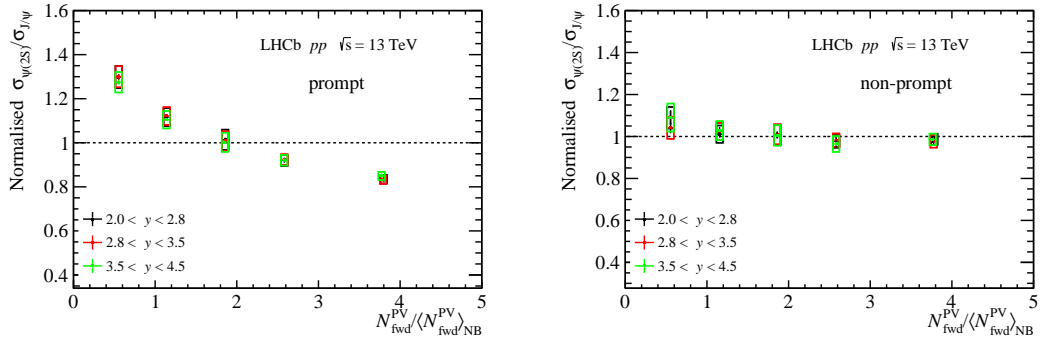


Figure 3.39 Normalised production ratio for (left) prompt and (right) non-prompt charmonia as a function of  $N_{\text{fwd}}^{\text{PV}}/\langle N_{\text{fwd}}^{\text{PV}} \rangle_{\text{NB}}$  in different  $y$  intervals.

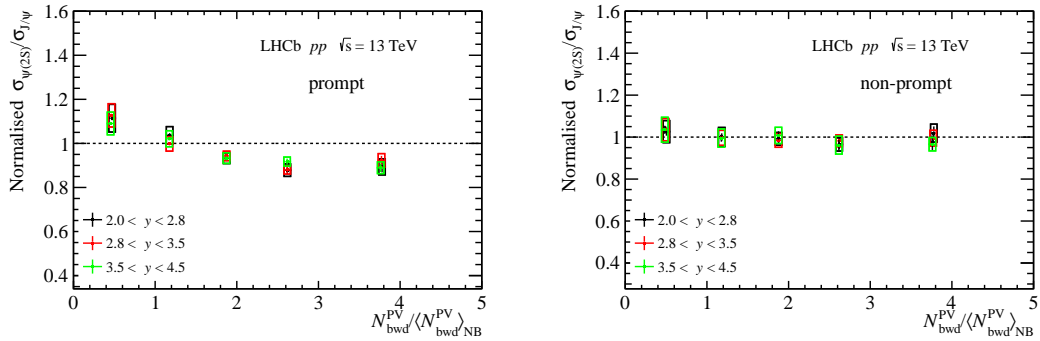


Figure 3.40 Normalised production ratio for (left) prompt and (right) non-prompt charmonia as a function of  $N_{\text{bwd}}^{\text{PV}}/\langle N_{\text{bwd}}^{\text{PV}} \rangle_{\text{NB}}$  in different  $y$  intervals.

### 3.7.3 Comparisons with other measurements

Measurements of  $\mathcal{B}_{\psi(2S)} \times \sigma_{\psi(2S)}$  and  $\mathcal{B}_{J/\psi} \times \sigma_{J/\psi}$  have been done across different collision systems and energies. The ratio of  $\sigma_{\psi(2S)}/\sigma_{J/\psi}$  alongside their branching fractions and systematic uncertainties can be obtained. Remarkably, these ratios are consistent regardless of the collision systems and energies. A comprehensive comparison of these measurements<sup>[54,69,166-174]</sup> is shown in Fig. 3.41. The LHCb data in this thesis shows a good agreement with other measurements, but with smaller uncertainties. The LHCb integrated value in this measurement is

$$\frac{\mathcal{B}_{\psi(2S)} \times \sigma_{\psi(2S)}}{\mathcal{B}_{J/\psi} \times \sigma_{J/\psi}} = (1.894 \pm 0.039)\%. \quad (3.19)$$

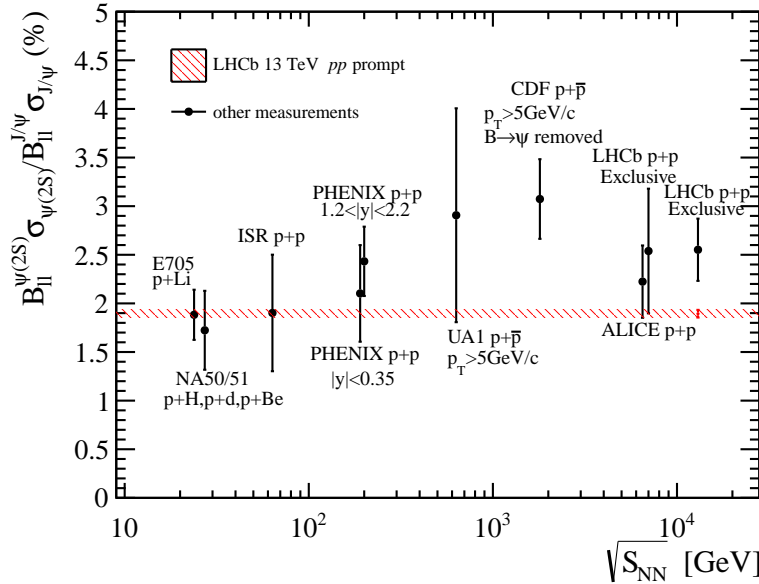


Figure 3.41 Production ratios compared to existing measurements<sup>[166]</sup>.

Fig 3.42 shows the ratios as function of  $p_T$ , with much higher precision, confirming the increasing trend toward higher  $p_T$ , consistent with the NRQCD calculations qualitatively.

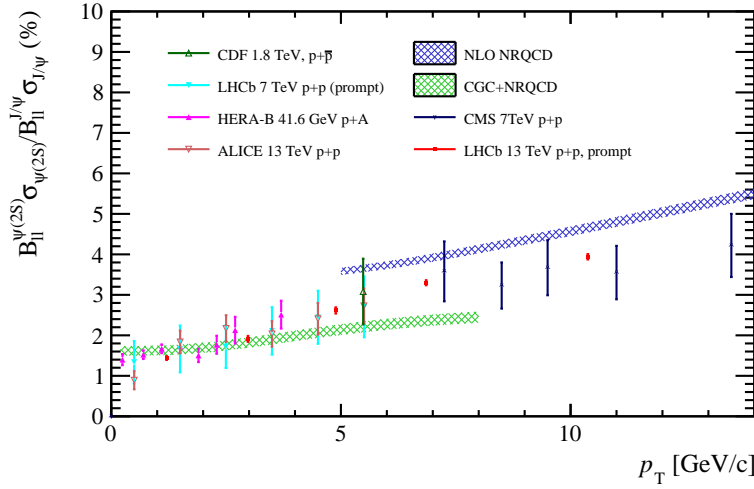


Figure 3.42 Production ratios as a function of  $p_T$  compared to existing measurements<sup>[166]</sup> and NRQCD models.

### 3.8 Conclusion

This analysis presents a measurement of the normalised  $\psi(2S)$ -to- $J/\psi$  cross-section ratio in  $pp$  collisions at  $\sqrt{s} = 13$  TeV, as a function of different charged-track multiplicity variables. The data, collected by the LHCb detector in 2016, corresponds to an integrated luminosity of  $658 \pm 13 \text{ pb}^{-1}$ .

To explore the co-mover effect and the existence of QGP in high-multiplicity small-system collisions, three multiplicity variables are considered: the numbers of charged particles in the forward ( $N_{\text{fwd}}^{\text{PV}}$ ) and backward ( $N_{\text{bwd}}^{\text{PV}}$ ) rapidity regions, and the number of charged particles used in the primary  $pp$  interaction vertex reconstruction ( $N_{\text{tracks}}^{\text{PV}}$ ), encompassing both the forward and backward regions.

For non-prompt production, the cross-section ratio shows no dependence on any of these multiplicity variables. In contrast, for prompt production, the ratio decreases with  $N_{\text{tracks}}^{\text{PV}}$ , consistent qualitatively with the predictions of the co-mover model. Additionally, the ratio for prompt production exhibits a similar trend with  $N_{\text{fwd}}^{\text{PV}}$  due to the correlation between multiplicity and charmonium production, also attributable to the co-mover effect. The use of  $N_{\text{bwd}}^{\text{PV}}$  helps mitigate this correlation, resulting in a small yet observable diminishing trend in relation to multiplicity. The slight dependence on  $N_{\text{bwd}}^{\text{PV}}$  may arise from the correlation between  $N_{\text{bwd}}^{\text{PV}}$  and  $N_{\text{fwd}}^{\text{PV}}$ .

The multiplicity dependence of the ratios is also measured in distinct  $p_{\text{T}}$  and  $y$  regions, revealing a stronger suppression pattern for the prompt  $\psi(2S)$ -to- $J/\psi$  ratio at low  $p_{\text{T}}$ . These distinct behaviors in prompt and non-prompt components highlight the substantial influence of interactions with other particles within the collision event on charmonium production, even in  $pp$  collisions. Finally, the results of the ratio  $\mathcal{B}_{\psi(2S)} \times \sigma_{\psi(2S)}$  over  $\mathcal{B}_{J/\psi} \times \sigma_{J/\psi}$  are compared with other measurements and found to be in agreement with much higher precision.

## CHAPTER 4 MULTIPLICITY DEPENDENCE OF $\sigma_{\psi(2S)}/\sigma_{J/\psi}$ IN $p\text{Pb}$ COLLISIONS

In this chapter, the multiplicity dependence of  $\sigma_{\psi(2S)}/\sigma_{J/\psi}$  is measured in the forward ( $p\text{Pb}$ ) and backward ( $\text{Pb}p$ ) rapidity regions. By comparing the different behaviors of the multiplicity dependence in  $p\text{Pb}$  and  $\text{Pb}p$  collisions, a transition from small systems ( $p\text{A}$  and  $pp$  collisions) to large system (AA collisions) is studied.

### 4.1 Data and simulated samples

The data used in this analysis was recorded during the heavy ion run in 2016, between Nov. 18th and Nov. 25th for the  $p\text{Pb}$  configuration and between Nov. 26th and Dec. 4th for the  $\text{Pb}p$  configuration, both at a center-of-mass energy of 8.16 TeV. The total recorded luminosity is of  $13.6 \pm 0.3\text{nb}^{-1}$  for  $p\text{Pb}$  and  $20.8 \pm 0.5\text{nb}^{-1}$  for  $\text{Pb}p$  collisions, where the  $p\text{Pb}$  and  $\text{Pb}p$  collisions differs in the beam-going direction. As illustrated in Fig 4.1, the  $p\text{Pb}$  collisions has its proton beam going forward in positive  $z$  direction while in  $\text{Pb}p$  collisions the Pb goes forward.

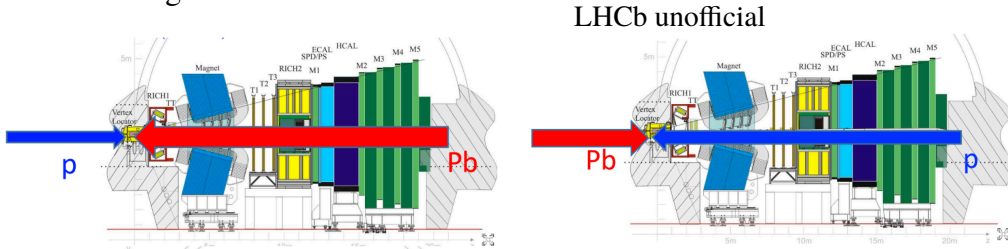


Figure 4.1 The (left)  $p\text{Pb}$  and (right)  $\text{Pb}p$  configurations for proton-lead collisions.

Due to the asymmetry in  $p\text{Pb}$  and  $\text{Pb}p$  colliding beams, the center-of-mass frames have relative speeds to laboratory frame, with a constant shift of rapidity  $\delta y = \frac{1}{2} \log(A_{\text{Pb}}/Z_{\text{Pb}}) \approx 0.465$  in the proton-going direction. The rapidity used in this analysis is in center-of-mass frame, which is  $y^* = y_{\text{lab}} - \delta y$ . The  $J/\psi$  and  $\psi(2S)$  candidates reconstructed with their dimuon channel online are used in this analysis.

The Monte Carlo sample is generated using the standard LHCb simulation software tools as the ones used for data. The simulation is done in two successive steps, first a generator phase based on several external tools such as event generators, and second a simulation phase based on the Geant4 package<sup>[175-176]</sup>. The signal of charmonia to dimuon are generated using an embedding technique: minimum bias events are generated using the

EPOS generator<sup>[177]</sup>. Then the charmonia are extracted from these minimum bias events and their decays are forced to the signal decay modes using the EvtGen package<sup>[153]</sup>, and the resulting decay chain is added to a single minimum bias EPOS event generated. The simulation phase is the same as the one used for the simulation of  $pp$  events within LHCb and is described in Ref<sup>[151]</sup> while the generation phase is specific to the heavy ion analysis. To study the efficiencies, 4 M full-simulation events of  $J/\psi$  and  $\psi(2S)$  to dimuon channel are generated for both  $p\text{Pb}$  and  $\text{Pb}p$  collisions, respectively. For the study of acceptance, 1 M candidates of generator-level simulated samples are generated for  $J/\psi$  and  $\psi(2S)$ , respectively.

## 4.2 Analysis strategy

The analysis strategy is quite similar to the previous analysis Sec 3.2 in  $pp$  collisions. So in this chapter, we will quickly go through the different parts.

Due to the limited data sample size, only multiplicity is divided into bins, and kinematic region is the full measured range, i.e.  $0 < p_{\text{T}} < 14 \text{ GeV}/c$  and  $1.5 < y^* < 4.0$  ( $-5.0 < y^* < -2.5$ ) for  $p\text{Pb}$  ( $\text{Pb}p$ ) collisions.

The absolute double differential cross-sections for  $J/\psi$  or  $\psi(2S)$  production are defined in Eq 4.1.

$$\frac{d^2\sigma}{dy^*dp_{\text{T}}} \Big|_{\text{Mult. bin}} = \frac{N}{\mathcal{L} \times \epsilon_{\text{tot}} \times \mathcal{B}_{\mu\mu} \times \Delta y^* \times \Delta p_{\text{T}}} \Big|_{\text{Mult. bin}}. \quad (4.1)$$

The definition of variables in Eq 4.1 can be found in Sec 3.2. The only difference is that the rapidity used here is in the center-of-mass frame. Cross-section ratio is defined in Eq. 4.2. The width of rapidity, transverse momentum and integrated luminosity are canceled out.

$$\frac{d^2\sigma_{\psi(2S)}/dy^*dp_{\text{T}}}{d^2\sigma_{J/\psi}/dy^*dp_{\text{T}}} \Big|_{\text{Mult. bin}} = \frac{\mathcal{B}(J/\psi \rightarrow \mu^+ \mu^-)}{\mathcal{B}(\psi(2S) \rightarrow e^+ e^-)} \times \frac{N_{\psi(2S)}}{N_{J/\psi}} \Big|_{\text{Mult. bin}} \times \frac{\epsilon_{\text{tot}, J/\psi}}{\epsilon_{\text{tot}, \psi(2S)}} \Big|_{\text{Mult. bin}}. \quad (4.2)$$

The binning schemes and mean values from NoBias data samples for different multiplicity variables are summarized in Table 4.1.  $N_{\text{tracks}}^{\text{PV}}$  starts at 4 since at least four tracks required to form a primary vertex.

Table 4.1 Binning schemes for different multiplicity variables.

Configurations	Mult. Variables	Schemes	Mean (NoBias)
$p$ Pb	$N_{\text{tracks}}^{\text{PV}}$	4, 45, 70, 90, 120, 270	60.54
$p$ Pb	$N_{\text{fwd}}^{\text{PV}}$	0, 25, 43, 57, 72, 150	33.17
$p$ Pb	$N_{\text{bwd}}^{\text{PV}}$	0, 17, 29, 40, 54, 140	27.37
$P$ b $p$	$N_{\text{tracks}}^{\text{PV}}$	4, 60, 90, 120, 160, 330	69.54
$P$ b $p$	$N_{\text{fwd}}^{\text{PV}}$	0, 35, 65, 85, 110, 250	47.07
$P$ b $p$	$N_{\text{bwd}}^{\text{PV}}$	0, 13, 22, 30, 47, 120	22.47

## 4.3 Online and offline selection

### 4.3.1 Global Event Selections

Only events with less than 8000 VELO clusters are considered in this analysis, as imposed by the trigger requirements. When measuring  $\psi(2S)$ -to- $J/\psi$  production ratio, the bias caused by this global cut is negligible since the data sample with more than 8000 VELO clusters account for less than 0.1% of total events. All events are also required to have exactly one reconstructed primary vertex to avoid pile-up.

The acceptance of VELO is not uniform along the beam direction, due to the fact that in the very up- and down-stream part of VELO, some tracks may not be reconstructed with enough hits. For the uniformity of VELO acceptance, we also need to restrict the  $z$  coordinate of primary vertex. The restriction is made according to which multiplicity variable we choose to represent the charged particle multiplicity. The distributions of different multiplicity variables in different collision systems are shown in Fig 4.2, where the multiplicity distribution of  $J/\psi$  is taken as example due to its high purity of signal. The  $z_{PV}$  restrictions are determined in the same way with the  $pp$  collision sample and is summarized in Table 4.2.

 Table 4.2 Global cuts on  $z_{PV}$ .

Configuration	Mult. Variable	$z_{PV}$
$p$ Pb	$N_{\text{tracks}}^{\text{PV}}$	[-30, 180] mm
$p$ Pb	$N_{\text{fwd}}^{\text{PV}}$	[-180, 180] mm
$p$ Pb	$N_{\text{bwd}}^{\text{PV}}$	[-30, 180] mm
$P$ b $p$	$N_{\text{tracks}}^{\text{PV}}$	[-60, 180] mm
$P$ b $p$	$N_{\text{fwd}}^{\text{PV}}$	[-180, 120] mm
$P$ b $p$	$N_{\text{bwd}}^{\text{PV}}$	[-30, 180] mm

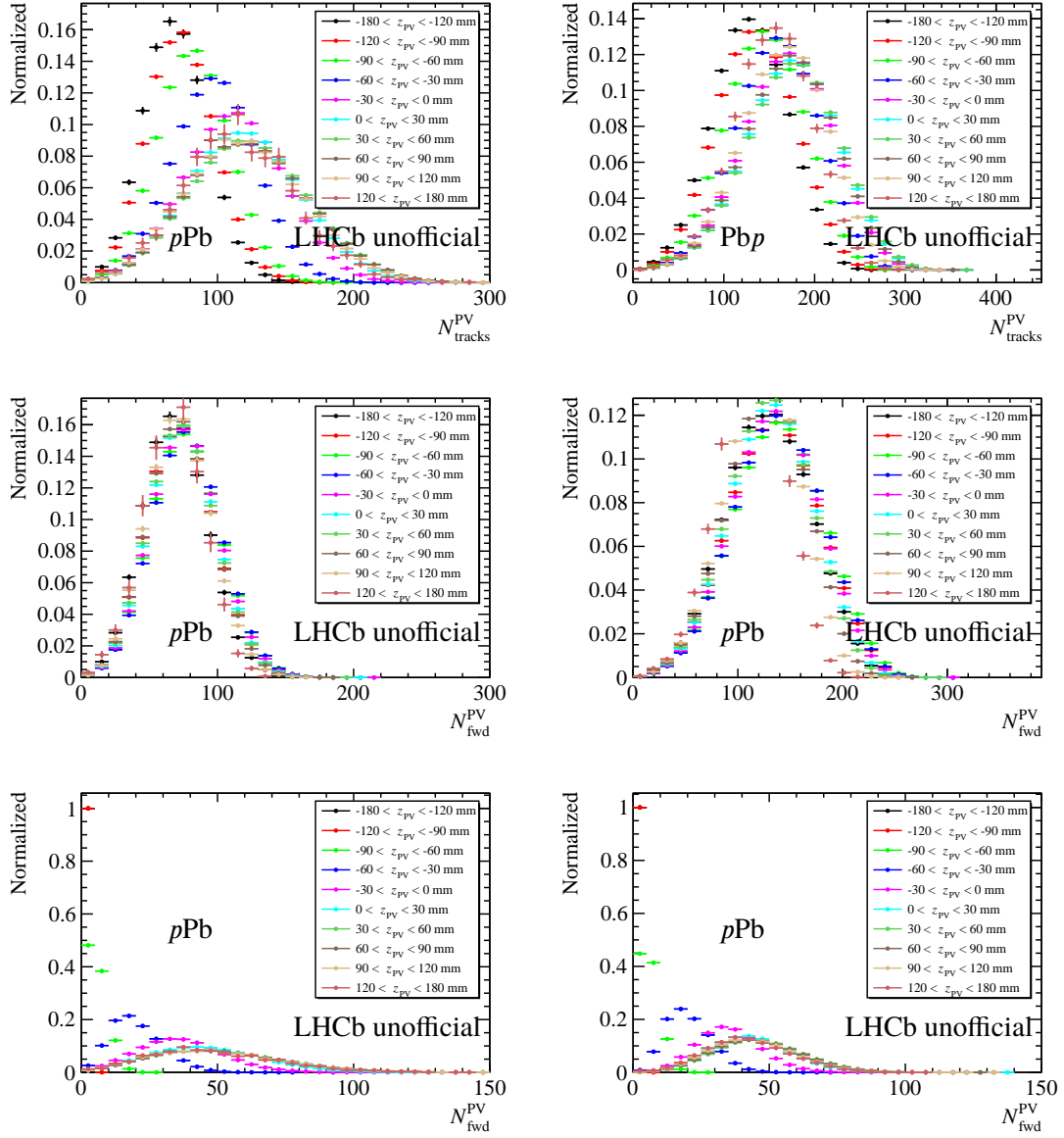


Figure 4.2 Multiplicity distribution in different  $z_{\text{PV}}$  regions in (left)  $p\text{Pb}$  and (right)  $\text{Pb}p$  collisions.

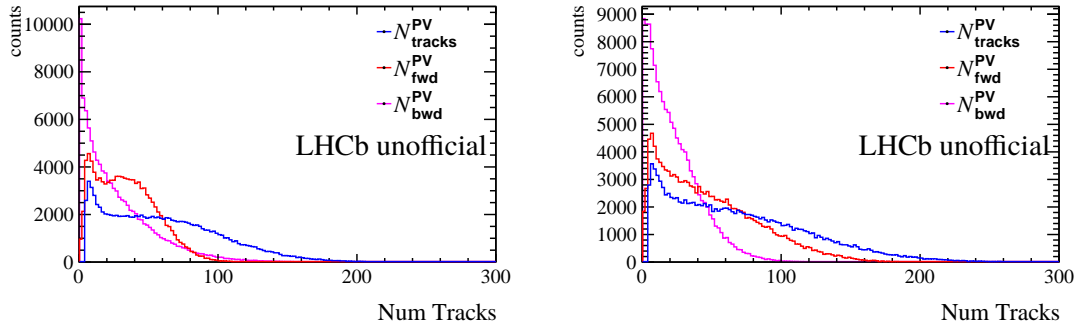


Figure 4.3 The distribution of  $N_{\text{tracks}}^{\text{PV}}$ ,  $N_{\text{fwd}}^{\text{PV}}$  and  $N_{\text{bwd}}^{\text{PV}}$  in (left)  $p\text{Pb}$  and (right)  $\text{Pb}\text{p}$  no-bias data.

Similar, the three multiplicity variables are normalised by their mean values in no-bias data. The multiplicity distributions for these three multiplicity variables in  $p\text{Pb}$  and  $\text{Pb}\text{p}$  no-bias data are shown in Fig 4.3. From Fig 3.1 and Fig 4.3 we can see that the multiplicity in  $\text{Pb}\text{p}$  collisions is much more than that in  $\text{pp}$  collisions in average and also larger than  $p\text{Pb}$  collisions.

### 4.3.2 Candidate Selection

The  $J/\psi$  and  $\psi(2S)$  candidates are reconstructed with two oppositely charged muons coming from a common vertex. Both decay modes are using same selection criteria. They are required to be TOS (Trigger On Signal) for the L0Muon and Hlt1DiMuonHighMass trigger lines, i.e. that the reconstructed candidate or its decay products are associated with a trigger object fulfilling the trigger requirements. Then the candidates used in this analysis are directly the ones reconstructed and selected by the Hlt2DiMuonJPsiTurbo and Hlt2DiMuonPsi2STurbo lines respectively, saved in the TURBO stream, without offline reconstruction. Additional cuts are applied at the analysis level. Muon tracks have to be in the geometrical acceptance of the spectrometer ( $2 < \eta < 5$ ) and to have  $p_{\text{T}} > 900$  MeV/c in order to improve the signal over background ratio. Both tracks are required to have a good fit quality,  $\chi^2/\text{ndof} < 3$  and a ghost probability less than 0.4. They are identified as muons by requiring  $\text{ProbNN}(\mu) > 0.9$  for both  $J/\psi$  and  $\psi(2S)$ . This is a strict but appropriate PID cut since it can significantly reduce the background of high-multiplicity  $\psi(2S)$  data sample. And for low-multiplicity region, it doesn't remove many of the signals. We can therefore achieve relatively low statistical uncertainties when fitting the invariant mass spectrum and pseudo decay time spectrum, since the dominant uncertainties are statistical uncertainties of  $\psi(2S)$  which will be discussed later. The mass spectrum for  $\psi(2S)$  after the harsh PID cut is shown in Fig 4.4. In addition, for both  $J/\psi$  and  $\psi(2S)$ ,

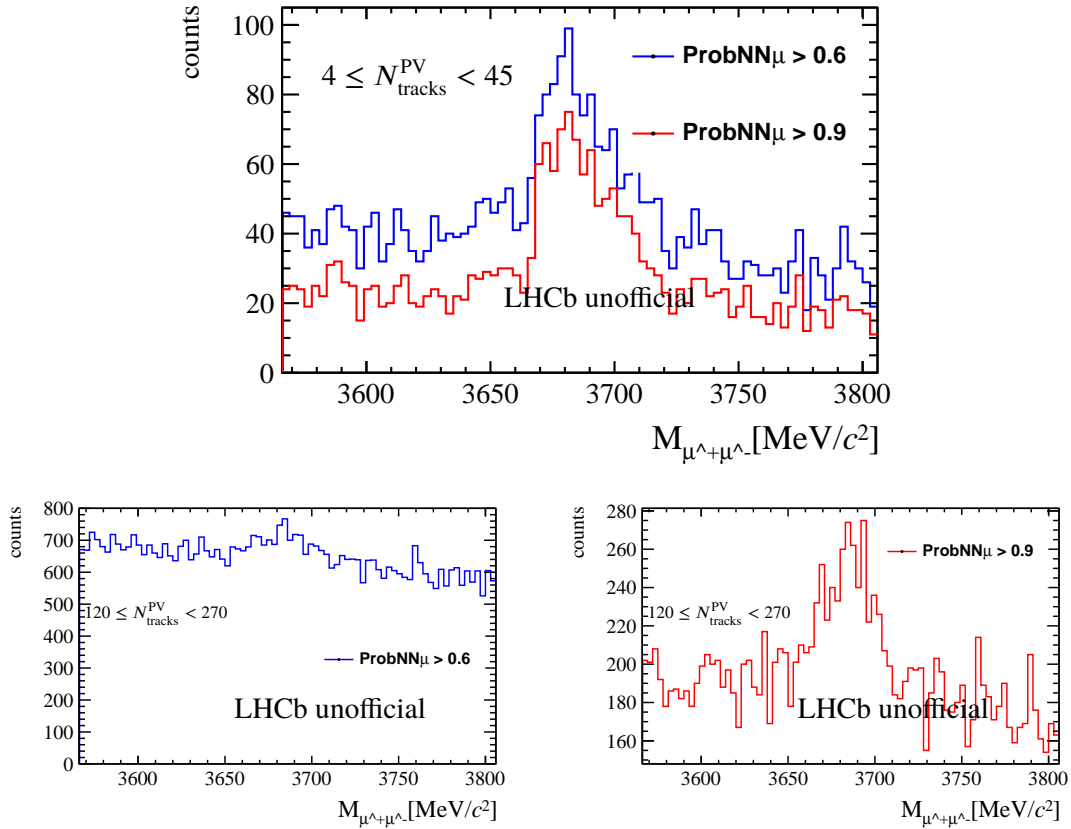


Figure 4.4 Mass spectrum of  $\psi(2S)$  after online and offline cuts with loose PID cut (blue) and tight PID cut (red). The first row is for lowest-multiplicity class and the second row is for highest-multiplicity class.

the two muons are required to form a good vertex with the vertex fit probability  $\text{Prob}(\chi^2) > 0.5\%$ . The  $\psi(2S)$  and  $J/\psi$  candidates are required to have a mass within  $120 \text{ MeV}/c^2$  of the PDG value. All online and offline selection criteria are listed in Table 4.3.

Table 4.3 Offline selections for  $J/\psi$  and  $\psi(2S)$ .

Online cuts	Variable	Offline cuts
	$\mu^\pm\eta$	$2 < \eta < 5$
(Hlt1) $> 500 \text{ MeV}/c$	$\mu^\pm p_T$	$> 900 \text{ MeV}/c$
	ProbNNmu	$> 0.9$
	TrackGhost Prob.	$< 0.4$
(Hlt1) $\chi^2 < 25$	Vertex $\chi^2$	Probability $> 0.5\%$
(L0) $< 4$	Track $\chi^2/n_{dof}$	$< 3$
(Hlt1) $150 \text{ MeV}/c^2$	mass window	$\pm 120 \text{ MeV}/c^2$
(L0) $< 8000$	nVeloCulster	

## 4.4 Signal extraction

The signal extraction for  $J/\psi$  and  $\psi(2S)$  following the strategy described in Section 3.4. Due to the limited sample size for  $\psi(2S)$ , the signal in mass spectrum is described by a single Crystal Ball function. An example of two-dimensional fit projected on invariant mass and  $t_z$  is shown in Fig 4.5.

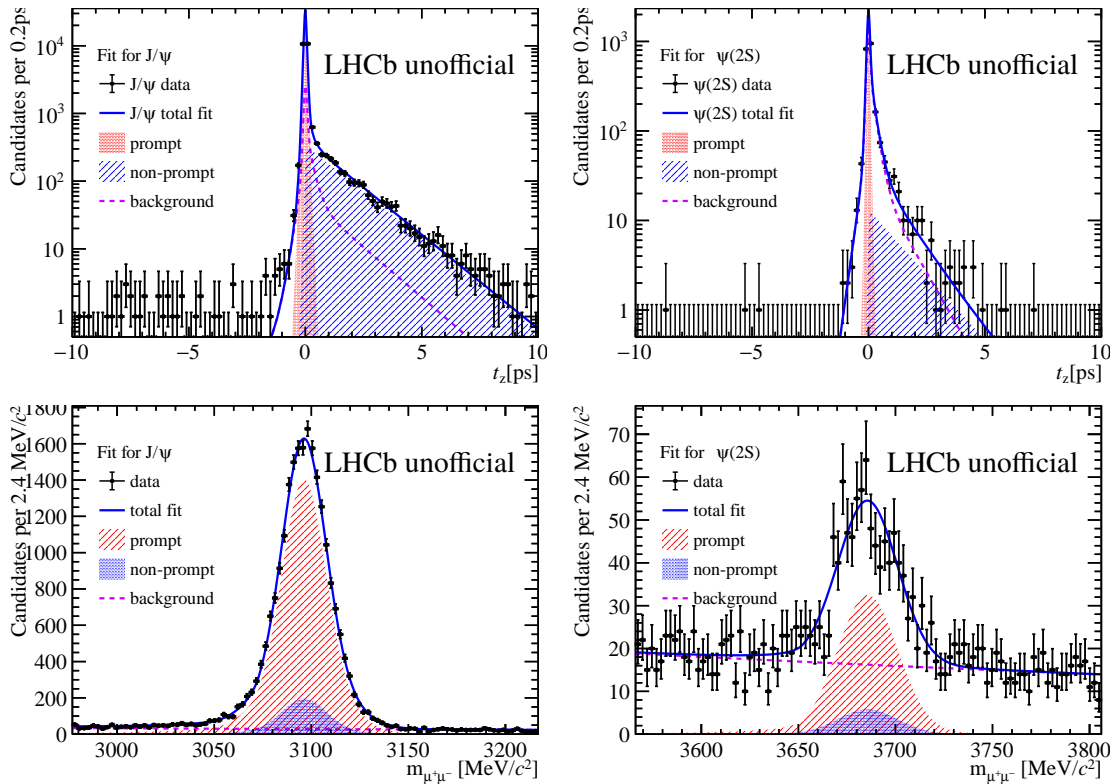


Figure 4.5 Two-dimensional fit projected on (top)  $t_z$  spectrum and (bottom) mass spectrum for (left)  $J/\psi$  and (right)  $\psi(2S)$  (right) for  $4 \leq N_{\text{tracks}}^{\text{PV}} < 45$  in  $p$ Pb configuration.

The yield for prompt and non-prompt charmonia as function of  $N_{\text{tracks}}^{\text{PV}}$  in  $p$ Pb collisions is shown in Fig 4.6.

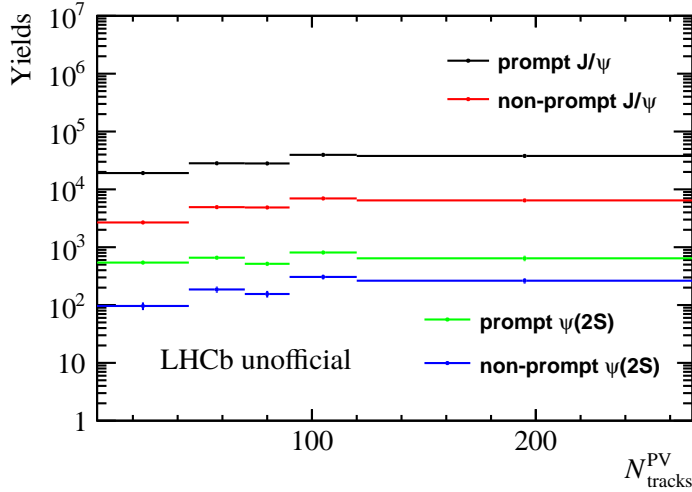


Figure 4.6 Prompt and non-prompt yields for  $J/\psi$  and  $\psi(2S)$  in  $p$ Pb collisions.

## 4.5 Efficiency ratio determination

The efficiencies are assumed to be equal for prompt and non-prompt signals based on the previous study in Chapter 3. The total efficiency is the product of the acceptance efficiency ( $\epsilon_{acc}$ ), the reconstruction and selection efficiency ( $\epsilon_{Reco\&Sel}$ ), the particle identification efficiency ( $\epsilon_{MuonID}$ ), the trigger efficiency ( $\epsilon_{Trigger}$ ). The acceptance efficiency is calculated for all multiplicity classes. The others are calculated in each multiplicity class. The efficiency ratio is calculated in each multiplicity class, which is defined as

$$\begin{aligned} R_{tot} &= \frac{\epsilon_{tot,J/\psi}}{\epsilon_{tot,\psi(2S)}} \Big|_{Mult. bin} \\ &= \frac{\epsilon_{acc,J/\psi}}{\epsilon_{acc,\psi(2S)}} \times \frac{\epsilon_{Reco\&Sel,J/\psi} \cdot \epsilon_{MuonID,J/\psi} \cdot \epsilon_{Trigger,J/\psi}}{\epsilon_{Reco\&Sel,\psi(2S)} \cdot \epsilon_{MuonID,\psi(2S)} \cdot \epsilon_{Trigger,\psi(2S)}} \Big|_{Mult. bin} \\ &= R_{acc} \times R_{eff} \Big|_{Mult. bin}, \end{aligned} \quad (4.3)$$

where  $R_{acc}$  is the ratio of acceptance efficiencies of  $J/\psi$  to  $\psi(2S)$  and  $R_{eff}$  is the ratio of the rest efficiencies of  $J/\psi$  and  $\psi(2S)$ . All steps are determined from simulation, with truth matched signal decays, except for the tracking efficiency and the particle identification, where data driven methods are used to correct the efficiencies obtained from the simulation or to obtain the single track PID efficiency. Their exact definitions are given in the following subsections. In the simulation,  $J/\psi$  and  $\psi(2S)$  mesons are assumed to be produced without polarization. For the simulation samples used for this analysis, the truth matching efficiency is equal to  $99.5 \pm 0.1\%$  for both  $p$ Pb and  $Pb$ p samples. It is assumed to be independent of  $p_T$  and  $y^*$ .

### 4.5.1 Re-weight on Monte Carlo sample

The distribution of  $N_{\text{tracks}}^{\text{PV}}$ ,  $N_{\text{fwd}}^{\text{PV}}$  and  $N_{\text{bwd}}^{\text{PV}}$  of Monte Carlo and s-weighted data for both  $J/\psi$  and  $\psi(2S)$  in  $p\text{Pb}$  and  $\text{Pb}p$  configurations are compared. As an example, we draw the distributions for Monte Carlo and s-weighted data in  $p\text{Pb}$  configuration in Figure 4.7. We can see that the multiplicity distribution for  $J/\psi$  and  $\psi(2S)$  signal events are compatible within uncertainties in both Monte Carlo sample and s-weighted data. Since only the ratio of total efficiencies is calculated in bins of multiplicity, the bias caused by the difference in multiplicity should be canceled, based on which the MC multiplicities are not weighted.

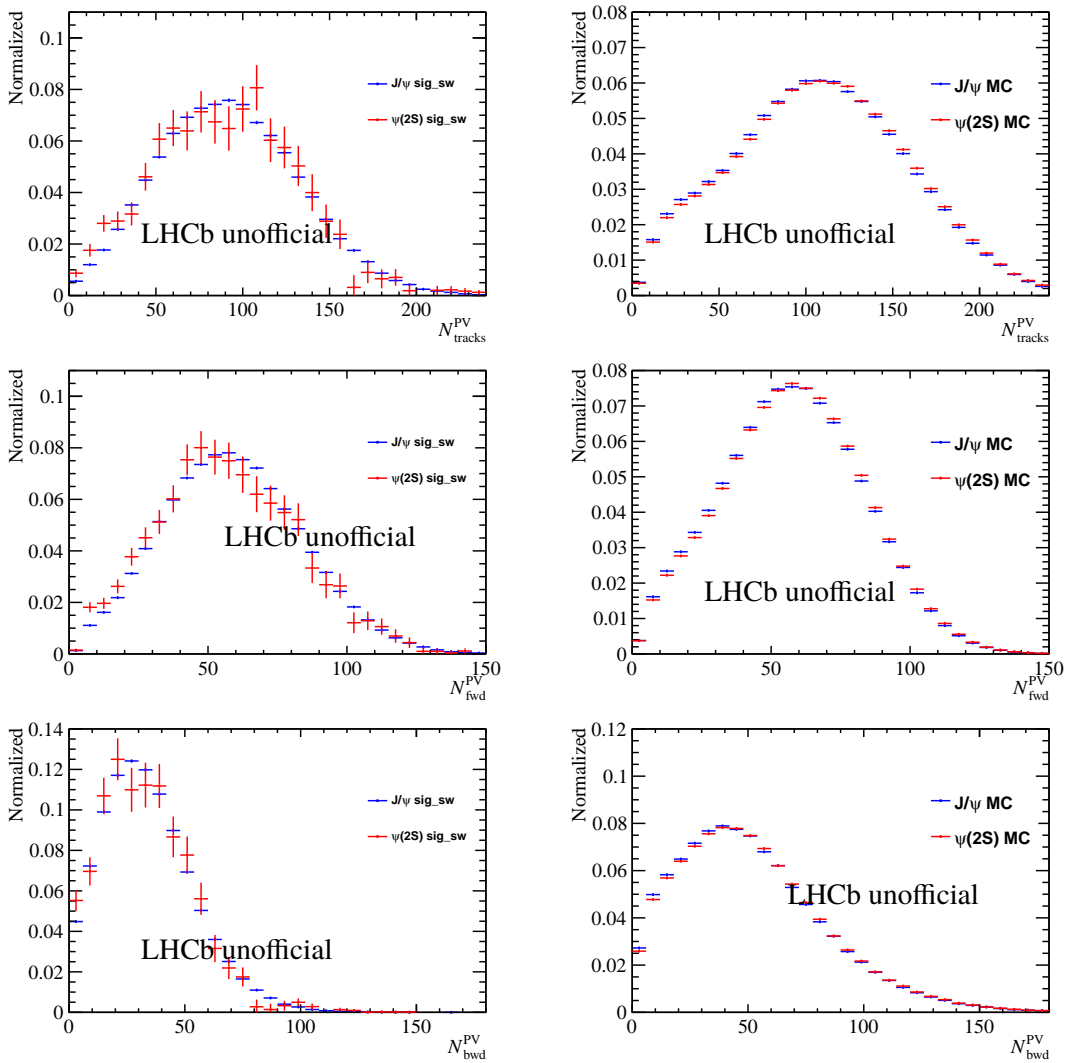


Figure 4.7 Distribution of multiplicity variables for s-weighted (left column) data and (right column) MC samples in  $p\text{Pb}$  configuration.

However, the difference between data and MC on  $p_T$  and  $y^*$  distribution is not negli-

gible in calculating the efficiencies. So two samples of high- and low-multiplicity classes are considered when re-weighting Monte Carlo sample to match s-weight data (the high- and low-multiplicity samples are separated by the mean values of multiplicity variables we choose accordingly). As an example, the re-weight of  $p_T$  and  $y^*$  for high- and low-multiplicity  $J/\psi$  MC samples when taking  $N_{\text{tracks}}^{\text{PV}}$  as multiplicity variable is shown in Figure 4.8. And those for  $\psi(2S)$  MC samples are shown in Figure 4.9.

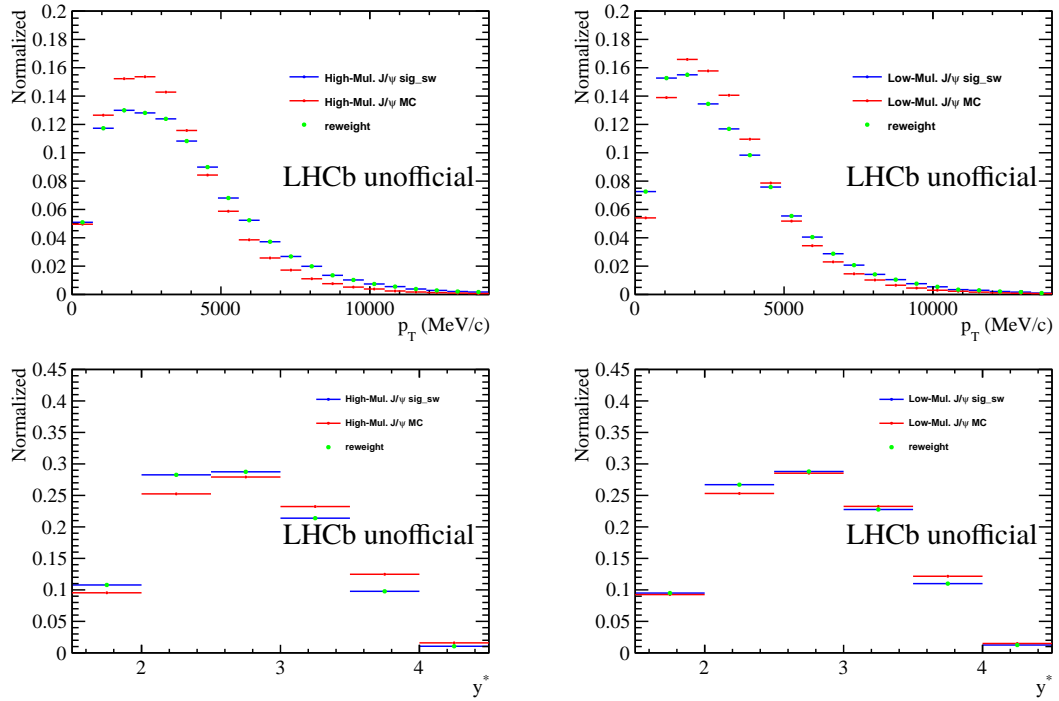


Figure 4.8 Re-weight of (top)  $p_T$  and (bottom)  $y^*$  for (left) high- (left) and low- $N_{\text{tracks}}^{\text{PV}}$  for  $J/\psi$  MC samples in  $p$ Pb configuration.

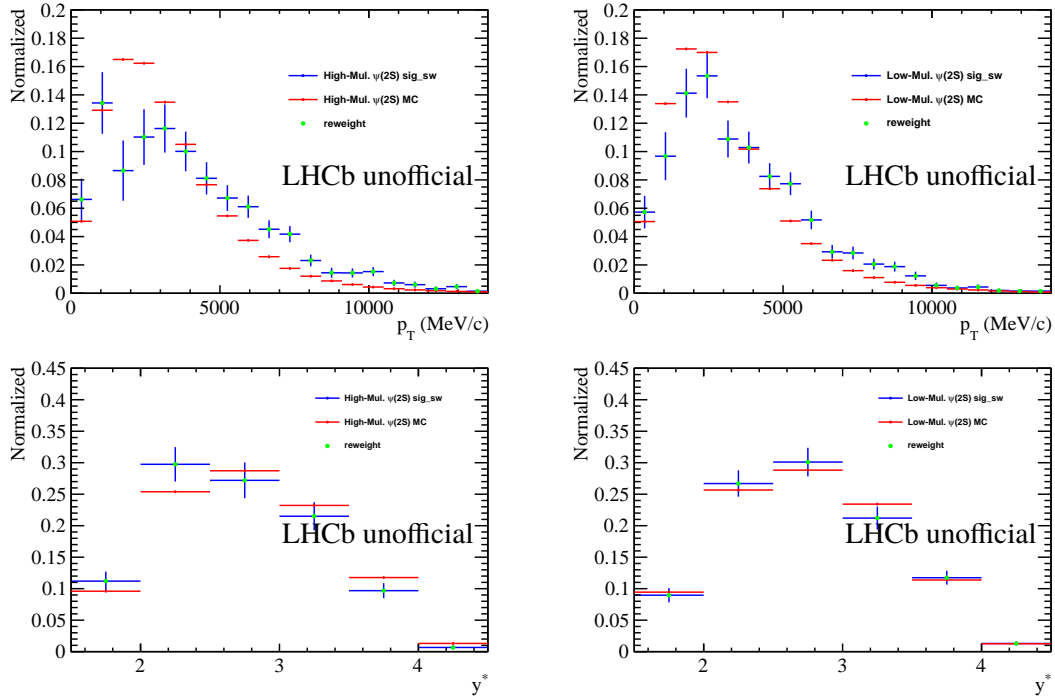


Figure 4.9 Re-weight of (top)  $p_T$  and (bottom)  $y^*$  for (left) high- (left) and low- $N_{\text{tracks}}^{\text{PV}}$  for  $\psi(2S)$  MC samples in  $p\text{Pb}$  configuration.

### 4.5.2 Acceptance

The acceptance efficiency is defined in Section 3.5. It is estimated from generator-level only simulations, using the settings described in Section 4.1.

In this analysis we only care about the ratio of acceptance efficiencies  $R_{\text{acc}}$ . Since the acceptance efficiencies depends on  $p_T$ - $y^*$  spectrum and the reweight in  $\psi(2S)$  samples has significant uncertainty due to limited sample size. When calculating the ratio of acceptance efficiencies, 50 random re-weight tables of  $p_T$  and  $y^*$  from high- and low-multiplicity samples are generated (100 in total) for both  $J/\psi$  and  $\psi(2S)$ , within each bin a Gaussian random number is generated with mean the content and sigma the uncertainty. Then the 100 tables are introduced as correction to acceptance efficiencies. Then 100 ratios of acceptance efficiencies are calculated. Fit these 100  $R_{\text{acc}}$  values with a Gaussian function we get the mean value as the ratio of acceptance efficiencies and the sigma be its systematic uncertainty. As an example, the fit result for  $R_{\text{acc}}$  when global cuts for  $N_{\text{tracks}}^{\text{PV}}$  as multiplicity are applied is shown in Figure 4.10. The value is as follows,

$$R_{\text{acc}} = \frac{\epsilon_{\text{acc}, J/\psi}}{\epsilon_{\text{acc}, \psi(2S)}} = 0.991 \pm 0.012. \quad (4.4)$$

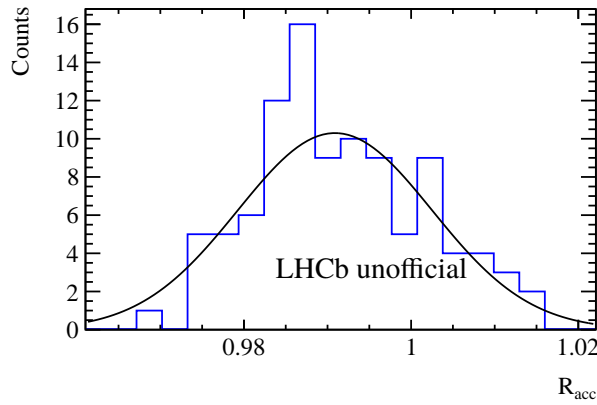


Figure 4.10 The distribution of  $\psi(2S)$  to  $J/\psi$  acceptance efficiency ratio,  $R_c c$ , from 100 trials of reweighting tables with  $N_{\text{tracks}}^{\text{PV}}$  as multiplicity variables.

### 4.5.3 Other efficiencies

The reconstruction and selection efficiency is defined Section 3.5. The reconstruction efficiency is further corrected using the data-over-simulation single tracking efficiency ratio. The ratio of tracking efficiencies for a single track in data and simulation determined with the Long Tag-Probe method is shown in Figure 4.11 which was given by the tracking group. For a given event the correction factor is determined by multiplying the efficiency ratios for each of the tracks in the final state.

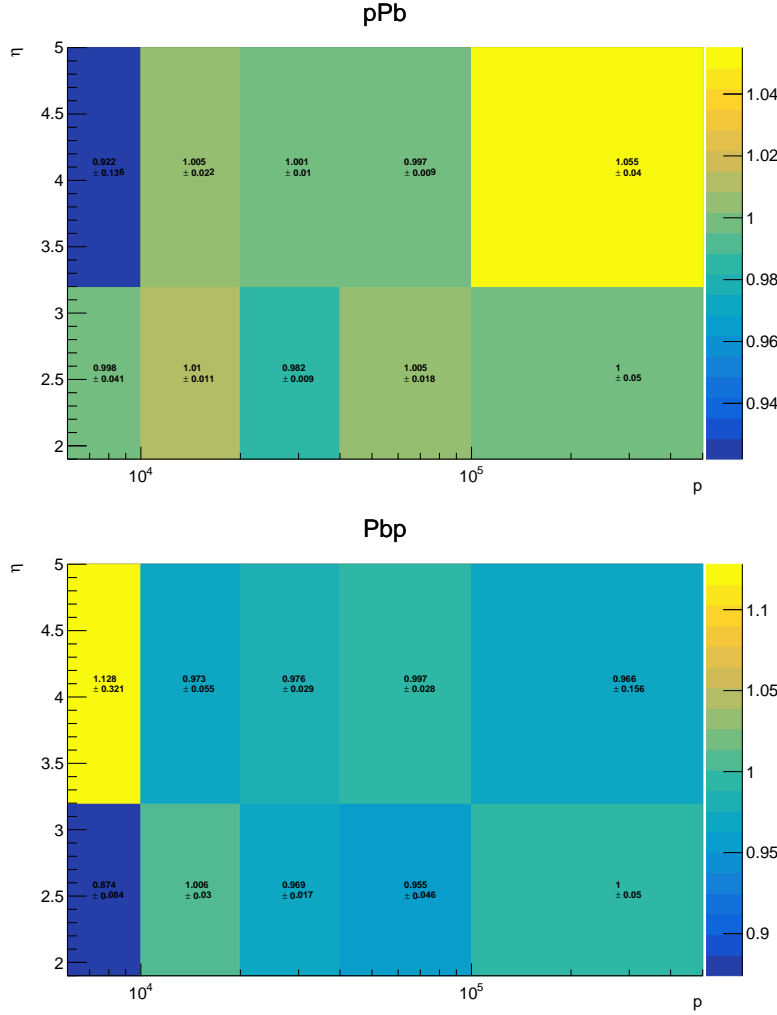


Figure 4.11 Ratio between data and  $p\text{Pb}$  (left) and  $\text{Pbpb}$  simulation of per-track tracking efficiency in bins of the track  $\eta$  and  $p$ .

From Eq. 4.3 we can see that, we calculate the ratio of all the efficiencies  $R_{eff}$  (except for acceptance efficiencies) as a whole part, since they are all calculated with full-simulation Monte Carlo sample. When calculating  $\epsilon_{\text{Reco\&Sel}}$ ,  $\epsilon_{\text{MuonID}}$  and  $\epsilon_{\text{Trigger}}$ , 500 random tables of  $p_T$  and  $y^*$  from high- and low-multiplicity samples are generated (1000 in total) for both  $J/\psi$  and  $\psi(2S)$  in  $p\text{Pb}$  and  $\text{Pbpb}$  configurations and introduced to correct the imperfection on simulation to data. For a certain trial, the re-weight on  $p_T$  (or  $y^*$ ) may under- or over-estimate  $\epsilon_{\text{Reco\&Sel}}$ ,  $\epsilon_{\text{MuonID}}$  and  $\epsilon_{\text{Trigger}}$  simultaneously, it is hard to determine the dependence between these efficiencies. So a good way is to calculate them as a whole, each time a certain random re-weight table is introduced. The definition of  $R_{eff}$  is in Eq. 4.5.

$$R_{eff} \Big|_{Mult. bin} = \frac{\epsilon_{\text{Reco\&Sel}, J/\psi} \cdot \epsilon_{\text{MuonID}, J/\psi} \cdot \epsilon_{\text{Trigger}, J/\psi}}{\epsilon_{\text{Reco\&Sel}, \psi(2S)} \cdot \epsilon_{\text{MuonID}, \psi(2S)} \cdot \epsilon_{\text{Trigger}, \psi(2S)}} \Big|_{Mult. bin}. \quad (4.5)$$

Similarly, 1000 random tables for data-over-simulation single tracking efficiency ratio are generated and introduced into the 1000 trials, and 1000 random tables for efficiency table obtained from PIDCalib package are introduced in each trial as well to calculate PID efficiencies, so as the trigger efficiency. Finally, an estimation on the total efficiency ratio  $R_{eff}$  is given by the mean value of 1000 trials and the standard deviation is treated as a source of systematic uncertainty.

#### 4.5.4 Total efficiency

The 1000 ratios of all the efficiencies except geometric acceptance  $R_{eff}$ 's are fitted with a Gaussian function. Hence, we can calculate the ratio of total efficiencies  $R_{tot} = R_{acc} \times R_{eff}$  with systematic uncertainties arised from,

- re-weight of  $p_T$  distribution from high- and low-multiplicity samples,
- re-weight of  $y^*$  distribution from high- and low-multiplicity samples,
- uncertainties due to the limit calibration sample size in PIDCalib efficiency table,
- uncertainties of data-over-simulation ratio of per tracking efficiency.

As an example, the fit results for  $R_{eff}$  in different  $N_{\text{tracks}}^{\text{PV}}$  classes for  $p\text{Pb}$  configuration are shown in Figure 4.12. The corresponding values of  $R_{eff}$  with uncertainties mentioned above are summarized in Table 4.4. Summary tables for other multiplicity variables and configurations can be found in appendix 5.2.

Table 4.4  $R_{eff}$  in different  $N_{\text{tracks}}^{\text{PV}}$  regions in  $p\text{Pb}$  configuration.

$4 \leq N_{\text{tracks}}^{\text{PV}} < 45$	$0.810 \pm 0.021$
$45 \leq N_{\text{tracks}}^{\text{PV}} < 70$	$0.811 \pm 0.020$
$70 \leq N_{\text{tracks}}^{\text{PV}} < 90$	$0.813 \pm 0.021$
$90 \leq N_{\text{tracks}}^{\text{PV}} < 120$	$0.803 \pm 0.021$
$120 \leq N_{\text{tracks}}^{\text{PV}} < 270$	$0.791 \pm 0.021$

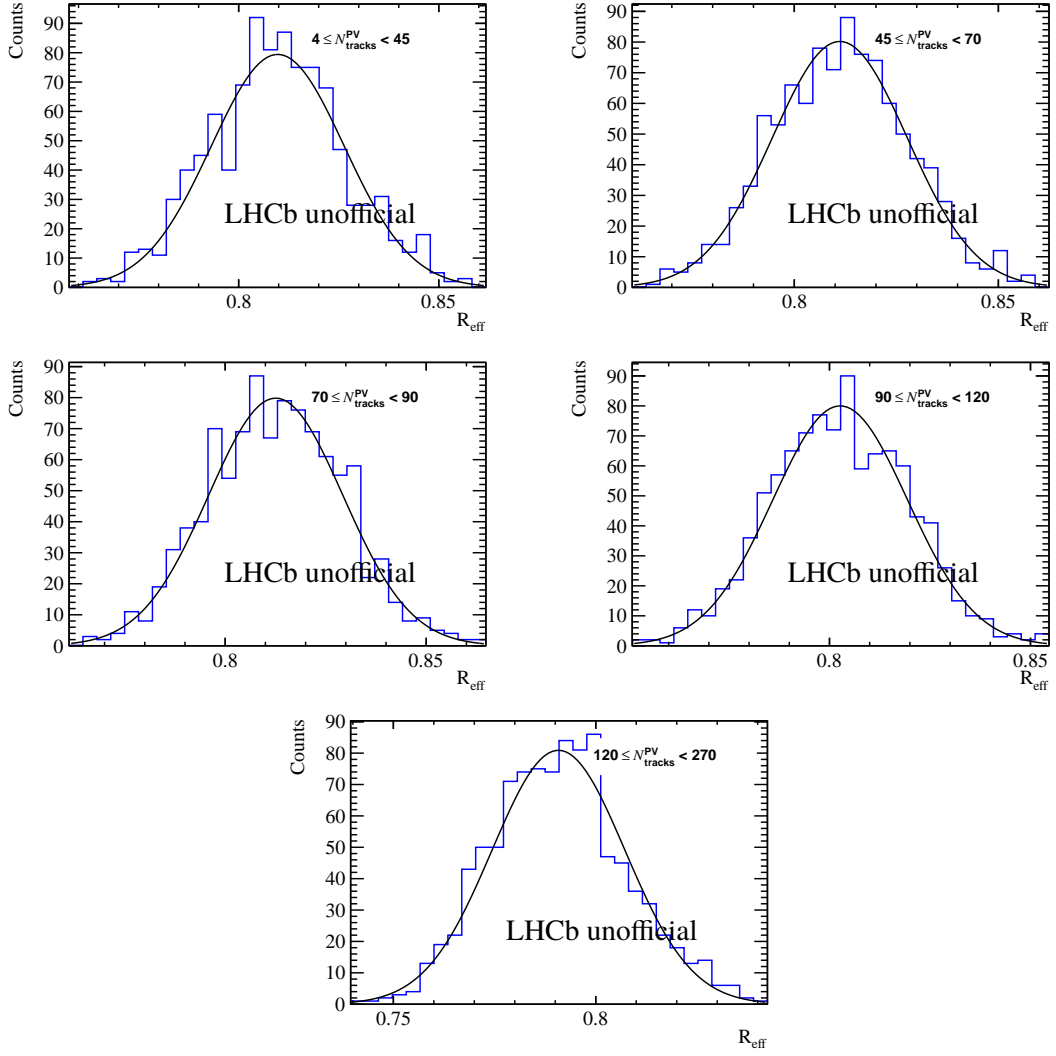


Figure 4.12 Fit Gaussian functions on the distributions of 1000-trial  $R_{\text{eff}}$ 's in different  $N^{\text{PV}}_{\text{tracks}}$  classes.

## 4.6 Systematic uncertainties

Before we proceed this section, let us mention the systematic uncertainties in previous sections,

- re-weight of  $p_T$  distribution from high- and low-multiplicity samples (for ratios of  $\epsilon_{\text{acc}}$  and the other efficiencies),
- re-weight of  $y^*$  distribution from high- and low-multiplicity samples (for ratios of  $\epsilon_{\text{acc}}$  and the other efficiencies),
- uncertainties due to the limit calibration sample size in PIDCalib efficiency table (for ratios of efficiencies except  $\epsilon_{\text{acc}}$ ),
- uncertainties of data-over-simulation ratio of per tracking efficiency (for ratios of efficiencies except  $\epsilon_{\text{acc}}$ ),
- global cut of nVeloClusters < 8000 (negligible),
- uncertainty of luminosity is canceled when calculating the ratio of  $\psi(2S)$ -to- $J/\psi$  production,
- relative uncertainty due to branching fraction is calculated to be 2.2%, this term is not considered when calculating the normalized ratio as function of multiplicity, but when we compare ratio in forward and backward regions, we do not normalize the ratio, hence, need to consider it in this case.

Other systematic uncertainties are reported in this section.

### 4.6.1 Monte Carlo statistics

This uncertainty is the statistical error on the ratio of efficiencies in different multiplicity bins, due to the finite size of the simulation samples. The uncertainty varies from 0.02% to 0.2% across all multiplicity classes categorized by three multiplicity variables and in  $p\text{Pb}$  and  $\text{Pb}p$  configurations, which is negligible compared to other systematic uncertainties.

### 4.6.2 Signal extraction

The choice of the fit model for the mass and  $t_z$  distributions affects the number of signal. The uncertainty associated with the choice of the signal model is estimated using an alternative two CB functions for  $\psi(2S)$ . The CB functions have common mean, and the width of wider CB function is determined by  $\sigma_2 = \sigma_1 + 25.7$ , and the ratio of the narrower one is fixed to 0.96 in accordance with the study in 13 TeV  $pp$  collisions<sup>[65]</sup>. With this

new fit model for  $\psi(2S)$  mass spectrum, a new two-dimensional fit for mass and  $t_z$  is performed. The difference in ratio of  $\psi(2S)$ -to- $J/\psi$  ratio and the statistical uncertainty in each  $N_{\text{tracks}}^{\text{PV}}$  bin are shown in Figure 4.13.

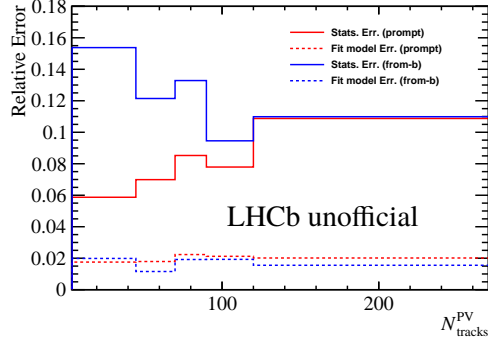


Figure 4.13 The statistical uncertainties and the systematic uncertainty of  $\psi(2S)$ -to- $J/\psi$  ratio arised from different signal models.

The variation caused by different fit model is much smaller than the statistical uncertainties. Fig 4.13 shows the later is larger than the uncertainty caused by fit model by at least a factor of 3. Similarly, by changing the  $t_z$  background model from mass-sideband sample to s-weighted sample of background, the induced variation is still much smaller than the statistical uncertainty across all multiplicity bins. Together with the  $t_z$  signal shape study conducted in  $pp$  collisions in Chapter 3, where the variation caused by  $t_z$  signal model is also much smaller than statistical uncertainty, we can completely treat the difference caused by fit model as statistical fluctuation, hence, negligible.

### 4.6.3 Trigger efficiency

The trigger efficiency in simulation is cross-checked with data, and the resulting difference in the ratio of  $e_{\text{Trigger}}$  between simulation and data is quoted as a systematic uncertainty as stated in Section 3.6. Due to the different global cuts under different multiplicity schemes and configurations, TISTOS method is carried out in each case and the result is summarized in Table 4.5.

Table 4.5 Systematic uncertainty of  $\epsilon_{\text{Trigger}}$  obtained by TISTOS method.

Configuration	Mult. Variable	Variation	Stats. Err.	Syst. Err. quoted
$p$ Pb	$N_{\text{tracks}}^{\text{PV}}$	2.7%	3.9%	3.9%
$p$ Pb	$N_{\text{fwd}}^{\text{PV}}$	3.2%	3.0%	3.2%
$p$ Pb	$N_{\text{bwd}}^{\text{PV}}$	2.7%	3.9%	3.9%
Pbp	$N_{\text{tracks}}^{\text{PV}}$	2.0%	3.8%	3.8%
Pbp	$N_{\text{fwd}}^{\text{PV}}$	1.7%	3.6%	3.6%
Pbp	$N_{\text{bwd}}^{\text{PV}}$	2.7%	4.1%	4.1%

#### 4.6.4 Binning scheme of PID table

Uncertainty due to binning scheme of the calibration sample, studied by varying the binning method in  $p_\mu$ ,  $\eta_\mu$ , and nSPDHits respectively. The default one and the two alternative binning schemes could be found below. The nominal binning scheme of the muon ID efficiency for muons we use to calculate the muon ID efficiency of  $J/\psi$  and  $\psi(2S)$  mesons is defined:

- $p_\mu$  boundaries [ GeV/c ]: 3, 10, 20, 25, 30, 35, 40, 45, 50, 60, 70, 80, 100, 1000.
- $\eta$  boundaries: 2.0, 2.5, 3.0, 3.5, 4.0, 4.5, 5.0.
- nSPDHits boundaries: 0, 300, 500, 700, 1400.

One of the two alternative binning schemes is defined as:

- $p_\mu$  boundaries [ GeV/c ]: 3, 12.5, 22.5, 27.5, 32.5, 37.5, 42.5, 47.5, 55, 65, 75, 85, 100, 1000.
- $\eta$  boundaries: 2.0, 2.6, 2.9, 3.6, 3.9, 4.5, 5.0.
- nSPDHits boundaries: 0, 250, 450, 650, 1400.

The other alternative binning scheme is defined as:

- $p_\mu$  boundaries [ GeV/c ]: 3, 9, 19, 24, 29, 34, 39, 44, 49, 59, 69, 79, 100, 1000.
- $\eta$  boundaries: 2.0, 2.4, 3.1, 3.4, 3.9, 4.5, 5.0.
- nSPDHits boundaries: 0, 320, 480, 720, 1400.

The maximum difference between the resulting two new ratios and the nominal one is quoted as the systematic uncertainty. The uncertainties are from 0.1% to 1.8% across different multiplicity bins and configurations.

#### 4.6.5 Summary of systematic uncertainties

All the systematic uncertainties are summarized in Table 4.6.

Table 4.6 Summary of systematic uncertainties on  $\psi(2S)$ -to- $J/\psi$  cross-section ratio. Sources marked with  $\dagger$  are considered to be correlated.

source	$p\text{Pb}$	$\text{Pb}p$
L0&HLT	3.2%-3.9%	3.6%-4.1%
Tracking table uncertainty&		
PID table uncertainty&		
$p_T$ &		
$y$ spectrum reweighting	1.7%-3.6%	2.1%-3.6%
PID table scheme	0.4%-1.7%	0.1%-1.8%
acceptance efficiency		
due to $p_T$ , $y^*$ reweighting	0.8%-1.2%	0.9%-1.3%
$\frac{\mathcal{B}(J/\psi \rightarrow \mu^+ \mu^-)}{\mathcal{B}(\psi(2S) \rightarrow \mu^+ \mu^-)}$ (canceled if normalized)	2.2%	2.2%
Fit model	negligible	negligible
MC sample size	negligible	negligible
Global event cut	negligible	negligible

All the systematic uncertainties listed in Table 4.6 and separated with horizontal lines are uncorrelated. Since the correlated uncertainties marked with  $\dagger$  are studied together through pseudo-experiments.

## 4.7 Results

### 4.7.1 Multiplicity dependence of production ratio

With the signal yields determined from the fitting to dimuon invariant mass distributions and  $t_z$  fit, the efficiency ratios estimated from simulation and calibrated control samples, the ratio of  $\psi(2S)$  and  $J/\psi$  production cross-sections are measured as a function of different multiplicity variables. As mentioned in Section 4.5, the multiplicity distribution of  $J/\psi$  and  $\psi(2S)$  can be treated as the same, and due to the large uncertainty of  $\psi(2S)$  multiplicity distribution, the multiplicity value used in this analysis is directly the average value of  $J/\psi$  multiplicity distribution in each bin, normalized by the mean value of multiplicity of no-bias data. The normalized  $\psi(2S)$ -to- $J/\psi$  ratios for prompt and non-prompt components as a function of  $N_{\text{tracks}}^{\text{PV}}$  in  $p\text{Pb}$  and  $\text{Pb}p$  collisions is shown in Figure 4.14. The box represents systematic uncertainty and the error bar represents the statistical uncertainty. In this analysis statistical uncertainty dominates.

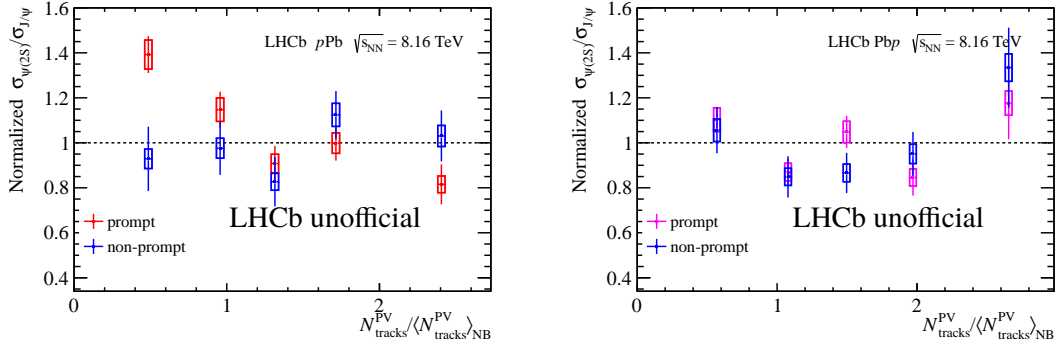


Figure 4.14 Normalized  $\psi(2S)$ -to- $J/\psi$  ratio as function of normalized  $N_{\text{tracks}}^{\text{PV}}$  in (left)  $p\text{Pb}$  (right)  $\text{PbP}$  collisions.

One can conclude that in  $p\text{Pb}$  collisions the prompt ratio decreases with increasing  $N_{\text{tracks}}^{\text{PV}}$ , while in  $\text{PbP}$  collisions, no any significant trend with  $N_{\text{tracks}}^{\text{PV}}$  is observed. For non-prompt  $J/\psi$  and  $\psi(2S)$  no dependence between the ratio and multiplicity in both  $p\text{Pb}$  and  $\text{PbP}$  collisions regardless of the choice of multiplicity variables. If we compare the prompt ratio (not normalized), we should include the uncertainties in branching fraction and the comparison is shown in Fig 4.15.

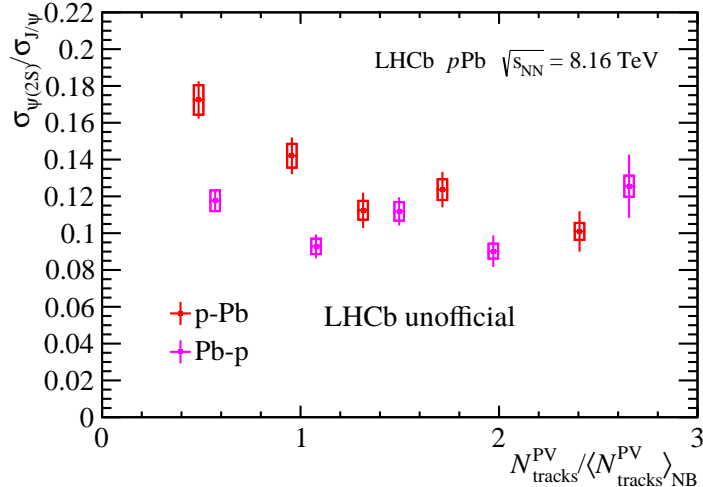


Figure 4.15  $\psi(2S)$ -to- $J/\psi$  ratio as function of normalized  $N_{\text{tracks}}^{\text{PV}}$ .

We find the ratio in  $\text{PbP}$  is generally lower than that in  $p\text{Pb}$  collisions. This could results from the higher charged particle multiplicity in  $\text{PbP}$  collisions, where  $\psi(2S)$ , with lower binding energy, is easier to dissociate when interacting with higher amount of co-moving particles. If this is valid, one should also expect a decreasing trend of the ratio with the increasing multiplicity, but it is not significant here. We further measure the normalized ratio and direct ratio as a functions of  $N_{\text{fwd}}^{\text{PV}}$ , as shown in Figure 4.16. The results are similar to those with  $N_{\text{tracks}}^{\text{PV}}$  as multiplicity. The ratio of non-prompt signals is

roughly constant with multiplicity in  $p\text{Pb}$  and  $\text{Pb}p$  collisions. And ratio of prompt signals decreases with increasing  $N_{\text{fwd}}^{\text{PV}}$  in  $p\text{Pb}$ , but not in  $\text{Pb}p$  collisions. If we compare the ratio in  $p\text{Pb}$  and  $\text{Pb}p$  collisions, the ratios in  $\text{Pb}p$  collisions are generally lower than that in  $p\text{Pb}$  collisions, as shown in Fig 4.17. But still, we do not observe a decreasing trend like in  $p\text{Pb}$  collisions. Some extra mechanisms might be needed to explain the phenomenon. Since for both  $N_{\text{tracks}}^{\text{PV}}$  and  $N_{\text{fwd}}^{\text{PV}}$  as multiplicity variables, we get the similar conclusions.

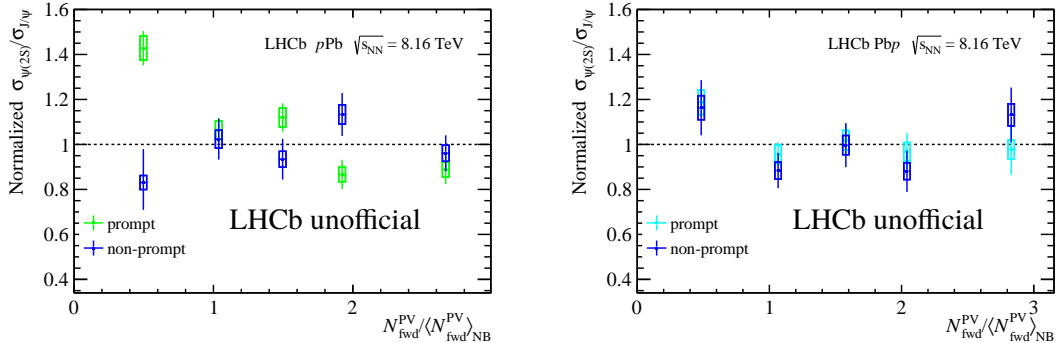


Figure 4.16 Normalized  $\psi(2S)$ -to- $J/\psi$  ratio as function of normalized  $N_{\text{fwd}}^{\text{PV}}$  in (left)  $p\text{Pb}$  (right)  $\text{Pb}p$  collisions.

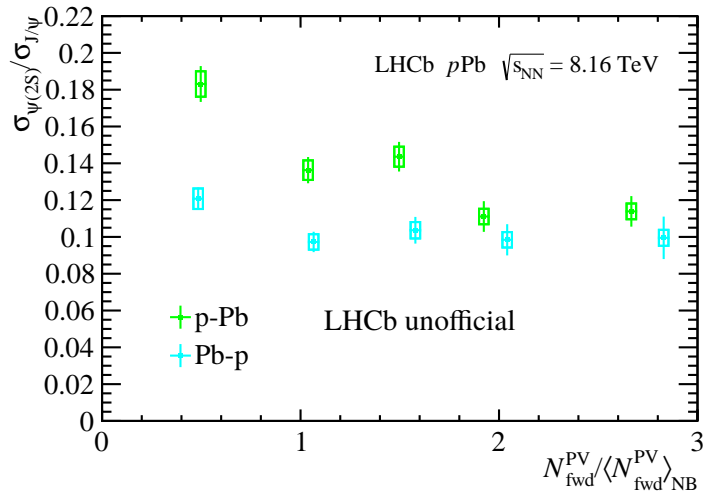


Figure 4.17 The  $\psi(2S)$ -to- $J/\psi$  ratio as function of normalized  $N_{\text{fwd}}^{\text{PV}}$  in  $p\text{Pb}$  and  $\text{Pb}p$  collisions.

When multiplicity is measured by  $N_{\text{bwd}}^{\text{PV}}$ , as shown in Figure 4.18, for ratio of prompt signals, the decreasing trend is much slower with increasing  $N_{\text{bwd}}^{\text{PV}}$  in  $p\text{Pb}$  collisions, and for  $\text{Pb}p$ , the ratio for both prompt and non-prompt signals are roughly constant. Since  $N_{\text{bwd}}^{\text{PV}}$  are measured in backward direction, the rapidity range is non-overlapping with where we measure the charmonia production, and co-mover effect is thought to not exist. Additionally, if QGP is not produced, the ratio should keep constant with  $N_{\text{bwd}}^{\text{PV}}$ . The sub-

tle decreasing trend for ratio of prompt signals could result from the correlation between  $N_{\text{bwd}}^{\text{PV}}$  and  $N_{\text{fwd}}^{\text{PV}}$  in  $p\text{Pb}$  collisions as we observed in  $pp$  collisions. Similarly, there is an overall reduction on the ratio in  $\text{Pbp}$  collisions compared to the ratio in  $p\text{Pb}$  collisions, as shown in Fig 4.19, which results in an overall larger amount of co-moving particles. But still, in  $\text{Pbp}$  collisions, no dependence was found between ratio and  $N_{\text{bwd}}^{\text{PV}}$ .

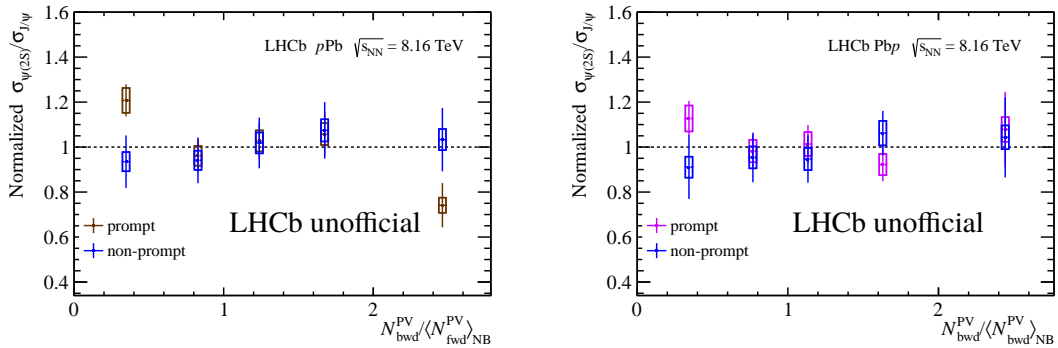


Figure 4.18 Normalized  $\psi(2S)$ -to- $J/\psi$  ratio as function of normalized  $N_{\text{bwd}}^{\text{PV}}$  in (left)  $p\text{Pb}$  and (right)  $\text{Pbp}$  collisions.

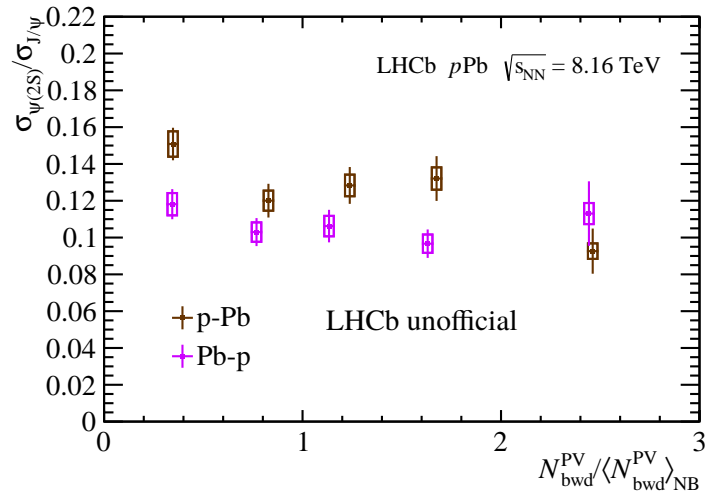


Figure 4.19 The  $\psi(2S)$ -to- $J/\psi$  ratio as function of normalized  $N_{\text{bwd}}^{\text{PV}}$  in  $p\text{Pb}$  and  $\text{Pbp}$  collisions.

### 4.7.2 Comparison in different collision systems

The multiplicity dependence of  $\psi(2S)$  to  $J/\psi$  ratio in different collision systems is compared as shown in Fig 4.20. Since restriction has been made on  $z_{PV}$  ranges across different collision systems, only ratio as function of  $N_{\text{fwd}}^{\text{PV}}$  is compared, under which multiplicity scheme, less than 0.1% of data is removed for different collision systems. Other global cuts including number of PV reconstructed is restricted to be exact one, is universal across different systems. Global cut on nVeloClusters, number of hits recorded in Velo,

is a multiplicity global cut, hence, remains different.

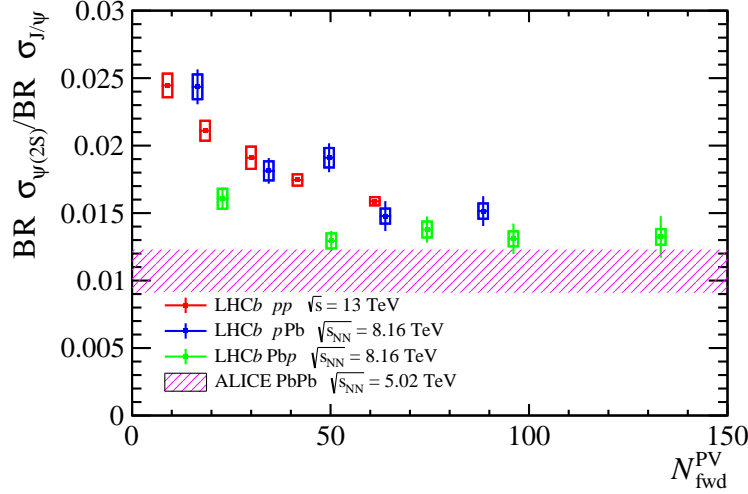


Figure 4.20 Comparisons on the ratio of  $\psi(2S)/J/\psi$  in  $pp$ ,  $p$ Pb ( $P\text{bp}$ ) and  $\text{PbPb}$  collisions<sup>[178]</sup>.

The multiplicity dependence in  $p$ Pb collisions is consistent with that in  $pp$  collisions. It is within expectation since both are measured in the  $p$  going direction, suggesting a similar environment. However, in  $P\text{bp}$  collisions, where the charmonia and multiplicity are measured in the Pb-going direction, a higher particle density will be achieved<sup>[179]</sup>, resulting in an environment closer to  $\text{PbPb}$  collisions. Therefore, a slower decreasing trend is observed in  $P\text{bp}$  collisions, which is very close to the results in  $\text{PbPb}$  collisions measured by ALICE<sup>[178]</sup>, where the results are averaged over all centrality class given that there is barely no dependence of the ratio on the centrality.

## 4.8 Conclusion

The ratio of production cross-sections of  $\psi(2S)$  to  $J/\psi$  in  $p$ Pb and  $P\text{bp}$  collisions at a center-of-mass energy  $\sqrt{s_{NN}} = 8.16 \text{ TeV}$  are reported with a data sample corresponding to an integrated luminosity of  $13.6 \pm 0.3 \text{ nb}^{-1}$  for  $p$ Pb and  $20.8 \pm 0.5 \text{ nb}^{-1}$  for  $P\text{bp}$  collected by the LHCb detector in 2016. The (normalized) ratios of prompt and non-prompt  $\psi(2S)$ -to- $J/\psi$  production, as functions of different multiplicity variables, are measured in region of  $0 \text{ GeV} < p_T < 14 \text{ GeV}$  and  $1.5 < y^* < 4.5$  for  $p$ Pb and  $-5.5 < y^* < -2.5$  for  $P\text{bp}$ . In  $p$ Pb collisions, we see an obvious decreasing trend for ratio of prompt production as a function of  $N_{\text{tracks}}^{\text{PV}}$  and  $N_{\text{fwd}}^{\text{PV}}$  in  $p$ Pb and a slower decreasing trend as a function of  $N_{\text{bwd}}^{\text{PV}}$ . In  $P\text{bp}$  collisions, even though the ratios have an overall lower value compared to  $p$ Pb with same multiplicity scheme, the prompt and non-prompt  $\psi(2S)$ -to- $J/\psi$  ratio does not show

an obvious decreasing trend with multiplicity as in  $p$ Pb. By comparing the multiplicity dependence of the ratio in  $pp$ ,  $p$ Pb,  $Pbp$  and  $PbPb$  collisions, a smooth transition from small collision systems to large systems is observed.

# CHAPTER 5 SUMMARY AND PROSPECT

## 5.1 Summary

This thesis presents the measurements on multiplicity dependence of  $\psi(2S)$ -to- $J/\psi$  cross-section ratio in proton-proton ( $pp$ ) collisions at  $\sqrt{s} = 13$  TeV and in proton-lead ( $p\text{Pb}$ ) collisions at  $\sqrt{s_{NN}} = 8.16$  TeV. The measured results provide insights into the possible final state effects on charmonia production in high-multiplicity small-system collisions. In particular, they provide more experimental references for identifying the possible existence of quark-gluon plasma (QGP) droplet in these collisions.

The  $\psi(2S)$ -to- $J/\psi$  cross-section ratio in proton-proton ( $pp$ ) collisions at  $\sqrt{s} = 13$  TeV are measured separately for prompt and non-prompt components using a data sample corresponding to an integrated luminosity of  $658 \pm 13 \text{ pb}^{-1}$  collected by the LHCb experiment in 2016. The ratio is measured in charmonia kinematic regions inside the full transverse momentum ( $p_T$ ) and rapidity ( $y$ ) range of  $0.3 < p_T < 20 \text{ GeV}/c$  and  $2.0 < y < 4.5$ . Several multiplicity variables are used for investigating the multiplicity dependence of the cross-section ratio: the number of charged particles used in the  $pp$  interaction primary vertex reconstruction ( $N_{\text{tracks}}^{\text{PV}}$ ), those in the forward and backward rapidity regions respectively ( $N_{\text{fwd}}^{\text{PV}}$  and  $N_{\text{bwd}}^{\text{PV}}$ ), and the rapidity density of primary charged particles ( $dN_{\text{ch}}/d\eta$ ). Notably, the cross-section ratio for non-prompt production shows almost no dependence on any of these multiplicity variables. In contrast, for prompt production, the ratio decreases as a function of  $N_{\text{tracks}}^{\text{PV}}$ ,  $N_{\text{fwd}}^{\text{PV}}$  and  $dN_{\text{ch}}/d\eta$ , exhibiting a trend consistent with the predictions of the co-mover interaction model. The decreasing trend is found to be more significant with the increase of  $N_{\text{fwd}}^{\text{PV}}$  than that of  $N_{\text{bwd}}^{\text{PV}}$ , indicating that the local particle multiplicity has more influence on the ratio. Additionally, the multiplicity dependence of the ratio is measured in transverse momentum and rapidity regions, revealing patterns of stronger  $\psi(2S)$  suppression at low  $p_T$  in high-multiplicity events and nearly multiplicity-independent behavior in the high- $p_T$  region for prompt  $\psi(2S)$  to  $J/\psi$  ratio. These results highlight the substantial influence of interactions with other particles within the collision event on charmonia production, even in  $pp$  collisions.

Similarly, the  $\psi(2S)$ -to- $J/\psi$  cross-section ratio in proton-lead ( $p\text{Pb}$ ) collisions at  $\sqrt{s_{NN}} = 8.16$  TeV are measured utilizing the data sample collected by the LHCb detector in 2016 with integrated luminosities of  $13.6 \pm 0.3 \text{ nb}^{-1}$  and  $20.8 \pm 0.5 \text{ nb}^{-1}$  for  $p\text{Pb}$

and  $\text{Pb}p$  collisions respectively. The  $p\text{Pb}$  ( $\text{Pb}p$ ) symbols denotes the proton (lead) beam going towards the LHCb detector. The ratio is measured in charmonia kinematic region of  $0 < p_{\text{T}} < 14 \text{ GeV}/c$  and  $1.5 < y^* < 4.5$  ( $-5.5 < y^* < -2.5$ ) for  $p\text{Pb}$  ( $\text{Pb}p$ ), for prompt and non-prompt components separately, as a function of different multiplicity variables. The non-prompt ratios still do not show obvious multiplicity dependence in both collision configurations. In  $p\text{Pb}$  collisions, a similar decreasing trend as  $pp$  collisions is observed for the ratio of prompt production as a function of  $N_{\text{tracks}}^{\text{PV}}$  (or  $N_{\text{fwd}}^{\text{PV}}$ ), while in  $\text{Pb}p$  collisions, the ratios exhibit an overall lower value compared to  $p\text{Pb}$  and  $pp$  collisions but do not show an obvious decreasing trend with multiplicity within current uncertainties. The prompt  $\psi(2S)$ -to- $J/\psi$  ratios in  $\text{Pb}p$  collisions are slightly larger but very close to the values measured in  $\text{PbPb}$  collisions at LHC, indicating a smooth transition from small-system collisions to large systems with the continuously increasing event multiplicity.

## 5.2 Prospect

With the on-going calculations for the efficiency correction for each charged track in no-bias data of  $pp$  and  $p\text{Pb}$  collisions, we may adapt our current ratio results to be as a function of generally used multiplicity variable, which is the normalized charged primary particles. Therefore the results can be directly compared to those from other experiments under the same multiplicity schemes.

To fully understand the heavy quarkonia production/suppression mechanism, one needs to extend the measurements to include other heavy flavor hadrons and quarkonia. For example, the multiplicity dependence of prompt  $J/\psi$ -to- $D^0$  ratio in different collision systems can provide insights on whether the ground state can be dissociated in high-multiplicity environments. The multiplicity dependence of  $\psi(2S)$ -to- $J/\psi$  ratio in  $\text{PbPb}$  collisions, which is currently being measured by LHCb, will also help to further extend the multiplicity dependence study from small systems to large systems.

## REFERENCES

- [1] Aad G, et al. Observation of a new particle in the search for the Standard Model Higgs boson with the ATLAS detector at the LHC[J/OL]. Phys. Lett. B, 2012, 716: 1-29. DOI: 10.1016/j.physletb.2012.08.020.
- [2] Greiner W, Schramm S, Stein E. Quantum chromodynamics[EB/OL]. 2002. DOI: 10.1007/978-3-662-04707-1.
- [3] Gell-Mann M. A schematic model of baryons and mesons[J/OL]. Phys. Lett., 1964, 8: 214-215. DOI: 10.1016/S0031-9163(64)92001-3.
- [4] Workman R L, et al. Review of Particle Physics[J/OL]. PTEP, 2022, 2022: 083C01. DOI: 10.1093/ptep/ptac097.
- [5] Workman R L, Others. Review of particle physics[J/OL]. PTEP, 2022, 2022: 083C01. DOI: 10.1093/ptep/ptac097.
- [6] Davies C T H, et al. High precision lattice QCD confronts experiment[J/OL]. Phys. Rev. Lett., 2004, 92: 022001. DOI: 10.1103/PhysRevLett.92.022001.
- [7] Bazavov A, et al. Equation of state in ( 2+1 )-flavor QCD[J/OL]. Phys. Rev. D, 2014, 90: 094503. DOI: 10.1103/PhysRevD.90.094503.
- [8] Chodos A, Jaffe R L, Johnson K, et al. A New Extended Model of Hadrons[J/OL]. Phys. Rev. D, 1974, 9: 3471-3495. DOI: 10.1103/PhysRevD.9.3471.
- [9] DeTar C E, Donoghue J F. BAG MODELS OF HADRONS[J/OL]. Ann. Rev. Nucl. Part. Sci., 1983, 33: 235-264. DOI: 10.1146/annurev.ns.33.120183.001315.
- [10] Elfner H, Müller B. The exploration of hot and dense nuclear matter: introduction to relativistic heavy-ion physics[J/OL]. J. Phys. G, 2023, 50(10): 103001. DOI: 10.1088/1361-6471/ace824.
- [11] Shen C. The standard model for relativistic heavy-ion collisions and electromagnetic tomography[D]. Ohio State U., 2014.
- [12] Wong C Y. Introduction to high-energy heavy ion collisions[M]. 1995.
- [13] Gale C, Paquet J F, Schenke B, et al. Event-plane decorrelation of photons produced in the early stage of heavy-ion collisions[J/OL]. PoS, 2021, HardProbes2020: 039. DOI: 10.22323/1.387.039.
- [14] Bjorken J D. Highly Relativistic Nucleus-Nucleus Collisions: The Central Rapidity Region [J/OL]. Phys. Rev. D, 1983, 27: 140-151. DOI: 10.1103/PhysRevD.27.140.
- [15] Song H, Heinz U W. Suppression of elliptic flow in a minimally viscous quark-gluon plasma [J/OL]. Phys. Lett. B, 2008, 658: 279-283. DOI: 10.1016/j.physletb.2007.11.019.
- [16] Song H, Heinz U W. Causal viscous hydrodynamics in 2+1 dimensions for relativistic heavy-ion collisions[J/OL]. Phys. Rev. C, 2008, 77: 064901. DOI: 10.1103/PhysRevC.77.064901.
- [17] Adare A, et al. High  $p_T$  direct photon and  $\pi^0$  triggered azimuthal jet correlations and measurement of  $k_T$  for isolated direct photons in  $p + p$  collisions at  $\sqrt{s} = 200$  GeV[J/OL]. Phys. Rev. D, 2010, 82: 072001. DOI: 10.1103/PhysRevD.82.072001.

---

REFERENCES

---

- [18] Adcox K, et al. Suppression of hadrons with large transverse momentum in central Au+Au collisions at  $\sqrt{s_{NN}} = 130$ -GeV[J/OL]. Phys. Rev. Lett., 2002, 88: 022301. DOI: 10.1103/PhysRevLett.88.022301.
- [19] Abelev B I, et al. Transverse momentum and centrality dependence of high- $p_T$  non-photonic electron suppression in Au+Au collisions at  $\sqrt{s_{NN}} = 200$  GeV[J/OL]. Phys. Rev. Lett., 2007, 98: 192301. DOI: 10.1103/PhysRevLett.98.192301.
- [20] Adam J, et al. Centrality and transverse momentum dependence of  $D^0$ -meson production at mid-rapidity in Au+Au collisions at  $\sqrt{s_{NN}} = 200$  GeV[J/OL]. Phys. Rev. C, 2019, 99(3): 034908. DOI: 10.1103/PhysRevC.99.034908.
- [21] Sirunyan A M, et al. Nuclear modification factor of  $D^0$  mesons in PbPb collisions at  $\sqrt{s_{NN}} = 5.02$  TeV[J/OL]. Phys. Lett. B, 2018, 782: 474-496. DOI: 10.1016/j.physletb.2018.05.074.
- [22] Chatrchyan S, et al. Observation and studies of jet quenching in PbPb collisions at nucleon-nucleon center-of-mass energy = 2.76 TeV[J/OL]. Phys. Rev. C, 2011, 84: 024906. DOI: 10.1103/PhysRevC.84.024906.
- [23] Bertens R A. Parton energy loss and particle production at high momenta from ALICE[C]// 50th Rencontres de Moriond on QCD and High Energy Interactions. 2015: 263-266.
- [24] Djordjevic M, Djordjevic M. Predictions of heavy-flavor suppression at 5.1 TeV Pb + Pb collisions at the CERN Large Hadron Collider[J/OL]. Phys. Rev. C, 2015, 92(2): 024918. DOI: 10.1103/PhysRevC.92.024918.
- [25] Xu J, Liao J, Gyulassy M. Bridging Soft-Hard Transport Properties of Quark-Gluon Plasmas with CUJET3.0[J/OL]. JHEP, 2016, 02: 169. DOI: 10.1007/JHEP02(2016)169.
- [26] Xu J, Buzzatti A, Gyulassy M. Azimuthal jet flavor tomography with CUJET2.0 of nuclear collisions at RHIC and LHC[J/OL]. JHEP, 2014, 08: 063. DOI: 10.1007/JHEP08(2014)063.
- [27] Xu J, Liao J, Gyulassy M. Consistency of Perfect Fluidity and Jet Quenching in semi-Quark-Gluon Monopole Plasmas[J/OL]. Chin. Phys. Lett., 2015, 32(9): 092501. DOI: 10.1088/0256-307X/32/9/092501.
- [28] Kang Z B, Lashof-Regas R, Ovanesyan G, et al. Jet quenching phenomenology from soft-collinear effective theory with Glauber gluons[J/OL]. Phys. Rev. Lett., 2015, 114(9): 092002. DOI: 10.1103/PhysRevLett.114.092002.
- [29] Chien Y T, Emerman A, Kang Z B, et al. Jet Quenching from QCD Evolution[J/OL]. Phys. Rev. D, 2016, 93(7): 074030. DOI: 10.1103/PhysRevD.93.074030.
- [30] Cao S, Luo T, Qin G Y, et al. Linearized Boltzmann transport model for jet propagation in the quark-gluon plasma: Heavy quark evolution[J/OL]. Phys. Rev. C, 2016, 94(1): 014909. DOI: 10.1103/PhysRevC.94.014909.
- [31] Cao S, Luo T, Qin G Y, et al. Heavy and light flavor jet quenching at RHIC and LHC energies [J/OL]. Phys. Lett. B, 2018, 777: 255-259. DOI: 10.1016/j.physletb.2017.12.023.
- [32] Song T, Berrehrah H, Cabrera D, et al. Tomography of the Quark-Gluon-Plasma by Charm Quarks[J/OL]. Phys. Rev. C, 2015, 92(1): 014910. DOI: 10.1103/PhysRevC.92.014910.
- [33] Miller M L, Reygers K, Sanders S J, et al. Glauber modeling in high energy nuclear collisions [J/OL]. Ann. Rev. Nucl. Part. Sci., 2007, 57: 205-243. DOI: 10.1146/annurev.nucl.57.090506.123020.

---

## REFERENCES

---

- [34] Zhao J, Zhou K, Chen S, et al. Heavy flavors under extreme conditions in high energy nuclear collisions[J/OL]. *Prog. Part. Nucl. Phys.*, 2020, 114: 103801. DOI: 10.1016/j.ppnp.2020.103801.
- [35] Voloshin S, Zhang Y. Flow study in relativistic nuclear collisions by Fourier expansion of Azimuthal particle distributions[J/OL]. *Z. Phys. C*, 1996, 70: 665-672. DOI: 10.1007/s00288-0050141.
- [36] Padula S S. Collective flow and charged hadron correlations in 2.76 TeV PbPb collisions at CMS[J/OL]. *PoS*, 2013, ICHEP2012: 420. DOI: 10.22323/1.174.0420.
- [37] Belt Tonjes M, et al. Flow in Au + Au collisions at RHIC[J/OL]. *J. Phys. G*, 2004, 30(8): S1243-S1246. DOI: 10.1088/0954-3899/30/8/099.
- [38] Rafelski J, Muller B. Strangeness Production in the Quark - Gluon Plasma[J/OL]. *Phys. Rev. Lett.*, 1982, 48: 1066. DOI: 10.1103/PhysRevLett.48.1066.
- [39] Abelev B B, et al. Multi-strange baryon production at mid-rapidity in Pb-Pb collisions at  $\sqrt{s_{NN}} = 2.76$  TeV[J/OL]. *Phys. Lett. B*, 2014, 728: 216-227. DOI: 10.1016/j.physletb.2014.05.052.
- [40] Antinori F, et al. Strangeness enhancements at central rapidity in 40 A GeV/c Pb-Pb collisions [J/OL]. *J. Phys. G*, 2010, 37: 045105. DOI: 10.1088/0954-3899/37/4/045105.
- [41] Abelev B I, et al. Strange particle production in p+p collisions at  $s^{**}(1/2) = 200$ -GeV[J/OL]. *Phys. Rev. C*, 2007, 75: 064901. DOI: 10.1103/PhysRevC.75.064901.
- [42] Quigg C, Rosner J L. Quantum mechanics with applications to quarkonium[J/OL]. *Phys. Rept.*, 1979, 56: 167-235. DOI: 10.1016/0370-1573(79)90095-4.
- [43] Badier J, et al. Experimental J/psi Hadronic Production from 150-GeV/c to 280-GeV/c[J/OL]. *Z. Phys. C*, 1983, 20: 101. DOI: 10.1007/BF01573213.
- [44] Baldit A, et al. Study of the isospin symmetry breaking in the light quark sea of the nucleon from the Drell-Yan process[J/OL]. *Phys. Lett. B*, 1994, 332: 244-250. DOI: 10.1016/0370-2693(94)90884-2.
- [45] Baglin C, et al. psi-Prime and J / psi production in p W, p U and S U interactions at 200-GeV/nucleon[J/OL]. *Phys. Lett. B*, 1995, 345: 617-621. DOI: 10.1016/0370-2693(94)01614-I.
- [46] Lourenco C. Recent results on dimuon production from the NA38 experiment[C]//23rd International Workshop on Gross Properties of Nuclei and Nuclear Excitations: Dynamical Properties of Hadrons in Nuclear Matter (Hirschegg '95). 1995.
- [47] Gonin M, et al. Anomalous J / psi suppression in Pb + Pb collisions at 158-A-GeV/c[J/OL]. *Nucl. Phys. A*, 1996, 610: 404C-417C. DOI: 10.1016/S0375-9474(96)00373-9.
- [48] Wong C Y. Signatures of absorption mechanisms for J / psi and psi-prime production in high-energy heavy ion collisions[J/OL]. *Nucl. Phys. A*, 1998, 630: 487-498. DOI: 10.1016/S0375-9474(97)00788-4.
- [49] Wong C Y. J / psi suppression as a signal for the quark gluon plasma[C]//7th Asia Pacific Physics Conference. 1997.
- [50] Khachatryan V, et al. Evidence for collectivity in pp collisions at the LHC[J/OL]. *Phys. Lett. B*, 2017, 765: 193-220. DOI: 10.1016/j.physletb.2016.12.009.

---

REFERENCES

---

- [51] Adam J, et al. Enhanced production of multi-strange hadrons in high-multiplicity proton-proton collisions[J/OL]. *Nature Phys.*, 2017, 13: 535-539. DOI: 10.1038/nphys4111.
- [52] Acharya S, et al. Multiplicity dependence of charged-particle jet production in pp collisions at  $\sqrt{s} = 13 \text{ TeV}$ [J/OL]. *Eur. Phys. J. C*, 2022, 82(6): 514. DOI: 10.1140/epjc/s10052-022-10405-x.
- [53] Cacciari M, Salam G P, Soyez G. The anti- $k_t$  jet clustering algorithm[J/OL]. *JHEP*, 2008, 04: 063. DOI: 10.1088/1126-6708/2008/04/063.
- [54] Abe F, et al.  $J/\psi$  and  $\psi(2S)$  production in  $p\bar{p}$  collisions at  $\sqrt{s} = 1.8 \text{ TeV}$ [J/OL]. *Phys. Rev. Lett.*, 1997, 79: 572-577. DOI: 10.1103/PhysRevLett.79.572.
- [55] Lansberg J P.  $\Psi(2S)$  production in proton-proton collisions at RHIC, Tevatron and LHC energies [J/OL]. PoS, 2013, ICHEP2012: 293. DOI: 10.22323/1.174.0293.
- [56] Bodwin G T, Braaten E, Lepage G P. Rigorous qcd analysis of inclusive annihilation and production of heavy quarkonium[J/OL]. *Phys. Rev. D*, 1995, 51: 1125-1171. <https://link.aps.org/doi/10.1103/PhysRevD.51.1125>.
- [57] Bodwin G T, Braaten E, Yuan T C, et al.  $p$ -wave charmonium production in  $b$ -meson decays [J/OL]. *Phys. Rev. D*, 1992, 46: R3703-R3707. <https://link.aps.org/doi/10.1103/PhysRevD.46.R3703>.
- [58] Halzen F. Cvc for Gluons and Hadroproduction of Quark Flavors[J/OL]. *Phys. Lett. B*, 1977, 69: 105-108. DOI: 10.1016/0370-2693(77)90144-7.
- [59] Adare A, et al. Ground and excited charmonium state production in  $p + p$  collisions at  $\sqrt{s} = 200 \text{ GeV}$ [J/OL]. *Phys. Rev. D*, 2012, 85: 092004. DOI: 10.1103/PhysRevD.85.092004.
- [60] Ma Y Q, Vogt R. Quarkonium production in an improved color evaporation model[J/OL]. *Phys. Rev. D*, 2016, 94: 114029. <https://link.aps.org/doi/10.1103/PhysRevD.94.114029>.
- [61] Kang Z B, Qiu J W, Sterman G. Factorization and quarkonium production[J/OL]. *Nucl. Phys. B Proc. Suppl.*, 2011, 214: 39-43. DOI: 10.1016/j.nuclphysbps.2011.03.054.
- [62] Chen A P, Ma Y Q, Zhang H. A Short Theoretical Review of Charmonium Production[J/OL]. *Adv. High Energy Phys.*, 2022, 2022: 7475923. DOI: 10.1155/2022/7475923.
- [63] Cacciari M, Greco M, Nason P. The  $p_T$  spectrum in heavy-flavour hadroproduction.[J/OL]. *JHEP*, 1998, 05: 007. DOI: 10.1088/1126-6708/1998/05/007.
- [64] Aaij R, et al. Measurement of forward  $J/\psi$  production cross-sections in  $pp$  collisions at  $\sqrt{s} = 13 \text{ TeV}$ [J/OL]. *JHEP*, 2015, 10: 172. DOI: 10.1007/JHEP10(2015)172.
- [65] Aaij R, et al. Measurement of  $\psi(2S)$  production cross-sections in proton-proton collisions at  $\sqrt{s} = 7$  and  $13 \text{ TeV}$ [J/OL]. *Eur. Phys. J. C*, 2020, 80(3): 185. DOI: 10.1140/epjc/s10052-020-7638-y.
- [66] Aaij R, et al. Measurement of  $J/\psi$  production cross-sections in  $pp$  collisions at  $\sqrt{s} = 5 \text{ TeV}$ [J/OL]. *JHEP*, 2021, 11: 181. DOI: 10.1007/JHEP11(2021)181.
- [67] Aaij R, et al. Measurement of  $J/\psi$  production in  $pp$  collisions at  $\sqrt{s} = 7 \text{ TeV}$ [J/OL]. *Eur. Phys. J. C*, 2011, 71: 1645. DOI: 10.1140/epjc/s10052-011-1645-y.

---

REFERENCES

---

- [68] Aad G, et al. Measurement of the differential cross-sections of inclusive, prompt and non-prompt  $J/\psi$  production in proton-proton collisions at  $\sqrt{s} = 7$  TeV[J/OL]. Nucl. Phys. B, 2011, 850: 387-444. DOI: 10.1016/j.nuclphysb.2011.05.015.
- [69] Adare A, et al. Ground and excited charmonium state production in  $p + p$  collisions at  $\sqrt{s} = 200$  GeV[J/OL]. Phys. Rev. D, 2012, 85: 092004. DOI: 10.1103/PhysRevD.85.092004.
- [70] Adamczyk L, et al.  $J/\psi$  production at high transverse momenta in  $p + p$  and Au+Au collisions at  $\sqrt{s_{NN}} = 200$  GeV[J/OL]. Phys. Lett. B, 2013, 722: 55-62. DOI: 10.1016/j.physletb.2013.04.010.
- [71] Ma Y Q, Venugopalan R. Comprehensive description of  $J/\psi$  production in proton-proton collisions at collider energies[J/OL]. Phys. Rev. Lett., 2014, 113(19): 192301. DOI: 10.1103/PhysRevLett.113.192301.
- [72] Aamodt K, et al. Rapidity and transverse momentum dependence of inclusive  $J/\psi$  production in  $pp$  collisions at  $\sqrt{s} = 7$  TeV[J/OL]. Phys. Lett. B, 2011, 704: 442-455. DOI: 10.1016/j.physletb.2011.09.054.
- [73] Aaij R, et al. Measurement of  $\psi(2S)$  meson production in  $pp$  collisions at  $\sqrt{s} = 7$  TeV[J/OL]. Eur. Phys. J. C, 2012, 72: 2100. DOI: 10.1140/epjc/s10052-012-2100-4.
- [74] Ma Y Q, Wang K, Chao K T. A complete NLO calculation of the  $J/\psi$  and  $\psi'$  production at hadron colliders[J/OL]. Phys. Rev. D, 2011, 84: 114001. DOI: 10.1103/PhysRevD.84.114001.
- [75] Dokshitzer Y L. Calculation of the structure functions for deep inelastic scattering and  $e^+e^-$  annihilation by perturbation theory in quantum chromodynamics.[J]. Sov. Phys. JETP, 1977, 46: 641-653.
- [76] Gribov V N, Lipatov L N. Deep inelastic e-p scattering in perturbation theory[J]. Sov. J. Nucl. Phys., 1972, 15: 438-450.
- [77] Altarelli G, Parisi G. Asymptotic freedom in parton language[J/OL]. Nucl. Phys. B, 1977, 126: 298-318. DOI: 10.1016/0550-3213(77)90384-4.
- [78] Eskola K J, Paakkinen P, Paukkunen H, et al. EPPS16: Nuclear parton distributions with LHC data[J/OL]. Eur. Phys. J. C, 2017, 77(3): 163. DOI: 10.1140/epjc/s10052-017-4725-9.
- [79] Malace S, Gaskell D, Higinbotham D W, et al. The Challenge of the EMC Effect: existing data and future directions[J/OL]. Int. J. Mod. Phys. E, 2014, 23(08): 1430013. DOI: 10.1142/S0218301314300136.
- [80] Norton P R. The EMC effect[J/OL]. Rept. Prog. Phys., 2003, 66: 1253-1297. DOI: 10.1088/0034-4885/66/8/201.
- [81] Geesaman D F, Saito K, Thomas A W. The nuclear EMC effect[J/OL]. Ann. Rev. Nucl. Part. Sci., 1995, 45: 337-390. DOI: 10.1146/annurev.ns.45.120195.002005.
- [82] Arneodo M. Nuclear effects in structure functions[J/OL]. Phys. Rept., 1994, 240: 301-393. DOI: 10.1016/0370-1573(94)90048-5.
- [83] Gelis F, Iancu E, Jalilian-Marian J, et al. The color glass condensate[J/OL]. Ann. Rev. Nucl. Part. Sci., 2010, 60: 463-489. DOI: 10.1146/annurev.nucl.010909.083629.
- [84] Arleo F, Peigne S.  $J/\psi$  suppression in p-A collisions from parton energy loss in cold QCD matter [J/OL]. Phys. Rev. Lett., 2012, 109: 122301. DOI: 10.1103/PhysRevLett.109.122301.

---

## REFERENCES

---

- [85] Arleo F, Jackson G, Peigné S. Impact of fully coherent energy loss on heavy meson production in pA collisions[J/OL]. JHEP, 2022, 01: 164. DOI: 10.1007/JHEP01(2022)164.
- [86] Leitch M J, et al. Measurement of  $J/\psi$  and  $\psi$ -prime suppression in p-A collisions at 800-GeV/c[J/OL]. Phys. Rev. Lett., 2000, 84: 3256-3260. DOI: 10.1103/PhysRevLett.84.3256.
- [87] Ferreiro E G. Excited charmonium suppression in proton–nucleus collisions as a consequence of comovers[J/OL]. Phys. Lett. B, 2015, 749: 98-103. DOI: 10.1016/j.physletb.2015.07.066.
- [88] Braaten E, He L P, Ingles K, et al. Production of  $X(3872)$  at High Multiplicity[J/OL]. Phys. Rev., 2021, D103(7): L071901. DOI: 10.1103/PhysRevD.103.L071901.
- [89] Esposito A, Ferreiro E G, Pilloni A, et al. The nature of  $X(3872)$  from high-multiplicity pp collisions[J/OL]. Eur. Phys. J., 2021, C81(7): 669. DOI: 10.1140/epjc/s10052-021-09425-w.
- [90] Ferreiro E G, Lansberg J P. Is bottomonium suppression in proton-nucleus and nucleus-nucleus collisions at LHC energies due to the same effects?[J/OL]. JHEP, 2018, 10: 094. DOI: 10.1007/JHEP10(2018)094.
- [91] Gavin S, Vogt R. Charmonium suppression by Comover scattering in Pb + Pb collisions[J/OL]. Phys. Rev. Lett., 1997, 78: 1006-1009. DOI: 10.1103/PhysRevLett.78.1006.
- [92] Abdallah M, et al. Measurement of cold nuclear matter effects for inclusive  $J/\psi$  in p+Au collisions at  $s_{NN}=200$  GeV[J/OL]. Phys. Lett. B, 2022, 825: 136865. DOI: 10.1016/j.physletb.2022.136865.
- [93] Morreale A. Quarkonium production in pp and p-A collisions with ALICE at the LHC[J/OL]. EPJ Web Conf., 2018, 171: 19002. DOI: 10.1051/epjconf/201817119002.
- [94] Eskola K J, Paukkunen H, Salgado C A. EPS09: A New Generation of NLO and LO Nuclear Parton Distribution Functions[J/OL]. JHEP, 2009, 04: 065. DOI: 10.1088/1126-6708/2009/04/065.
- [95] Ma Y Q, Venugopalan R, Zhang H F.  $J/\psi$  production and suppression in high energy proton–nucleus collisions[J/OL]. Phys. Rev. D, 2015, 92: 071901. DOI: 10.1103/PhysRevD.92.071901.
- [96] Ducloué B, Lappi T, Mäntysaari H. Forward  $J/\psi$  production in proton-nucleus collisions at high energy[J/OL]. Phys. Rev. D, 2015, 91(11): 114005. DOI: 10.1103/PhysRevD.91.114005.
- [97] Albacete J L, et al. Predictions for  $p+\text{Pb}$  Collisions at  $\sqrt{s_{\text{NN}}} = 5$  TeV[J/OL]. Int. J. Mod. Phys. E, 2013, 22: 1330007. DOI: 10.1142/S0218301313300075.
- [98] Lansberg J P, Shao H S. Towards an automated tool to evaluate the impact of the nuclear modification of the gluon density on quarkonium, D and B meson production in proton–nucleus collisions[J/OL]. Eur. Phys. J. C, 2017, 77(1): 1. DOI: 10.1140/epjc/s10052-016-4575-x.
- [99] Chen B, Guo T, Liu Y, et al. Cold and Hot Nuclear Matter Effects on Charmonium Production in  $p+\text{Pb}$  Collisions at LHC Energy[J/OL]. Phys. Lett. B, 2017, 765: 323-327. DOI: 10.1016/j.physletb.2016.12.021.
- [100] Boente García O. Quarkonia production in  $p\text{Pb}$  collisions[J/OL]. PoS, 2021, HardProbes2020: 075. DOI: 10.22323/1.387.0075.
- [101] Matsui T, Satz H.  $J/\psi$  Suppression by Quark-Gluon Plasma Formation[J/OL]. Phys. Lett. B, 1986, 178: 416-422. DOI: 10.1016/0370-2693(86)91404-8.

---

REFERENCES

---

- [102] Kanaya K, Satz H. Correlation and Screening in Finite Temperature SU(2) Gauge Theory[J/OL]. Phys. Rev. D, 1986, 34: 3193. DOI: 10.1103/PhysRevD.34.3193.
- [103] Craigie N S. Lepton and Photon Production in Hadron Collisions[J/OL]. Phys. Rept., 1978, 47: 1-108. DOI: 10.1016/0370-1573(78)90167-9.
- [104] Mocsy A. Potential Models for Quarkonia[J/OL]. Eur. Phys. J. C, 2009, 61: 705-710. DOI: 10.1140/epjc/s10052-008-0847-4.
- [105] Peskin M E. Short Distance Analysis for Heavy Quark Systems. 1. Diagrammatics[J/OL]. Nucl. Phys. B, 1979, 156: 365-390. DOI: 10.1016/0550-3213(79)90199-8.
- [106] Bhanot G, Peskin M E. Short Distance Analysis for Heavy Quark Systems. 2. Applications [J/OL]. Nucl. Phys. B, 1979, 156: 391-416. DOI: 10.1016/0550-3213(79)90200-1.
- [107] Brambilla N, Ghiglieri J, Vairo A, et al. Static quark-antiquark pairs at finite temperature[J/OL]. Phys. Rev. D, 2008, 78: 014017. DOI: 10.1103/PhysRevD.78.014017.
- [108] Chen S, He M. Heavy quarkonium dissociation by thermal gluons at next-to-leading order in the Quark–Gluon Plasma[J/OL]. Phys. Lett. B, 2018, 786: 260-267. DOI: 10.1016/j.physletb.2018.09.056.
- [109] Yan L, Zhuang P, Xu N. Competition between J / psi suppression and regeneration in quark-gluon plasma[J/OL]. Phys. Rev. Lett., 2006, 97: 232301. DOI: 10.1103/PhysRevLett.97.232301.
- [110] Zhou K, Xu N, Xu Z, et al. Medium effects on charmonium production at ultrarelativistic energies available at the CERN Large Hadron Collider[J/OL]. Phys. Rev. C, 2014, 89(5): 054911. DOI: 10.1103/PhysRevC.89.054911.
- [111] Du X, Rapp R. Sequential Regeneration of Charmonia in Heavy-Ion Collisions[J/OL]. Nucl. Phys. A, 2015, 943: 147-158. DOI: 10.1016/j.nuclphysa.2015.09.006.
- [112] Zhou K, Xu N, Xu Z, et al. Medium effects on charmonium production at ultrarelativistic energies available at the cern large hadron collider[J/OL]. Phys. Rev. C, 2014, 89: 054911. <https://link.aps.org/doi/10.1103/PhysRevC.89.054911>.
- [113] Yao X, Müller B. Approach to equilibrium of quarkonium in quark-gluon plasma[J/OL]. Phys. Rev. C, 2018, 97(1): 014908. DOI: 10.1103/PhysRevC.97.014908.
- [114] He M, Wu B, Rapp R. Collectivity of  $j/\psi$  mesons in heavy-ion collisions[J/OL]. Phys. Rev. Lett., 2022, 128: 162301. <https://link.aps.org/doi/10.1103/PhysRevLett.128.162301>.
- [115] Gago J M. Dilepton production in heavy-ion collisions at the CERN-SPS[J]. Conf. Proc., 1991, 2: 1099-1101.
- [116] Adam J, et al.  $J/\psi$  suppression at forward rapidity in Pb-Pb collisions at  $\sqrt{s_{NN}} = \mathbf{5.02}$  TeV [J/OL]. Phys. Lett. B, 2017, 766: 212-224. DOI: 10.1016/j.physletb.2016.12.064.
- [117] Adam J, et al. Differential studies of inclusive  $J/\psi$  and  $\psi(2S)$  production at forward rapidity in Pb-Pb collisions at  $\sqrt{s_{NN}} = 2.76$  TeV[J/OL]. JHEP, 2016, 05: 179. DOI: 10.1007/JHEP05(2016)179.
- [118] Zhao X, Rapp R. Medium Modifications and Production of Charmonia at LHC[J/OL]. Nucl. Phys. A, 2011, 859: 114-125. DOI: 10.1016/j.nuclphysa.2011.05.001.

---

## REFERENCES

---

- [119] Adam J, et al. Measurement of inclusive  $J/\psi$  suppression in Au+Au collisions at  $\sqrt{s_{NN}} = 200$  GeV through the dimuon channel at STAR[J/OL]. *Phys. Lett. B*, 2019, 797: 134917. DOI: 10.1016/j.physletb.2019.134917.
- [120] Hu Z, Leonardo N T, Liu T, et al. Review of bottomonium measurements from CMS[J/OL]. *Int. J. Mod. Phys. A*, 2017, 32(19n20): 1730015. DOI: 10.1142/S0217751X17300150.
- [121] Chatrchyan S, et al. Event Activity Dependence of  $\Upsilon(nS)$  Production in  $\sqrt{s_{NN}}=5.02$  TeV pPb and  $\sqrt{s}=2.76$  TeV pp Collisions[J/OL]. *JHEP*, 2014, 04: 103. DOI: 10.1007/JHEP04(2014)103.
- [122] Sirunyan A M, et al. Investigation into the event-activity dependence of  $\Upsilon(nS)$  relative production in proton-proton collisions at  $\sqrt{s} = 7$  TeV[J/OL]. *JHEP*, 2020, 11: 001. DOI: 10.1007/JHEP11(2020)001.
- [123] Aaij R, Abellán Beteta C, Ackernley T, et al. Observation of multiplicity dependent prompt  $\chi_{c1}(3872)$  and  $\psi(2s)$  production in  $pp$  collisions[J/OL]. *Phys. Rev. Lett.*, 2021, 126: 092001. <https://link.aps.org/doi/10.1103/PhysRevLett.126.092001>.
- [124] Tork T. Charmonium production as a function of charged-particle multiplicity in pp and p-Pb collisions with ALICE at the LHC[C]/29th International Workshop on Deep-Inelastic Scattering and Related Subjects. 2022.
- [125] Aaij R, et al. LHCb detector performance[J/OL]. *Int. J. Mod. Phys. A*, 2015, 30(07): 1530022. DOI: 10.1142/S0217751X15300227.
- [126] Alves A A, Jr., et al. The LHCb detector at the LHC[J/OL]. *JINST*, 2008, 3: S08005. DOI: 10.1088/1748-0221/3/08/S08005.
- [127] Mobs E. The CERN accelerator complex - August 2018. Complexe des accélérateurs du CERN - Août 2018[EB/OL]. 2018. <http://cds.cern.ch/record/2636343>.
- [128] van Hunen J J. The lhcb tracking system[J/OL]. *Nuclear Instruments and Methods in Physics Research Section A: Accelerators, Spectrometers, Detectors and Associated Equipment*, 2007, 572 (1): 149-153. <https://www.sciencedirect.com/science/article/pii/S0168900206020316>. DOI: <https://doi.org/10.1016/j.nima.2006.10.179>.
- [129] Aaij R, et al. Performance of the LHCb Vertex Locator[J/OL]. *JINST*, 2014, 9: P09007. DOI: 10.1088/1748-0221/9/09/P09007.
- [130] Kopciewicz P, Maccolini S, Szumlak T. The LHCb vertex locator upgrade — the detector calibration overview[J/OL]. *JINST*, 2022, 17(01): C01046. DOI: 10.1088/1748-0221/17/01/C01046.
- [131] Gassner J, Lehner F, Steiner F. The mechanical design of the LHCb silicon trigger tracker[Z]. 2005.
- [132] LHCb: Outer tracker technical design report[Z]. 2001.
- [133] Arink R, et al. Performance of the LHCb Outer Tracker[J/OL]. *JINST*, 2014, 9(01): P01002. DOI: 10.1088/1748-0221/9/01/P01002.
- [134] LHCb magnet: Technical design report[Z]. 2000.
- [135] Needham M. Combined Long Tracking Performance[Z]. 2007.
- [136] Aaij R, et al. Measurement of the track reconstruction efficiency at LHCb[J/OL]. *JINST*, 2015, 10(02): P02007. DOI: 10.1088/1748-0221/10/02/P02007.

---

## REFERENCES

---

- [137] Powell A. Particle Identification at LHCb. Particle ID in LHCb[EB/OL]. 2011. <https://cds.cern.ch/record/1322666>.
- [138] Adinolfi M, et al. LHCb Upgraded RICH 1 Engineering Design Review[Z]. 2016.
- [139] Garsed P J, et al. LHCb Upgraded RICH 2 Engineering Design Review Report[Z]. 2016.
- [140] Picatoste Olloqui E. LHCb preshower(PS) and scintillating pad detector (SPD): Commissioning, calibration, and monitoring[J/OL]. *J. Phys. Conf. Ser.*, 2009, 160: 012046. DOI: 10.1088/1742-6596/160/1/012046.
- [141] Abellán Beteta C, et al. Calibration and performance of the LHCb calorimeters in Run 1 and 2 at the LHC[A]. 2020. arXiv: 2008.11556.
- [142] Calabrese R, et al. Performance of the LHCb RICH detectors during LHC Run 2[J/OL]. *JINST*, 2022, 17(07): P07013. DOI: 10.1088/1748-0221/17/07/P07013.
- [143] Santovetti E. The LHCb muon detector[J/OL]. *Nucl. Instrum. Meth. A*, 2001, 462: 297-300. DOI: 10.1016/S0168-9002(01)00127-9.
- [144] Archilli F, et al. Performance of the muon identification at LHCb[J/OL]. *JINST*, 2013, 8: P10020. DOI: 10.1088/1748-0221/8/10/P10020.
- [145] Hocker A, et al. TMVA - Toolkit for multivariate data analysis[A]. 2007. arXiv: physics/0703039.
- [146] Dziurda A. The LHCb trigger and its upgrade[J/OL]. *Nucl. Instrum. Meth. A*, 2016, 824: 277-279. DOI: 10.1016/j.nima.2015.10.041.
- [147] Albrecht J. The lhcb trigger system[J/OL]. *Nuclear Physics B - Proceedings Supplements*, 2009, 187: 237-244. <https://www.sciencedirect.com/science/article/pii/S0920563209000395>. DOI: <https://doi.org/10.1016/j.nuclphysbps.2009.01.033>.
- [148] Ferreiro E G. Charmonium dissociation and recombination at LHC: Revisiting comovers[J/OL]. *Phys. Lett.*, 2014, B731: 57-63. DOI: 10.1016/j.physletb.2014.02.011.
- [149] Aaij R, et al. Precision luminosity measurements at LHCb[J/OL]. *JINST*, 2014, 9(12): P12005. DOI: 10.1088/1748-0221/9/12/P12005.
- [150] Ball P, Braun V M, Lenz A. Higher-twist distribution amplitudes of the K meson in QCD[J/OL]. *JHEP*, 2006, 05: 004. DOI: 10.1088/1126-6708/2006/05/004.
- [151] Belyaev I, et al. Handling of the generation of primary events in Gauss, the LHCb simulation framework[J/OL]. *J. Phys. Conf. Ser.*, 2011, 331: 032047. DOI: 10.1088/1742-6596/331/3/032047.
- [152] Bargiotti M, Vagnoni V. Heavy quarkonia sector in PYTHIA 6.324: Tuning, validation and perspectives at LHCb[Z]. 2007.
- [153] Lange D J. The EvtGen particle decay simulation package[J/OL]. *Nucl. Instrum. Meth. A*, 2001, 462: 152-155. DOI: 10.1016/S0168-9002(01)00089-4.
- [154] Golonka P, Was Z. PHOTOS Monte Carlo: A precision tool for QED corrections in  $Z$  and  $W$  decays[J/OL]. *Eur. Phys. J.*, 2006, C45: 97-107. DOI: 10.1140/epjc/s2005-02396-4.
- [155] Agostinelli S, et al. GEANT4—a simulation toolkit[J/OL]. *Nucl. Instrum. Meth. A*, 2003, 506: 250-303. DOI: 10.1016/S0168-9002(03)01368-8.

---

## REFERENCES

---

- [156] Clemencic M, Corti G, Easo S, et al. The LHCb simulation application, Gauss: Design, evolution and experience[J/OL]. *J. Phys. Conf. Ser.*, 2011, 331: 032023. DOI: 10.1088/1742-6596/331/3/032023.
- [157] Aaij R, et al. Measurement of forward  $J/\psi$  production cross-sections in  $pp$  collisions at  $\sqrt{s} = 13$  TeV[J/OL]. *JHEP*, 2015, 10: 172. DOI: 10.1007/JHEP10(2015)172.
- [158] Skwarnicki T. A study of the radiative CASCADE transitions between the  $\Upsilon'$  and  $\Upsilon$  resonances [D/OL]. Cracow, INP, 1986. [http://www-library.desy.de/preparch/desy/int\\_rep/f31-86-02.pdf](http://www-library.desy.de/preparch/desy/int_rep/f31-86-02.pdf).
- [159] Lefrancous J. Crystal ball fits[Z].
- [160] Pivk M, Le Diberder F R. SPlot: A statistical tool to unfold data distributions[J/OL]. *Nucl. Instrum. Meth. A*, 2005, 555: 356-369. DOI: 10.1016/j.nima.2005.08.106.
- [161] Aaij R, et al. Measurement of the track reconstruction efficiency at LHCb[J/OL]. *JINST*, 2015, 10: P02007. DOI: 10.1088/1748-0221/10/02/P02007.
- [162] Anderlini L, Contu A, Jones C R, et al. The PIDCalib package[R/OL]. Geneva: CERN, 2016. <https://cds.cern.ch/record/2202412>.
- [163] Tolk S, Albrecht J, Dettori F, et al. Data driven trigger efficiency determination at LHCb[R/OL]. Geneva: CERN, 2014. <http://cds.cern.ch/record/1701134>.
- [164] Tracking correction table[Z].
- [165] Aaij R, et al. The LHCb trigger and its performance in 2011[J/OL]. *JINST*, 2013, 8: P04022. DOI: 10.1088/1748-0221/8/04/P04022.
- [166] Adare A, et al. Measurement of the relative yields of  $\psi(2S)$  to  $J/\psi$  mesons produced at forward and backward rapidity in  $p+p$ ,  $p+Al$ ,  $p+Au$ , and  ${}^3He+Au$  collisions at  $\sqrt{s_{NN}} = 200$  GeV[J/OL]. *Phys. Rev.*, 2017, C95(3): 034904. DOI: 10.1103/PhysRevC.95.034904.
- [167] Alessandro B, et al.  $J/\psi$  and  $\psi'$  production and their normal nuclear absorption in proton-nucleus collisions at 400-GeV[J/OL]. *Eur. Phys. J.*, 2006, C48(CERN-PH-EP-2006-018): 329. DOI: 10.1140/epjc/s10052-006-0079-4.
- [168] Antoniazzi L, et al. Production of  $J/\psi$  via  $\psi(2S)$  and  $\Xi$  decay in 300-GeV/c proton and  $\pi^\pm$  nucleon interactions[J/OL]. *Phys. Rev. Lett.*, 1993, 70(FERMILAB-PUB-92-140-E): 383-386. DOI: 10.1103/PhysRevLett.70.383.
- [169] Abreu M C, et al.  $J/\psi$ ,  $\psi'$  and Drell-Yan production in  $pp$  and  $pd$  interactions at 450-GeV/c [J/OL]. *Phys. Lett.*, 1998, B438: 35-40. DOI: 10.1016/S0370-2693(98)01014-4.
- [170] Clark A G, et al. Electron pair production at the CERN ISR[J/OL]. *Nucl. Phys.*, 1978, B142 (PRINT-78-0636 (CERN)): 29. DOI: 10.1016/0550-3213(78)90400-5.
- [171] Albajar C, et al.  $J/\psi$  and  $\psi'$  production at the CERN  $p\bar{p}$  collider[J/OL]. *Phys. Lett.*, 1991, B256 (CERN-PPE-90-154): 112-120. DOI: 10.1016/0370-2693(91)90227-H.
- [172] Aaij R, et al. Exclusive  $J/\psi$  and  $\psi(2S)$  production in  $pp$  collisions at  $\sqrt{s} = 7$  TeV[J/OL]. *J. Phys. G*, 2013, G40(CERN-PH-EP-2013-005, LHCb-PAPER-2012-044): 045001. DOI: 10.1088/0954-3899/40/4/045001.
- [173] Chatrchyan S, et al.  $J/\psi$  and  $\psi(2S)$  production in  $pp$  collisions at  $\sqrt{s} = 7$  TeV[J/OL]. *JHEP*, 2012, 02: 011. DOI: 10.1007/JHEP02(2012)011.

---

## REFERENCES

---

- [174] Acharya S, et al. Energy dependence of forward-rapidity  $J/\psi$  and  $\psi(2S)$  production in  $pp$  collisions at the LHC[J/OL]. *Eur. Phys. J. C*, 2017, 77(6): 392. DOI: 10.1140/epjc/s10052-017-4940-4.
- [175] Agostinelli S, Allison J, Amako K, et al. Geant4—a simulation toolkit[J/OL]. *Nuclear Instruments and Methods in Physics Research Section A: Accelerators, Spectrometers, Detectors and Associated Equipment*, 2003, 506(3): 250-303. <https://www.sciencedirect.com/science/article/pii/S0168900203013688>. DOI: [https://doi.org/10.1016/S0168-9002\(03\)01368-8](https://doi.org/10.1016/S0168-9002(03)01368-8).
- [176] Allison J, Amako K, Apostolakis J, et al. Geant4 developments and applications[J/OL]. *IEEE Transactions on Nuclear Science*, 2006, 53(1): 270-278. DOI: 10.1109/TNS.2006.869826.
- [177] Pierog T, Karpenko I, Katzy J M, et al. EPOS LHC: Test of collective hadronization with data measured at the CERN Large Hadron Collider[J/OL]. *Phys. Rev. C*, 2015, 92(3): 034906. DOI: 10.1103/PhysRevC.92.034906.
- [178]  $\psi(2S)$  suppression in Pb-Pb collisions at the LHC[A]. 2022. arXiv: 2210.08893.
- [179] Aaij R, et al. Measurement of the Nuclear Modification Factor and Prompt Charged Particle Production in  $p - Pb$  and  $pp$  Collisions at  $\sqrt{s_{NN}}=5$  TeV[J/OL]. *Phys. Rev. Lett.*, 2022, 128(14): 142004. DOI: 10.1103/PhysRevLett.128.142004.

## RESULT TABLES OF $\psi(2S)$ -TO- $J/\psi$ RATIO IN $pp$ COLLISIONS

Table 5.1 Ratios (%) of double differential production cross-section for  $\psi(2S)$  to  $J/\psi$  in bins of  $(p_T, y)$  for  $4 \leq N_{\text{tracks}}^{\text{PV}} < 20$ . The first uncertainties are statistical, the second are systematic.

prompt			
$p_T$ ( GeV/ $c$ )	$2 < y < 2.8$	$2.8 < y < 3.5$	$3.5 < y < 4.5$
0-2	$14.95 \pm 0.19 \pm 0.54$	$15.18 \pm 0.15 \pm 0.44$	$15.54 \pm 0.15 \pm 0.48$
2-4	$20.45 \pm 0.30 \pm 0.72$	$18.97 \pm 0.22 \pm 0.54$	$19.49 \pm 0.24 \pm 0.56$
4-6	$29.18 \pm 0.60 \pm 1.02$	$23.22 \pm 0.39 \pm 0.68$	$22.75 \pm 0.45 \pm 0.75$
6-8	$34.60 \pm 1.08 \pm 1.45$	$26.74 \pm 0.76 \pm 0.97$	$27.89 \pm 0.93 \pm 1.16$
8-20	$33.05 \pm 1.39 \pm 1.52$	$27.67 \pm 1.19 \pm 1.15$	$29.83 \pm 1.65 \pm 1.70$
non-prompt			
$p_T$ ( GeV/ $c$ )	$2 < y < 2.8$	$2.8 < y < 3.5$	$3.5 < y < 4.5$
0-2	$21.88 \pm 1.19 \pm 1.16$	$19.99 \pm 0.91 \pm 1.01$	$21.04 \pm 1.16 \pm 1.74$
2-4	$28.29 \pm 1.17 \pm 1.37$	$27.02 \pm 0.90 \pm 1.09$	$27.60 \pm 1.11 \pm 1.56$
4-6	$32.89 \pm 1.53 \pm 1.61$	$29.53 \pm 1.13 \pm 1.46$	$33.70 \pm 1.57 \pm 1.98$
6-8	$34.89 \pm 2.10 \pm 1.88$	$31.70 \pm 1.69 \pm 1.41$	$32.33 \pm 2.23 \pm 1.96$
8-20	$43.93 \pm 2.36 \pm 1.97$	$39.96 \pm 2.16 \pm 1.77$	$39.78 \pm 2.95 \pm 2.80$

Table 5.2 Ratios (%) of double differential production cross-section for  $\psi(2S)$  to  $J/\psi$  in bins of  $(p_T, y)$  for  $20 \leq N_{\text{tracks}}^{\text{PV}} < 45$ . The first uncertainties are statistical, the second are systematic.

prompt			
$p_T$ ( GeV/ $c$ )	$2 < y < 2.8$	$2.8 < y < 3.5$	$3.5 < y < 4.5$
0-2	$11.50 \pm 0.14 \pm 0.54$	$10.92 \pm 0.11 \pm 0.53$	$11.62 \pm 0.11 \pm 0.63$
2-4	$16.48 \pm 0.17 \pm 0.74$	$15.33 \pm 0.13 \pm 0.65$	$15.81 \pm 0.14 \pm 0.67$
4-6	$22.41 \pm 0.25 \pm 0.98$	$20.68 \pm 0.18 \pm 0.86$	$20.62 \pm 0.21 \pm 0.88$
6-8	$29.18 \pm 0.40 \pm 1.41$	$26.20 \pm 0.32 \pm 1.14$	$25.11 \pm 0.38 \pm 1.16$
8-20	$35.01 \pm 0.53 \pm 1.65$	$29.31 \pm 0.43 \pm 1.35$	$28.46 \pm 0.54 \pm 1.39$
non-prompt			
$p_T$ ( GeV/ $c$ )	$2 < y < 2.8$	$2.8 < y < 3.5$	$3.5 < y < 4.5$
0-2	$19.03 \pm 0.57 \pm 1.04$	$20.24 \pm 0.49 \pm 1.00$	$20.72 \pm 0.56 \pm 1.14$
2-4	$26.92 \pm 0.55 \pm 1.30$	$25.65 \pm 0.43 \pm 1.24$	$27.27 \pm 0.56 \pm 1.37$
4-6	$34.28 \pm 0.68 \pm 1.58$	$28.18 \pm 0.49 \pm 1.33$	$29.32 \pm 0.67 \pm 1.55$
6-8	$34.61 \pm 0.83 \pm 1.89$	$32.17 \pm 0.71 \pm 1.57$	$34.12 \pm 1.02 \pm 2.38$
8-20	$41.47 \pm 0.84 \pm 1.99$	$36.17 \pm 0.78 \pm 1.78$	$34.52 \pm 1.04 \pm 1.80$

RESULT TABLES OF  $\psi(2S)$ -TO- $J/\psi$  RATIO IN  $pp$  COLLISIONS

---

Table 5.3 Ratios (%) of double differential production cross-section for  $\psi(2S)$  to  $J/\psi$  in bins of  $(p_T, y)$  for  $45 \leq N_{\text{tracks}}^{\text{PV}} < 70$ . The first uncertainties are statistical, the second are systematic.

prompt			
$p_T$ ( GeV/ $c$ )	$2 < y < 2.8$	$2.8 < y < 3.5$	$3.5 < y < 4.5$
0-2	$9.04 \pm 0.22 \pm 0.27$	$8.79 \pm 0.18 \pm 0.20$	$9.42 \pm 0.16 \pm 0.29$
2-4	$13.03 \pm 0.21 \pm 0.29$	$12.38 \pm 0.16 \pm 0.24$	$13.53 \pm 0.17 \pm 0.29$
4-6	$20.18 \pm 0.28 \pm 0.52$	$17.62 \pm 0.21 \pm 0.33$	$18.83 \pm 0.23 \pm 0.44$
6-8	$25.17 \pm 0.38 \pm 0.68$	$23.94 \pm 0.31 \pm 0.52$	$23.65 \pm 0.37 \pm 0.60$
8-20	$31.32 \pm 0.43 \pm 0.84$	$29.02 \pm 0.41 \pm 0.71$	$27.94 \pm 0.50 \pm 0.88$
non-prompt			
$p_T$ ( GeV/ $c$ )	$2 < y < 2.8$	$2.8 < y < 3.5$	$3.5 < y < 4.5$
0-2	$20.93 \pm 0.68 \pm 0.83$	$18.99 \pm 0.56 \pm 0.81$	$19.55 \pm 0.62 \pm 0.70$
2-4	$23.54 \pm 0.54 \pm 0.68$	$24.22 \pm 0.45 \pm 0.68$	$23.76 \pm 0.55 \pm 0.87$
4-6	$31.83 \pm 0.66 \pm 0.82$	$26.85 \pm 0.49 \pm 0.78$	$27.46 \pm 0.67 \pm 1.16$
6-8	$32.65 \pm 0.77 \pm 1.03$	$31.71 \pm 0.69 \pm 1.02$	$34.16 \pm 0.96 \pm 1.55$
8-20	$39.44 \pm 0.74 \pm 1.12$	$37.75 \pm 0.73 \pm 1.14$	$38.58 \pm 1.07 \pm 1.71$

Table 5.4 Ratios (%) of double differential production cross-section for  $\psi(2S)$  to  $J/\psi$  in bins of  $(p_T, y)$  for  $70 \leq N_{\text{tracks}}^{\text{PV}} < 95$ . The first uncertainties are statistical, the second are systematic.

prompt			
$p_T$ ( GeV/ $c$ )	$2 < y < 2.8$	$2.8 < y < 3.5$	$3.5 < y < 4.5$
0-2	$7.71 \pm 0.44 \pm 0.28$	$7.89 \pm 0.34 \pm 0.23$	$7.55 \pm 0.28 \pm 0.51$
2-4	$11.29 \pm 0.37 \pm 0.34$	$11.58 \pm 0.31 \pm 0.28$	$12.18 \pm 0.30 \pm 0.45$
4-6	$17.92 \pm 0.43 \pm 0.56$	$15.68 \pm 0.31 \pm 0.33$	$16.52 \pm 0.36 \pm 0.47$
6-8	$23.07 \pm 0.54 \pm 0.78$	$20.16 \pm 0.43 \pm 0.57$	$21.77 \pm 0.52 \pm 0.75$
8-20	$29.65 \pm 0.59 \pm 1.14$	$27.43 \pm 0.55 \pm 0.95$	$25.27 \pm 0.66 \pm 1.00$
non-prompt			
$p_T$ ( GeV/ $c$ )	$2 < y < 2.8$	$2.8 < y < 3.5$	$3.5 < y < 4.5$
0-2	$17.74 \pm 1.03 \pm 1.07$	$17.59 \pm 0.80 \pm 0.75$	$19.41 \pm 0.99 \pm 0.83$
2-4	$26.99 \pm 0.92 \pm 0.95$	$24.29 \pm 0.69 \pm 0.73$	$25.62 \pm 0.89 \pm 1.23$
4-6	$32.36 \pm 0.99 \pm 1.04$	$26.84 \pm 0.71 \pm 0.89$	$26.85 \pm 0.95 \pm 1.18$
6-8	$31.96 \pm 1.12 \pm 1.24$	$31.70 \pm 1.01 \pm 1.27$	$28.69 \pm 1.32 \pm 1.59$
8-20	$41.22 \pm 1.06 \pm 1.22$	$35.64 \pm 1.01 \pm 1.35$	$34.33 \pm 1.47 \pm 1.58$

---

 RESULT TABLES OF  $\psi(2S)$ -TO- $J/\psi$  RATIO IN  $pp$  COLLISIONS
 

---

Table 5.5 Ratios (%) of double differential production cross-section for  $\psi(2S)$  to  $J/\psi$  in bins of  $(p_T, y)$  for  $95 \leq N_{\text{tracks}}^{\text{PV}} < 200$ . The first uncertainties are statistical, the second are systematic.

prompt			
$p_T$ (GeV/c)	$2 < y < 2.8$	$2.8 < y < 3.5$	$3.5 < y < 4.5$
0-2	$9.91 \pm 1.05 \pm 0.83$	$7.13 \pm 0.79 \pm 0.51$	$8.93 \pm 0.77 \pm 0.69$
2-4	$9.18 \pm 0.74 \pm 0.55$	$9.23 \pm 0.59 \pm 0.40$	$10.99 \pm 0.61 \pm 0.51$
4-6	$17.20 \pm 0.86 \pm 1.02$	$14.79 \pm 0.61 \pm 0.67$	$15.31 \pm 0.66 \pm 1.08$
6-8	$22.16 \pm 1.04 \pm 1.89$	$19.04 \pm 0.78 \pm 1.61$	$22.02 \pm 1.00 \pm 1.60$
8-20	$28.98 \pm 1.05 \pm 3.33$	$26.00 \pm 0.93 \pm 1.53$	$24.66 \pm 1.17 \pm 1.85$
non-prompt			
$p_T$ (GeV/c)	$2 < y < 2.8$	$2.8 < y < 3.5$	$3.5 < y < 4.5$
0-2	$23.68 \pm 2.65 \pm 3.06$	$20.28 \pm 1.84 \pm 1.64$	$21.47 \pm 2.45 \pm 2.05$
2-4	$24.12 \pm 1.55 \pm 1.89$	$25.31 \pm 1.39 \pm 1.30$	$24.29 \pm 1.61 \pm 1.71$
4-6	$30.40 \pm 1.81 \pm 1.85$	$28.96 \pm 1.41 \pm 1.83$	$28.78 \pm 1.85 \pm 2.25$
6-8	$35.56 \pm 2.30 \pm 3.36$	$36.19 \pm 1.99 \pm 4.03$	$25.80 \pm 2.46 \pm 2.30$
8-20	$35.20 \pm 1.79 \pm 2.08$	$33.68 \pm 1.78 \pm 1.74$	$37.92 \pm 2.77 \pm 3.16$

Table 5.6 Ratios (%) of double differential production cross-section for  $\psi(2S)$  to  $J/\psi$  in bins of  $(p_T, y)$  for  $0 \leq N_{\text{bwd}}^{\text{PV}} < 8$ . The first uncertainties are statistical, the second are systematic.

prompt			
$p_T$ (GeV/c)	$2 < y < 2.8$	$2.8 < y < 3.5$	$3.5 < y < 4.5$
0-2	$12.78 \pm 0.18 \pm 0.89$	$12.48 \pm 0.14 \pm 0.66$	$12.88 \pm 0.13 \pm 0.75$
2-4	$17.26 \pm 0.23 \pm 0.81$	$16.40 \pm 0.18 \pm 0.68$	$16.36 \pm 0.18 \pm 0.66$
4-6	$23.45 \pm 0.36 \pm 1.07$	$21.17 \pm 0.26 \pm 0.87$	$20.84 \pm 0.29 \pm 0.88$
6-8	$30.78 \pm 0.62 \pm 1.63$	$26.87 \pm 0.47 \pm 1.26$	$26.21 \pm 0.53 \pm 1.31$
8-20	$32.25 \pm 0.71 \pm 1.68$	$28.28 \pm 0.60 \pm 1.42$	$27.93 \pm 0.76 \pm 1.46$
non-prompt			
$p_T$ (GeV/c)	$2 < y < 2.8$	$2.8 < y < 3.5$	$3.5 < y < 4.5$
0-2	$21.71 \pm 0.88 \pm 2.39$	$20.83 \pm 0.72 \pm 1.38$	$21.28 \pm 0.82 \pm 1.67$
2-4	$26.41 \pm 0.79 \pm 1.31$	$26.46 \pm 0.63 \pm 1.29$	$26.41 \pm 0.75 \pm 1.35$
4-6	$34.65 \pm 1.00 \pm 1.70$	$29.13 \pm 0.71 \pm 1.39$	$30.13 \pm 0.95 \pm 1.69$
6-8	$33.39 \pm 1.23 \pm 2.17$	$31.37 \pm 1.02 \pm 1.85$	$33.99 \pm 1.40 \pm 2.61$
8-20	$41.81 \pm 1.26 \pm 2.03$	$36.94 \pm 1.11 \pm 2.00$	$35.45 \pm 1.45 \pm 2.12$

RESULT TABLES OF  $\psi(2S)$ -TO- $J/\psi$  RATIO IN  $pp$  COLLISIONS

Table 5.7 Ratios (%) of double differential production cross-section for  $\psi(2S)$  to  $J/\psi$  in bins of  $(p_T, y)$  for  $8 \leq N_{\text{bwd}}^{\text{PV}} < 15$ . The first uncertainties are statistical, the second are systematic.

prompt			
$p_T$ ( GeV/c )	$2 < y < 2.8$	$2.8 < y < 3.5$	$3.5 < y < 4.5$
0-2	$10.88 \pm 0.21 \pm 0.53$	$10.31 \pm 0.17 \pm 0.40$	$11.35 \pm 0.16 \pm 0.55$
2-4	$15.30 \pm 0.24 \pm 0.56$	$13.74 \pm 0.18 \pm 0.43$	$14.85 \pm 0.19 \pm 0.47$
4-6	$21.98 \pm 0.33 \pm 0.78$	$18.69 \pm 0.23 \pm 0.60$	$19.23 \pm 0.27 \pm 0.64$
6-8	$27.76 \pm 0.49 \pm 1.19$	$25.11 \pm 0.38 \pm 0.91$	$24.65 \pm 0.47 \pm 1.04$
8-20	$33.44 \pm 0.60 \pm 1.44$	$28.62 \pm 0.51 \pm 1.09$	$29.46 \pm 0.66 \pm 1.52$
non-prompt			
$p_T$ ( GeV/c )	$2 < y < 2.8$	$2.8 < y < 3.5$	$3.5 < y < 4.5$
0-2	$21.38 \pm 0.82 \pm 1.35$	$19.44 \pm 0.63 \pm 1.01$	$19.59 \pm 0.71 \pm 1.30$
2-4	$25.22 \pm 0.68 \pm 1.05$	$24.62 \pm 0.53 \pm 0.91$	$26.11 \pm 0.70 \pm 1.00$
4-6	$32.12 \pm 0.80 \pm 1.27$	$27.71 \pm 0.60 \pm 1.04$	$28.15 \pm 0.81 \pm 1.36$
6-8	$33.65 \pm 0.99 \pm 1.64$	$33.25 \pm 0.88 \pm 1.46$	$32.86 \pm 1.20 \pm 2.38$
8-20	$39.68 \pm 0.95 \pm 1.75$	$37.19 \pm 0.94 \pm 1.58$	$35.36 \pm 1.31 \pm 2.08$

Table 5.8 Ratios (%) of double differential production cross-section for  $\psi(2S)$  to  $J/\psi$  in bins of  $(p_T, y)$  for  $15 \leq N_{\text{bwd}}^{\text{PV}} < 22$ . The first uncertainties are statistical, the second are systematic.

prompt			
$p_T$ ( GeV/c )	$2 < y < 2.8$	$2.8 < y < 3.5$	$3.5 < y < 4.5$
0-2	$8.97 \pm 0.27 \pm 0.32$	$9.42 \pm 0.23 \pm 0.32$	$9.58 \pm 0.21 \pm 0.39$
2-4	$13.41 \pm 0.28 \pm 0.34$	$12.68 \pm 0.22 \pm 0.27$	$13.57 \pm 0.24 \pm 0.36$
4-6	$20.29 \pm 0.38 \pm 0.55$	$17.52 \pm 0.27 \pm 0.39$	$18.62 \pm 0.33 \pm 0.48$
6-8	$25.76 \pm 0.52 \pm 0.90$	$23.21 \pm 0.41 \pm 0.69$	$22.37 \pm 0.49 \pm 0.78$
8-20	$32.96 \pm 0.62 \pm 1.24$	$28.41 \pm 0.55 \pm 0.91$	$28.58 \pm 0.73 \pm 1.04$
non-prompt			
$p_T$ ( GeV/c )	$2 < y < 2.8$	$2.8 < y < 3.5$	$3.5 < y < 4.5$
0-2	$18.28 \pm 0.84 \pm 0.91$	$19.54 \pm 0.74 \pm 0.91$	$21.70 \pm 0.89 \pm 1.02$
2-4	$26.99 \pm 0.78 \pm 0.89$	$24.53 \pm 0.61 \pm 0.84$	$24.61 \pm 0.76 \pm 1.15$
4-6	$31.88 \pm 0.91 \pm 1.02$	$25.95 \pm 0.64 \pm 1.11$	$27.80 \pm 0.93 \pm 1.13$
6-8	$35.26 \pm 1.08 \pm 1.48$	$31.24 \pm 0.93 \pm 1.30$	$32.19 \pm 1.34 \pm 1.96$
8-20	$40.96 \pm 1.06 \pm 1.57$	$36.60 \pm 1.00 \pm 1.41$	$37.63 \pm 1.47 \pm 1.93$

RESULT TABLES OF  $\psi(2S)$ -TO- $J/\psi$  RATIO IN  $pp$  COLLISIONS

---

Table 5.9 Ratios (%) of double differential production cross-section for  $\psi(2S)$  to  $J/\psi$  in bins of  $(p_T, y)$  for  $22 \leq N_{\text{bwd}}^{\text{PV}} < 30$ . The first uncertainties are statistical, the second are systematic.

prompt			
$p_T$ ( GeV/c )	$2 < y < 2.8$	$2.8 < y < 3.5$	$3.5 < y < 4.5$
0-2	$8.84 \pm 0.42 \pm 0.38$	$8.44 \pm 0.31 \pm 0.30$	$9.44 \pm 0.30 \pm 0.62$
2-4	$12.34 \pm 0.39 \pm 0.44$	$11.70 \pm 0.29 \pm 0.25$	$13.21 \pm 0.32 \pm 0.31$
4-6	$17.14 \pm 0.46 \pm 0.52$	$16.60 \pm 0.35 \pm 0.39$	$17.25 \pm 0.42 \pm 0.48$
6-8	$24.94 \pm 0.65 \pm 1.00$	$21.02 \pm 0.49 \pm 0.65$	$23.60 \pm 0.66 \pm 0.93$
8-20	$30.78 \pm 0.71 \pm 1.12$	$27.47 \pm 0.66 \pm 0.91$	$26.57 \pm 0.84 \pm 1.39$

non-prompt			
$p_T$ ( GeV/c )	$2 < y < 2.8$	$2.8 < y < 3.5$	$3.5 < y < 4.5$
0-2	$19.08 \pm 1.06 \pm 1.17$	$18.33 \pm 0.91 \pm 0.95$	$18.24 \pm 1.04 \pm 1.54$
2-4	$24.53 \pm 0.93 \pm 0.87$	$24.59 \pm 0.75 \pm 0.65$	$24.82 \pm 0.98 \pm 0.96$
4-6	$34.04 \pm 1.14 \pm 1.13$	$27.68 \pm 0.83 \pm 0.92$	$28.05 \pm 1.18 \pm 1.49$
6-8	$30.65 \pm 1.25 \pm 1.21$	$30.66 \pm 1.13 \pm 1.30$	$31.91 \pm 1.65 \pm 1.99$
8-20	$38.03 \pm 1.20 \pm 1.20$	$36.79 \pm 1.24 \pm 1.45$	$35.96 \pm 1.79 \pm 2.19$

Table 5.10 Ratios (%) of double differential production cross-section for  $\psi(2S)$  to  $J/\psi$  in bins of  $(p_T, y)$  for  $30 \leq N_{\text{bwd}}^{\text{PV}} < 80$ . The first uncertainties are statistical, the second are systematic.

prompt			
$p_T$ ( GeV/c )	$2 < y < 2.8$	$2.8 < y < 3.5$	$3.5 < y < 4.5$
0-2	$10.05 \pm 0.65 \pm 0.70$	$8.74 \pm 0.49 \pm 0.34$	$8.60 \pm 0.43 \pm 0.40$
2-4	$11.00 \pm 0.52 \pm 0.40$	$12.93 \pm 0.46 \pm 0.58$	$13.28 \pm 0.44 \pm 0.39$
4-6	$19.54 \pm 0.67 \pm 0.72$	$15.82 \pm 0.44 \pm 0.45$	$17.01 \pm 0.52 \pm 0.70$
6-8	$21.82 \pm 0.78 \pm 1.10$	$21.98 \pm 0.68 \pm 1.17$	$21.93 \pm 0.79 \pm 0.90$
8-20	$28.63 \pm 0.87 \pm 1.25$	$25.73 \pm 0.78 \pm 0.98$	$22.99 \pm 0.96 \pm 1.05$

non-prompt			
$p_T$ ( GeV/c )	$2 < y < 2.8$	$2.8 < y < 3.5$	$3.5 < y < 4.5$
0-2	$20.03 \pm 1.60 \pm 1.77$	$19.62 \pm 1.20 \pm 1.13$	$20.23 \pm 1.49 \pm 1.20$
2-4	$26.02 \pm 1.26 \pm 1.00$	$23.62 \pm 1.01 \pm 0.83$	$24.16 \pm 1.25 \pm 0.91$
4-6	$33.55 \pm 1.45 \pm 1.31$	$28.41 \pm 1.07 \pm 1.14$	$27.64 \pm 1.44 \pm 1.67$
6-8	$35.20 \pm 1.81 \pm 2.00$	$34.75 \pm 1.62 \pm 2.78$	$27.33 \pm 2.10 \pm 2.32$
8-20	$40.75 \pm 1.57 \pm 1.72$	$33.67 \pm 1.46 \pm 1.26$	$34.87 \pm 2.28 \pm 1.82$

RESULT TABLES OF  $\psi(2S)$ -TO- $J/\psi$  RATIO IN  $pp$  COLLISIONS

---

Table 5.11 Ratios (%) of double differential production cross-section for  $\psi(2S)$  to  $J/\psi$  in bins of  $(p_T, y)$  for  $0 \leq N_{\text{fwd}}^{\text{PV}} < 12$ . The first uncertainties are statistical, the second are systematic.

prompt			
$p_T$ ( GeV/ $c$ )	$2 < y < 2.8$	$2.8 < y < 3.5$	$3.5 < y < 4.5$
0-2	$16.01 \pm 0.22 \pm 0.69$	$15.86 \pm 0.18 \pm 0.62$	$16.07 \pm 0.18 \pm 0.64$
2-4	$21.67 \pm 0.37 \pm 0.92$	$19.67 \pm 0.27 \pm 0.76$	$20.59 \pm 0.31 \pm 0.80$
4-6	$28.37 \pm 0.70 \pm 1.21$	$24.31 \pm 0.51 \pm 1.00$	$23.25 \pm 0.58 \pm 1.01$
6-8	$34.96 \pm 1.38 \pm 1.75$	$27.17 \pm 1.00 \pm 1.31$	$28.99 \pm 1.26 \pm 1.47$
8-20	$33.65 \pm 1.77 \pm 1.87$	$27.14 \pm 1.59 \pm 1.41$	$28.53 \pm 2.28 \pm 2.00$

non-prompt			
$p_T$ ( GeV/ $c$ )	$2 < y < 2.8$	$2.8 < y < 3.5$	$3.5 < y < 4.5$
0-2	$22.02 \pm 1.35 \pm 1.27$	$21.28 \pm 1.08 \pm 1.27$	$23.51 \pm 1.43 \pm 1.48$
2-4	$29.87 \pm 1.36 \pm 1.82$	$26.89 \pm 1.03 \pm 1.41$	$27.32 \pm 1.33 \pm 2.18$
4-6	$35.66 \pm 1.82 \pm 1.71$	$30.86 \pm 1.42 \pm 1.81$	$35.67 \pm 1.97 \pm 2.15$
6-8	$36.27 \pm 2.50 \pm 2.10$	$35.57 \pm 2.18 \pm 2.07$	$34.00 \pm 2.92 \pm 2.13$
8-20	$48.13 \pm 3.00 \pm 2.48$	$40.55 \pm 2.76 \pm 2.12$	$39.03 \pm 3.58 \pm 3.07$

Table 5.12 Ratios (%) of double differential production cross-section for  $\psi(2S)$  to  $J/\psi$  in bins of  $(p_T, y)$  for  $12 \leq N_{\text{fwd}}^{\text{PV}} < 24$ . The first uncertainties are statistical, the second are systematic.

prompt			
$p_T$ ( GeV/ $c$ )	$2 < y < 2.8$	$2.8 < y < 3.5$	$3.5 < y < 4.5$
0-2	$12.52 \pm 0.16 \pm 0.51$	$12.00 \pm 0.12 \pm 0.45$	$12.79 \pm 0.12 \pm 0.51$
2-4	$17.29 \pm 0.20 \pm 0.69$	$16.64 \pm 0.15 \pm 0.61$	$16.81 \pm 0.16 \pm 0.62$
4-6	$24.11 \pm 0.32 \pm 0.95$	$21.80 \pm 0.23 \pm 0.81$	$22.20 \pm 0.27 \pm 0.84$
6-8	$30.99 \pm 0.54 \pm 1.38$	$27.27 \pm 0.42 \pm 1.07$	$25.82 \pm 0.50 \pm 1.08$
8-20	$34.20 \pm 0.69 \pm 1.46$	$28.33 \pm 0.59 \pm 1.21$	$28.99 \pm 0.77 \pm 1.33$

non-prompt			
$p_T$ ( GeV/ $c$ )	$2 < y < 2.8$	$2.8 < y < 3.5$	$3.5 < y < 4.5$
0-2	$19.02 \pm 0.69 \pm 1.00$	$20.54 \pm 0.60 \pm 0.90$	$20.53 \pm 0.69 \pm 1.05$
2-4	$27.70 \pm 0.70 \pm 1.17$	$26.41 \pm 0.55 \pm 1.15$	$27.35 \pm 0.69 \pm 1.20$
4-6	$33.87 \pm 0.87 \pm 1.40$	$28.73 \pm 0.63 \pm 1.24$	$28.92 \pm 0.85 \pm 1.66$
6-8	$34.24 \pm 1.10 \pm 1.97$	$31.66 \pm 0.95 \pm 1.53$	$36.00 \pm 1.40 \pm 2.05$
8-20	$42.40 \pm 1.14 \pm 1.83$	$36.58 \pm 1.06 \pm 1.62$	$37.08 \pm 1.47 \pm 1.96$

---

 RESULT TABLES OF  $\psi(2S)$ -TO- $J/\psi$  RATIO IN  $pp$  COLLISIONS
 

---

Table 5.13 Ratios (%) of double differential production cross-section for  $\psi(2S)$  to  $J/\psi$  in bins of  $(p_T, y)$  for  $24 \leq N_{\text{fwd}}^{\text{PV}} < 36$ . The first uncertainties are statistical, the second are systematic.

prompt			
$p_T$ ( GeV/c )	$2 < y < 2.8$	$2.8 < y < 3.5$	$3.5 < y < 4.5$
0-2	$10.25 \pm 0.19 \pm 0.50$	$9.94 \pm 0.15 \pm 0.45$	$10.47 \pm 0.14 \pm 0.49$
2-4	$15.01 \pm 0.21 \pm 0.74$	$14.06 \pm 0.16 \pm 0.63$	$15.27 \pm 0.17 \pm 0.69$
4-6	$22.14 \pm 0.30 \pm 1.03$	$19.72 \pm 0.21 \pm 0.88$	$19.45 \pm 0.24 \pm 0.89$
6-8	$27.15 \pm 0.43 \pm 1.36$	$24.99 \pm 0.34 \pm 1.15$	$24.87 \pm 0.42 \pm 1.26$
8-20	$34.19 \pm 0.55 \pm 1.69$	$29.95 \pm 0.48 \pm 1.41$	$28.70 \pm 0.59 \pm 1.56$
non-prompt			
$p_T$ ( GeV/c )	$2 < y < 2.8$	$2.8 < y < 3.5$	$3.5 < y < 4.5$
0-2	$20.86 \pm 0.70 \pm 1.14$	$19.55 \pm 0.57 \pm 1.06$	$20.70 \pm 0.66 \pm 1.15$
2-4	$24.64 \pm 0.59 \pm 1.30$	$25.44 \pm 0.49 \pm 1.22$	$25.49 \pm 0.61 \pm 1.24$
4-6	$33.39 \pm 0.75 \pm 1.71$	$28.38 \pm 0.55 \pm 1.50$	$28.53 \pm 0.75 \pm 1.59$
6-8	$34.21 \pm 0.91 \pm 1.88$	$32.26 \pm 0.78 \pm 1.66$	$33.53 \pm 1.12 \pm 2.48$
8-20	$39.71 \pm 0.87 \pm 2.00$	$36.66 \pm 0.85 \pm 1.87$	$34.49 \pm 1.16 \pm 2.10$

Table 5.14 Ratios (%) of double differential production cross-section for  $\psi(2S)$  to  $J/\psi$  in bins of  $(p_T, y)$  for  $36 \leq N_{\text{fwd}}^{\text{PV}} < 48$ . The first uncertainties are statistical, the second are systematic.

prompt			
$p_T$ ( GeV/c )	$2 < y < 2.8$	$2.8 < y < 3.5$	$3.5 < y < 4.5$
0-2	$8.97 \pm 0.27 \pm 0.34$	$8.91 \pm 0.21 \pm 0.28$	$9.18 \pm 0.19 \pm 0.35$
2-4	$12.98 \pm 0.25 \pm 0.40$	$12.24 \pm 0.20 \pm 0.35$	$13.34 \pm 0.21 \pm 0.40$
4-6	$19.67 \pm 0.33 \pm 0.66$	$17.34 \pm 0.24 \pm 0.48$	$18.71 \pm 0.27 \pm 0.62$
6-8	$25.22 \pm 0.45 \pm 0.91$	$24.19 \pm 0.37 \pm 0.77$	$22.53 \pm 0.43 \pm 0.93$
8-20	$30.83 \pm 0.52 \pm 1.17$	$29.39 \pm 0.48 \pm 1.01$	$26.80 \pm 0.58 \pm 1.10$
non-prompt			
$p_T$ ( GeV/c )	$2 < y < 2.8$	$2.8 < y < 3.5$	$3.5 < y < 4.5$
0-2	$19.55 \pm 0.82 \pm 0.94$	$18.95 \pm 0.68 \pm 0.89$	$18.66 \pm 0.73 \pm 0.97$
2-4	$24.04 \pm 0.66 \pm 0.87$	$24.03 \pm 0.55 \pm 0.86$	$24.57 \pm 0.67 \pm 0.97$
4-6	$32.21 \pm 0.79 \pm 1.18$	$26.33 \pm 0.56 \pm 0.83$	$27.16 \pm 0.79 \pm 1.37$
6-8	$32.09 \pm 0.91 \pm 1.37$	$33.16 \pm 0.85 \pm 1.31$	$31.59 \pm 1.13 \pm 2.03$
8-20	$38.94 \pm 0.89 \pm 1.47$	$37.14 \pm 0.87 \pm 1.45$	$39.10 \pm 1.30 \pm 1.88$

RESULT TABLES OF  $\psi(2S)$ -TO- $J/\psi$  RATIO IN  $pp$  COLLISIONS

Table 5.15 Ratios (%) of double differential production cross-section for  $\psi(2S)$  to  $J/\psi$  in bins of  $(p_T, y)$  for  $48 \leq N_{\text{fwd}}^{\text{PV}} < 130$ . The first uncertainties are statistical, the second are systematic.

$p_T$ (GeV/c)	prompt		
	$2 < y < 2.8$	$2.8 < y < 3.5$	$3.5 < y < 4.5$
0-2	$7.83 \pm 0.35 \pm 0.31$	$7.63 \pm 0.28 \pm 0.31$	$8.44 \pm 0.25 \pm 0.25$
2-4	$10.93 \pm 0.30 \pm 0.35$	$10.96 \pm 0.24 \pm 0.28$	$11.58 \pm 0.23 \pm 0.29$
4-6	$18.12 \pm 0.35 \pm 0.63$	$15.04 \pm 0.24 \pm 0.35$	$16.48 \pm 0.28 \pm 0.60$
6-8	$23.28 \pm 0.44 \pm 0.83$	$19.97 \pm 0.32 \pm 0.54$	$22.83 \pm 0.42 \pm 0.82$
8-20	$29.91 \pm 0.46 \pm 0.98$	$27.16 \pm 0.41 \pm 1.04$	$25.68 \pm 0.51 \pm 1.07$
non-prompt			
$p_T$ (GeV/c)	$2 < y < 2.8$	$2.8 < y < 3.5$	$3.5 < y < 4.5$
	$19.00 \pm 0.87 \pm 1.09$	$17.31 \pm 0.66 \pm 1.00$	$19.72 \pm 0.79 \pm 0.85$
2-4	$24.67 \pm 0.68 \pm 0.83$	$24.22 \pm 0.55 \pm 0.70$	$24.98 \pm 0.68 \pm 0.83$
4-6	$30.68 \pm 0.76 \pm 0.98$	$27.65 \pm 0.57 \pm 0.94$	$27.95 \pm 0.74 \pm 1.13$
6-8	$32.93 \pm 0.89 \pm 1.21$	$32.79 \pm 0.78 \pm 1.22$	$29.56 \pm 1.01 \pm 1.59$
8-20	$39.20 \pm 0.79 \pm 1.35$	$35.10 \pm 0.75 \pm 1.30$	$34.72 \pm 1.11 \pm 1.71$

## RESULT TABLES OF $\psi(2S)$ -TO- $J/\psi$ RATIO IN $p\text{Pb}$ COLLISIONS

Table 5.16 Ratio(%) of production cross-section for  $\psi(2S)$  to  $J/\psi$ . The first uncertainties are statistical, the second are the systematic uncertainties.

$p\text{Pb}$					
$N_{\text{tracks}}^{\text{PV}}$	4 45	45 70	70 90	90 120	120 270
prompt	$0.172 \pm 0.010 \pm 0.008$	$0.142 \pm 0.010 \pm 0.006$	$0.112 \pm 0.010 \pm 0.005$	$0.124 \pm 0.010 \pm 0.006$	$0.101 \pm 0.011 \pm 0.005$
non-prompt	$0.219 \pm 0.034 \pm 0.012$	$0.230 \pm 0.028 \pm 0.011$	$0.195 \pm 0.026 \pm 0.009$	$0.265 \pm 0.025 \pm 0.011$	$0.243 \pm 0.027 \pm 0.010$
$\text{Pb}p$					
$N_{\text{tracks}}^{\text{PV}}$	4 60	60 90	90 120	120 160	160 330
prompt	$0.118 \pm 0.006 \pm 0.006$	$0.093 \pm 0.006 \pm 0.004$	$0.112 \pm 0.008 \pm 0.005$	$0.090 \pm 0.009 \pm 0.004$	$0.126 \pm 0.017 \pm 0.006$
non-prompt	$0.240 \pm 0.023 \pm 0.012$	$0.193 \pm 0.021 \pm 0.009$	$0.197 \pm 0.020 \pm 0.010$	$0.216 \pm 0.022 \pm 0.009$	$0.304 \pm 0.040 \pm 0.013$

Table 5.17 Ratio(%) of production cross-section for  $\psi(2S)$  to  $J/\psi$ . The first uncertainties are statistical, the second are the systematic uncertainties.

$p\text{Pb}$					
$N_{\text{fwd}}^{\text{PV}}$	0 25	25 43	43 57	57 72	72 150
prompt	$0.183 \pm 0.010 \pm 0.007$	$0.136 \pm 0.007 \pm 0.005$	$0.144 \pm 0.008 \pm 0.005$	$0.111 \pm 0.008 \pm 0.004$	$0.114 \pm 0.008 \pm 0.004$
non-prompt	$0.192 \pm 0.034 \pm 0.009$	$0.236 \pm 0.021 \pm 0.009$	$0.216 \pm 0.021 \pm 0.009$	$0.262 \pm 0.022 \pm 0.009$	$0.222 \pm 0.018 \pm 0.008$
$\text{Pb}p$					
$N_{\text{fwd}}^{\text{PV}}$	0 35	35 65	65 85	85 110	110 250
prompt	$0.121 \pm 0.006 \pm 0.006$	$0.097 \pm 0.006 \pm 0.004$	$0.104 \pm 0.007 \pm 0.004$	$0.098 \pm 0.008 \pm 0.004$	$0.099 \pm 0.012 \pm 0.004$
non-prompt	$0.262 \pm 0.028 \pm 0.012$	$0.199 \pm 0.018 \pm 0.009$	$0.225 \pm 0.022 \pm 0.010$	$0.198 \pm 0.021 \pm 0.009$	$0.255 \pm 0.027 \pm 0.010$

Table 5.18 Ratio(%) of production cross-section for  $\psi(2S)$  to  $J/\psi$ . The first uncertainties are statistical, the second are the systematic uncertainties.

$p\text{Pb}$					
$N_{\text{bwd}}^{\text{PV}}$	0 17	17 29	29 40	40 54	54 180
prompt	$0.151 \pm 0.009 \pm 0.007$	$0.120 \pm 0.009 \pm 0.005$	$0.128 \pm 0.010 \pm 0.006$	$0.132 \pm 0.012 \pm 0.006$	$0.093 \pm 0.012 \pm 0.004$
non-prompt	$0.219 \pm 0.027 \pm 0.011$	$0.220 \pm 0.024 \pm 0.010$	$0.238 \pm 0.026 \pm 0.011$	$0.252 \pm 0.029 \pm 0.011$	$0.242 \pm 0.033 \pm 0.009$
$\text{Pb}p$					
$N_{\text{bwd}}^{\text{PV}}$	0 13	13 22	22 30	30 47	47 120
prompt	$0.118 \pm 0.008 \pm 0.006$	$0.103 \pm 0.008 \pm 0.005$	$0.106 \pm 0.009 \pm 0.006$	$0.097 \pm 0.008 \pm 0.005$	$0.113 \pm 0.018 \pm 0.006$
non-prompt	$0.209 \pm 0.032 \pm 0.012$	$0.219 \pm 0.025 \pm 0.011$	$0.217 \pm 0.024 \pm 0.012$	$0.243 \pm 0.023 \pm 0.012$	$0.239 \pm 0.041 \pm 0.012$

## ACKNOWLEDGEMENTS

### 5.3 实验室篇

感谢我的导师朱相雷。朱老师学识深广，儒雅随和，对待科研工作严谨认真，在科研道路上为我提供诸多建议与帮助。谢谢您（鞠躬）！

感谢杨振伟老师，张黎明老师。在科研路上为我树立榜样。

感谢实验室遇到的所有小伙伴，王梦臻，陈晨，王剑桥，许立，沈志宏，王子睿，董宸志，从你们身上我学到了很多。

### 5.4 家人篇

感谢我的父母康必录和官秀玉，不仅给予我生命，更给予我关怀和爱，让我身心健康成长。

感谢我的最爱，即我的妻子马淑玉，多年来我们相互陪伴相互扶持相互学习相互成就，庆幸与你共度余生。

感谢我的两位姐姐康雅芳和康蒙爱，和带给我无限欢乐的三位小外甥张宸泽，江崇一和江鸣一。

## 声 明

本人郑重声明：所呈交的学位论文，是本人在导师指导下，独立进行研究工作所取得的成果。尽我所知，除文中已经注明引用的内容外，本学位论文的研究成果不包含任何他人享有著作权的内容。对本论文所涉及的研究工作做出贡献的其他个人和集体，均已在文中以明确方式标明。

签 名： \_\_\_\_\_ 日 期： \_\_\_\_\_

## **COMMENTS FROM THESIS SUPERVISOR**

**RESOLUTION OF THESIS DEFENSE COMMITTEE**